A Spectroscopic and Photometric Study of Gravitational Microlensing Events

by

Stephen Robert Kane, B.Sc.(Hons.)

Submitted in fulfillment of the requirements
for the degree of
Doctor of Philosophy
at the
University of Tasmania

Physics

October, 2000

Declaration

This thesis contains no material which has been accepted for the award of any other higher degree or graduate diploma in any tertiary institution. To the best of my knowledge and belief, this thesis contains no material previously published or written by another person, except where due reference has been made in the text of the thesis.

Stephen Kane

Stephen Kane

Statement of Authority of Access

This thesis may be made available for loan and limited copying in accordance with the *Copyright Act 1968*.

Stephen Kane

Stephen Kane
11th October, 2000

Dedicated to

Those who inspired me,

Those who encouraged me,

and Those who believed in me.

Abstract

Gravitational microlensing has generated a great deal of scientific interest over recent years. This has been largely due to the realization of its wide-reaching applications, such as the search for dark matter, the detection of planets, and the study of Galactic structure. A significant observational advance has been that most microlensing events can be identified in real-time while the source is still being lensed. More than 400 microlensing events have now been detected towards the Galactic bulge and Magellanic Clouds by the microlensing survey teams EROS, MACHO, OGLE, DUO, and MOA. The real-time detection of these events allows detailed follow-up observations with much denser sampling, both photometrically and spectroscopically.

The research undertaken in this project on photometric studies of gravitational microlensing events has been performed as a member of the PLANET (**P**robing **L**ensing **A**nomalies **NET**work) collaboration. This is a worldwide collaboration formed in the early part of 1995 to study microlensing anomalies - departures from an achromatic point source, point lens light curve - through rapidly-sampled, multi-band, photometry. PLANET has demonstrated that it can achieve 1% photometry under ideal circumstances, making PLANET observations sensitive to detection of Earth-mass planets which require characterization of 1%–2% deviations from a standard microlensing light curve.

The photometric work in this project involved over 5 months using the 1.0 m telescope at Canopus Observatory in Australia, and 3 separate observing runs using the 0.9 m telescope at the Cerro Tololo Inter-American Observatory (CTIO) in Chile. Methods were developed to reduce the vast amount of photometric data using the image analysis software MIDAS and the photometry package DoPHOT. Modelling routines were then written to analyse a selection of the resulting light curves in order to detect any deviation from an achromatic point source - point lens light curve.

The photometric results presented in this thesis are from observations of 34 microlensing events over three consecutive bulge seasons. These results are presented along with a discussion of the observations and the data reduction procedures. The colour-magnitude diagrams indicate that the microlensed sources are main sequence and red clump giant stars. Most of the events appear to exhibit standard Paczyński point source - point lens curves whilst a few deviate

significantly from the standard model. Various microlensing models that include anomalous structure are fitted to a selection of the observed events resulting in the discovery of a possible binary source event. These fitted events are used to estimate the sensitivity to extra-solar planets and it is found that the sampling rate for these events was insufficient by about a factor of 7.5 for detecting a Jupiter-mass planet. This result assumes that deviations of 5% can be reliably detected.

If microlensing is caused predominantly by bulge stars, as has been suggested by Kiraga and Paczyński [54], the lensed stars should have larger extinction than other observed stars since they would preferentially be located at the far side of the Galactic bulge. Hence, spectroscopy of Galactic microlensing events may be used as a tool for studying the kinematics and extinction effects in the Galactic bulge.

The spectroscopic work in this project involved using Kurucz model spectra to create theoretical extinction effects for various spectral classes towards the Galactic centre. These extinction effects are then used to interpret spectroscopic data taken with the 3.6 m ESO telescope. These data consist of a sample of microlensed stars towards the Galactic bulge and are used to derive the extinction offsets of the lensed source with respect to the average population and a measurement of the fraction of bulge-bulge lensing is made. Hence, it is shown statistically that the microlensed sources are generally located on the far side of the Galactic bulge. Measurements of the radial velocities of these sources are used to determine the kinematic properties of the far side of the Galactic bulge.

Acknowledgements

The work performed on the research described in this thesis has benefited in many ways by the assistance provided by my supervisors, co-workers, and friends.

Firstly, I would like to express my sincere gratitude to my supervisors, Dr. John Greenhill and Dr. Kailash Sahu, for their support of my project. Their guidance, interest in the project, and their eagerness to share ideas concerning the research was much appreciated throughout the course of my work.

I also owe many thanks to those who helped me to "learn the ropes" of the software packages that I was to use in the course of my research. Many thanks to Paul Vreeswijk for his invaluable assistance in learning DoPHOT, MIDAS, C shell scripts, and SuperMongo. It was a week long crash course that was most invaluable. Thanks to Mike Potter for his help in learning DoPHOT and introducing me to the analysis of photometric data. Also, thanks to Edwin Huizinga for his constant assistance with matters concerning MIDAS and SuperMongo.

In this regard, a special thanks is reserved for Dr. Kym Hill who helped me greatly with not only learning to write MIDAS routines, but also served as computer support and observer support during my time at the University of Tasmania. His friendship and advice throughout the course of my project was invaluable and much needed during those stressful times that come with writing a Ph.D. thesis.

My thanks go to the National Optical Astronomy Observatories (NOAO) for their funding of my observing trips to the Cerro Tololo Inter-American Observatory (CTIO). I'd also like to thank the observer support staff at CTIO for their friendliness and help during my stay, particularly to Mauricio Navarrete for his tremendous help in storing the raw data on EXABYTE tapes in time for my departure.

I'd like to express many thanks to the PLANET collaboration, that I was so proud to be a part of, for their help in the conduct of my research and for humouring my suggestion of a "group hug" at each of the PLANET meetings. Particularly, I'd like to thank Dr. Jean-Philippe Beaulieu and Dr. John Menzies for their help with the PLANET pipeline and archiving software. My thanks go to Dr. Penny Sackett for her leadership within the PLANET collaboration and for providing colour-magnitude diagrams constructed from the PLANET archives. Also, I'd like to thank Dr. Martin Dominik, Pierre Vermaak, and Dr. Eric

Agol for their help with understanding the theory of gravitational microlensing. Additional thanks are reserved for Dr. Simon Wotherspoon for his help with the theory and also with the statistics used in the analysis of the results. My thanks also go to Dr. Robert Watson for taking the time to read through and comment on my draft thesis.

My thanks go to my fellow postgraduate students, both at the Space Telescope Science Institute and at the University of Tasmania, for sharing this journey with me. Also, I'd like to thank my friends who have supported me and encouraged me along the path that I have taken. Special thanks go to my wife, Theresa, who forced me to work when she knew it was required and forced me to take a break when she felt it was needed. Her love and support have helped me during this time more than I can say.

Lastly, I would like to thank, and indeed give all credit to, the one whose presence has guided me, whose love has comforted me, and whose strength has lifted me - the Lord Jesus Christ.

Contents

Chapter 1

Introduction

1.1 Gravitational Microlensing

1.1.1 The Search for Dark Matter

In astronomy, as in other sciences, objects can be detected either directly through observation, or indirectly through the effects they have on their surroundings. Indirect detection plays a key role in the discovery of bodies which are non-luminous but for which their gravitational influence can be observed to effect neighbouring bright objects.

The first evidence that there exists a significant amount of matter that we cannot readily see came from observations of clusters of galaxies. It was found from the virial theorem (assuming that the virial theorem holds true for dynamics on such a large scale) that the radial velocities of the galaxies in a cluster indicated that visible stars only contribute a few percent of the total mass of the cluster. Some of the missing mass was later found to be attributed to hot X-ray gas, but that still left approximately 85% of the mass unaccounted for [92, 97].

Further evidence for missing mass was found in the rotation curves of galaxies. The Doppler effect can be used to accurately measure the radial velocity of stars and gas in spiral galaxies as a function of galactocentric distance. It is found from studying the resulting rotation curves that the mass profile of the galaxies is much more extended than the distribution of starlight.

It is the prevailing view that much of the mass in the universe takes the form of *dark matter.* Although the nature of dark matter is not known, two broad classes have been postulated: subatomic particles, a subset of which are called Weakly Interacting Massive Particles (WIMPs), and astrophysical size objects called Massive Compact Halo Objects (MACHOs). MACHOs were originally thought to provide the dominant mass for the Galactic halo but they have been found to play a more important role in the Galactic disk and bulge. MACHOs emit little or no electromagnetic radiation but can be detected indirectly by their participation in *gravitational microlensing.*

1.1.2 Microlensing Principles

The topic of light rays being bent due to the presence of a gravitational field has a history dating as far back as to the writings of Sir Isaac Newton in 1704. The most notable progress on this subject was made by Albert Einstein in the development of his General Theory of Relativity which led to an equation for the deflection α of a light ray at a distance r from a mass M.

$$\alpha = \frac{4GM}{c^2 r}$$

In 1936 Einstein published a paper [36] at the request of a friend. In this paper he imagined an observed star A and a star B located in the line of sight from the observer to star A (see Figure 1.1). He then calculated the deflection of light from star A due to star B and found that star A will be *lensed*. The images resulting from the gravitational lens can be highly magnified if the observer and the two stars are sufficiently closely aligned but, for Galactic distances, the angular separation between the images will be of the order of milli-arcseconds. Conventionally, however, gravitational lensing due to stars has come to be called *microlensing*, not millilensing.

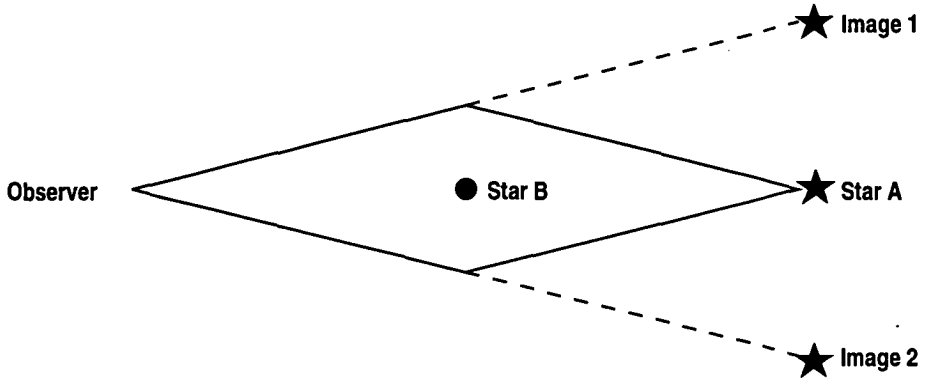

Figure 1.1: Light deflection of star A due to star B.

While the images produced are too small to be resolved, the sum of the luminosity of the images will cause the observed luminosity of star A to vary with time as star B moves relative to star A. However, the chance of observing one star passing in front of another in this fashion is extremely small so, Einstein concluded his 1936 paper by saying that "there is no great chance of observing this phenomenon."

A paper published by Paczyński [74] in 1986 suggested that microlensing could be used to detect compact objects in the halo of our Galaxy. This, he proposed, could be achieved by monitoring the brightness of a few million stars in the Magellanic Clouds. The new CCD technology brought this into the realm of possibility and the project was taken up by several survey groups. This led to the first observed microlensing events towards the LMC in 1993 [12, 19].

1.1.3 Microlensing Signatures

It may be thought that a variable star could easily be confused for an observed microlensing event but in fact a microlensing event and its associated light curve have distinct features which prevent this [20, 97]. The signatures of a microlensing event may be summarised as follows:

- Since the optical depth to microlensing is $\approx 10^{-6}$, one would expect that any given star is only microlensed once.
- Microlensing events are achromatic, hence the microlensed star should not change colour during the amplification.
- Light curves produced from microlensing events have a special characteristic shape, often called a *Paczyński* curve.
- The microlensing light curves should be symmetrical in shape since the acceleration of Galactic stars is negligible on the timescales of these events.

By comparison, most variable stars have a periodic or quasi-periodic luminosity, have an asymmetrical light curve, and change colour due to a change in surface temperature as the star expands and contracts. Flare stars, which brighten and relapse sporadically, can also be distinguished from microlensed stars due to their change in colour.

1.1.4 Microlensing Anomalies

A standard microlensing light curve, or Paczyński curve, (see Figure 1.2) is produced when the foreground object, called the *lens*, and the background object, called the *source*, can be considered as simple point masses. In most cases this approximation is completely adequate to describe and model the microlensing event. However, in some situations there are additional factors which result in observed deviations from the standard microlensing light curve.

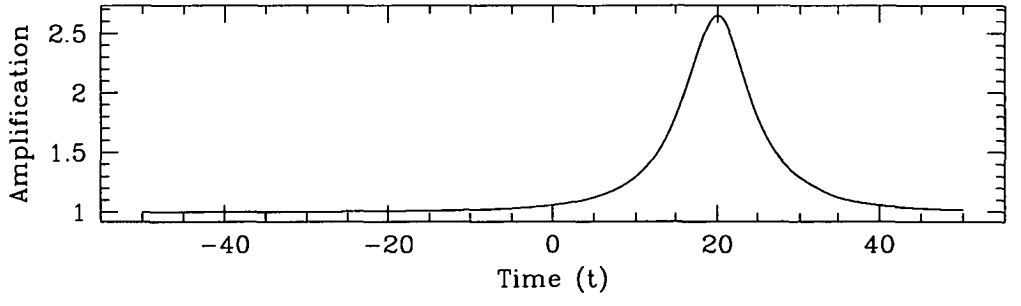

Figure 1.2: An example of a microlensing light curve.

The most common anomaly is *blending* which is caused by a fraction of light from the vicinity of the microlensed source being due to a close, unresolved blended star. Most microlensing searches are performed in very crowded fields, so this effect is commonly observed. Astrometric means can be used to detect the blend in some cases through a correlation between the image centroid and the apparent brightness. Otherwise the effect has to be corrected for statistically by placing artificial stellar images on the image frames. [117].

For long duration microlensing events, the orbital motion of the Earth has a non-neglible effect on the microlensing light curve. The resulting perturbation in the light curve serve as an extremely useful tool for determining the transverse velocity of the lens and hence constrain the mass and distance to the lens. This *parallax* effect was first predicted by Gould [41] and subsequently observed.

Although the standard model assumes a point source, this may not be acceptable if the angular size of the source is comparable to the minimum angular distance between the lens and the source. The magnification for an extended source is significantly different from that for a point source [115]. The *finite source effects* are of great astrophysical value because the differential magnification can be used to reconstruct the radial intensity profile across the face of the star. The MACHO collaboration detected finite source effects in event MB95030 [16] and the PLANET collaboration were able to use the transit of a lens across an extended source in event MB97028 to produce the stellar profile and hence calculate the limb-darkening coefficients [8].

By far the most interesting anomalous behaviour that a microlensing event can exhibit is that resulting from a binary lens [60]. The inherent astigmatism in a binary lens can lead to extremely complicated light curves caused by regions of high magnification contained within closed curves called *caustics*. The solutions to light curves of binary lenses can be described by the introduction of three additional free parameters; the mass ratio, the separation of the lens components, and the orientation of the binary relative to the source path. These parameters are useful in placing constraints on the modelling and can be used to predict the timing of future caustic crossings.

A special case of the binary lens becomes apparent when the mass ratio is such that one lens component can be considered as a planet or a brown dwarf. Since it has been found that most stars reside in binary systems, and it is presumed that most stars have planetary companions, it is expected that a substantial number of the observed microlensing events should show a planetary signature in the corresponding light curve. However, several papers written on the subject [21, 23, 42] have shown that the perturbation due to a compact dark companion of planetary mass are of short duration and so require intense monitoring to be detected.

1.1.5 Microlensing Searches

There are several collaborative groups conducting searches for microlensing events towards the Galactic bulge and the Magellanic Clouds. These have included MACHO, OGLE, EROS, DUO, and MOA. The history of these groups as well as their current status will be briefly outlined.

The MACHO (Massive Compact Halo Objects) collaboration [11] has been the most active of all the microlensing search groups. Since the collaboration started in 1992, they have been using the 1.3 m telescope located at Mt. Stromlo Observatory near Canberra, Australia. Their high data rate has allowed them to discover almost 300 microlensing events since they began in 1993 until the end of 1998. Most of these events are towards the Galactic bulge but about 15 are LMC events (see Figure 1.3) and 2 are SMC events. MACHO is continuing to alert the astronomical community of on-going microlensing events during 1999 and maintains a web site located at:
http://wwwmacho.mcmaster.ca/

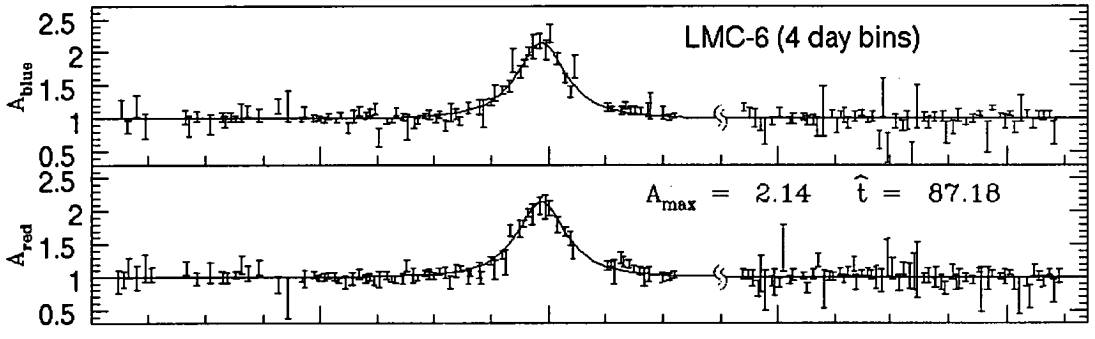

Figure 1.3: MACHO LMC light curve. [15]

The OGLE (Optical Gravitational Lensing Experiment) collaboration [98] began in 1992 using the 1.0 m Swope telescope at the Las Campanas Observatory in Chile. In 1993 OGLE detected the first microlensing event towards the Galactic bulge [104]. Though successful, their initial observing campaigns were hampered by limited availability of telescope time. However, in 1996 the newly constructed 1.3 m Warsaw Telescope at Las Campanas saw "first light" and, with the addition of their Early Warning System [106], OGLE were able to alert more than 40 microlensing events during the 1998 season. OGLE is continuing to issue alerts during 1999 and maintains a web site located at:
http://www.astrouw.edu.pl/ ftp/ogle/index.html

The EROS (Experience pour la Recherche d'Objets sombres) collaboration [47] began in 1990 and performs research on dark stellar bodies as well as variable stars and supernovae. In 1993 EROS announced the detection of two microlensing events towards the LMC along with MACHO and has since detected and alerted a few new microlensing candidates towards the Galactic bulge during the 1998

observing season. EROS maintains a web site located at:
http://www.lal.in2p3.fr/recherche/eros/

The DUO (Disk Unseen Objects) collaboration [2] has had great success considering the small number of people working on the project. Analysing photographic plates collected using the ESO 1.0 m Schmidt telescope at La Silla in Chile, DUO was able to detect about 10 microlensing events towards the Galactic bulge during the 1994 observing season.

The MOA (Microlensing Observations in Astrophysics) collaboration began in 1995 and is a joint Japanese/New Zealand experiment. The collaboration uses the facilities available at the Mount John University Observatory (MJUO), the 0.6 m Boller & Chivens telescope in particular. Once their automated system is operational, MOA plans to collect wide-field images of the LMC and to start issuing microlensing alerts. MOA maintains a web site located at:
http://www.vuw.ac.nz/scps/moa/

1.2 The PLANET Collaboration

The PLANET collaboration [4, 5, 6] was brought into existence in January, 1995 by Penny Sackett and Kailash Sahu after they attended the first workshop on gravitational microlensing which was held in Livermore, California. Since then PLANET (**P**robing **L**ensing **A**nomalies **NET**work) has grown into a worldwide collaboration of astronomers which performs intensive follow-up monitoring of the events detected by the survey teams with a primary goal of studying microlensing anomalies.

Figure 1.4 shows the location of PLANET telescopes used during the bulge season (the season during which it is possible to observe the Galactic bulge). When PLANET began its first season in 1995 it used the South African Astronomical Observatory (SAAO), the Dutch/ESO telescope at La Silla Observatory in Chile, and Perth Observatory in Australia. In the 1996 bulge season, Canopus Observatory in Tasmania, Australia was added to improve the longitude coverage, bringing the total to four participating sites. Beginning in 1997, PLANET observations were made at the Cerro Tololo Inter-American Observatory (CTIO) in Chile and in 1998 a substantial number of PLANET observations took place at the Yale telescope, also located at CTIO. By the end of the 1998 observing season, the PLANET collaboration had grown to include the following members and telescopes:

1. Kapteyn Institute, Groningen, The Netherlands

   - Telescope: 0.9 m at La Silla
   - Members: Martin Dominik, Richard Naber, Jan-Willem Pel, Penny Sackett

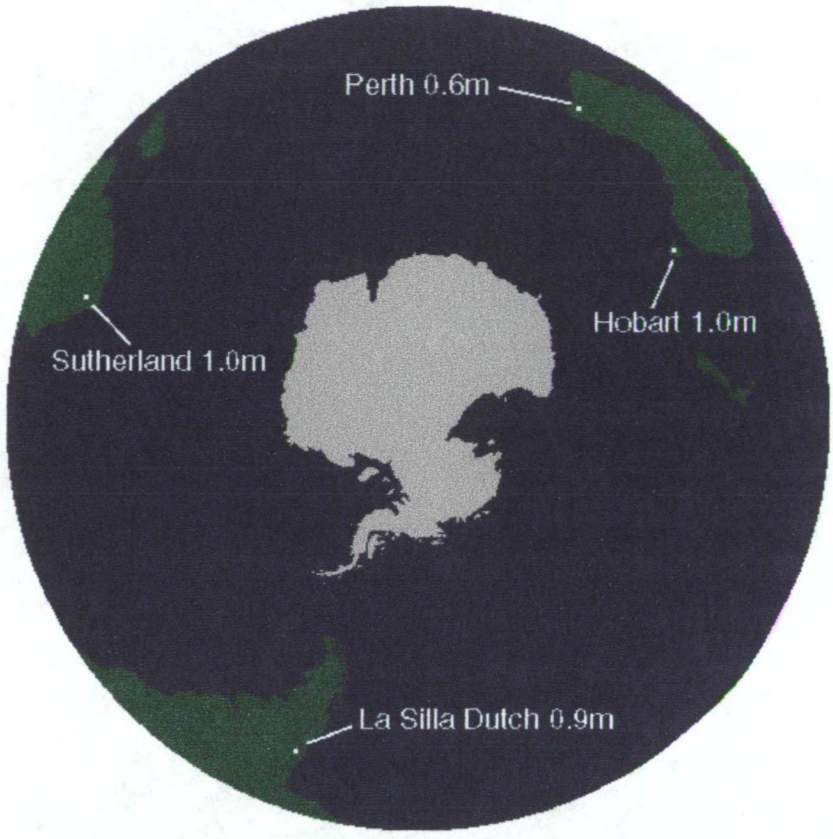

Figure 1.4: PLANET telescope locations.

2. Space Telescope Science Institute, Baltimore, U.S.A.
   - Telescope: 0.9 m at CTIO
   - Members: Michael Albrow, Kailash Sahu
3. South African Astronomical Observatory, Capetown, South Africa
   - Telescope: 1.0 m
   - Members: John Caldwell, John Menzies, Pierre Vermaak
4. University of Canterbury, Christchurch, New Zealand
   - Members: Karen Pollard
5. Perth Observatory, Bickley, Australia
   - Telescope: 0.6 m
   - Members: Ralph Martin, Andrew Williams

6. Canopus Observatory, Hobart, Australia

   - Telescope: 1.0 m
   - Members: John Greenhill, Kym Hill, Stephen Kane, Robert Watson

7. Ohio State University, Columbus, U.S.A.

   - Telescope: 1.0 m Yale
   - Members: Darren DePoy, Scott Gaudi, Andrew Gould, Richard Pogge

8. Institut d'Astrophysique de Paris, Paris, France

   - Members: Jean-Philippe Beaulieu

The longitude coverage provided by these telescopes allows PLANET to obtain (weather permitting) almost continuous coverage of on-going microlensing events. Through rapidly-sampled, multi-band photometry of microlensing anomalies, an ultimate goal of PLANET is to place constraints on the number and distribution of planets around other stars. Since PLANET is able to dedicate its telescope time to follow-up observations, it is much more sensitive to microlensing anomalies which the survey teams might miss.

During the 1995 PLANET pilot campaign [7], 11 alerts were monitored towards the Galactic bulge (see Figure 1.5). The alerts were issued by the MACHO and OGLE projects using their real-time electronic alert systems.

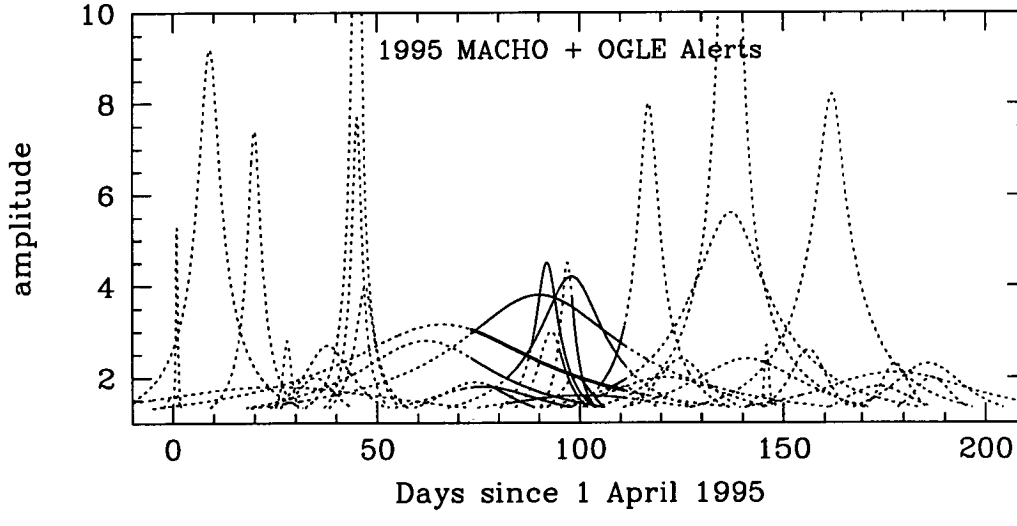

Figure 1.5: Light curves alerted by MACHO and OGLE during the 1995 pilot season. The coverage obtained by PLANET corresponds to days 73 to 111 on this plot. [7]

During each of the bulge seasons, the frequency of on-going microlensing events at any one time was large enough to assure that observations continued when weather was favourable. The events were typically sampled in both I and V band with a frequency of 1-3 hours depending on the duration of the event. PLANET has demonstrated that it can achieve 1% photometry under ideal circumstances, making PLANET observations sensitive to detection of Earth-mass planets which require characterization of 1%-2% deviations from a standard microlensing light curve [6].

The PLANET data has so far been reduced using a reduction software facility called *DoPHOT*. The on-line reduction which is operating at some of the PLANET sites has allowed the collaboration to issue secondary alerts to the rest of the microlensing survey teams in the event of a caustic crossing or any other deviation from the standard light curve. Performing photometry on all stars in the crowded bulge fields has led to a large database of magnitudes and colours for 6000-10000 stars in each field. The PLANET database is particularly well-suited for the study of short-period, low-amplitude variables as well as the discovery of short-duration microlensing events.

1.3 Spectroscopy

A significant observational advance has been that most microlensing events can be identified in real-time while they are still being lensed. This allows detailed follow-up observations with much denser sampling, both photometrically and spectroscopically. Successful spectroscopic observations have been made of several on-going microlensing events [58, 86] providing valuable contributions to the modelling of these events.

1.3.1 Breaking the Degeneracy

A normal microlensing event provides the observer with only three directly measurable quantities: the amplification, the time of maximum amplification, and the duration of the event. Of these three, only the duration of the event provides any information about the lens. The duration of the event is a function of the mass, distance, and velocity of the lens. A measurement of the duration allows the relationship between these three quantities to be determined. However, the lens parameters cannot be determined independently, which leads to degeneracies in the modelling of the light curves, as is represented in Figure 1.6. This means that there exists a continuum of lens parameters which can produce similar duration microlensing events. For example, a lens with a high velocity may be confused with a less massive lens [16].

The information needed to break these degeneracies can sometimes be provided by anomalies resulting from deviations from the standard microlensing

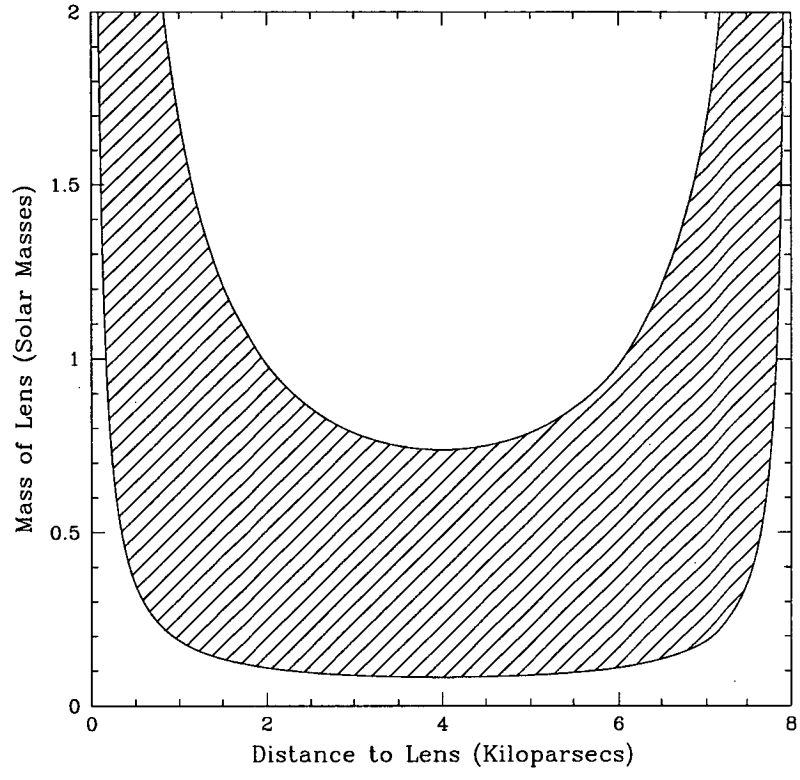

Figure 1.6: The degeneracy inherent in the lens parameters of a standard microlensing event is shown graphically. Assuming an event duration of 40 days and a lens velocity of between 100 and 300 $\mathrm{km\,s^{-1}}$, the possible values of the mass and distance to the lens can lie anywhere within the shaded region.

light curve. The observation of parallax for long duration microlensing events, the effects of an extended source, and the detection of binary microlensing each contain light curve fine structure which may help to restrict the lens parameters. A valuable contribution in these situations is the additional information which can be extracted from the spectra of microlensed sources.

Typing of the spectra of the lensed source star helps to provide an estimate of physical quantities related to the source star such as the source radius, temperature, and surface gravity. In the case of extended source effects, knowledge of the source radius and the time taken for the lens to cross the source star allows the relative angular speed of the lens to be determined. In the case of limb-darkening, estimates of the source temperature and surface gravity help to define the limb-darkening coefficients which can then be compared with limb-darkening effects in the photometric data.

From spectra taken at baseline, one can determine the contribution of the lens to the spectra. The lens contribution, along with an estimate of the mass of the

lens from the time scale of the event, can help to determine whether the lens is in the disk or the halo. Extinction effects in the spectra will also help to provide an estimate of the distance to the source, which then allows an estimate of the distance to the lens to be made [53].

If a lens magnifies different parts of a rotating source star by varying amounts then the differential magnification will cause a shift in the centroid of the spectral lines of the star during the lensing event [52, 66]. Since the centroid displacement is proportional to the projected rotation velocity of the source and to the ratio of the source radius to the projected separation of the lens from the source, it provides an indirect measure of the proper motion of the lens.

1.3.2 Estimating Optical Depth

A useful measurable quantity in a statistical study of gravitational microlensing is the microlensing optical depth, τ, which is the instantaneous probability that any given source is microlensed [20] (see Figure 1.6). The two major microlensing survey teams, MACHO and OGLE, have both calculated the observed optical depth towards the Galactic bulge from the time scales of the events that they have observed in that line of sight. The comparison of estimated (or theoretical) optical depths to observed optical depths has been a much debated topic due to the discrepancy between the two values [48, 105]. Further studies revealed that there were several unaccounted for effects which help to explain the differences found between theory and observation.

Early calculations of the optical depth used models which treated the Galactic bulge as an axisymmetric rotator. However, when both the OGLE and MACHO microlensing experiments found an unexpectedly large number of microlensing events towards the Galactic bulge it was shown that this could be at least partially explained by taking into account the bar of the Galaxy which has its long axis elongated towards us [77, 119, 120]. Additional contributions to the total microlensing optical depth taken into consideration included a further analysis of the intervening disk population [69], the dominant role of stars within the bulge [54], and the effects of disk stars located behind the bulge [72]. Also, extinction effects towards the Galactic bulge have been shown to have a non-negligible effect on the observed optical depth, the effects of which can be seen in the reddening of spectra of microlensed sources [53].

1.3.3 Studying Galactic Structure

Kiraga and Paczyński [54] have pointed out that the stars within the Galactic bulge may play a dominant role as gravitational lenses, and a significant fraction of the detected events may be due to lensing by stars within the bulge. If a significant fraction of these events are indeed due to lenses within the bulge, this can provide a very powerful technique of deriving the stellar mass density, and mass

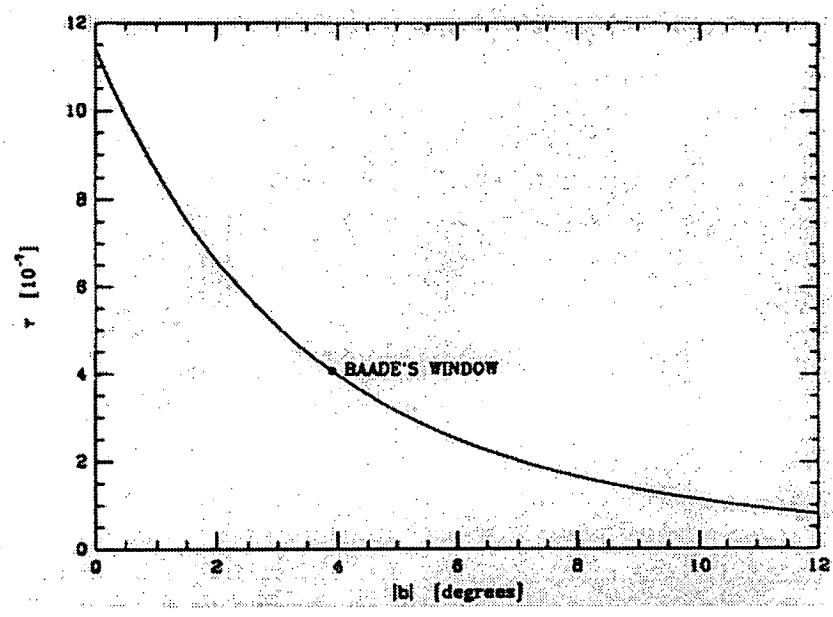

Figure 1.7: An early estimate of the optical depth towards the Galactic bulge as a function of Galactic latitude b. The position of "Baade's window", a line of sight of minimum extinction, is shown. [75]

function within the Galactic bulge [119]. However, there remains considerable uncertainty in the contribution of different populations to the microlensing optical depth, and their determination is important to determine the mass function of the lensing stars.

If the lensing is caused predominantly by bulge stars, then most of the lensed stars will be at the far side of the bulge so that there are enough stars in front to cause the lensing. Thus they would be fainter in general, and it was shown by Stanek [95] that the magnitude offset between the lensed sources and non-lensed sources is a good measure of the fraction of the events caused by bulge lenses. A similar test that can be applied is through the measurement of extinction [53]. If the lensing is due to bulge stars, the lensed stars should have larger extinction since they would predominantly be on the far side.

Since the estimated contribution of the bulge-bulge lensing is large, the microlensed sources are statistically expected to be in the far side of the Galactic bulge. Thus the spectra of these sources give a unique opportunity to derive the radial velocities of the objects in the far side of the Galactic bulge. The radial velocities derived from the observed spectra can be combined with the proper motion derived from the microlensing time scales to determine the 3-dimensional velocity structure of the far side of the Galactic bulge.

1.4 Outline of Thesis

This project is essentially divided into two halves - photometric and spectroscopic. Chapter 2 outlines the theory of gravitational microlensing that will be drawn upon throughout the remainder of the thesis. Chapter 3 begins the photometric study by describing the facilities and methods used to acquire and reduce the photometric data. Chapter 4 presents the resulting light curves from the PLANET observations during the 1996, 1997, and 1998 bulge seasons. The modelling of a selection of these light curves is presented in Chapter 5 and the significance of these results is discussed. Chapter 6 introduces the spectroscopic study by developing various models of the Galactic bulge in order to calculate the contributions of the different layers in the bulge to the microlensing optical depth. The effects of extinction on stars of different spectral classes located on the far side of the bulge is then investigated. Chapter 7 describes the reduction of the spectroscopic data acquired from the ESO 3.6 m telescope. These results are then presented in Chapter 8 and the extinction in the spectra is modelled.

Chapter 2

The Theory of Microlensing

This chapter outlines the basic theory of gravitational microlensing that will be applied in the following chapters. The light curves shown in this chapter were calculated using a SuperMongo program called `curve.sm` (see Appendix A.3). The first section describes the situation of a single point source and a single point lens and is frequently all the theory needed to describe a microlensing event. The second section uses these ideas to discuss the microlensing event rate and the optical depth to microlensing. The third section investigates a binary source scenario and the fourth section describes additional effects due to parallax, blending, and a finite source. The fifth section develops the theory required to understand the caustic structures found in binary lens events and in lenses containing planetary systems. The sixth section deals with how microlensing models can be fitted to real data and the last section investigates observing strategies and the detection efficiency to stellar and planetary companions.

2.1 Point Source - Point Lens

In explaining the theory underlying the point source - point lens model (hereafter referred to as PSPL), I have drawn upon a number of references [87, 92] but mostly I have used publications by Paczyński [74, 78].

Microlensing occurs when a foreground compact object, such as a star, passes between the observer and a luminous background object. The total flux received by the observer from the multiple images produced is larger than that from the unlensed source alone. The resulting magnification of the background source reveals the presence of the intervening lens system. To demonstrate this principle, let us consider a point lens L of mass M at a distance D_d from the observer, and a point source S at a distance D_s from the observer, as shown in Figure 2.1.

As a consequence of General Relativity, light rays from the source that pass

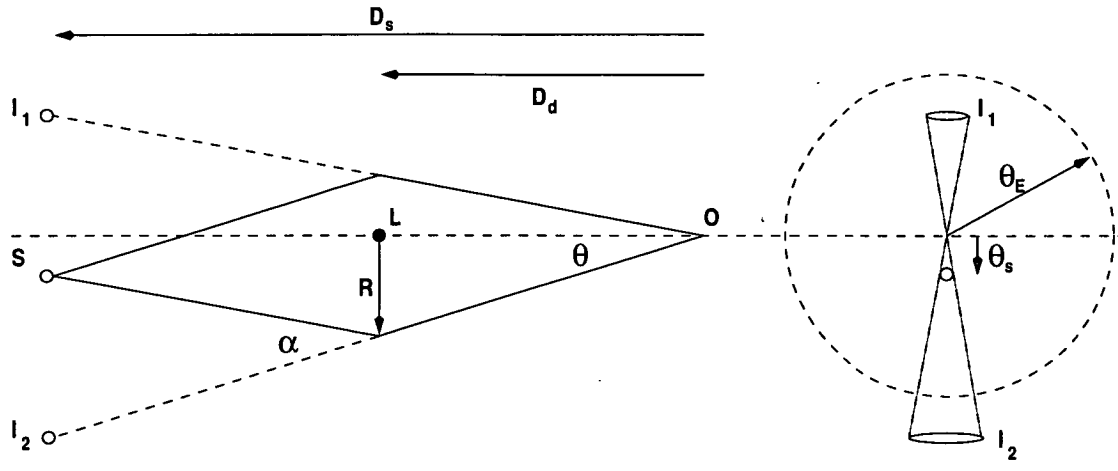

Figure 2.1: The geometry of gravitational lensing is shown. **Left:** The observer, the lensing mass, and the source are located at O, L, and S respectively. Light rays deflected by differing amounts α create images at I_1 and I_2. **Right:** To an observer at O, the source is not seen at its angular sky position θ_s but only at I_1 and I_2. The Einstein ring is shown as a dashed circle.

at a distance R from the lens are deflected by an amount

$$\alpha = \frac{4GM}{Rc^2} \tag{2.1}$$

so that the light from the source appears as two images in the source plane, I_1 and I_2.

Let the source be located at an angular distance of θ_s from the lens and image I_2 be located at an angular distance of θ from the lens. From Figure 2.1, simple geometry requires that

$$\theta_s D_s = R\frac{D_s}{D_d} - (D_s - D_d)\alpha(R) \tag{2.2}$$

Dividing by the distance to the source yields

$$\theta_s = \theta - \frac{(D_s - D_d)}{D_s}\alpha(R) \tag{2.3}$$

Equation 2.3 is called the *lens* (or ray-trace) *equation* and describes the relation between the angular position of an unlensed source and the position of its images if the light rays emanating from the source are perturbed by a gravitational field.

The lens equation may be rewritten to yield a quadratic equation

$$\theta^2 - \theta_s\theta - \theta_E^2 = 0 \tag{2.4}$$

where θ_E (the angular *Einstein ring radius*) is defined as

$$\theta_E = \sqrt{\frac{4GM}{c^2}\frac{(D_s - D_d)}{D_d D_s}} \tag{2.5}$$

which corresponds to a physical size given by $R_E = D_d\theta_E$.

The quadratic in Equation 2.4 has two solutions

$$\theta_{1,2} = \frac{1}{2}\left(\theta_s \pm \sqrt{\theta_s^2 + 4\theta_E^2}\right) \tag{2.6}$$

These two solutions correspond to the positions of images I_1 and I_2, located at angular distances from the lens L of θ_1 and θ_2 respectively. As an example, a source located at 8 kpc and a solar mass lens located at 3 kpc would result in an angular Einstein ring radius of $\approx 1.3 \times 10^{-3}$ mas. Hence, the image separation of $\approx 2\theta_E$ will be of the order of a milliarcsecond, far below the resolution of current optical telescopes (the recently constructed *Gemini* telescopes and the future *Space Interferometry Mission* (SIM) may change this). As such, we can only see the combined light intensity rather than the two separate images. Shown in Figure 2.1 are the distorted images relative to the source and lens as they would appear in a very high resolving power telescope. It is clear from Equation 2.6 that when $\theta_s = 0$ then the images form a ring of radius θ_E.

A property of any lensing is the conservation of surface brightness. The cross-sectional area of a collection of light rays from the source is distorted during the lensing but since the photon number is conserved, the flux of the image is determined by this area distortion. This means that the ratio of the image to source intensity can be simply calculated from the ratio of their areas using

$$A_{1,2} = \left|\frac{\theta_{1,2}}{\theta_s}\frac{d\theta_{1,2}}{d\theta_s}\right| \tag{2.7}$$

The quantity A is called the *magnification* or *amplification*. After a small amount of calculation (see Appendix A.1), Equation 2.7 yields

$$A_{1,2} = \frac{u^2 + 2}{2u\sqrt{u^2 + 4}} \pm 0.5 \tag{2.8}$$

where the dimensionless *impact parameter* $u \equiv \theta_s/\theta_E$ is the angular separation of the source and lens in units of the Einstein ring radius. The total magnification due to images I_1 and I_2 is then given by

$$A = A_1 + A_2 = \frac{u^2 + 2}{u\sqrt{u^2 + 4}} \tag{2.9}$$

The impact parameter may be determined from the magnification by rewriting Equation 2.9 (see Appendix A.2) as

$$u = \sqrt{\frac{2A}{\sqrt{A^2 - 1}} - 2} \tag{2.10}$$

The resultant light curve is symmetric and has a magnification of 1.34 when the source crosses the Einstein ring radius (when $u = 1$), as shown in Figure 2.2. If the source becomes directly aligned with the lens ($u = 0$) then an infinite magnification is produced for a point source.

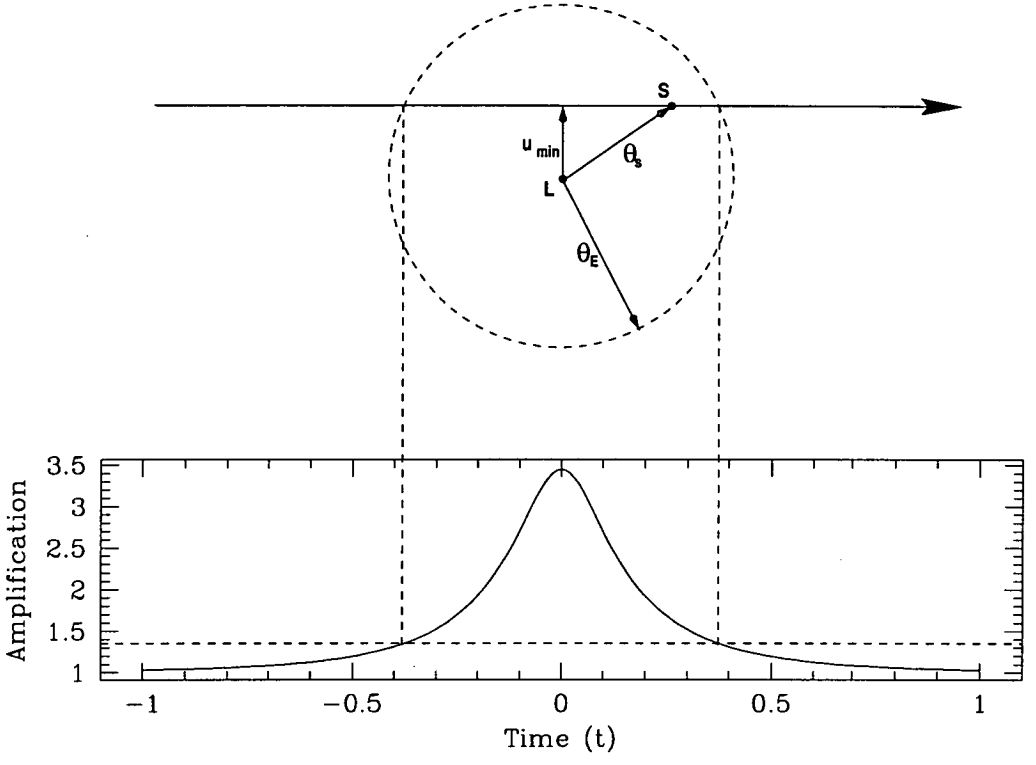

Figure 2.2: A theoretical light curve showing the relative positions of the source S and lens L for the duration of the event. The minimum impact parameter in this case is $u_{min} = 0.3$, resulting in a peak amplification of $A_{max} = 3.44$.

The time scale of a microlensing event is dependant on the relative transverse velocity of the lens with respect to the source as well as the size of the Einstein ring radius. The *characteristic time scale* of an event is normally defined as the time taken for the source to move with respect to the lens by one Einstein ring radius (some MACHO publications use an Einstein ring diameter rather than an Einstein ring radius in their definition). This is expressed as

$$t_E \equiv \frac{R_E}{v_\perp} \tag{2.11}$$

where $v_\perp$ is the transverse velocity of the lens relative to the observer-source line of sight. From Figure 2.2 it is clear that the impact parameter may be written as

$$u(t) = \sqrt{u_{min}^2 + [p(t)]^2} \tag{2.12}$$

where $p(t)$ is given by

$$p(t) = \frac{t - t_0}{t_E} \tag{2.13}$$

and t_0 is the time at which u is a minimum and the magnification is maximum. Shown in Figure 2.3 are PSPL light curves for various values of the minimum impact paramater.

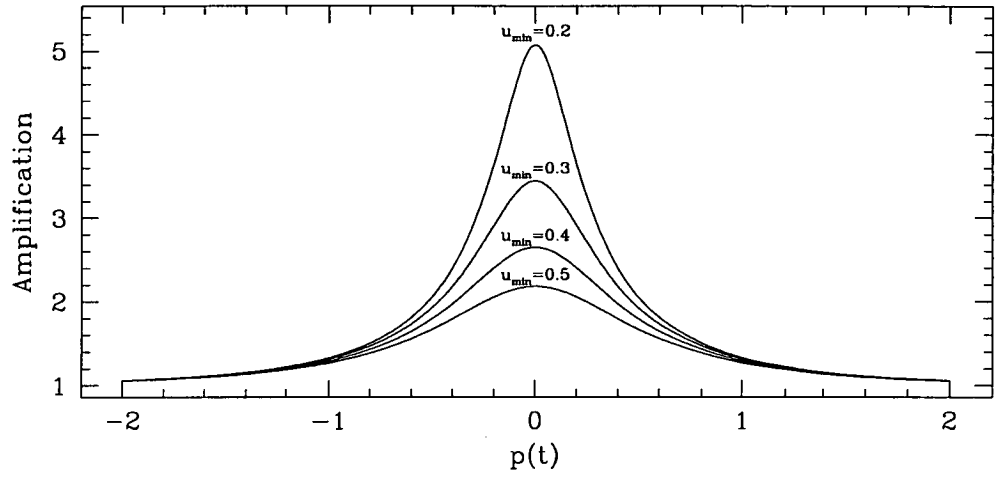

Figure 2.3: PSPL light curves for minimum impact parameter values of $u_{min} = 0.2, 0.3, 0.4, 0.5$.

Event durations $\hat{t} = 2t_E$ for microlensing events detected towards the Galactic bulge have been found to typically be on the order of a few weeks to a few months. PSPL microlensing light curves (such as the ones shown in Figure 2.3) can be completely described using the three parameters u_{min}, t_0, and t_E. Since this method was first suggested as a use for probing Galactic dark matter by Paczyński [74], these curves are often known as *Paczyński curves.*

2.2 Optical Depth and Event Rate

Two of the most important parameters in microlensing analyses are the *optical depth* and the *event rate.* In a publication by Vietri & Ostriker [110] the optical depth τ is defined as the probability of a microlensing event occurring. This simply means the number of lenses lying within one Einstein ring radius around the line of sight to a given source. Another way of stating this is the instantaneous probability that a given star is lensed with an amplification of $A > 1.34$ at any given time.

The optical depth may be expressed mathematically as

$$\tau = \pi \int_0^{D_s} \frac{\rho(D_d)}{M} R_E^2 \, dD_d$$

$$= \int_0^{D_s} \frac{4\pi G}{c^2}\rho(D_d)\frac{D_d(D_s - D_d)}{D_s}\,dD_d \tag{2.14}$$

By defining $x \equiv D_d/D_s$, the optical depth becomes

$$\begin{aligned}
\tau &= \frac{4\pi G}{c^2}\int_0^1 \rho(x)x\left(\frac{D_d}{x} - xD_s\right)D_s\,dx \\
&= \frac{4\pi G}{c^2}D_s\int_0^1 \rho(x)(D_d - x^2D_s)\,dx \\
&= \frac{4\pi G}{c^2}D_s\int_0^1 \rho(x)\frac{(D_dD_s - x^2D_s^2)}{D_s}\,dx \\
&= \frac{4\pi G}{c^2}D_s^2\int_0^1 \rho(x)\left(\frac{D_d}{D_s} - x^2\right)dx \\
&= \frac{4\pi G}{c^2}\int_0^1 \rho(x)x(1-x)\,dx
\end{aligned} \tag{2.15}$$

In the simplest case we can assume a constant density of matter. In this case, Equation 2.15 may be evaluated as

$$\tau = \frac{2\pi}{3}\frac{G\rho}{c^2}D_s^2 \tag{2.16}$$

Of course the distribution of mass will greatly depend upon the distance and the line of sight and so a more accurate estimate of the optical depth would be obtained by choosing to evaluate the integral with an appropriate mass density function.

Since $R_E \propto \sqrt{M}$ and the stellar number density $n(D_d) = \rho(D_d)/M \propto M^{-1}$ then we see from Equation 2.14 that the optical depth is independent of the individual lens masses. Using the virial theorem, a crude but simple estimate of the optical depth for a system of self-gravitating lenses can be made from

$$\tau \approx \frac{V^2}{c^2} \tag{2.17}$$

where V is the rotation speed of the system.

Consider a stationary source and observer with intervening lenses all moving with the same relative transverse velocity $v_\perp$. If n_s sources are monitored over a time interval Δt then the number of microlensing events expected is given as

$$\begin{aligned}
N &= \frac{2v_\perp}{\pi R_E^2}n_s\tau\Delta t \\
&= \frac{2R_E}{\pi R_E^2}n_s\tau\frac{\Delta t}{t_E} \\
&= \frac{2}{\pi}n_s\tau\frac{\Delta t}{t_E}
\end{aligned} \tag{2.18}$$

where N is expressed in terms of the Einstein ring radius ($R_E = 1$) [62, 74, 78]. This only takes into account those events for which the impact parameter is smaller than the Einstein ring radius.

The event rate Γ is simply the number of events divided by the duration time of observation [26]

$$\Gamma = \frac{N}{\Delta t} = \frac{2}{\pi}\frac{n_s \tau}{t_E} \tag{2.19}$$

Equation 2.18 can be rewritten to obtain the equation that is usually used to estimate the optical depth from observations of n_s stars over a time interval Δt [40, 48, 105]

$$\tau = \frac{\pi}{2 n_s \Delta t} \sum_{j=1}^{N} \frac{t_{E,j}}{\epsilon_j} \tag{2.20}$$

where ϵ_j is the efficiency of detecting the event. The detection efficiency can be determined by a process of adding "fake" stars with the same luminosity function as the real stars to the raw images and then modulating their brightnesses according to random microlensing light curves. The analysis can then be run on these "fake" stars to see how many events are recovered [20].

With the large number of microlensing events that have been so far detected, observational estimates of the optical depth in the direction of the Galactic centre have been made by the various microlensing survey groups. OGLE has estimated a value of $(3.3 \pm 1.2) \times 10^{-6}$ [105] and MACHO has estimated a value of $(3.9^{+1.8}_{-1.2}) \times 10^{-6}$ [14]. Theoretical models which assume accepted density profiles for the Galactic bulge and disk predict a much lower value, typically in the range $(0.5\text{–}1.0) \times 10^{-6}$ [45, 54, 75]. Several explanations have arisen in an attempt to explain the discrepancy, most notably that of taking the bar of the Galaxy into account [77, 119, 120].

2.3 Binary Source - Point Lens

Microlensing involving a binary source can introduce various factors which may destroy most, if not all, of the microlensing signatures outlined in Section 1.1.3 since these are valid only for a PSPL event. Such a binary event will normally be asymmetric in time and, if the two stars in the binary system are of different colours, may also be chromatic. In this section the anomalies arising from a binary source - point lens event (hereafter referred to as BSPL) will be discussed using the notation adopted by Dominik [29]. Note that, though a binary source is often considered to be gravitationally bound, these results also apply to "optical binaries", that is, stars which appear close on the sky but are not members of the same system.

Consider a source consisting of two stars, S_1 and S_2, separated by a distance 2λ (in units of Einstein ring radii) and of apparent luminosities L_1 and L_2, as shown

in Figure 2.4. As the lens L moves close to the observer-source line of sight, each point source is magnified independently by amounts $A_1 = A_1(u_1(t))$ and $A_2 = A_2(u_2(t))$ respectively, as given by Equation 2.9. The total magnification is given by

$$A = \frac{A_1 L_1 + A_2 L_2}{L_1 + L_2} = (1 - \omega)A_1 + \omega A_2 \tag{2.21}$$

where ω is the *luminosity offset ratio*

$$\omega = \frac{L_2}{L_1 + L_2} \tag{2.22}$$

which is related to the luminosity ratio $r = L_1/L_2$ by

$$\omega = \frac{1}{1 + r} \tag{2.23}$$

Hence, the resulting lightcurve for a binary source is simply a superposition of two standard light curves.

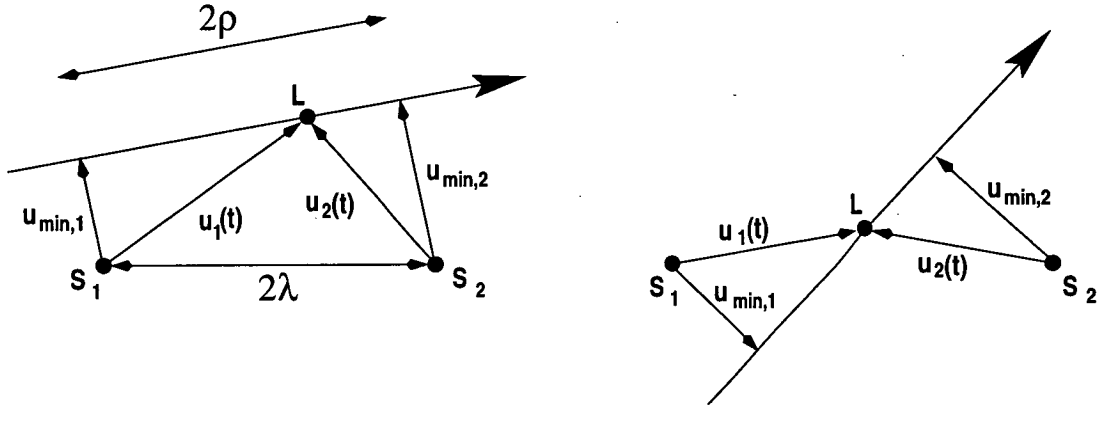

Figure 2.4: Trajectory of a lens with respect to two source stars during a BSPL event. **Left:** cis-configuration **Right:** trans-configuration

There is an inherent degeneracy in BSPL light curves arising from the two different physical configurations which produce the same light curve. The lens trajectory can pass between the sources or pass to one side of the sources without changing the associated impact parameters. When the sources are located on the same side of the lens trajectory the configuration is called the *cis-configuration*, and when the sources are located on opposite sides of the lens trajectory the configuration is called the *trans-configuration* [31] (see Figure 2.4).

Let 2ρ be the distance between the points of closest approach of the lens to the two source components measured in units of Einstein ring radii. This can be expressed as

$$\rho = \frac{t_{0,2} - t_{0,1}}{2t_E} \tag{2.24}$$

where $t_{0,1}$ and $t_{0,2}$ are the times of maximum amplification of S_1 and S_2 respectively. The quantity ρ is related to the angle β created by the intersection of the lens trajectory with the orientation of the binary source by

$$\beta = \arctan\left(\frac{u_{min,2} \pm u_{min,1}}{2\rho}\right) \tag{2.25}$$

where the + sign applies to the cis-configuration and the − sign applies to the trans-configuration. It follows that the half separation of the source components may be written as

$$\lambda = \rho/\cos\beta \tag{2.26}$$

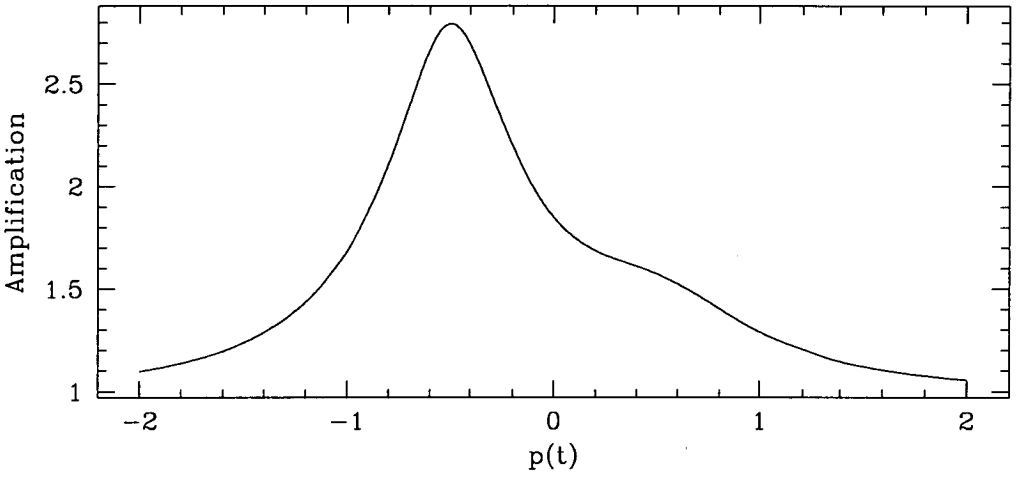

Figure 2.5: Light curve for BSPL model with asymmetric peak. $\omega = 0.3$, $\rho = 0.5$, $u_{min,1} = 0.3$, $u_{min,2} = 0.5$.

From Equation 2.12, the impact parameters for S_1 and S_2 respectively are given by

$$u_1(t) = \sqrt{u_{min,1}^2 + [p_1(t)]^2} \text{ and } u_2(t) = \sqrt{u_{min,2}^2 + [p_2(t)]^2} \tag{2.27}$$

where

$$p_1(t) = \frac{t - t_{0,1}}{t_E} \text{ and } p_2(t) = \frac{t - t_{0,2}}{t_E} \tag{2.28}$$

The time at which the mid-point of the light curve occurs t_{mid} is chosen such that $t_{0,1} = -t_{0,2}$ and so $t_{mid} = 0$. In this case we have

$$p(t) = \frac{1}{2}(p_1(t) + p_2(t)) = \frac{t}{t_E} \tag{2.29}$$

From Equation 2.24 and Equation 2.29 it follows that

$$p_1(t) = p(t) + \rho \text{ and } p_2(t) = p(t) - \rho \tag{2.30}$$

Hence, using these equations we can create light curves of binary microlensing events, as shown in Figure 2.5 and Figure 2.6. BSPL light curves may have a nearly symmetric peak or asymmetric peak (see Figure 2.5) or they may have a double peak (see Figure 2.6). The various shapes of BSPL light curves have been studied in depth and classified by Griest & Hu [46].

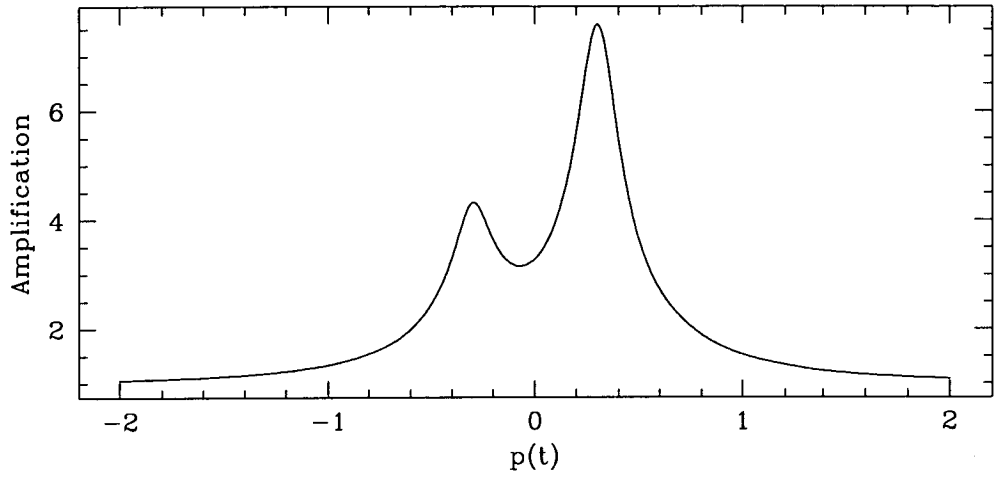

Figure 2.6: Light curve for BSPL model with double peak. $\omega = 0.7$, $\rho = 0.3$, $u_{min,1} = 0.1$, $u_{min,2} = 0.1$.

The introduction of parallactic effects in the light curves of gravitationally bound binary sources due to the binary motion of the source has been investigated by Paczyński [79]. The periodic photometric modulation of the source may indicate that the source is an ellipsoid variable, the variability resulting from tidal distortions in the binary components. A study of short-period binary sources has been conducted by Han & Gould [49] which, in particular, may be used to determine whether the lenses are Galactic or whether they are located in the LMC. The large number of parameters needed to model this effect make spectroscopic observations of the source necessary in order to determine its binary nature.

It has been estimated that a large fraction of stars exist in binary or multiple star systems [1]. This correspondingly means that a large fraction of observed microlensed sources are binary sources and it was predicted by Griest & Hu [46] that around 10% – 20% of events on binary sources should have features distinguishable from single source events. It has since been argued by Dominik [31] that the lack of claimed binary source events may be due to the fact that most of these events can be explained by a blended single source. It has further been pointed out by Han & Jeong [50] that many binary source events can be missed in the modelling if the flux ratio is large or the separation of the components is small, the resulting light curves mimicking those of PSPL events.

2.4 Additional Effects to Consider

The standard microlensing light curve assumes a single point source, a single point lens, and uniform relative motion between the lens and the observer-source line of sight. Although this is a good approximation in most cases, significant deviations from the standard shape can occur, the additional information from which can be used to break the intrinsic degeneracy in a PSPL event.

2.4.1 Blending

The most common deviation from the standard light curve is caused by *blending* which occurs when, in addition to light from the source, there is additional light contributed by the lens or from an unresolved background star.

Let f_L be the flux from the lensed star and let f_U be the flux from the unresolved unlensed star. The observed magnification in this case is given by

$$\begin{aligned} A_{obs} &= \frac{f_U + A f_L}{f_U + f_L} \\ &= fA + 1 - f \end{aligned} \tag{2.31}$$

where f is called the *blending parameter* and is given by

$$f = \frac{f_L}{f_U + f_L} \tag{2.32}$$

and A is the magnification of the source as described by Equation 2.9.

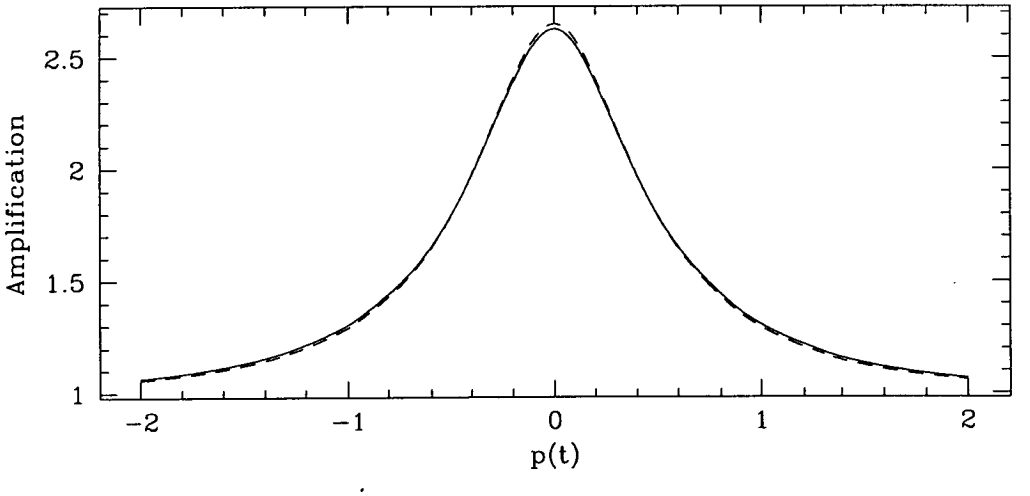

Figure 2.7: Large impact parameter degeneracy. A blended event with $u_{min} = 0.36$, $t_E = 1.1$ and $f = 0.85$ (solid line) is almost indistinguishable from an unblended model with $u_{min} = 0.4$ and $t_E = 1.0$ (dashed line).

There are two regions of parameter space for which there is a near degeneracy in that the light curve of a blended event may be well fitted by a model of an unblended event of lower A_{max} and shorter t_E [117]. This means that for a reasonable estimate of the accuracy of the measurements, a unique solution of the model parameters cannot be found.

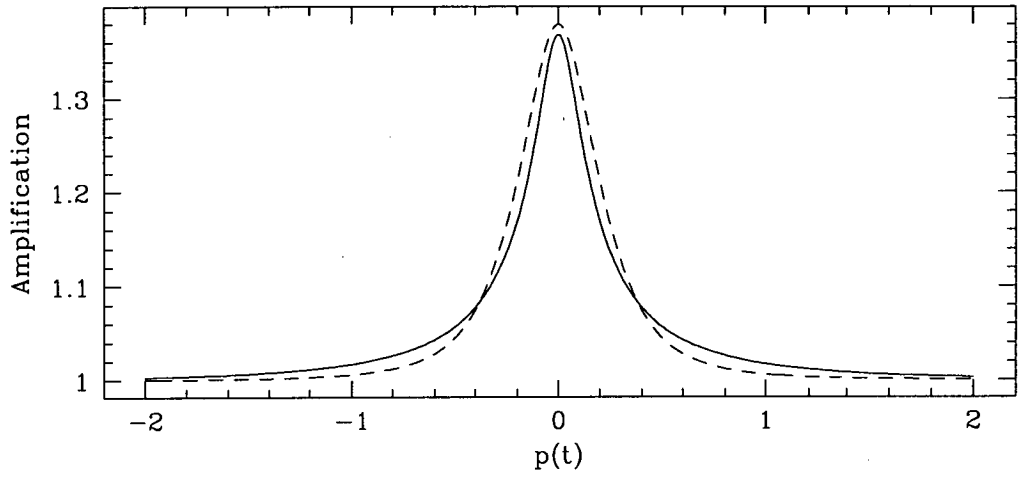

Figure 2.8: Strong blending degeneracy. A blended event with $u_{min} = 0.12$, $t_E = 1.0$ and $f = 0.05$ (solid line) is quite well fitted by an unblended model with $u_{min} = 0.95$ and $t_E = 0.25$ (dashed line).

The first case occurs when the minimum impact parameter is large, although in practise this degeneracy covers a broad range of impact parameters. Figure 2.7 shows how a typical PSPL event may be almost flawlessly modelled by a blend that is photometrically undetectable in the measured light curve.

The second case occurs when the baseline flux is dominated by a blending star, which means that the microlensing event is only detectable when the minimum impact parameter is very small. Since most microlensing surveys are conducted in very crowded fields, this degeneracy is quite common. Shown in Figure 2.8 is an example where an event with strong blending and a small minimum impact parameter may be mistaken for an unblended event with a high minimum impact parameter.

There are several ways to detect blending or correct for it statistically. In cases where the angular separation between the lens star and the blend is not too small, the blend can be detected through a correlation between the image centroid and the apparent brightness. Post-event *Hubble Space Telescope* (HST) imaging could be used to resolve the blending component. In the case of a double lens (see Section 2.5), a blend may reduce the apparent magnification between caustic crossings below the theoretical minimum value of $A_{min} = 3$ [116]. If the statistics of binary stars are known in the target population, blending can be

corrected for statistically by placing artificial stars in the CCD frames [117].

2.4.2 Parallax

A standard microlensing light curve assumes a constant relative velocity between the lens and the observer-source line of sight. However, the time symmetry of a standard light curve can be broken by the orbital motion of the Earth. The distortion caused by this *parallax* effect is only observable in long duration events but it allows one to compare the projected Einstein ring radius with the known size of the Earth's orbit, thereby obtaining an additional constraint relating the mass, distance, and velocity of the lens [24].

The effect of parallax in microlensing was first predicted in a 1992 paper by Gould [41] and in 1995 the effect was observed by the MACHO collaboration [13], in which it was found that the light curve fit could be dramatically improved by including extra parameters which take the Earth's orbital motion into account. To do this, the expression for $u(t)$ given in Equation 2.12 needs to be replaced by

$$\begin{aligned}[u(t)]^2 &= u_{min}^2 + \omega^2(t-t_0)^2 + \hat{\alpha}^2 \sin^2[\Omega(t-t_c)] \\ &\quad +2\hat{\alpha}\sin[\Omega(t-t_c)][\omega(t-t_0)\sin\theta + u_{min}\cos\theta] \\ &\quad +\hat{\alpha}^2 \sin^2\beta\cos^2[\Omega(t-t_c)] + 2\hat{\alpha}\sin\beta\cos[\Omega(t-t_c)] \\ &\quad \cdot[\omega(t-t_0)\cos\theta - u_{min}\sin\theta] \end{aligned} \tag{2.33}$$

where u_{min} is now the minimum distance between the lens and the Sun-source line, $\omega = 1/t_E$, t_c is the time that the Earth is closest to the Sun-source line, θ is the angle between $v_\perp$ and the north ecliptic axis, and β is the ecliptic latitude. The coordinates of a star located at right ascension α and declination δ need to be converted to ecliptic coordinates using the formulae

$$\lambda = \arctan\left(\frac{\sin\alpha\cos\xi + \tan\delta\sin\xi}{\cos\alpha}\right) \tag{2.34}$$

and

$$\beta = \arcsin(\sin\delta\cos\xi - \cos\delta\sin\xi\sin\alpha) \tag{2.35}$$

where ξ is the obliquity of the ecliptic [67]. At the standard equinox of J2000, the value of the obliquity is $\xi = 23.43929°$. The parameters α and Ω are given by

$$\alpha = \frac{\omega a_\oplus}{\tilde{v}}(1 - \epsilon\cos[\Omega_0(t-t_p)]) \tag{2.36}$$

and

$$\Omega(t-t_c) = \Omega_0(t-t_c) + 2\epsilon\sin[\Omega_0(t-t_p)] \tag{2.37}$$

where $a_\oplus$ is the semimajor axis of the Earth's orbit, $\tilde{v} = v_\perp D_s/(D_s - D_d)$ is the transverse velocity of the lens projected to the solar position, $\epsilon = 0.0167$ is the

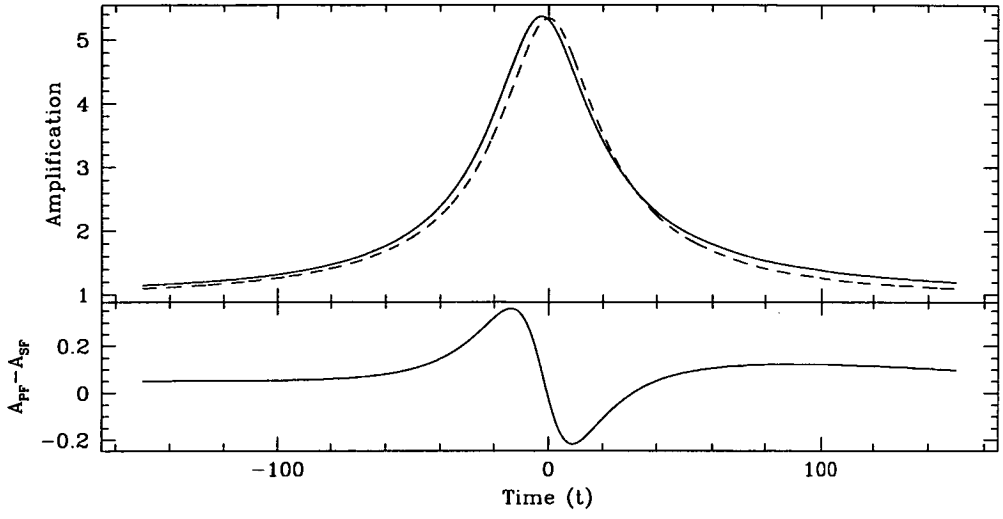

Figure 2.9: The effect of the Earth's orbital motion. Only observable in long duration events, a PSPL light curve with $u_{min} = 0.19$ and $t_E = 89.8$ days (dashed line) is fit closely by a PSPL light curve including parallax with $u_{min} = 0.24$ and $t_E = 118.1$ days (solid line). Residuals are shown in the bottom panel.

Earth's orbital eccentricity, t_p is the time of perihelion, and $\Omega_0 = 2\pi/T$ where T is the period of the Earth's orbit.

Shown in Figure 2.9 is an example of a microlensing light curve with a deviation resulting from parallax. The microlensed source is located at α = 18:03:34.05, δ = -28:00:18.9 (J2000) which is equivalent to ecliptic coordinates of $\lambda = 270.8°$, $\beta = -4.6°$. In this example a PSPL light curve with $u_{min} = 0.19$ and $t_E = 89.8$ days is compared to a PSPL light curve including parallax with $u_{min} = 0.24$ and $t_E = 118.1$ days. The bottom panel shows the residuals (parallax fit A_{PF} minus standard PSPL fit A_{SF}) which illustrates the time asymmetry of the parallax effect. Other parameters for the parallax fit are $t_0 = t_p = 0$, $t_c = 212$ days, $\theta = -0.7$ rad, $\beta = -0.08$ rad, and a transverse velocity of $\tilde{v} = 75\,\mathrm{km\,s^{-1}}$.

This method was also used to model a microlensing parallax event discovered by the OGLE collaboration towards the Carina spiral arm, the calculations of which also included the effects of blending [65]. An alternative method of treating parallax in microlensing has been formulated by Dominik [29, 30] which lets the source move in the opposite direction to that in the MACHO formalism [13].

2.4.3 Finite Source

An often reasonable assumption in gravitational microlensing is that of a point source. This assumption becomes unreasonable in the case of a *finite source*, that is, when the source size is comparable to the minimum angular distance between the lens and the source. It has been shown that this can lead to significant devi-

ations from the standard PSPL light curve and there have been various methods published for taking into account the effect of a uniformly bright source and a limb-darkened source [29, 32, 64, 115]. The limb-darkening effect is due to the differential magnification across the face of the star and can be used to constrain the centre-to-limb variations in the spectrum of the star.

Finite source effects have been detected using a uniformly bright model by the MACHO collaboration in event MB95030 [16]. The first observation of limb-darkening in microlensing was made by the PLANET collaboration by using the transit of a lens across an extended source in event MB97028 to produce the stellar profile and hence calculate the limb-darkening coefficients [8].

Uniform Brightness

For a source with uniform brightness, the magnification is simply the ratio of the area of the images to the area of the source. This is given by

$$A = \frac{\int d^2y\, A_p(\mathbf{y})}{\int d^2y} \tag{2.38}$$

where $A_p(\mathbf{y})$ is the magnification of a point source at position $\mathbf{y}$ and the integration is performed over the entire region of the source.

Consider a circular source of radius R_s, where R_s is in units of the Einstein ring radius projected to the source plane R'_E given by

$$R'_E = \sqrt{\frac{4GM}{c^2}\frac{D_s(D_s - D_d)}{D_d}} \tag{2.39}$$

Then the magnification of the extended source when behind a point lens is given by

$$A = \begin{cases} \frac{2}{\pi R_s^2} \int_{u-R_s}^{u+R_s} \frac{r^2+2}{\sqrt{r^2+4}} \arccos\frac{u^2+r^2-R_s^2}{2ur}\, dr & \text{for } u > R_s \\ \frac{2}{\pi R_s^2} \int_{R_s-u}^{R_s+u} \frac{r^2+2}{\sqrt{r^2+4}} \arccos\frac{u^2+r^2-R_s^2}{2ur} + \frac{R_s-u}{R_s^2}\sqrt{(R_s^2-u)^2+4}\, dr & \text{for } u < R_s \\ \frac{2}{\pi}\left[\left(1+\frac{1}{R_s^2}\right)\arcsin\frac{1}{\sqrt{1+\frac{1}{R_s^2}}} + \frac{1}{R_s}\right] & \text{for } u = R_s \end{cases} \tag{2.40}$$

where r is defined as $r \equiv |\mathbf{y}|$ [29]. Solving for $u_{min} = 0$ yields the maximum magnification of an extended source which is lensed by a point mass

$$A_{max} = \sqrt{1 + \frac{4}{R_s^2}} \tag{2.41}$$

Shown in Figure 2.10 is a comparison of the light curve resulting from an extended source with that from a point source. In this case the source radius

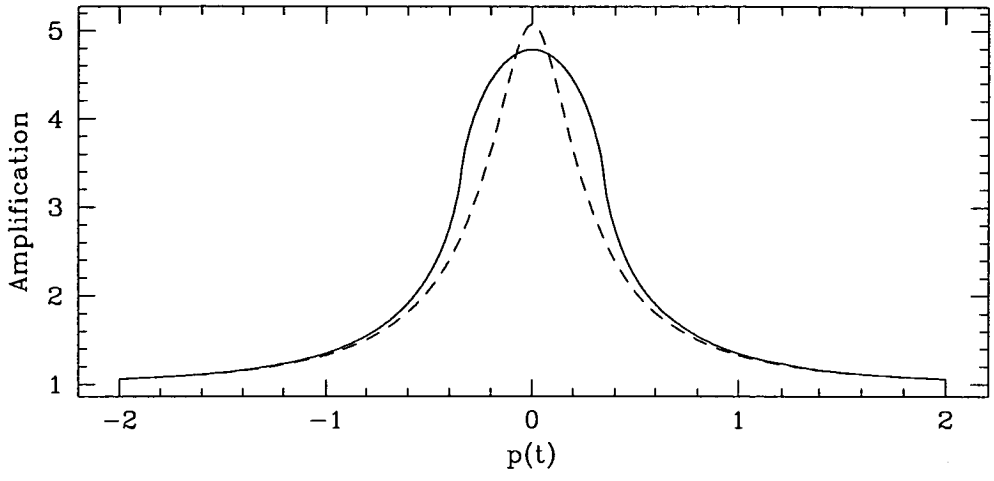

Figure 2.10: The effect of an extended source of uniform brightness. Given a minimum impact parameter of $u_{min} = 0.2$, a light curve due to an extended source of radius $R_s = 0.4$ (solid line) is compared with a standard PSPL light curve (dashed line).

is $R_s = 0.4$ and the minimum impact parameter is $u_{min} = 0.2$. The light curve resulting from an extended source may yield a larger or smaller peak magnification than that for a point source event.

Limb-darkening

In the case of limb-darkening, different parts of the source will be magnified differently and the net magnification is given by

$$A = \frac{\int d^2y\, I(\mathbf{y}) A_p(\mathbf{y})}{\int d^2y\, I(\mathbf{y})} \tag{2.42}$$

where $A_p(\mathbf{y})$ and $I(\mathbf{y})$ are the magnification of a point source and the intensity respectively at position $\mathbf{y}$ and the integration is performed over the source plane [29]. The intensity may be expressed as a function of the distance from the centre of the source $r \in [0, 1]$ in units of the source radius R_s

$$I(r) = I(0)[1 - \kappa_1 Y - \kappa_2 Y^2] \tag{2.43}$$

where $Y = 1 - \sqrt{1 - r^2}$ [38, 43]. Equation 2.43 describes the limb profile of the source where κ_1 and κ_2 are called the *limb-darkening coefficients*. The surface brightness profiles for a uniformly bright source and a limb-darkened source are shown in Figure 2.11. The limb-darkened profile has been normalized to give a total flux equal to unity and the coefficients for a cool giant star ($T = 4500$ K) of $\kappa_1 = 0.567$ and $\kappa_2 = 0.114$ have been adopted [59].

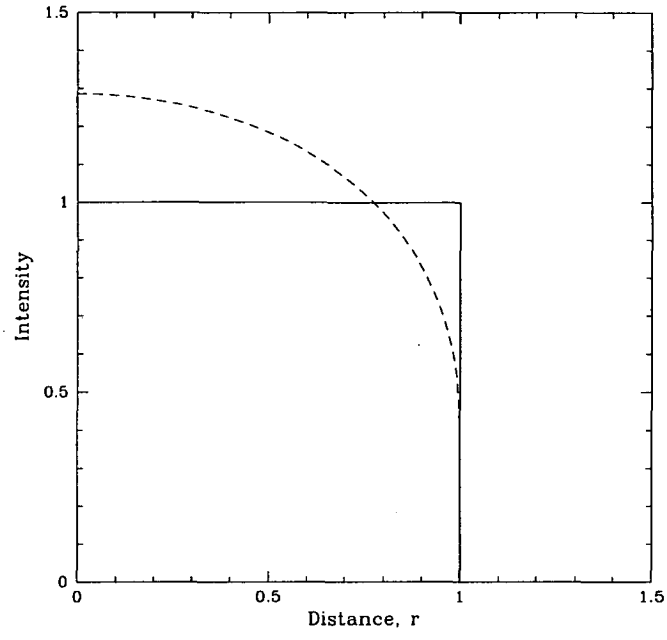

Figure 2.11: Surface brightness profiles for a uniformly bright source (solid line) and a limb-darkened source (dashed line). The limb-darkened profile has been normalized to give a total flux equal to unity.

The magnification of a limb-darkened source with its centre projected to the lens plane is then given by

$$A = \frac{1}{\pi R_s^2} \int_F I(r) A_p(\rho)\, dF \tag{2.44}$$

where ρ is the distance of a projected source point from the lens in units of the Einstein ring radius R_E. A numerical method for evaluating this 2-dimensional integral has been described by Dominik [29]. This method performs an outer integration along the line connecting the lens and the centre of the source

$$A = \frac{1}{\pi R_s^2} \int_{u-R}^{u+R} H(D, u, R_s)\, dD \tag{2.45}$$

and an inner integration along the perpendicular direction

$$H(D, u, R_s) = 2 \int_0^{\sqrt{R_s^2-(D-u)^2}} I(r) A_p(\rho)\, ds \tag{2.46}$$

where $\rho = \sqrt{D^2 + s^2}$ and $r = \sqrt{(D-u)^2 + s^2}$. Due to a singularity in the inner integration for $\rho \to 0$, the outer integration must be performed in two parts

$$A = \frac{1}{\pi R_s^2} \left(\int_0^{u+R} H(D, u, R_s)\, dD + \int_{u-R}^{0} H(D, u, R_s)\, dD \right) \tag{2.47}$$

These integrations were evaluated by writing a FORTRAN program which incorporates the integration routines described in the book "Numerical Recipes in FORTRAN" [82]. In particular, the subroutine `qgaus` was used to perform integrations where $u > R_s$ and the subroutines `midsql` and `midsqu` were used to perform integrations where $u < R_s$.

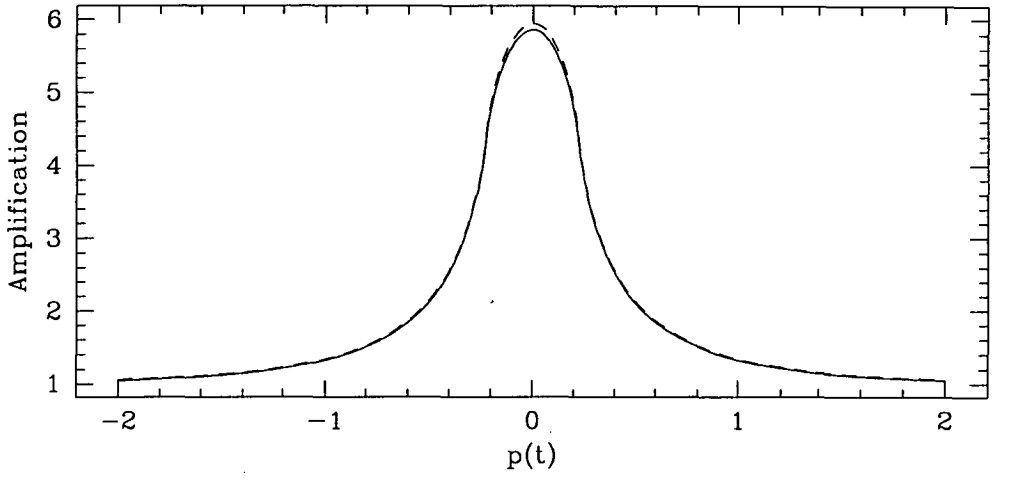

Figure 2.12: The effect of a limb-darkened extended source. Given a minimum impact parameter of $u_{min} = 0.2$ and a source radius of $R_s = 0.3$, a limb-darkened light curve with limb-darkening coefficients of $\kappa_1 = 0.567$ and $\kappa_2 = 0.144$ (solid line) is compared with a light curve resulting from an extended source with uniform brightness (dashed line).

Figure 2.12 shows a comparison of a light curve resulting from a limb-darkened extended source to a light curve resulting from a uniformly bright extended source. The difference between the two light curves is small and so reasonably high-quality photometry is required for the effect of limb-darkening to be detected.

2.5 Double Lenses and Planets

The most interesting deviation from a standard PSPL light curve occurs in the case of a binary lens event. This introduces a caustic structure, the boundaries of which represent potential source positions for which the magnification is infinite for a point source. Three additional free parameters are also introduced; the mass ratio, the separation of the lens components, and the orientation of the binary relative to the source path. The complicated shape of the caustics together with the large number of free parameters can lead to a seemingly endless variety of elaborate light curves but in fact, with good sampling, the parameters can be

useful in placing constraints on the modelling and can be used to predict the timing of future caustic crossings.

The theoretical work underlying binary lens calculations has been developed for some time [61, 91, 114] and the first observed binary lens was discovered by the OGLE collaboration [107]. The effect of a rotating binary has been considered [30] and has been observed by the PLANET collaboration [10]. The theory underlying microlensing by planets has also been considered for some time [21, 37, 42, 60] but it has not been conclusively demonstrated that such an event has been observed.

2.5.1 The Binary Lens

The dramatic difference between a binary lens and a single lens microlensing event is due to the astigmatism caused by a binary lens. This results in potential source positions for which the magnification is formally infinite called *caustics*. The caustics are closed curves in the source plane which map to *critical curves* in the lens plane. If the source passes into one of these caustic regions then a pair of new high amplification images appear.

Gravitational lensing is often described as a mapping from the lens plane (x, y) onto the source plane (ξ, η). The lens equation may be expressed in complex notation as

$$\zeta = z + \frac{m_1}{\bar{z}_1 - \bar{z}} + \frac{m_2}{\bar{z}_2 - \bar{z}} \tag{2.48}$$

where m_1 and m_2 are the masses of the lenses, z_1 and z_2 are the positions of the lenses, $\zeta = \xi + i\eta$ and $z = x + iy$ are the source and the image positions, and $\bar{z}$ denotes the complex conjugate of z. It is convenient to set $z_2 = -z_1$ and put the lenses on the real axis such that $z_1 = \bar{z}_1$. Also, $\Delta m = m_2 - m_1$ and $m_1 + m_2 = 1$ such that m_1 and m_2 denote the fractional masses.

Taking the complex conjugate of Equation 2.48 and substituting for $\bar{z}$ results in a fifth-order polynomial [114, 116] of the form

$$p_5(z) = \sum_{i=0}^{5} c_i z^i = 0$$

where

$$\begin{aligned}
c_5 &= z_1^2 - \bar{\zeta}^2 \\
c_4 &= -\bar{\zeta} + \zeta\bar{\zeta} - \Delta m z_1 - \zeta z_1^2 \\
c_3 &= 2\zeta\bar{\zeta} + 2\Delta m \zeta z_1 + 2\bar{\zeta}^2 z_1^2 - 2z_1^4 \\
c_2 &= \zeta + \Delta m z_1 - 2\Delta m \zeta\bar{\zeta} z_1 - 2\zeta\bar{\zeta}^2 z_1^2 + 2\Delta m z_1^3 + 2\zeta z_1^4 \\
c_1 &= -2\Delta m \zeta z_1 - (\Delta m)^2 z_1^2 - z_1^2 - 2\zeta\bar{\zeta} z_1^2 - 2\Delta m \bar{\zeta} z_1^3 - \bar{\zeta}^2 z_1^4 + z_1^6 \\
c_0 &= z_1^2[(\Delta m)^2 \zeta + \Delta m z_1 + 2\Delta m \zeta\bar{\zeta} z_1 + \bar{\zeta} z_1^2 + \zeta\bar{\zeta}^2 z_1^2 - \Delta m z_1^3 - \zeta z_1^4]
\end{aligned} \tag{2.49}$$

The transformation to a polynomial allows the use of the FORTRAN subroutines `laguer` and `zroots` [82] to solve for all five complex roots uniquely by reducing the order of the polynomial by one for every root found. There are either three or five solutions for the lens equation depending on whether the source is inside or outside the caustics.

The total magnification is then the sum of all roots of the polynomial that satisfy the lens equation, which is the sum of the absolute magnification of each image. For n images, this is given by

$$A_{tot} = \sum_{i=1}^{n} A_i = \sum_{i=1}^{n} \left. \frac{1}{|\det J|} \right|_{z=z_i} \tag{2.50}$$

where

$$\det J = 1 - \frac{\partial\zeta}{\partial\bar{z}} \frac{\overline{\partial\zeta}}{\partial\bar{z}} \tag{2.51}$$

is the Jacobian determinant of the mapping. Hence, it follows that the critical curves and caustics occur at points where $\det J = 0$. Events where the source trajectory crosses a caustic are called *strong* binaries and events where no caustic crossing occurs are called *weak* binaries [60].

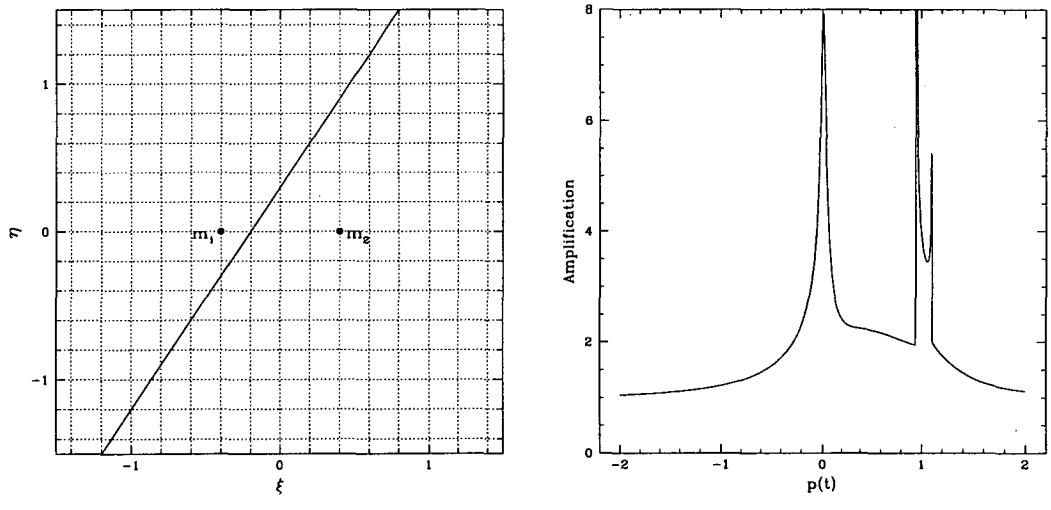

Figure 2.13: A point source - binary lens event with $b = 0.8$, $q = 0.43$, and $\phi = 0.98$ rad. **Left:** The configuration of the binary lens is shown where the positions of the masses are indicated by m_1 and m_2 and the line indicates the path of the source (from bottom to top). Dimensions are normalized to the Einstein ring radius of the combined system. **Right:** The resulting binary lens light curve.

In addition to the parameters which describe a single lens light curve, a binary lens introduces three additional parameters; the projected separation b of the

lenses in units of the Einstein ring radius, the mass ratio $q = m_1/m_2$ of the two lenses, and the angle ϕ that the source trajectory makes with respect to the binary axis. Shown in Figure 2.13 is an example of a point source - binary lens event showing the trajectory of the source relative to the lens masses and the resulting light curve.

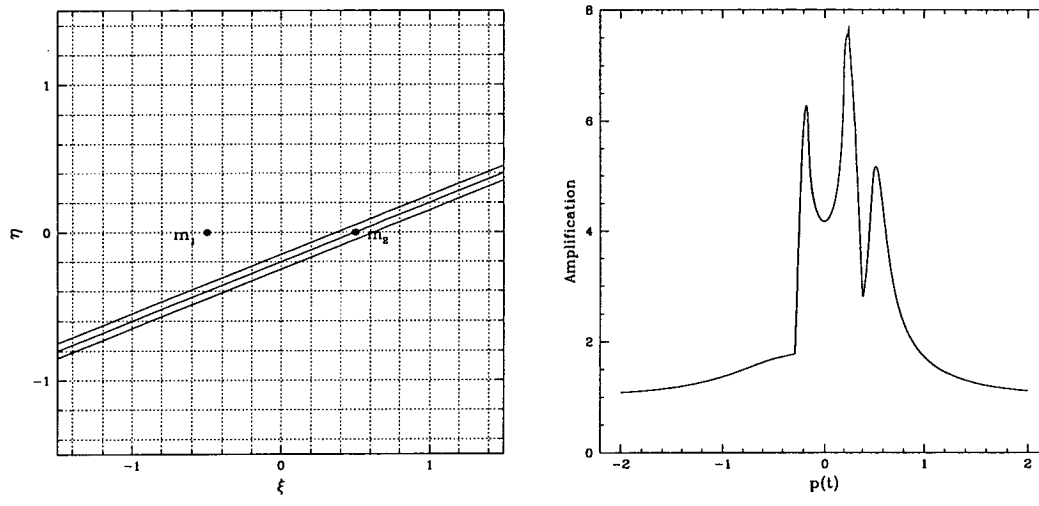

Figure 2.14: An extended source - binary lens event with $b = 1.0$, $q = 1.0$, $\phi = 0.38$ rad, and $R_s = 0.05$. **Left:** The configuration of the binary lens is shown where the positions of the masses are indicated by m_1 and m_2. The multiple lines indicate the path of the extended source (from left to right). Dimensions are normalized to the Einstein ring radius of the combined system. **Right:** The resulting binary lens light curve.

In the case of an extended source, the magnification remains finite when a caustic crossing occurs and the behaviour near the caustic depends upon the source size. Shown in Figure 2.14 is an example of a binary lens event where the source is extended and of uniform brightness.

2.5.2 Planetary Signatures

In the case of lensing by a star with a planetary system, the caustics are much smaller. Such an event will appear like a single lens event with a small probability of a deviation if one image passes near a planet. A source that passes over the central caustic will produce new images near the Einstein ring of the primary lens. If the source crosses the caustic of the planet then new images will be produced near the Einstein ring of the planet. If the projected separation of the primary lens and the planet is in the range 0.6–1.6 R_E then the caustics due to the planet will be inside the Einstein ring of the primary lens [37]. This range is called the *lensing zone* and planets that lie in this range will have a higher probability of

being detected since the source must also be inside the Einstein ring radius of the primary lens in order for the microlensing event to be alerted.

The actual physical size of the lensing zone will depend upon the mass of the lens and the distances to the lens and source. For a source located at $D_s = 8\,\mathrm{kpc}$ and a one solar mass primary lens, the size of the lensing zone would be 2.4–6.4 AU for $D_d = 4\,\mathrm{kpc}$ and 2.1–5.5 AU for $D_d = 6\,\mathrm{kpc}$. In our own Solar System, Jupiter has a mass ratio of $q \approx 10^{-3}$ and an orbital radius of 5.2 AU, placing it in the lensing zone for the distances mentioned above. Thus, if we assume our system with a Jovian-mass planet is common, this increases the probability that planets will be detected using microlensing. It has in fact been suggested that this coincidence between the Jovian orbital radius and the solar Einstein radius could lead to detection probabilities as high as 17% [42].

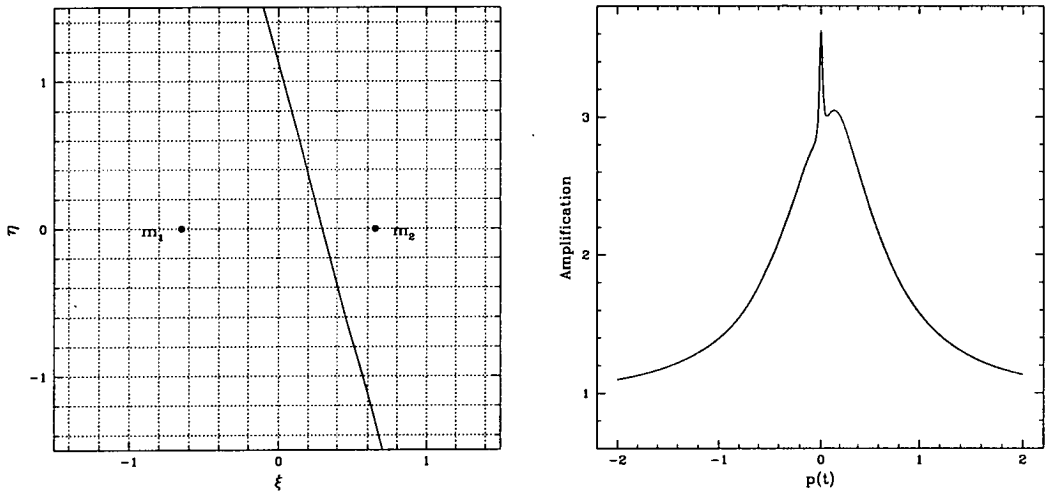

Figure 2.15: A point source - binary lens event in which one of the binary components is planet. The parameters are $b = 1.3$, $q = 0.001$, and $\phi = -1.31$ rad. **Left:** The configuration of the planet m_1 and primary lens m_2 is shown and the line indicates the path of the source (from top to bottom). Dimensions are normalized to the Einstein ring radius of the combined system. **Right:** The resulting light curve clearly shows the signature of the planet.

Shown in Figure 2.15 is an example of a binary lens light curve which clearly shows the signature of a planet of mass ratio $q = 10^{-3}$. A point source has been assumed but such an approximation becomes inadequate for companions of terrestrial mass ($q = 10^{-5}$) when the size of the planetary caustic becomes comparable to the size of the source. The duration of a planetary perturbation will depend upon the source trajectory amongst other factors, but is roughly given by the time taken by the source to cross the planetary Einstein ring diameter.

For a slightly larger mass ratio, the width of the perturbation increases which makes them easier to detect. Figure 2.16 shows an example of a binary lens light

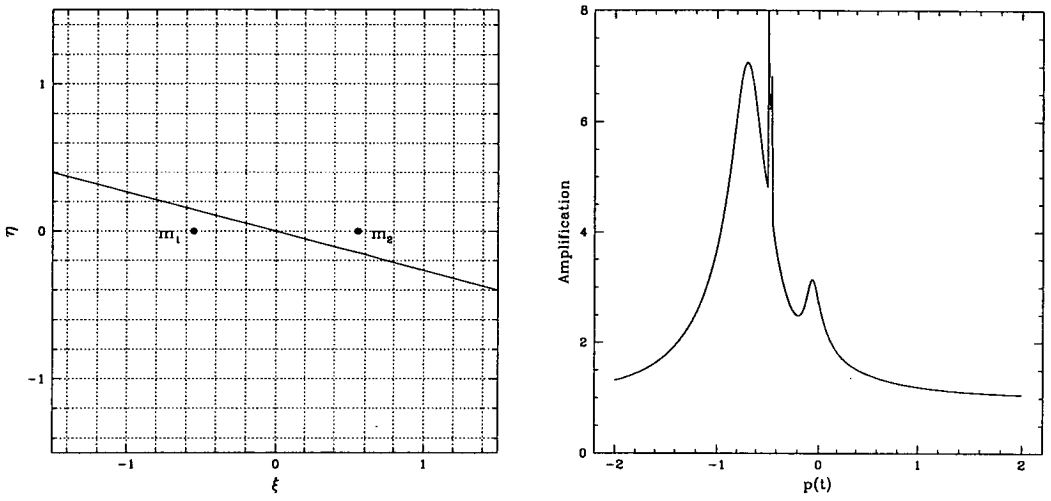

Figure 2.16: A point source - binary lens event in which one of the binary components is brown dwarf. The parameters are $b = 1.1$, $q = 0.01$, and $\phi = 1.83$ rad. **Left:** The configuration of the brown dwarf m_1 and primary lens m_2 is shown and the line indicates the path of the source (from right to left). Dimensions are normalized to the Einstein ring radius of the combined system. **Right:** The resulting binary lens light curve.

curve produced by a mass ratio of $q = 0.01$ in which one of the binary components is a brown dwarf. It has been calculated [23] that 95% of binary lens events that contain a brown dwarf should produce sufficient perturbation to be identified by the current observing programs of the various microlensing survey teams. The current null result may indicate that the frequency of brown dwarfs in binary systems may not be as common as previously thought.

2.6 Modelling of Light Curves

Given a set of observations of a microlensing event, one would like to condense and summarize the data by fitting it to a *model.* The general form of the mathematical function that defines the model will typically have a number of *free parameters*, variables which can be adjusted to change the shape of the curve.

For experimental data to be an adequate fit to the model, it is expected that the data points will be scattered randomly around the fit and that the size of the scatter should be approximately the same as the size of the error. Rather than attempting to determine this by eye, it is useful to calculate a statistical measure of the *goodness-of-fit* and then the probability that the data are consistent with the fitting function. This can be done by calculating the quantity χ^2 (chi-squared)

which is defined as

$$\chi^2 = \sum_{i=1}^{N} \frac{(y(x_i) - y_i)^2}{\sigma_i^2} \tag{2.52}$$

where N is the number of data points, $y(x_i)$ is the model function evaluated at the experimental value of $x = x_i$, y_i is the measured value of y, and σ_i is the magnitude of the error in the value of y_i. Hence, each point's deviation from the fit is measured in units of its uncertainty. Since it is expected that each term in the sum will have a value approximately equal to 1, it is expected that the computed value of χ^2 will have a value of order N. Therefore if χ^2 is much greater than N then the deviations from model are larger than that predicted by the error bars and a poor fit may be assumed. If χ^2 is much less than N then it is likely that the errors have been overestimated and an over fit may be assumed.

A polynomial of degree n may be uniquely defined by a number of points equal to $n + 1$ which will result in a χ^2 value of zero. To account for this, the concept of *degrees of freedom* (d.o.f.) is used and the number of degrees of freedom is given by $d = N - f$, where f is the number of free parameters in the function. The *reduced* χ^2 is then χ^2 divided by the number of degrees of freedom. The probability that the function represents the data set may be estimated from the reduced χ^2 using tables that frequently appear in appendicies to statistics books.

This general description of the χ^2 statistic is well suited to the modelling of light curves such as those outlined in the previous sections. This involves a tedious and time-consuming search throughout parameter space in order to find the best-fit parameters that will minimize the value of χ^2. Writing a computer program to conduct this search removes a large amount of the tediousness and hence a large amount of the time involved.

2.7 Detection Efficiencies

A great deal of time has been invested by the various microlensing survey teams into developing optimal observing strategies for detecting microlensing events. These efforts have been successful in improving the detection rate by several orders of magnitude since the first microlensing event was discovered. Factors which will improve this detection rate are an increased telescope aperture, larger and more efficient detectors, improved seeing, a fainter sky, and, of course, better weather. These factors have recently been examined in detail by Gould [44] and strategies for the survey teams of EROS and MACHO have been suggested which will, in theory, increase the detection of LMC events to more than $100\,\mathrm{yr}^{-1}$.

More recently, substantial interest has been shown in calculating the detection efficiencies of microlensing observations to stellar and planetary companions [39]. In this case, a companion is considered to have been detected if a binary lens model is found to produce a substantially better fit to the observed light curve than a single lens model. A substantially better fit will mean that the best

binary fit exceeds the best single fit by some threshold value, or $\chi^2_{single} - \chi^2_{binary} > \Delta\chi^2_{thresh}$. The detection efficiency $\epsilon(b,q)$ is then the probability that a companion with mass ratio q and angular separation b would be detected in an observed light curve, assuming a random source trajectory.

A method for calculating the detection efficiency has been proposed by Gaudi & Sackett [39] which entails the following steps:

1. A PSPL model is fitted to the light curve by minimizing χ^2.
2. Holding b and q at fixed values, the binary lens model that best fits the light curve is found for each source trajectory α and the value of $\Delta\chi^2$ is evaluated.
3. The fraction of binary lens fits for a given (b,q) that satify $\Delta\chi^2 > \Delta\chi^2_{thresh}$ is calculated. This detection efficiency is given by

$$\epsilon(b,q) \equiv \frac{1}{2\pi}\int_0^{2\pi} d\alpha\, \Theta[\Delta\chi^2(b,q,\alpha) - \Delta\chi^2_{thresh}] \tag{2.53}$$

   where $\Theta[x]$ is a step function.
4. Steps 2. and 3. are repeated for a grid of (b,q) values which results in the detection efficiency $\epsilon(b,q)$ for the observed light curve.

These steps assume that the baseline flux is perfectly known and that the event is not blended. It has been suggested [39] that the resulting integrated detection efficiency be considered as a primary outcome of monitoring microlensing events as it incorporates all the information from the observations. Limits on companions to the primary lens have been calculated for the MACHO event MB98035 [83] and the OGLE event OB98014 [9].

Chapter 3

Observations and Data Reduction

This chapter describes the facilities used to acquire the photometric data and the methods used to reduce them. The first section outlines the facilities used at Canopus Observatory in Australia, at which most of the data were collected. The second section outlines the facilities used at CTIO in Chile. The third section details the operation and applications of DoPHOT, a point-spread function fitting CCD photometry program. The final section describes the two methods that were used to reduce the photometric data and provides a comparison between the two.

3.1 Observations at Canopus Observatory

Observations were made during the bulge seasons in 1996 and 1997 using the 1.0 m telescope at Canopus Observatory (shown in Figure 3.1) located about 12 km east of Hobart, Tasmania, Australia during the bulge seasons in 1996 and 1997. Its southerly latitude of $-42.85°$ makes it an excellent site from which to observe the Galactic bulge and the Magellanic Clouds.

3.1.1 Telescope Description

The 1.0 m telescope is a Cassegrain telescope with a focus ratio of f/11.3 and a scale at focus of 18.2 arcsec/mm [112]. Although the telescope employs a spectrograph, and in fact the original purpose of the telescope was high dispersion at Coudé focus, the telescope is dedicated almost exclusively to photometric observations. The main instrumentation used at the telescope is a 2 channel high speed photometer and a CCD camera.

Figure 3.1: Canopus Observatory located near Hobart, Australia.

3.1.2 CCD Camera

A Charge Coupled Device (CCD) camera consists of a silicon chip covered with light-sensitive cells (or *pixels*), the associated mechanical and electronic components for signal processing, and the computer hardware and software. The silicon chip is often referred to as the *detector* and its basic function is to convert incoming photons of light to electrons which can be read out and displayed as an image on a computer. There are many sources of detailed information concerning the principles and operation of CCD cameras [25].

The CCD camera used for the 1996 and 1997 bulge seasons was a SBIG ST-6 CCD camera. This camera has a gain of 6.7 electrons/count and a read-out noise (RON) of 36.85 electrons.

The camera has a pixel array of 375×242 where the pixels are rectangular with a size of $23 \times 27\,\mu$m. When mounted at the focus of the 1.0 m telescope, one obtains a pixel scale of 0.418×0.491 arcsec/pixel. For the purpose of seeing calculations, an average pixel scale of 0.455 arcsec/pixel was used.

The 1996 images were rebinned to have square pixels resulting in a pixel array of 375×283 and a scale of 0.418 arcsec/pixel. During the 1996 bulge season we used a transfer lens to increase the size of the field of view. To estimate the effect of the transfer lens on the pixel scale, two raw images of the same field were examined (one with the transfer lens and one without) and the distances between various stars was determined. It was found that the transfer lens increases the pixel scale by a factor of ≈ 2.1 making the scale for the 1996 bulge season 0.88 arcsec/pixel.

3.1.3 Dark Subtraction and Flat-Fielding

Although a CCD chip is normally cooled, thermal noise remaining in the system results in all images taken with a CCD camera having a contribution due to *dark counts*. The noise due to pixel-to-pixel variations in the dark current can be substantially reduced by taking a measurement of the signal produced by the CCD camera when no light is incident on the CCD chip and then subtracting the measurement from the raw image. This measurement must have sufficient integration time to measure the dark counts due to the current which then need to be scaled to the integration time of the raw image. This must be taken at the same temperature as the raw image and is called a *dark frame*. The ST-6 camera at Canopus Observatory was generally cooled to a temperature of 223 K and 4-5 dark frames were averaged together and then subtracted from the raw images.

Since the response of each pixel on a CCD chip is slightly different, dark-subtracted images need to be corrected by dividing them by a *flat field image*. A flat field image can be created by taking an exposure of a featureless extended object with a uniform or flat brightness. This is usually the sky (producing *sky flats*) or a flat white-painted board inside the dome of the telescope (producing *dome flats*). Sky flats are often the favourable option as dome flats generally do not reflect well the large-scale flat field pattern due to differences in the vignetting and colour between a sky flat and a dome flat. For the observations at Canopus observatory, several sky flats in each filter were taken every few days at dawn or just after sunset and then averaged together to flat field the dark-subtracted images.

3.2 Observations at CTIO

Observations were made using the 0.9 m telescope at the Cerro Tololo Inter-American Observatory (CTIO) located about 70 km east of La Serena, Chile at an altitude of 2200 m. These observations were made during the 1997 and 1998 bulge seasons. Shown in Figure 3.2 are some of the telescope domes at the peak of Cerro Tololo.

3.2.1 Telescope Description

The 0.9 m telescope is a Cassegrain telescope with a focus ratio of f/13.5 and a scale at focus of 16.5 arcsec/mm. The telescope is mounted on an off-axis symmetrical mounting and used on the east side of the pier. The main instrumentation used at the telescope is the Cassegrain Focus CCD Imager (CFCCD).

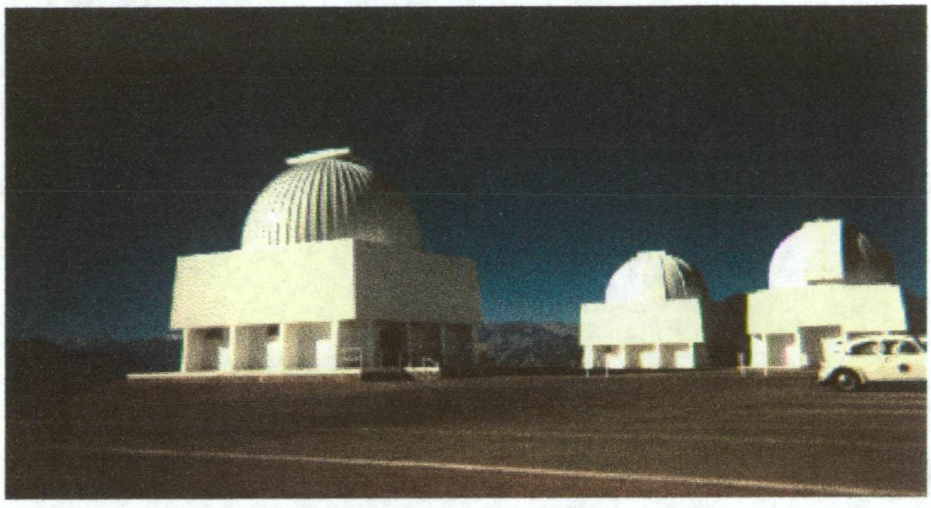

Figure 3.2: Some of the telescope domes at the Cerro Tololo Inter-American Observatory. Shown from left to right are the 0.9 m, the Yale 1.0 m, and the Curtis/Schmidt Telescope.

3.2.2 CCD Camera

At the time of observing during the 1997 and 1998 bulge seasons, the 0.9 m telescope was equipped with a Tek 2K CCD camera. The camera has a pixel array of 2048×2048 but only the central 320×320 was used for processing. The pixel scale of the camera is 0.396 arcsec/pixel. The orientation of the camera is such that east is left and north is down. The gain and read-out noise of the CCD camera was set at different values for the various observing runs (see Table 3.1) and was accordingly taken into account in the reduction procedures.

Observing Run	**Gain**				**RON**			
	11	12	21	22	11	12	21	22
May 20–23, 1997	1.6	1.6	1.6	1.6	3.4	3.4	2.7	2.7
July 17–20, 1997	3.3	3.2	3.2	3.2	4.1	4.1	3.9	3.9
August 3–10, 1997	2.5	2.4	2.4	2.4	3.8	3.9	3.6	3.6
August 12–19, 1997	2.5	2.4	2.4	2.4	3.8	3.9	3.6	3.6
June 5–14, 1998	3.3	3.2	3.2	3.2	4.1	4.1	3.9	3.9

Table 3.1: The gain and read-out noise for the quadrants of the CCD (denoted as 11, 12, 21, and 22) for the different observing runs.

The CCD was operated using the Array Controller (ARCON) hardware and software system which is used on all CTIO telescopes. The ARCON controllers consist of a small box bolted to the dewar which contains all the electronics needed to operate the CCD. This is connected via a fiber-optic cable to a Transputer Modules (TRAMS) box which is linked to a SUN SPARC station. This allows

the ARCON to be operated from within an Image Reduction Analysis Facility (IRAF)-based integrated data acquisition-data reduction environment.

3.2.3 Bias Correction and Flat-Fielding

If the temperature of the CCD is below 193 K then the thermal counts are so few that their effect can be considered as negligible. In this case, dark frames are not required to be subtracted from the raw images. However, the total counts in a dark frame include a contribution from the control voltages present on each pixel. These voltages are called *bias voltages* and can be corrected for by taking a series of 1 second *bias frames* and then subtracting the averaged bias frame from the raw images. The observations at CTIO normally used 10 bias frames to perform the correction.

The flat fields used for the CTIO observations were sky flats when conditions were favourable but mainly consisted of dome flats. Normally 10 dome flats in each filter were taken at the beginning of every night and then averaged together to perform the flat-fielding. Both the bias correction and the flat-fielding of the CTIO data was performed using the IRAF package *quadproc*, a package which was designed for use on the quad CCD cameras at CTIO.

3.3 DoPHOT

DoPHOT is a CCD photometry program which is designed to search for "objects" on a digital image of the sky and produce positions, magnitudes, and crude classifications for those objects [89]. DoPHOT is optimized for the reduction of a large number of low signal-to-noise (S/N) images and so is very well suited to performing photmetry on the often faint microlensed stars found in the crowded bulge fields. Another method becoming more popular for use in microlensing data reduction is the use of image subtraction [3] but this will not be discussed here.

Another advantage of DoPHOT is that it is written in FORTRAN and so it runs independently of any image processing software. However, it was found that DoPHOT does not behave exactly the same under all operating systems. A test was performed in which the same image was processed using DoPHOT under Unix and Linux. The result was that the Linux processing found 18 more stars than the Unix processing, the additional stars being inserted at various places throughout the DoPHOT output file. This can cause problems if you are relying on the order of the stars found in a template image which was processed under two different operating systems.

DoPHOT's ease of use makes it ideal to automate on a large amount of data. All that is required from the user is the modification of a small number of parameters which are then combined with a complete list of parameters called a

default parameter file (see Appendix B.1). Once the parameters have been set, DoPHOT proceeds to reduce the data by adopting a model for different kinds of objects.

Two of the most important parameters for the user to specify in the DoPHOT parameter file are values for the full-width at half-maximum of the star image profile (input parameter FWHM) and the sky intensity (input parameter SKY) estimated to within 10%. DoPHOT uses the two starting values to fit functions to the stellar image profiles in two orthogonal directions. During this process, DoPHOT determines an improved estimate of the two parameters.

3.3.1 Point Spread Function Fitting

DoPHOT seeks to identify objects within an image by applying the most suitable model for that object. Cosmic rays are identified by a single high pixel and stars are typically identified as an elliptical gaussian. The reliability of the relative photometry performed on crowded fields assumes that every star in the frame has approximately the same point spread function (PSF), in most cases a reasonable assumption for small fields.

Whereas reduction packages such as DAOphot allow the user to choose various analytical functions with which to fit the PSF, DoPHOT uses one model for stellar images that is a function of only seven parameters. This consists of similar ellipses of the form

$$I(x,y) = I_0 \left(1 + z^2 + \frac{1}{2}\beta_4(z^2)^2 + \frac{1}{6}\beta_6(z^2)^3\right)^{-1} + I_s \tag{3.1}$$

where

$$z^2 = \left[-\frac{1}{2}\left(\frac{x^2}{\sigma_x^2} + 2\sigma_{xy}xy + \frac{y^2}{\sigma_y^2}\right)\right] \tag{3.2}$$

and

$$x = (x' - x_0)\ ;\ y = (y' - y_0) \tag{3.3}$$

with the seven free parameters being the stellar profile centre (x_0, y_0), the shape parameters $(\sigma_x, \sigma_y, \sigma_{xy})$, the central intensity I_0, the background intensity I_s, and the user-specifiable dimensionless quantities β_4 and β_6 which are ordinarily left at their default value of unity. DoPHOT is able to use only one analytical function due to the assumption stated above, that every star can be fitted with the same PSF. Furthermore, DoPHOT reduces no more than two stars simultaneously, whereas DAOphot allows simultaneous reductions of large numbers of stars. This leads to a dramatic decrease in processing time and in fact a test performed [3] showed that DoPHOT decreases the processing time over DAOphot by at least a factor of 8.

As DoPHOT identifies objects in an image, the objects are subtracted using the best current model for the object. As successive passes over the data are

made, fainter objects are identified and after each search the shape parameters for all objects are redetermined. The stars are fitted again with the new values and the objects that have been subtracted are temporarily added back so they can be fitted and then subtracted again. In this way, fit magnitudes are obtained for objects down to a lower threshold specified by the user.

DoPHOT attempts to classify objects based on the determined shape parameters for the object. If DoPHOT finds that the shape parameters of an object differ from those of a stellar object by a user specifiable minimum scatter (input parameters SIGMA1, SIGMA2, and SIGMA3) the object will be classified as a double star or a galaxy depending on the value of the input parameter STARGALKNOB. DoPHOT will classify objects by assigning a type number which is included in the output file. This will be one of the following:

1. A 'perfect' star.
2. Interpreted to be a 'galaxy'.
3. Interpreted to be two very close stars.
4. Failed to converge on a 4-parameter fit using mean single star shape resulting in extremely unreliable photometry.
5. Succeeded in 4-parameter fit but failed in 7-parameter fit due to lack of points with adequate S/N resulting in unreliable photometry.
6. Not enough points to attempt 4-parameter fit with mean star shapes.
7. Object was too faint to attempt a 7-parameter fit resulting in inability to successfully classify the object. The photometry is reliable but the object may not be a star.
8. Obliterated regions.

3.3.2 Fixed Position Warmstart

Version 2.0 of DoPHOT includes the useful feature of being able to apply a *fixed position warmstart.* This allows the user to specify an input file containing the positions of a selection of objects (see input parameter FIXPOS). This file is then used by DoPHOT to perform photometry on the objects listed with five fitting parameters rather than seven, with the two position parameters being fixed at the specified values. A fixed position DoPHOT run produces an output file in which the star types are augmented by 10. A 'perfect' star of type 1 then becomes type 11 and so on.

A useful application of this feature is to run DoPHOT on an image taken in good seeing, then use the DoPHOT output file as a fixed position *template* on each

of the other images of the same field. The coordinate transformation between the template frame and the frames at other epochs can be performed using a program (included with DoPHOT) called OFFSET which searches for similar triangles and computes the translation and rotation between the two frames. This fixed position method has the advantages of decreasing the processing time, increasing the quality of the photometry, and increasing the number of objects recovered by DoPHOT.

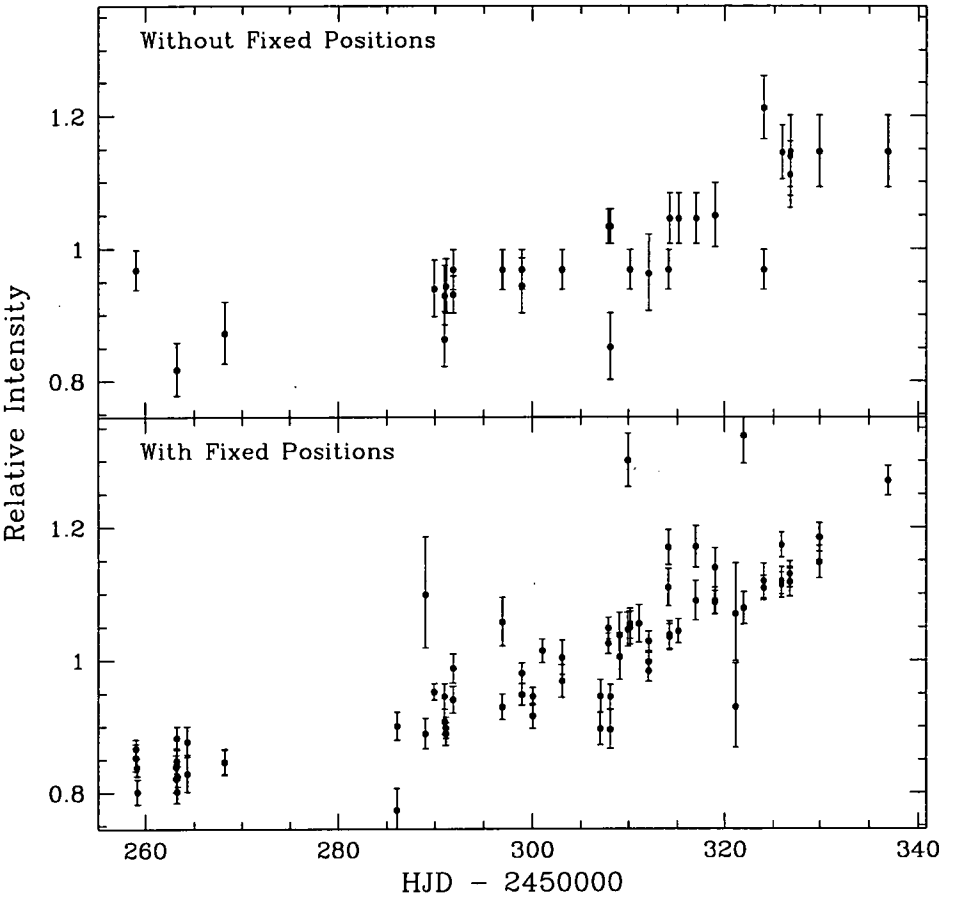

Figure 3.3: A comparison of light curves for the event MB96012 resulting from running DoPHOT without using fixed positions (top) and using fixed positions (bottom).

Shown in Figure 3.3 is a comparison of a light curve using fixed positions and without using fixed positions. The relative intensity of the event is shown with respect to the average flux of 10 reference stars. These MB96012 I band data were originally reduced using DoPHOT without applying the fixed positions method. However, the use of a template image to create a list of accurate star positions

enabled the fixed positions method to transform the coordinates to images taken under less desirable conditions. The result was that the microlensed star was identified by DoPHOT in 75 out of 76 frames (as opposed to 40 out of 76 frames for the non-fixed position run) and the errors were improved by a factor of 2.

3.3.3 DoPHOT Errors

The DoPHOT output file provides a fit magnitude with an estimate of the associated error. The DoPHOT manual does not describe how the formal error is determined, but it is described elsewhere [89] that the errors in the magnitudes are the same as the errors in determining the height parameter of the fitted stellar models.

For each of the MACHO fields observed by PLANET, reference stars were chosen to be used as relative flux standards. These were chosen to be relatively bright and isolated, so that effects from seeing are minimal, and also uniformly distributed around the microlensed star. As such, the error in the relative photometry is dominated by the magnitude and crowding of the microlensed star.

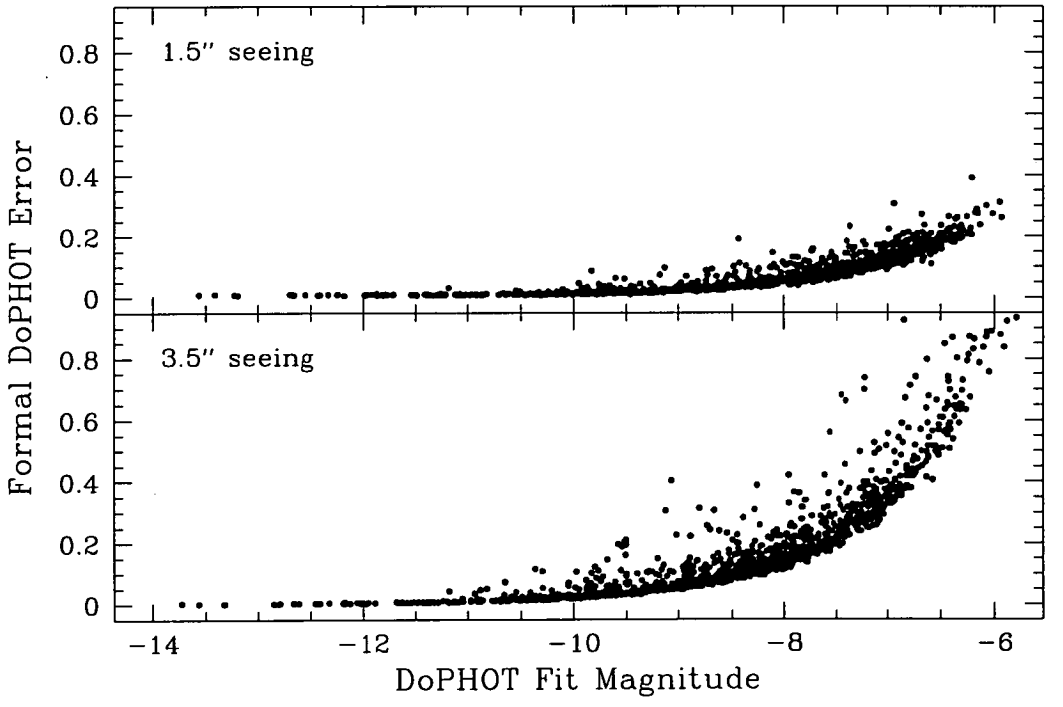

Figure 3.4: Formal DoPHOT error in magnitudes as a function of DoPHOT fit magnitude for good seeing conditions (top) and bad seeing conditions (bottom). These plots use DoPHOT types 1, 3, and 7.

Figure 3.4 shows a plot of the formal DoPHOT error as a function of the DoPHOT fit magnitude for a good seeing image (1.5″) and a bad seeing image

(3.5″) of the MB97026 field. Both frames were taken at Canopus Observatory with an exposure time of 5 minutes. As expected, bad seeing results in a larger number of unreliable measurements for fainter magnitudes, and the reliability of photometry in bad seeing for stars with a fit magnitude greater than -6 deteriorates rapidly.

It has been found that the formal DoPHOT error is not always a reliable indication of the actual scatter. After examining a collection of constant stars, the PLANET collaboration found the true scatter to be as much as 1.5–2.0 times the mean DoPHOT error, with the factor being less for fainter stars [7]. Additional discrepancies may be introduced by systematic errors, such as scattered light incident upon the CCD and the sky brightness due to the phase and position of the moon.

3.4 Reduction Methods

Two different methods were used to reduce the photometric data. The first method uses a collection of Munich Image Data Analysis System (MIDAS) scripts to examine and process the images with DoPHOT. The second method consists of a collection of C shell scripts and C programs written by Jean-Philippe Beaulieu for the PLANET collaboration to serve as a pipeline for automatic PLANET data reduction.

3.4.1 The MIDAS Method

The MIDAS method was used to reduce the data obtained at Canopus Observatory during the 1996 and 1997 bulge seasons and at CTIO during the 1997 and 1998 bulge seasons. Five MIDAS scripts (see Appendix B.2) were written to perform this task.

1. The first script prepares the images for DoPHOT. The image pixels are scaled to lie between 0 and 32767 and are converted to 16 bit integers. The gain is scaled accordingly (referred to by DoPHOT as electrons per data number, input parameter EPERDN) and written to an image descriptor. The Heliocentric Julian Date (HJD) at the middle of the exposure is also calculated and written to an image descriptor. The CTIO script extracts a 320×320 subframe from the centre of the frame.

2. The second script is used to estimate the FWHM and sky values for each frame by fitting a 2-dimensional gaussian to several stars in each frame and then taking the average value.

3. The third script prepares the frame to be used as a template for the fixed position warmstart. The template image is normally chosen such that the

seeing conditions are reasonably good and the microlensed star is fairly well centred and fairly bright.

4. The fourth script "cleans" the template DoPHOT output file by removing all objects except those of type 1, 3, and 7.

5. The fifth script performs the fixed position warmstart on each of the images and then uses a file (created by the user) containing the positions of the microlensed star and the reference stars in the template image to extract the photometry for the specified objects. This information, along with the time of observation in the image header, is written to an ascii output file.

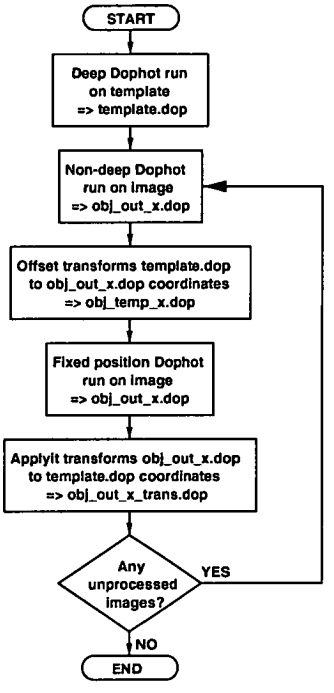

Figure 3.5: The MIDAS Method flowchart

The most important parts of the processing are the creation of the template and the fixed position DoPHOT run contained in the third, fourth, and fifth scripts, as summarized in Figure 3.5. A deep DoPHOT run is performed on the template image using the parameter file *param_template*, from which the template DoPHOT output file *template_raw.dop* is produced. This file is then "cleaned" and renamed as *template.dop*. The fifth MIDAS script then processes an image as follows:

- The parameter file *param_mod_x* is used to perform a non-deep DoPHOT run on the image, the output of which is *obj_out_x.dop*.

- *obj_out_x.dop* is used to obtain the coordinate transformation from the image to the template. This transformation is applied to the objects in *template.dop* using OFFSET, the output of which is *obj_temp_x.dop*.

- The parameter file *param_mod_xt* is used to perform a deep DoPHOT run on the image with fixed position stars from the template *obj_temp_x.dop*, the output of which is *obj_out_x.dop*. This output file also includes stars down to a threshold of about 25 ADU (analogue to digital units) in addition to the fixed position photometry.

- The coordinate transformation that was earlier used to transform the coordinates of the template to those of the image being processed is now used to transform the coordinates of *obj_out_x.dop* to those of the template using a program called *applyit*, the output of which is *obj_out_x_trans.dop*. This is the final DoPHOT output file.

3.4.2 The Pipeline Method

The pipeline method was used to reduce the data obtained at Canopus Observatory during the 1998 bulge season and to archive all the reduced data so that it could be added to the PLANET database. Mastery of the pipeline involves becoming familiar with a range of C shell scripts which are described in detail in Appendix B.3. The pipeline was designed to automate the reduction process so that images from a CCD camera are detected by a continuously running *cron* job and are processed by DoPHOT using fixed position stars from a previously chosen template. This automation has been successful to some degree with some manual input still needed for a few steps. The basic steps of the pipeline method are as follows:

1. The images are prepared for the pipeline with a pre-designed script which performs the necessary dark subtraction and flat-fielding and also estimates FWHM and SKY (using a program called CCDProc) which are written into the header of the image.

2. Before starting the pipeline, the shell environment variables need to be set up using a file called *csh_set*. A template image is then chosen from the available images.

3. The pipeline is started by setting up a cron job which executes the script *csh_kron* once per minute. This script looks in the *$IN_IMAGE* directory to determine if there are any new images. If there is a new image, it starts a fixed position DoPHOT run on the image using the previously chosen template as the source for the fixed position stars.

4. A script called *csh_archive* may be used to archive the output data from the pipeline. This places it in a form which is consistent with the existing PLANET database.

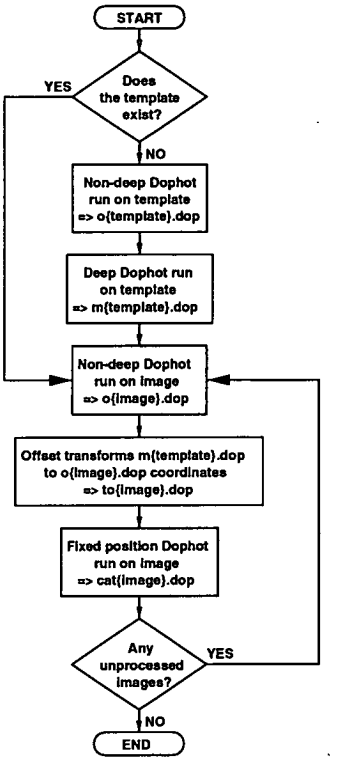

Figure 3.6: The Pipeline Method flowchart

The pipeline handles the fixed position photometry slightly differently than the MIDAS method as can be seen in the summary shown in Figure 3.6. The pipeline uses the script *csh_kron* to call upon the scripts *csh_thres, csh_template_fs*, and *csh_off_fs*. This follows the following general pattern:

- *csh_kron* begins by checking to see if the template DoPHOT output file ($m\{template\}.dop$) exists. If the file does not exist then it calls upon *csh_template_fs*. This script calls upon *csh_thres* twice: firstly to perform a non-deep DoPHOT run on the template to produce $o\{template\}.dop$, and secondly to perform a deep DoPHOT run on the template to produce $m\{template\}.dop$.

- *csh_kron* then processes an image and *csh_off_fs* is called upon to do this. This script calls upon *csh_thres* to perform a non-deep DoPHOT run on the image to produce $o\{image\}.dop$.

- *csh_off_fs* then uses OFFSET to calculate the geometrical transformation between *o{image}.dop* and *o{template}.dop*. OFFSET then applies this transformation to the template *m{template}.dop* and outputs the resulting file as *to{image}.dop*, thereby transforming the coordinate system of the template to the coordinate system of the image being processed.

- Lastly, *csh_off_fs* performs a fixed position DoPHOT run on the image using *to{image}.dop* to produce *cat{image}.dop*. This is the final DoPHOT output file.

The interesting thing to note is that the final product, *cat{image}.dop*, is not transformed to have the same coordinate system as the template. This is because the pipeline relies on the fact that DoPHOT does not rearrange the stars after doing a fixed position run, and the relative position in the *cat{image}.dop* file and in the archive is assumed to be the same. Type 8 stars are ignored, as are type 5 and 4, so even though there may be a saturated star in the template near the beginning of the file, if it is unsaturated in the image being processed it will be added to the end of the *cat{image}.dop* file with type < 10. It will be ignored by the pipeline, which keeps only type 11 and above to put in the archive.

Chapter 4

Photometry Results

This chapter presents the results from the PLANET observations during the 1996, 1997, and 1998 bulge seasons. The first section presents the results from the 1996 bulge season with observations from Canopus Observatory. The second section presents the results from the 1997 bulge season with observations from Canopus Observatory and from CTIO. The third section presents the results from the 1998 bulge season with observations from CTIO. The reduction of the data presented in this chapter has been performed entirely by the author.

The majority of microlensing events observed by the PLANET collaboration are alerted by the MACHO or OGLE collaborations. In order to distinguish between these, the prefixes "MB" and "OB" have been chosen to signify a MACHO bulge event or an OGLE bulge event respectively.

For each event, a $44'' \times 44''$ image centred on the event is shown where a circle indicates the location of the microlensed source. This is useful for indicating the level of crowding in the vicinity of the event and sources of possible blending. The image in all cases is from observations at Canopus Observatory unless indicated otherwise. With the exception of the 1998 OGLE events, the baseline V and R magnitudes of the source (as conveyed in the original MACHO alerts) is also given. It should be noted that MACHO uses specially designed wide-pass filters which results in magnitudes that differ slightly from the standard Johnson-Cousins system used by PLANET. The orientation of the fields is such that east is left and north is up.

An uncalibrated colour-magnitude diagram (CMD) is shown for each event and the location of the microlensed stars are indicated. These CMDs were created using a MIDAS script which matches stars between the DoPHOT output files from an I image and a V image taken at approximately the same time. The relative baseline magnitude of the event was determined by estimating the magnitude offset at the given time using the fit parameters given on the MACHO and OGLE alert web pages.

For both the I and V band filters a plot of the relative intensity of the microlensed source is shown along with plots of the 10 reference stars and a plot

showing the variation in seeing. The seeing includes tracking errors and the effects of poor focussing in addition to the photometric conditions. The dates labelled on the plots are the Heliocentric Julian Dates (HJD) calculated at the middle of the exposure. The light curve plots of the 10 reference stars include dashed lines which indicate the 1 σ errors. The manner in which the reference stars are used to calculate the relative intensity of the microlensed source is described in Appendix C.

4.1 The 1996 Bulge Season

Event	Coordinates		# Frames	
	R.A. (J2000)	DEC. (J2000)	I	V
MB96004	18:06:11.9	-28:16:53	4	4
MB96009	18:04:57.7	-27:33:18	7	3
MB96010	18:00:01.9	-28:45:18	4	0
MB96011	18:09:15.8	-29:19:49	23	9
MB96012	18:03:53.2	-27:57:36	76	38
MB96014	18:05:15.4	-27:58:25	3	3
MB96016	18:01:09.0	-27:57:59	118	34
MB96018	18:11:40.7	-29:27:20	2	1
MB96019	18:02:11.4	-29:19:21	9	2
MB96020	17:59:40.6	-28:47:25	128	41
MB96021	17:58:43.2	-29:00:29	79	21
MB96023	18:06:23.6	-30:59:03	52	14
MB96025	18:10:58.8	-27:31:02	29	13
MB96026	18:03:54.0	-27:33:31	0	12
MB96027	17:59:19.6	-29:06:07	7	0
MB96028	18:04:09.0	-29:03:11	1	0

Table 4.1: Events observing during the 1996 bulge season.

1996 was the first year that Canopus Observatory took part in monitoring microlensing events with the PLANET collaboration. A total of 16 events were monitored during the 1996 bulge season, as shown in Table 4.1. Of these 16 events, the results of 4 are presented in this section. The remainder of the events either suffered from lack of data points or the event was too faint in which case DoPHOT was unable to find an adequate fit to the star.

MB96011

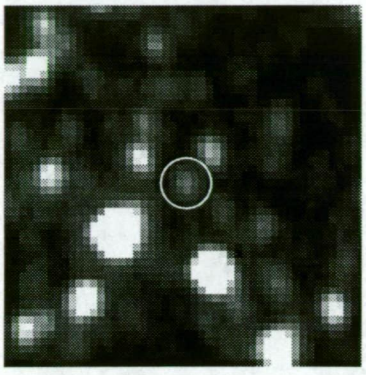

Figure 4.1: Bulge field MB96011. The event has a baseline magnitude of $V = 18.1$ and $R = 17.4$ and is relatively uncrowded.

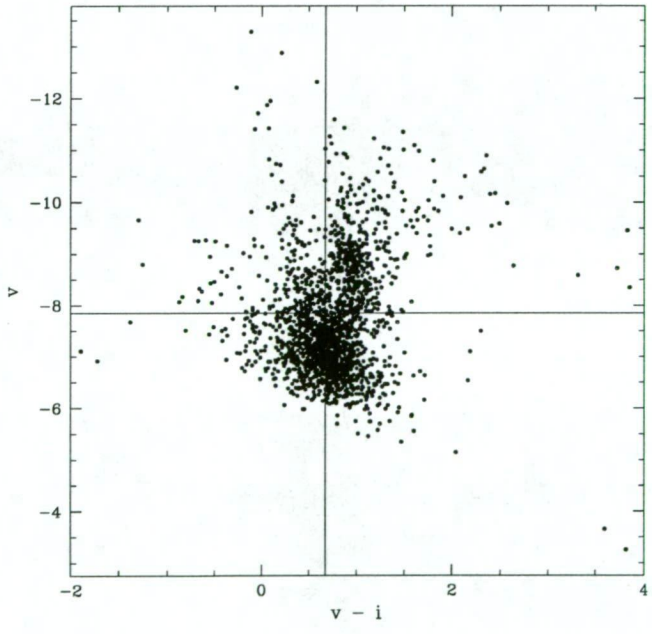

Figure 4.2: The colour-magnitude diagram of bulge field MB96011 is shown in which 2070 stars are plotted. The location of the microlensed source at baseline is indicated by the cross-hairs where the DoPHOT fit magnitudes are $I = -8.5$ and $V = -7.9$.

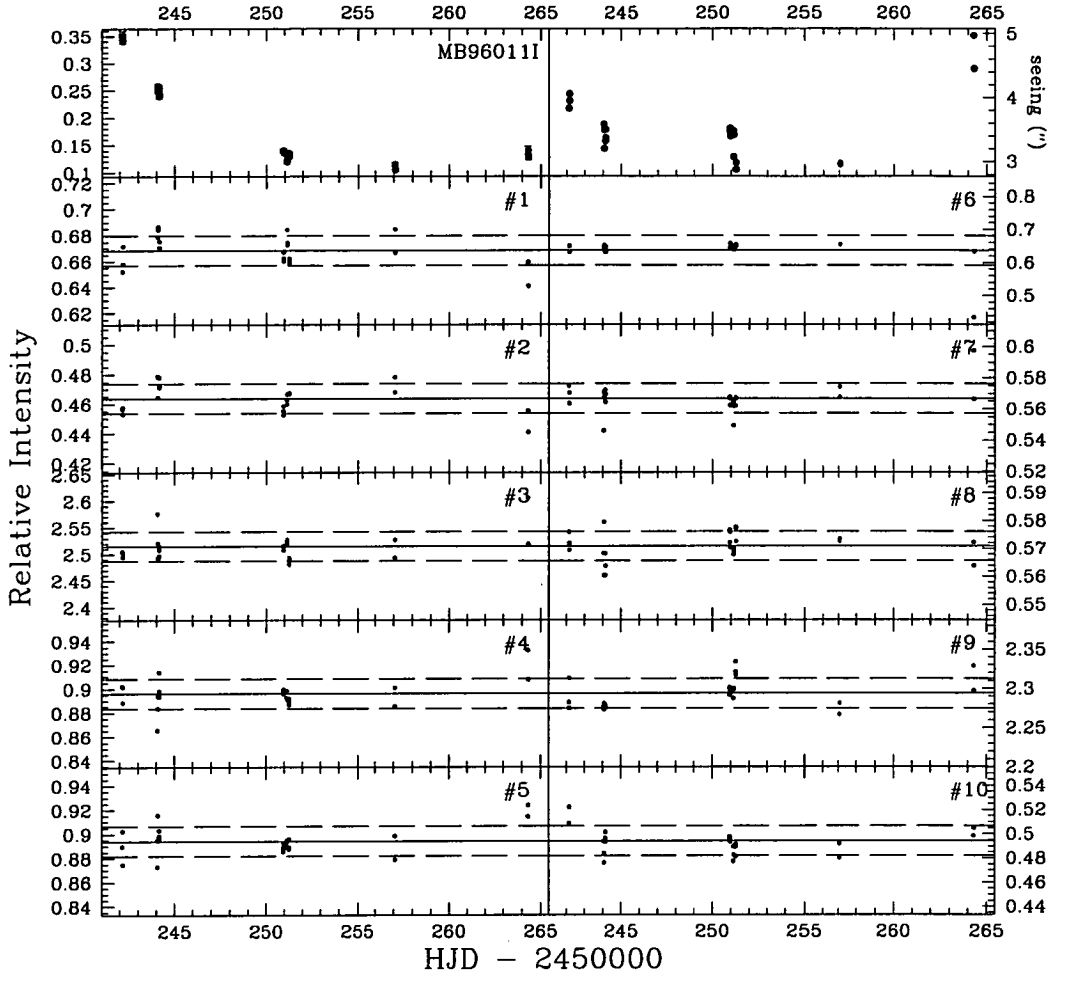

Figure 4.3: I band light curve for event MB96011. The relative intensity of the microlensed source with respect to the average flux of the reference stars is shown in the top left panel. The light curve includes a total of 23 data points. All 10 reference stars were used with an average scatter of 0.021. The last few spurious data points are likely due to the bad seeing conditions as can be seen in the top right panel.

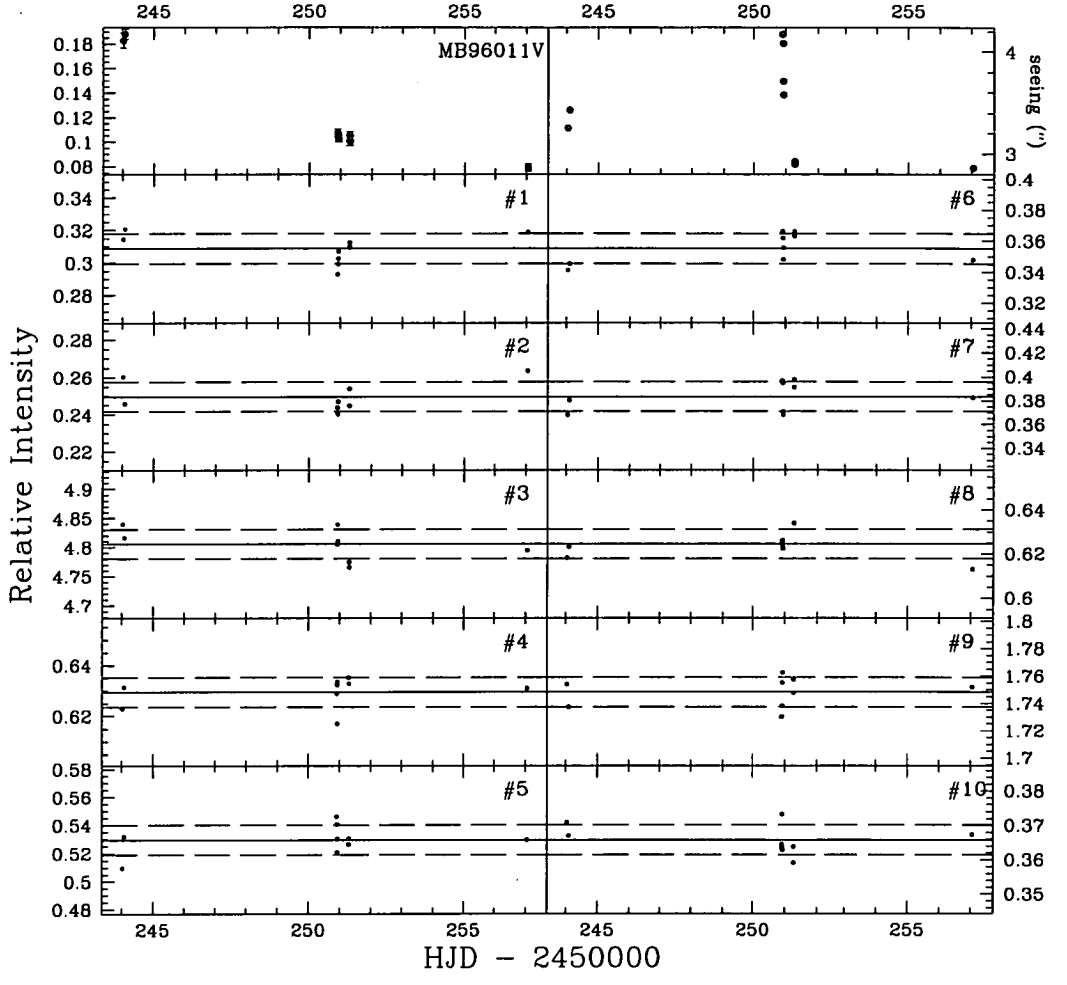

Figure 4.4: V band light curve for event MB96011. The relative intensity of the microlensed source with respect to the average flux of the reference stars is shown in the top left panel. The light curve includes a total of 9 data points. All 10 reference stars were used with an average scatter of 0.018.

MB96012

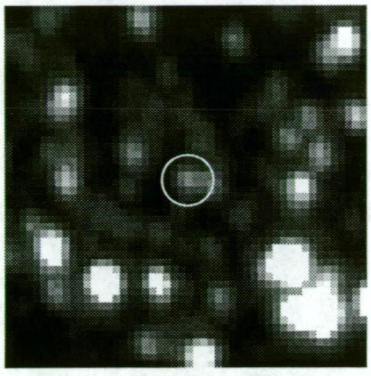

Figure 4.5: Bulge field MB96012. The event has a baseline magnitude of $V = 17.7$ and $R = 16.9$. The event has a close companion which can lead to an increase in photometric errors when observed in conditions of bad seeing.

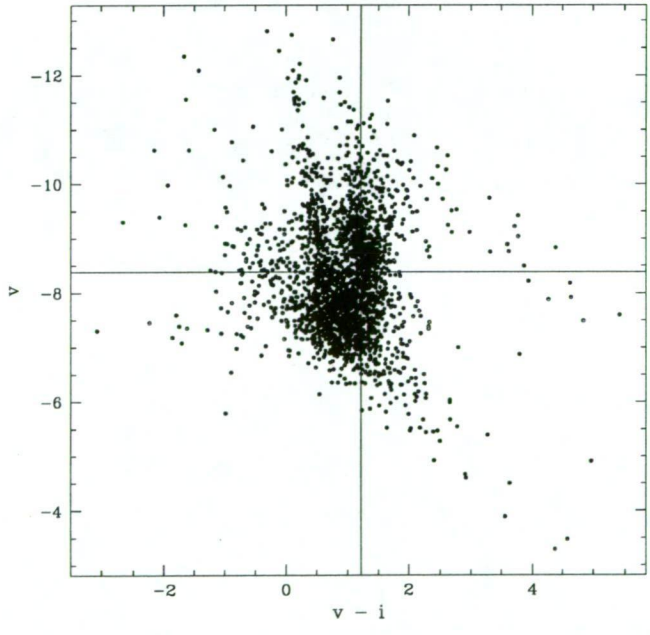

Figure 4.6: The colour-magnitude diagram of bulge field MB96012 is shown in which 2673 stars are plotted. The location of the microlensed source at baseline is indicated by the cross-hairs where the DoPHOT fit magnitudes are $I = -9.6$ and $V = -8.4$.

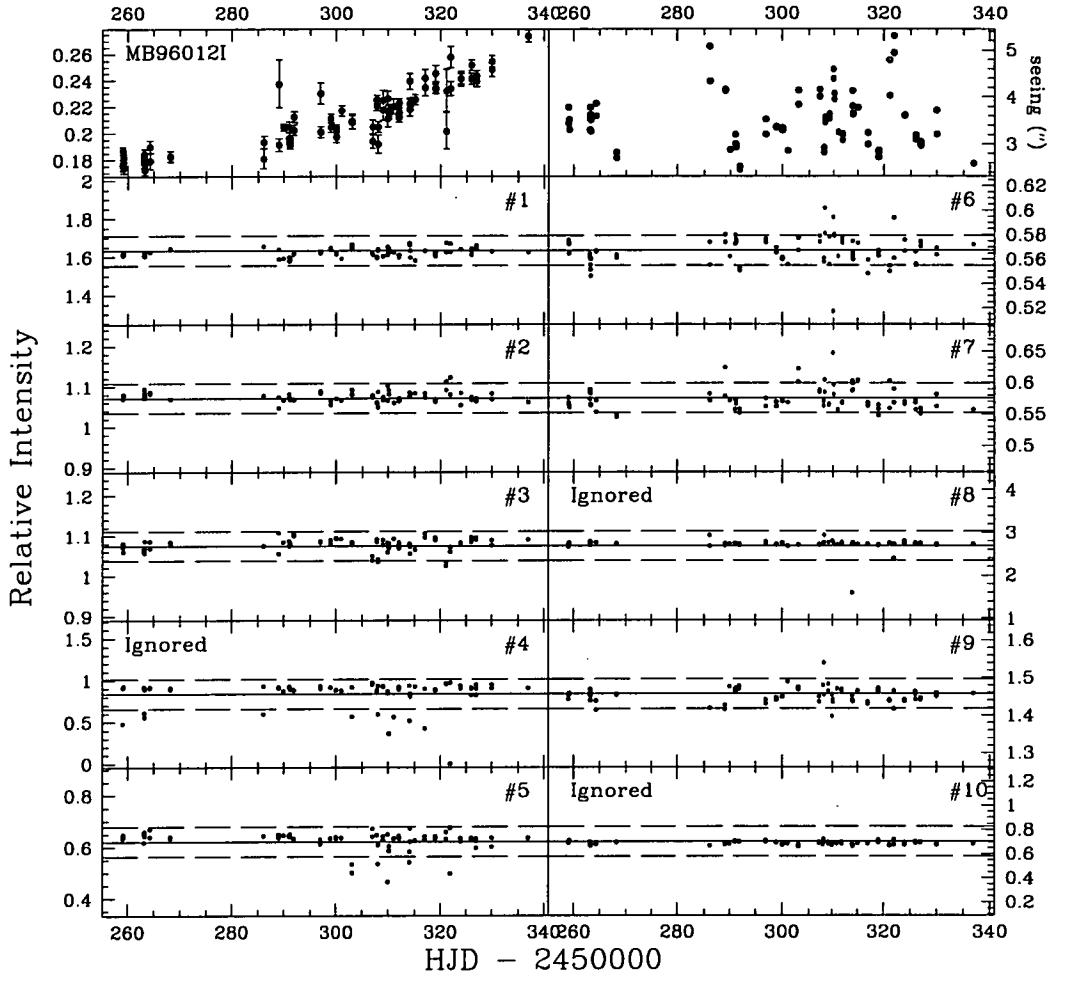

Figure 4.7: *I* band light curve for event MB96012. The relative intensity of the microlensed source with respect to the average flux of the reference stars is shown in the top left panel. The light curve includes a total of 75 data points. Including all 10 reference stars results in an average scatter of 0.093 but excluding reference stars 4, 8, and 10 reduces the average scatter to 0.042.

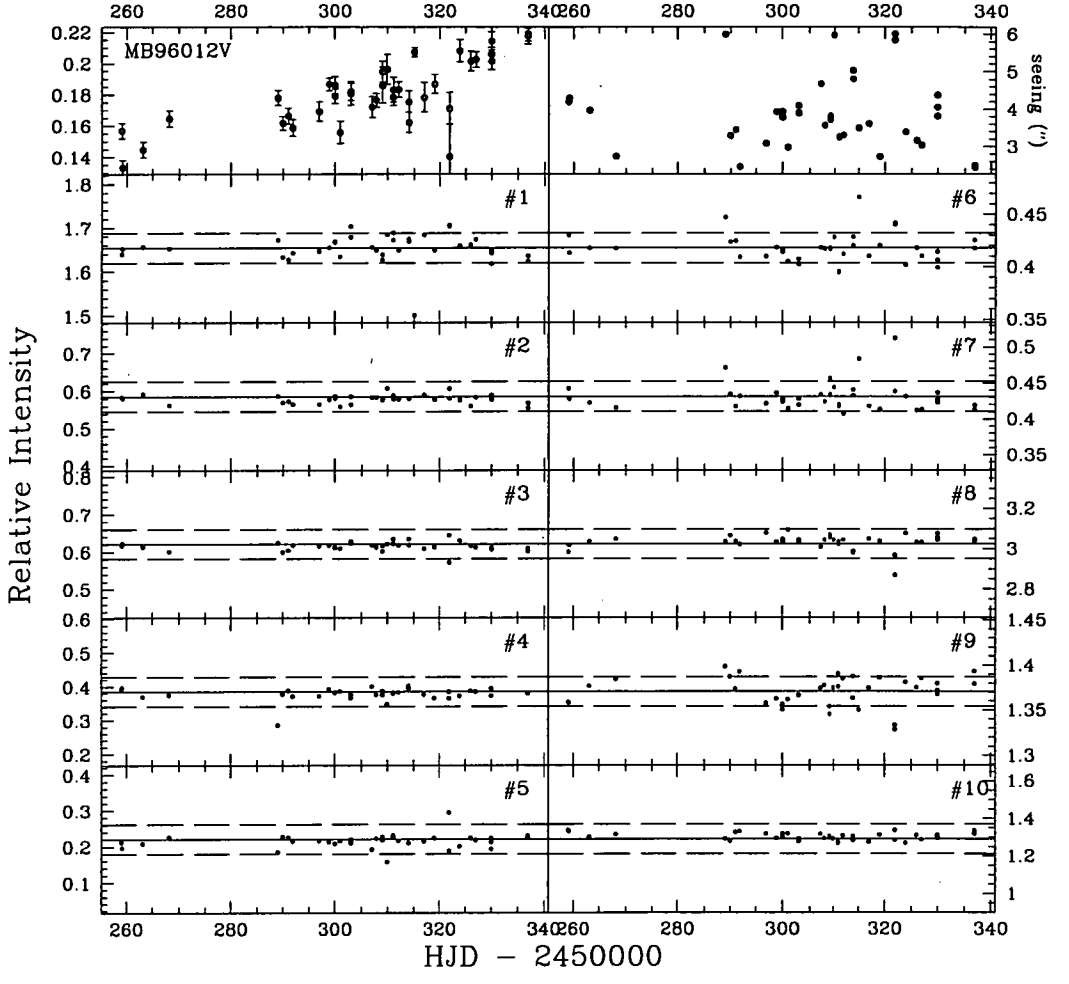

Figure 4.8: V band light curve for event MB96012. The relative intensity of the microlensed source with respect to the average flux of the reference stars is shown in the top left panel. The light curve includes a total of 38 data points. All 10 reference stars were used with an average scatter of 0.063.

MB96016

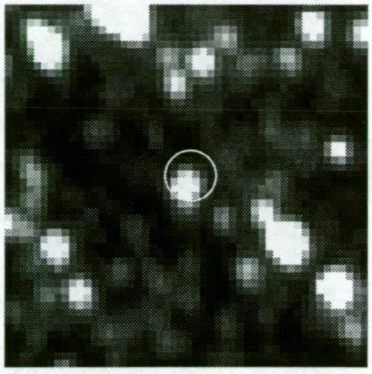

Figure 4.9: Bulge field MB96016. The event has a baseline magnitude of $V = 18.3$ and $R = 17.5$. The event is highly blended and almost indistinguishable from the bright source located just below the microlensed source.

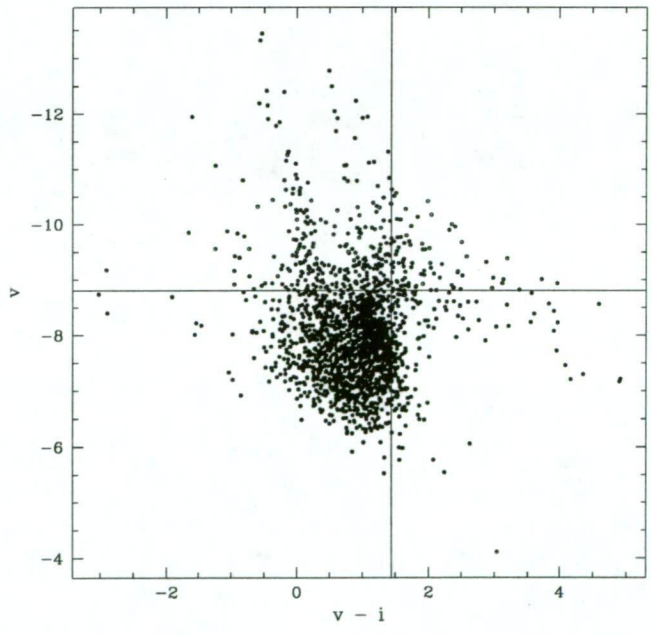

Figure 4.10: The colour-magnitude diagram of bulge field MB96016 is shown in which 2098 stars are plotted. The location of the microlensed source at baseline is indicated by the cross-hairs where the DoPHOT fit magnitudes are $I = -10.2$ and $V = -8.8$.

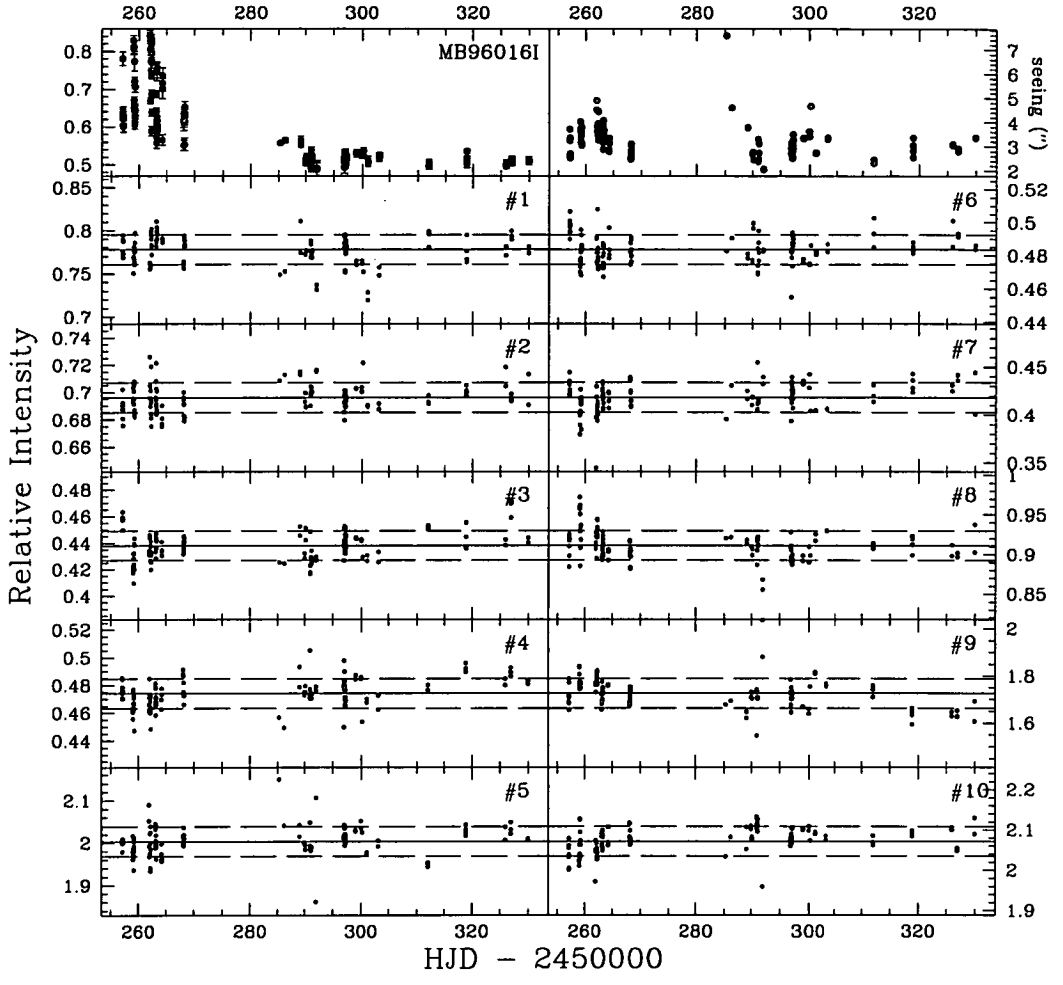

Figure 4.11: I band light curve for event MB96016. The relative intensity of the microlensed source with respect to the average flux of the reference stars is shown in the top left panel. The light curve includes a total of 116 data points. All 10 reference stars were used with an average scatter of 0.023. There is a high scatter in the initial part of the plot due to the event being highly blended with a nearby star.

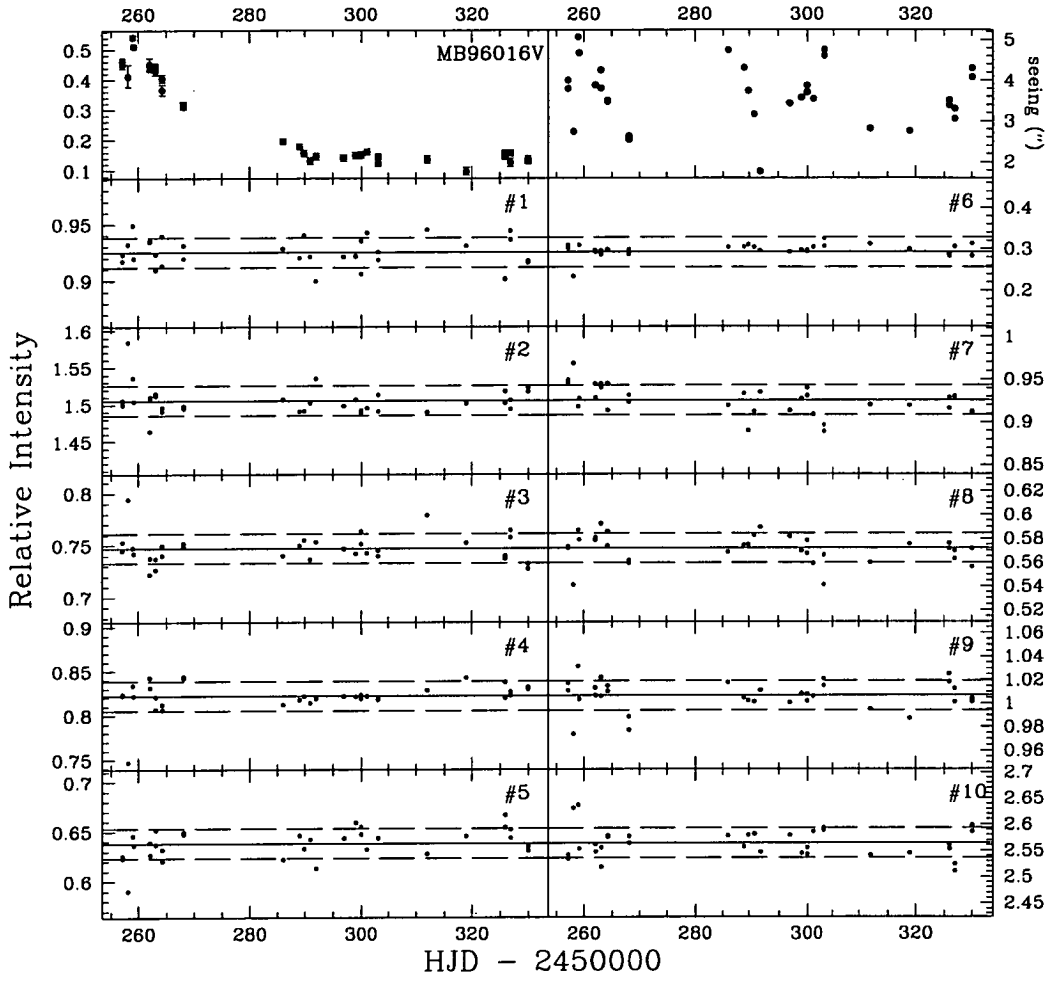

Figure 4.12: V band light curve for event MB96016. The relative intensity of the microlensed source with respect to the average flux of the reference stars is shown in the top left panel. The light curve includes a total of 33 data points. All 10 reference stars were used with an average scatter of 0.028.

MB96020

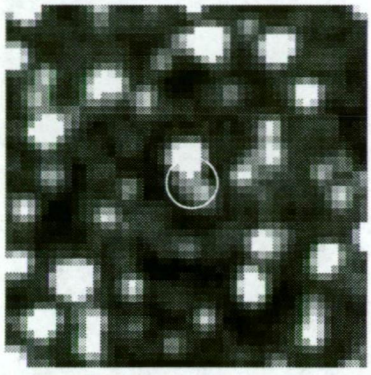

Figure 4.13: Bulge field MB96020. The event has a baseline magnitude of $V = 18.4$ and $R = 17.5$. The event is reasonably faint and highly blended with nearby stars.

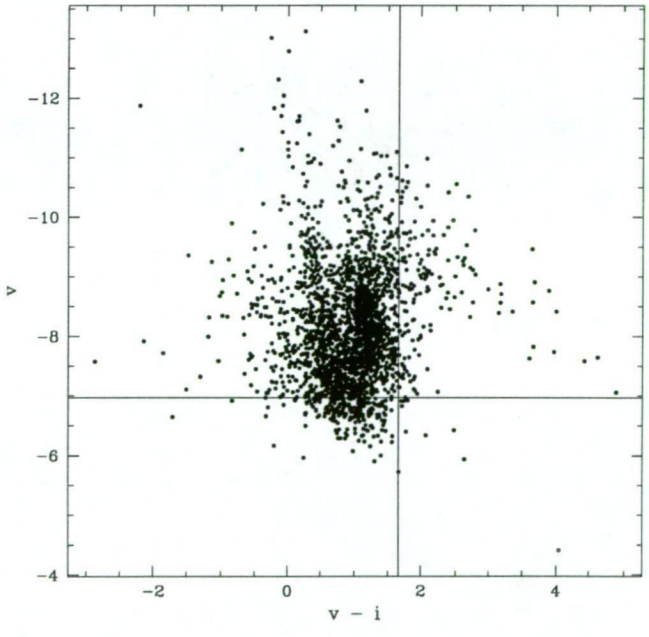

Figure 4.14: The colour-magnitude diagram of bulge field MB96020 is shown in which 2524 stars are plotted. The location of the microlensed source at baseline is indicated by the cross-hairs where the DoPHOT fit magnitudes are $I = -8.6$ and $V = -7.0$.

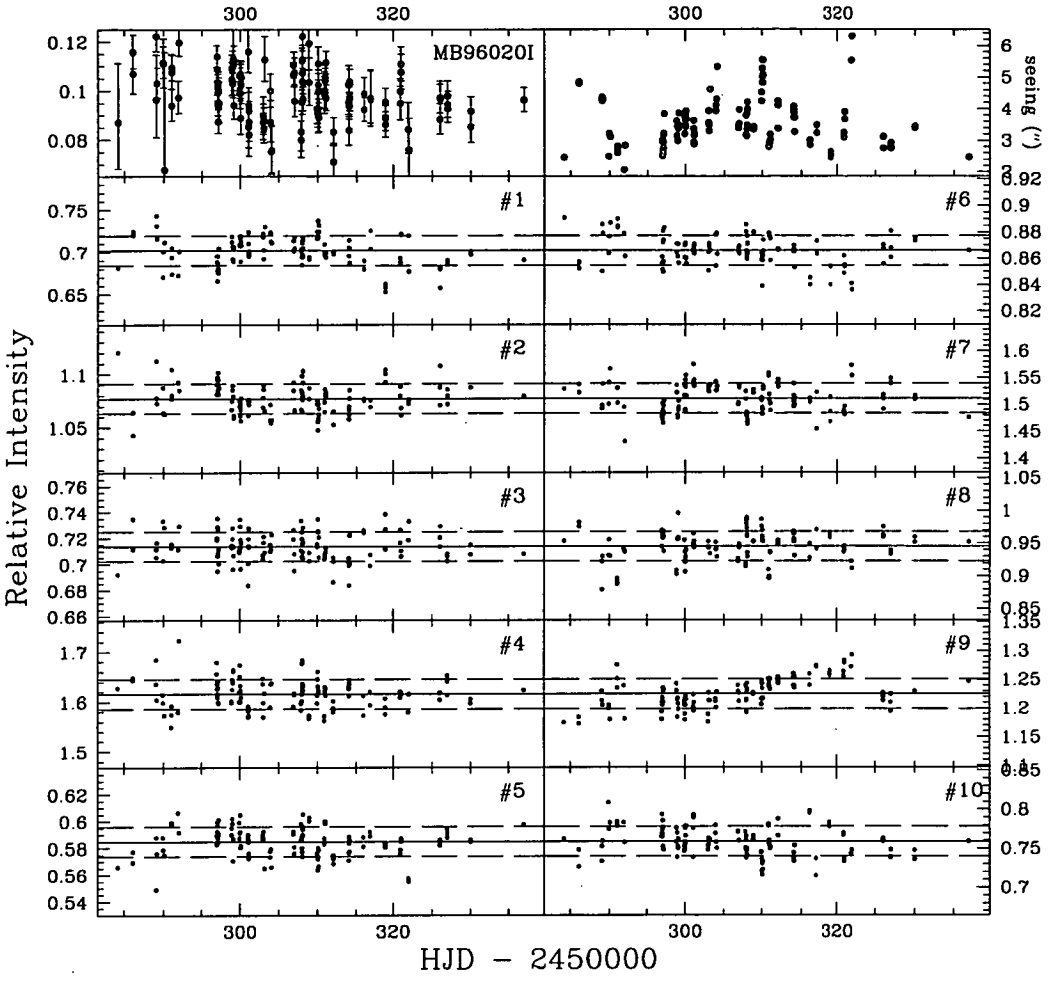

Figure 4.15: *I* band light curve for event MB96020. The relative intensity of the microlensed source with respect to the average flux of the reference stars is shown in the top left panel. The light curve includes a total of 116 data points. All 10 reference stars were used with an average scatter of 0.019. There is a large scatter due to severe blending. The DoPHOT processing resulted in a DoPHOT classification of type 13 for this event and it is not clear what proportion of the measured light is from the microlensed source. This is an example of an event for which much data was obtained but was too faint to be useful.

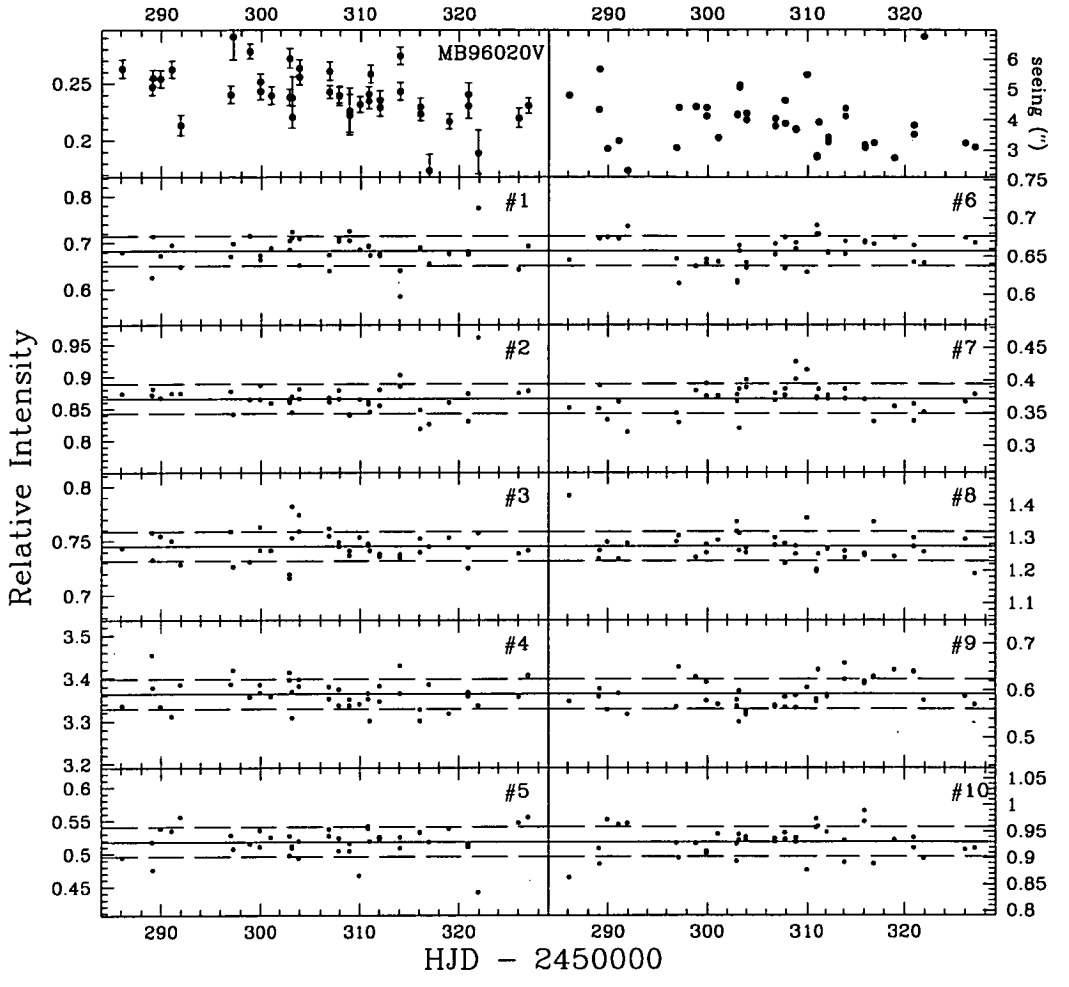

Figure 4.16: V band light curve for event MB96020. The relative intensity of the microlensed source with respect to the average flux of the reference stars is shown in the top left panel. The light curve includes a total of 41 data points. All 10 reference stars were used with an average scatter of 0.035. Unlike the I frames, DoPHOT claasified the event as type 11 although once again it is uncertain what proportion of the measured light is from the microlensed source.

4.2 The 1997 Bulge Season

Event	Coordinates		# Frames	
	R.A. (J2000)	DEC. (J2000)	I	V
MB97018	18:03:15.3	-28:00:14	60(16)	43(11)
MB97024	18:04:20.3	-27:24:45	23	10
MB97025	18:12:07.3	-29:47:54	10	5
MB97026	18:00:06.9	-29:38:06	112(24)	46(12)
MB97028	18:00:33.8	-28:01:10	150(15)	61(2)
MB97030	18:10:09.4	-27:56:46	27	11
MB97031	18:07:08.4	-25:49:21	79	25
MB97037	18:03:58.7	-29:58:49	6	4
MB97041	17:56:20.7	-28:47:42	172(60)	63(18)
MB97042	18:04:56.3	-27:10:41	3	1
MB97050	17:58:58.9	-28:16:30	26(27)	10(8)
MB97052	18:04:29.2	-29:22:23	25	10
MB97054	18:06:07.9	-29:59:26	12	3
MB97055	18:18:04.4	-23:02:11	2	3
MB97058	18:04:09.7	-27:44:35	9	3
MB97059	18:00:52.2	-28:29:52	4	3

Table 4.2: Events observing during the 1997 bulge season. The number of frames shown in brackets are those that were observed at CTIO.

1997 was the second year that Canopus Observatory took part in monitoring microlensing events with the PLANET collaboration and the first year in which data was obtained from CTIO. A total of 16 events were monitored during the 1997 bulge season, as shown in Table 4.2. Of these 16 events, the results of 6 are presented in this section. The remainder of the events either suffered from lack of data points or the event was too faint in which case DoPHOT was unable to find an adequate fit to the star.

The removal of the transfer lens for the 1997 bulge season resulted in a reduction in the size of the field of view by a factor of approximately 4. Hence, there are substantially fewer stars included in the CMDs for this section.

MB97018

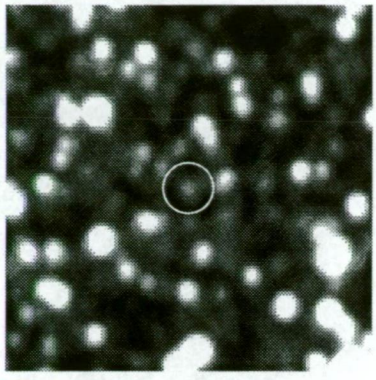

Figure 4.17: Bulge field MB97018. The event has a baseline magnitude of $V = 18.6$ and $R = 17.7$. This CTIO image shows the event to be relatively uncrowded.

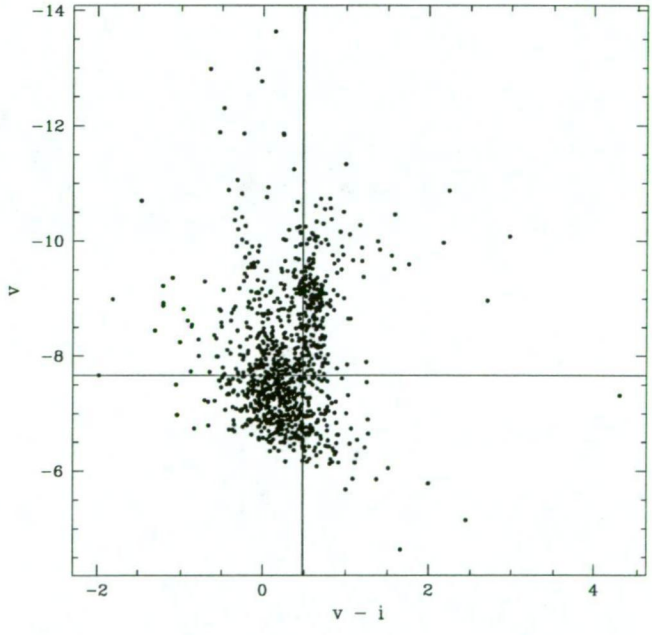

Figure 4.18: The colour-magnitude diagram of bulge field MB97018 is shown in which 1102 stars are plotted. The location of the microlensed source at baseline is indicated by the cross-hairs where the DoPHOT fit magnitudes are $I = -8.1$ and $V = -7.7$.

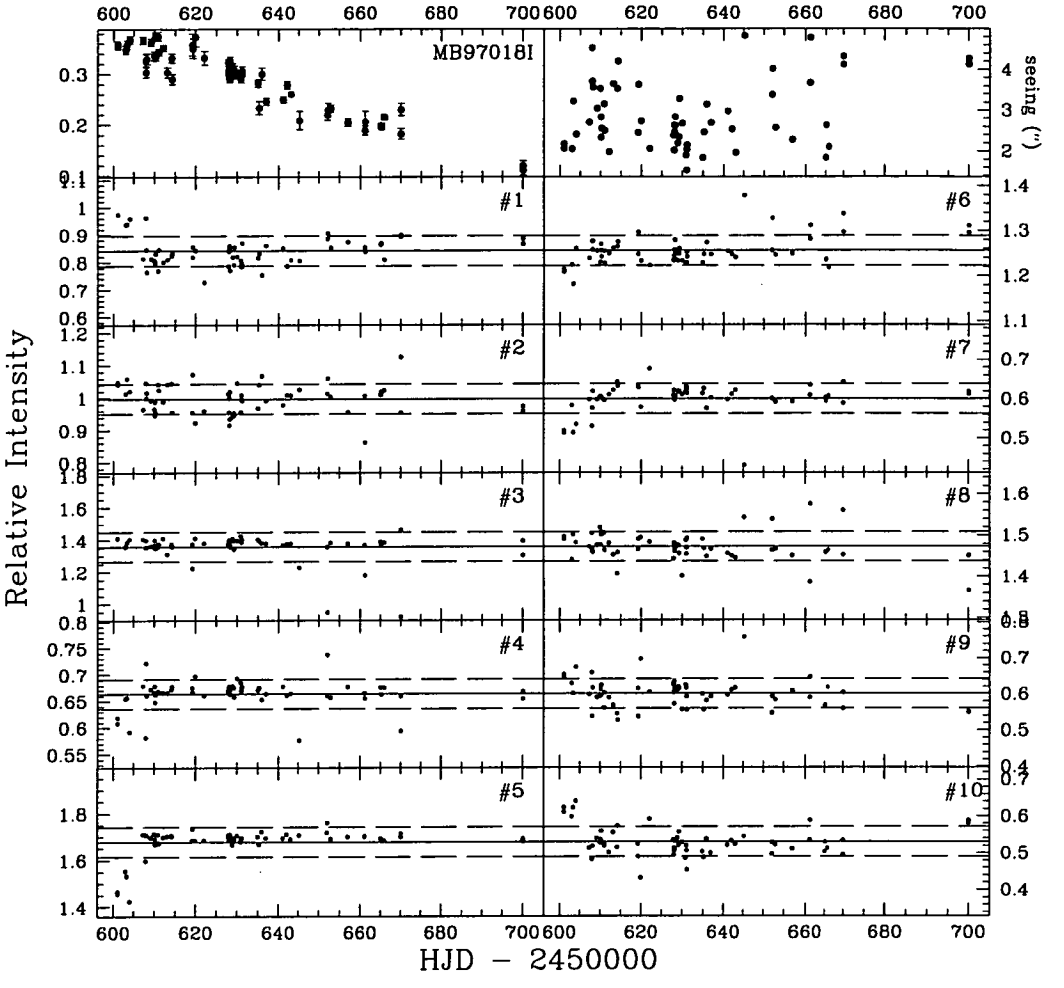

Figure 4.19: Canopus Observatory I band light curve for event MB97018. The relative intensity of the microlensed source with respect to the average flux of the reference stars is shown in the top left panel. The light curve includes a total of 59 data points. All 10 reference stars were used with an average scatter of 0.051.

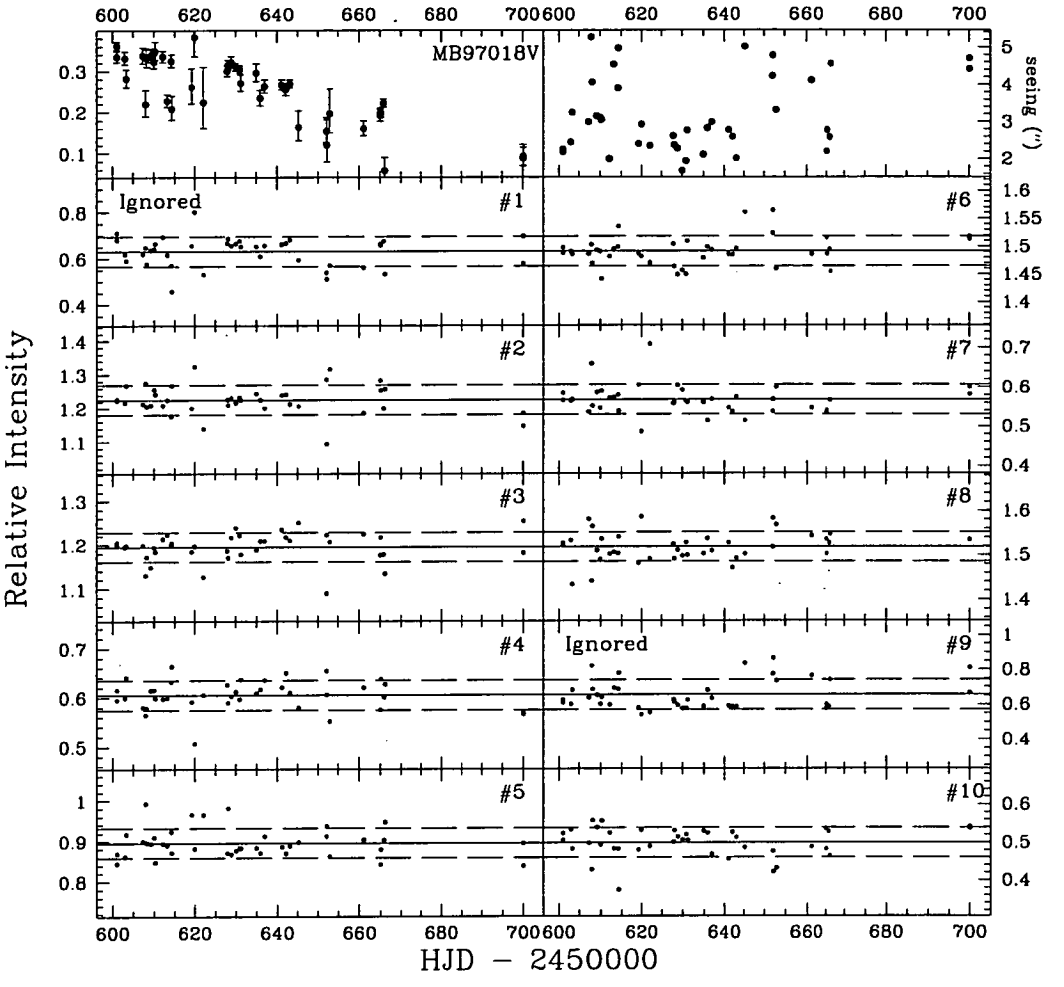

Figure 4.20: Canopus Observatory V band light curve for event MB97018. The relative intensity of the microlensed source with respect to the average flux of the reference stars is shown in the top left panel. The light curve includes a total of 40 data points. Including all 10 reference stars results in an average scatter of 0.057 but excluding reference stars 1 and 9 reduces the average scatter to 0.042.

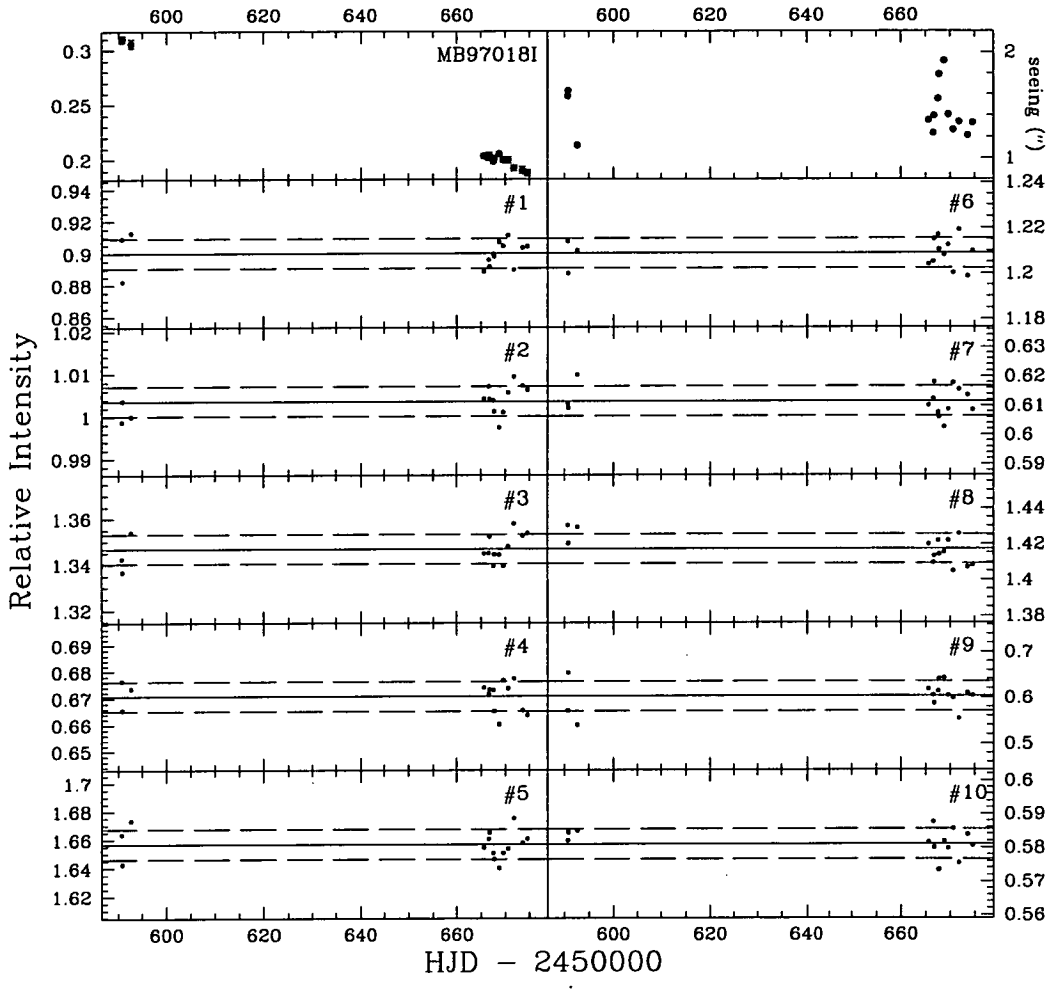

Figure 4.21: CTIO I band light curve for event MB97018. The relative intensity of the microlensed source with respect to the average flux of the reference stars is shown in the top left panel. The light curve includes a total of 14 data points. All 10 reference stars were used with an average scatter of 0.011.

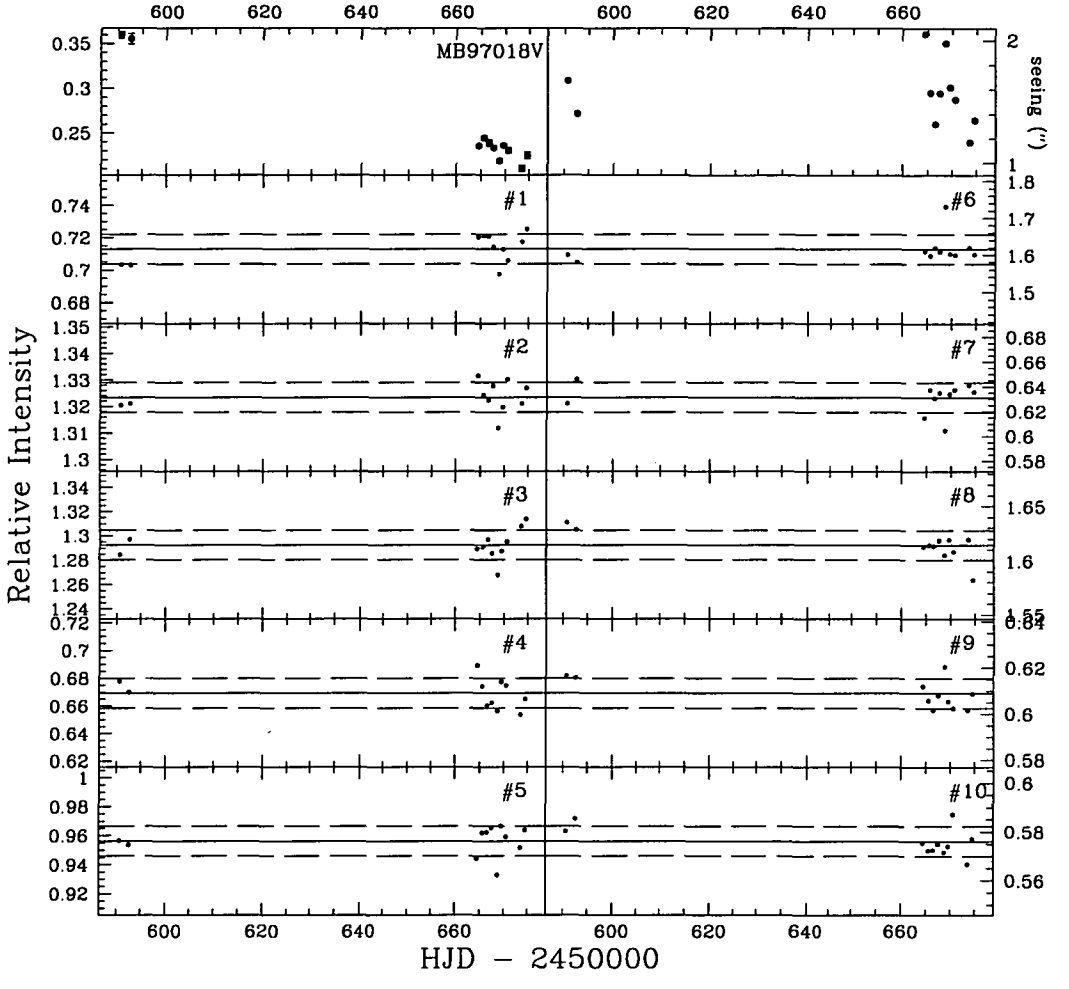

Figure 4.22: CTIO V band light curve for event MB97018. The relative intensity of the microlensed source with respect to the average flux of the reference stars is shown in the top left panel. The light curve includes a total of 11 data points. All 10 reference stars were used with an average scatter of 0.013.

MB97026

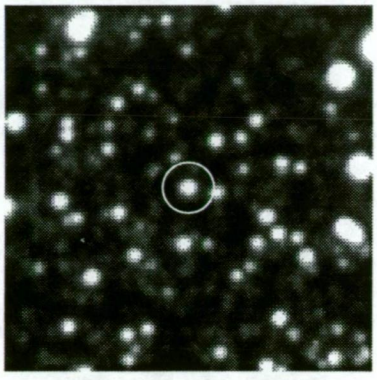

Figure 4.23: Bulge field MB97026. The event has a baseline magnitude of $V = 19.3$ and $R = 18.1$. This CTIO image shows the event to be relatively uncrowded.

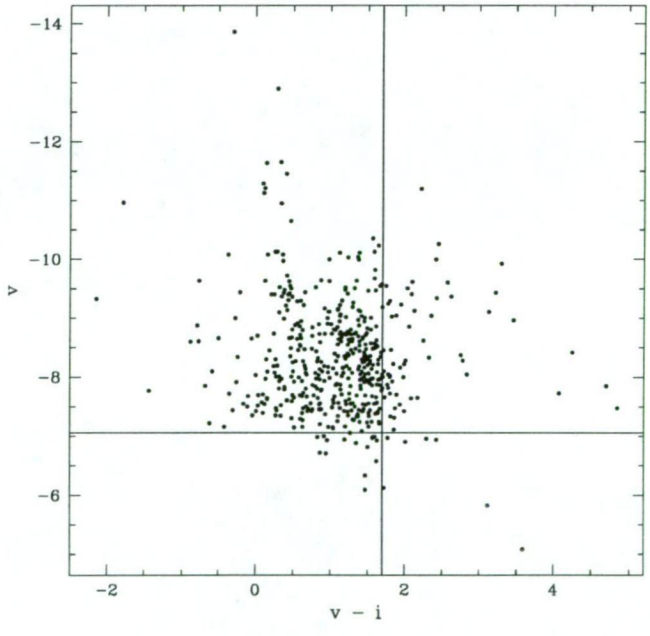

Figure 4.24: The colour-magnitude diagram of bulge field MB97026 is shown in which 494 stars are plotted. The location of the microlensed source at baseline is indicated by the cross-hairs where the DoPHOT fit magnitudes are $I = -8.8$ and $V = -7.1$.

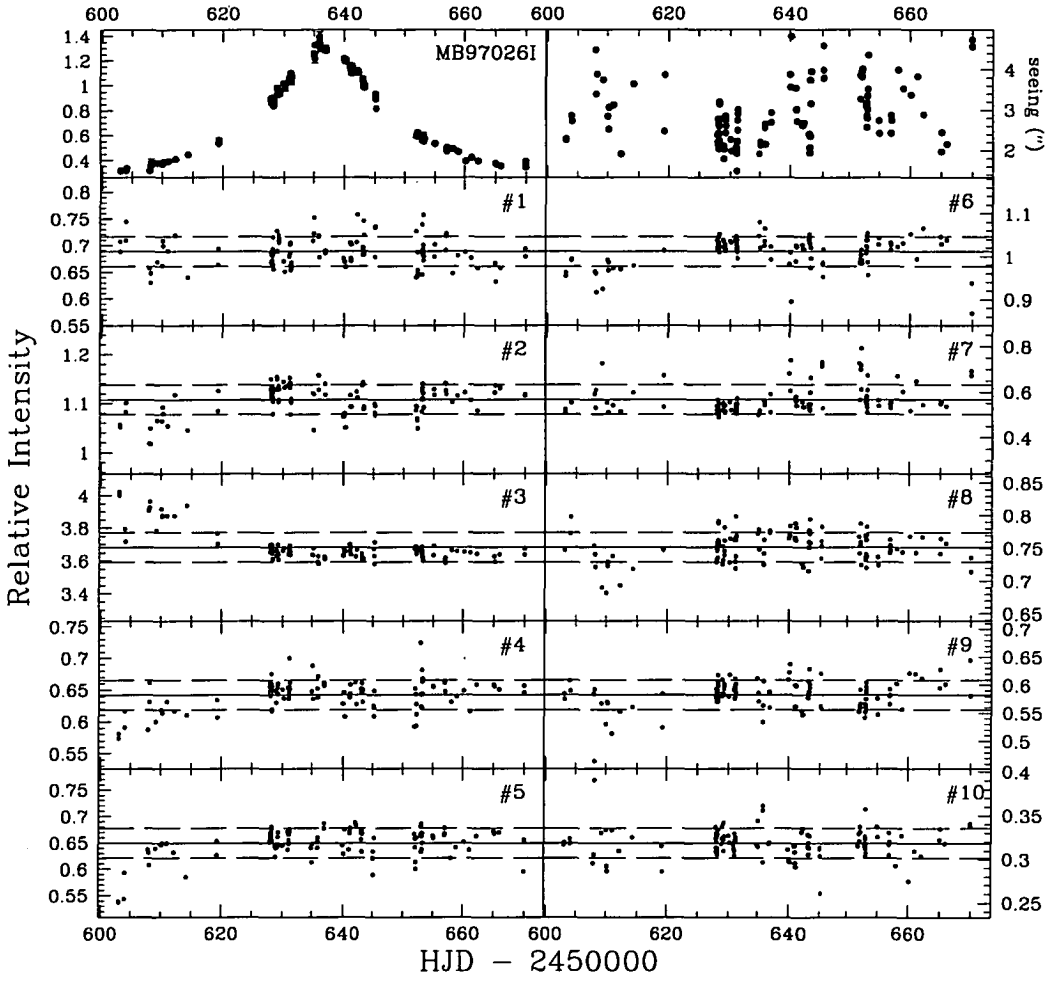

Figure 4.25: Canopus Observatory I band light curve for event MB97026. The relative intensity of the microlensed source with respect to the average flux of the reference stars is shown in the top left panel. The light curve includes a total of 111 data points. All 10 reference stars were used with an average scatter of 0.045. The high amplification of the event and the good coverage made this one of the best light curves of the 1997 bulge season.

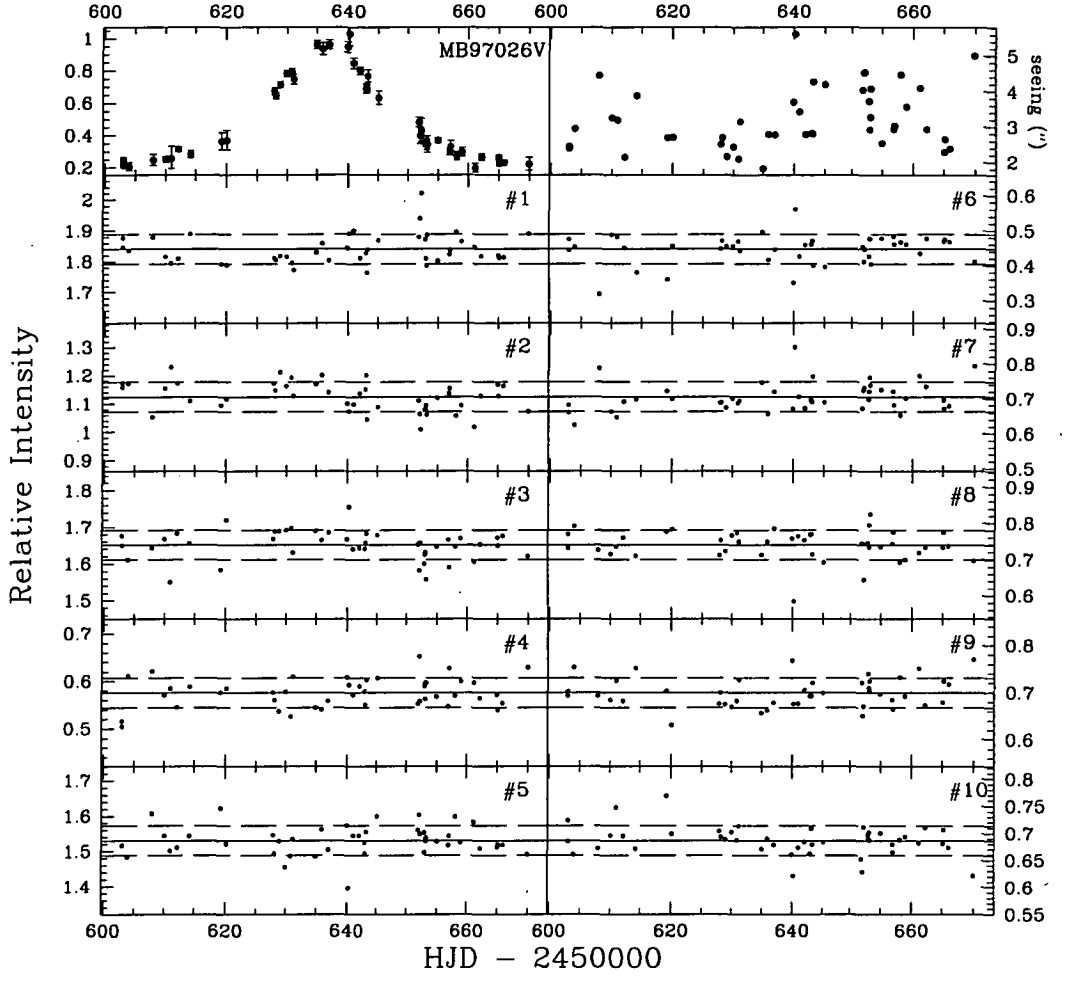

Figure 4.26: Canopus Observatory V band light curve for event MB97026. The relative intensity of the microlensed source with respect to the average flux of the reference stars is shown in the top left panel. The light curve includes a total of 45 data points. All 10 reference stars were used with an average scatter of 0.047.

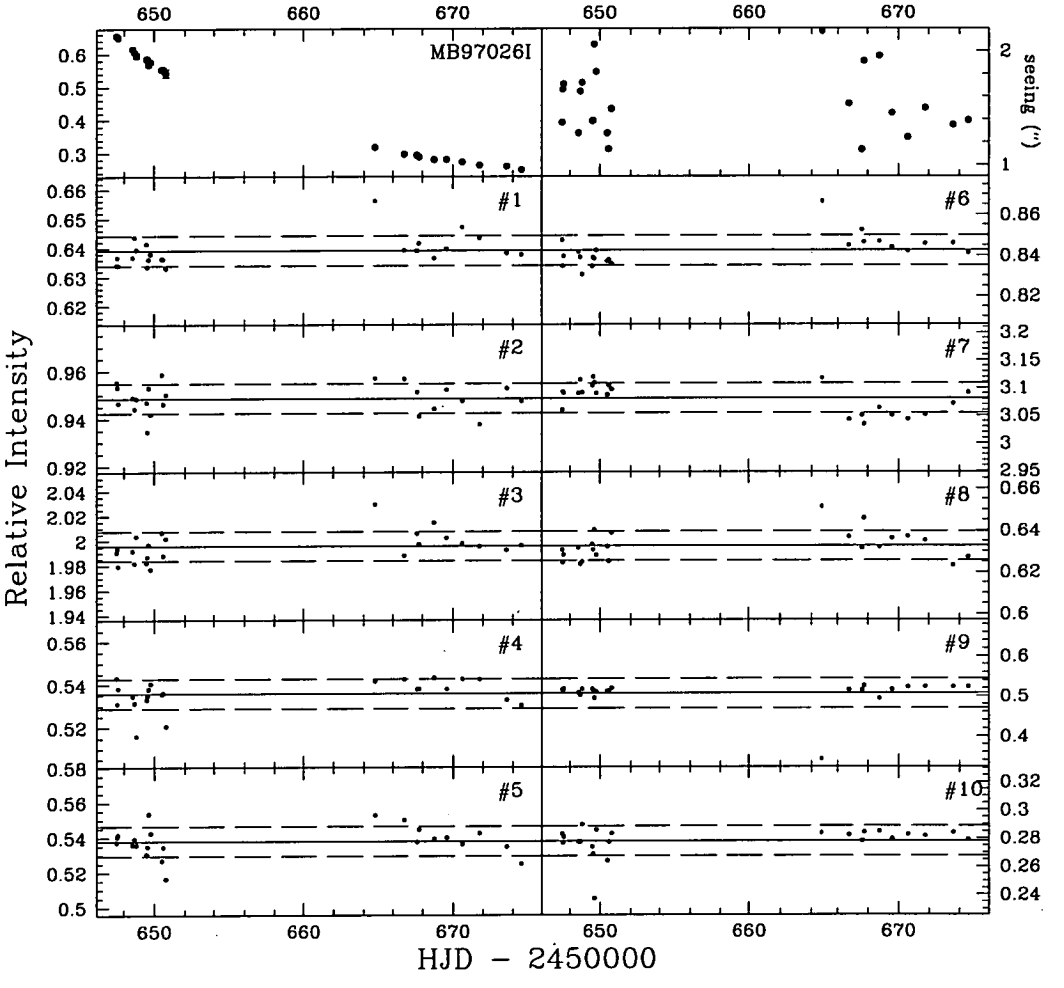

Figure 4.27: CTIO I band light curve for event MB97026. The relative intensity of the microlensed source with respect to the average flux of the reference stars is shown in the top left panel. The light curve includes a total of 23 data points. All 10 reference stars were used with an average scatter of 0.019.

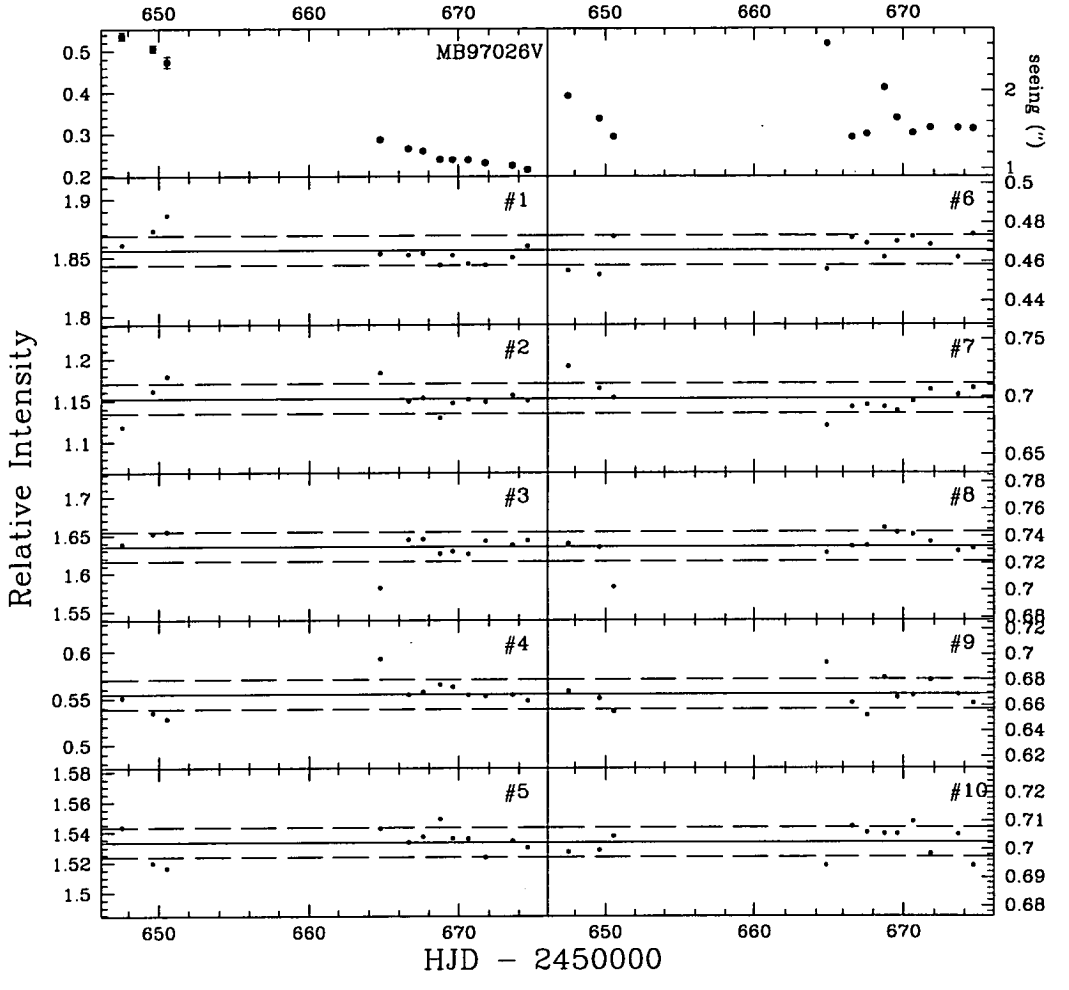

Figure 4.28: CTIO V band light curve for event MB97026. The relative intensity of the microlensed source with respect to the average flux of the reference stars is shown in the top left panel. The light curve includes a total of 12 data points. All 10 reference stars were used with an average scatter of 0.014.

MB97028

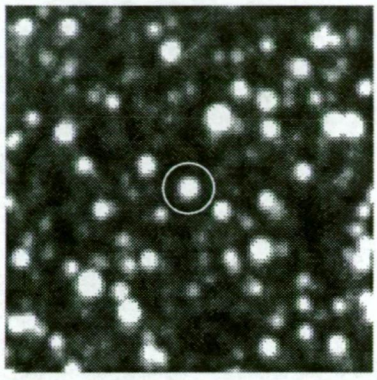

Figure 4.29: Bulge field MB97028. The event has a baseline magnitude of $V = 18.1$ and $R = 16.9$. This CTIO image shows the event to be relatively uncrowded.

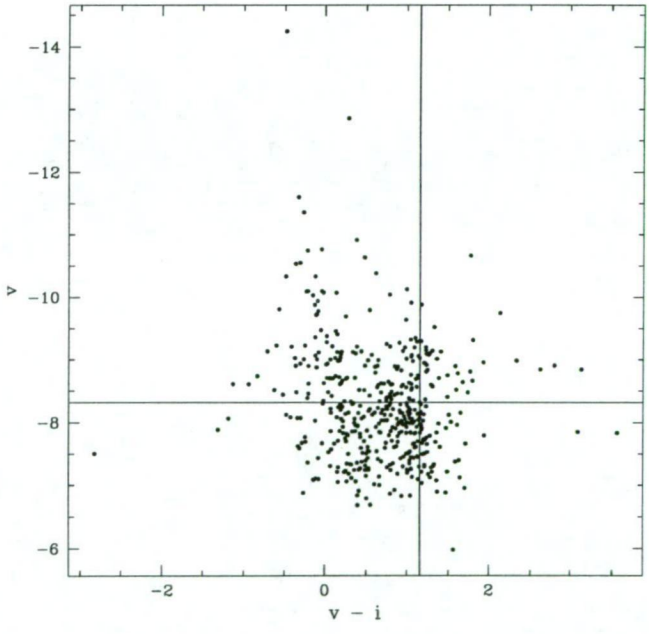

Figure 4.30: The colour-magnitude diagram of bulge field MB97028 is shown in which 470 stars are plotted. The location of the microlensed source at baseline is indicated by the cross-hairs where the DoPHOT fit magnitudes are $I = -9.5$ and $V = -8.3$.

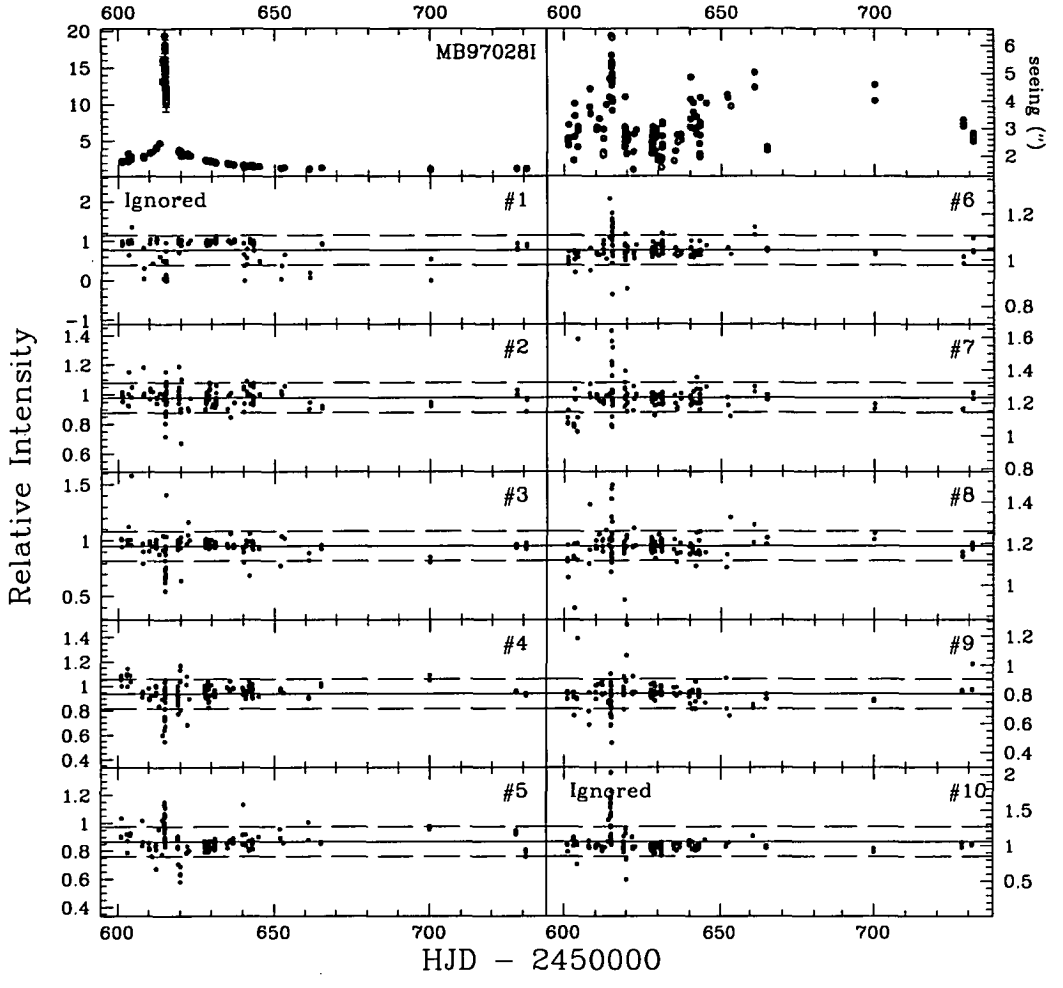

Figure 4.31: Canopus Observatory I band light curve for event MB97028. The relative intensity of the microlensed source with respect to the average flux of the reference stars is shown in the top left panel. The light curve includes a total of 135 data points. Including all 10 reference stars results in an average scatter of 0.154 but excluding reference stars 1 and 10 reduces the average scatter to 0.102. It was demonstrated by PLANET that this extraordinary event allowed the limb-darkening coefficients to be measured across the face of the microlensed source, the first time this has been achieved for a star at such a large distance [8]. The large scatter is mostly due to the bad seeing conditions during the night of maximum amplification as can be seen in the top right panel.

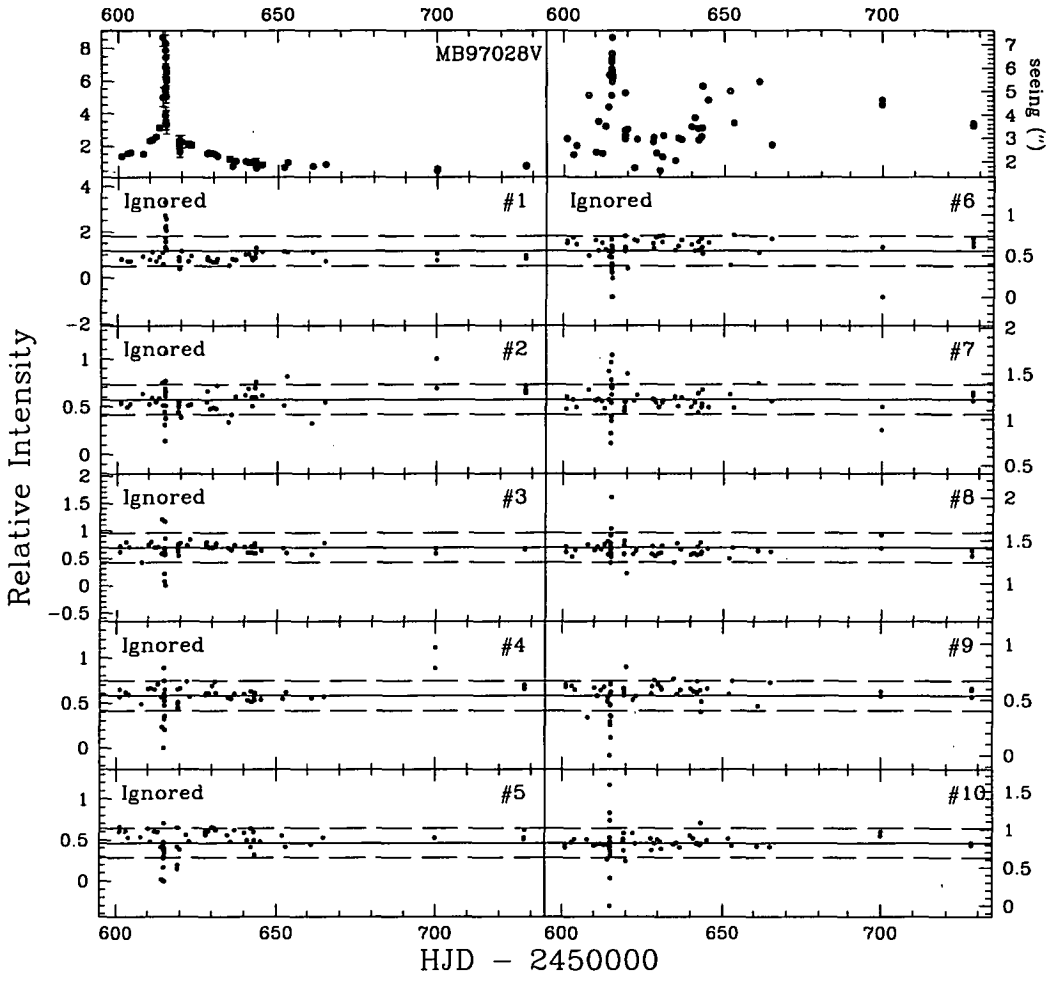

Figure 4.32: Canopus Observatory V band light curve for event MB97028. The relative intensity of the microlensed source with respect to the average flux of the reference stars is shown in the top left panel. The light curve includes a total of 57 data points. Including all 10 reference stars results in an average scatter of 0.279 but excluding reference stars 1, 2, 3, 4, 5, and 6 reduces the average scatter to 0.184. Once again, the large scatter is mostly due to the bad seeing conditions during the night of maximum amplification as can be seen in the top right panel.

MB97030

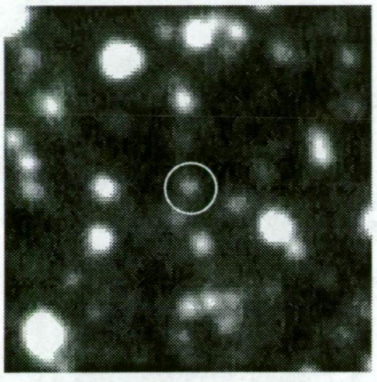

Figure 4.33: Bulge field MB97030. The event has a baseline magnitude of $V = 19.4$ and $R = 18.7$ and is relatively uncrowded.

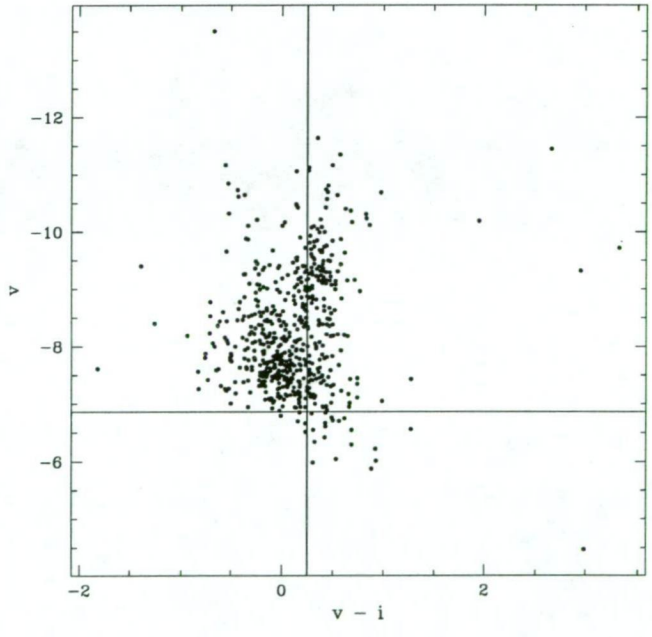

Figure 4.34: The colour-magnitude diagram of bulge field MB97030 is shown in which 612 stars are plotted. The location of the microlensed source at baseline is indicated by the cross-hairs where the DoPHOT fit magnitudes are $I = -7.1$ and $V = -6.9$.

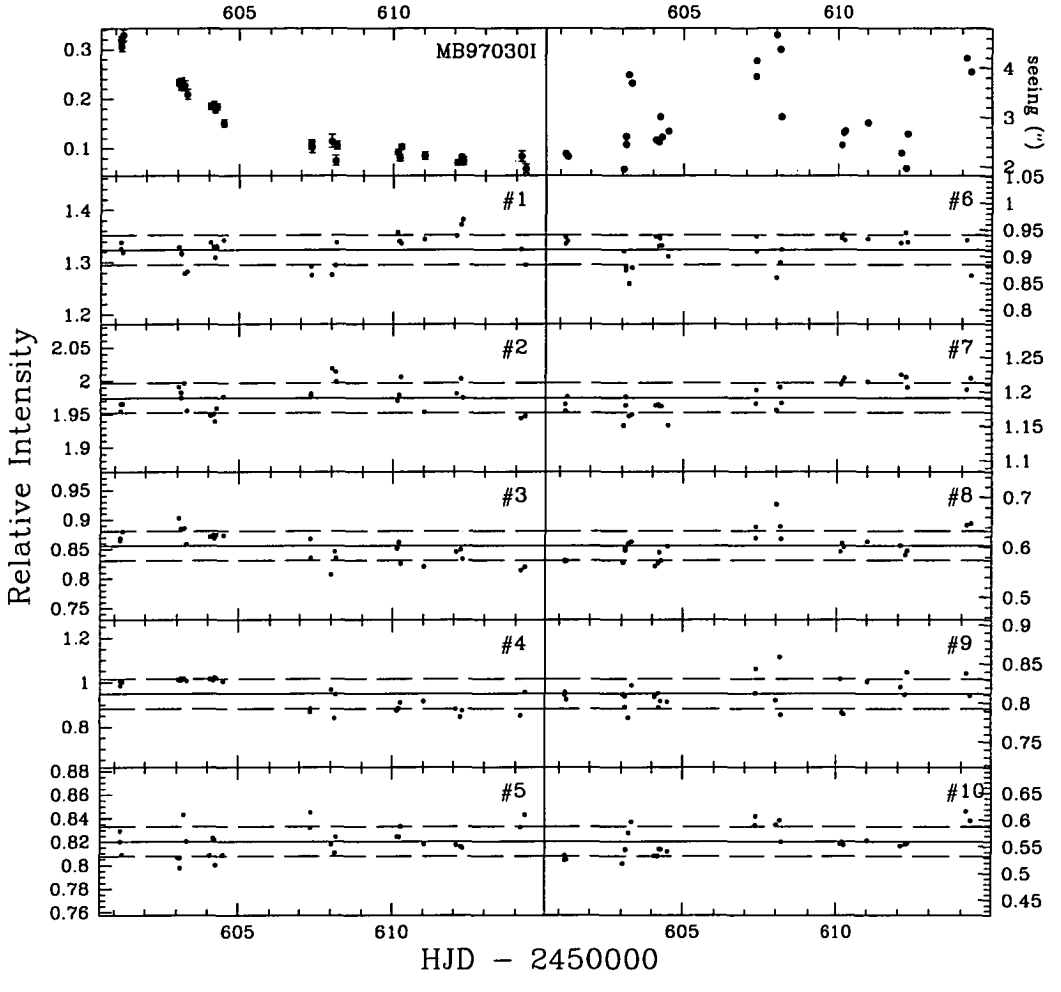

Figure 4.35: *I* band light curve for event MB97030. The relative intensity of the microlensed source with respect to the average flux of the reference stars is shown in the top left panel. The light curve includes a total of 27 data points. All 10 reference stars were used with an average scatter of 0.032.

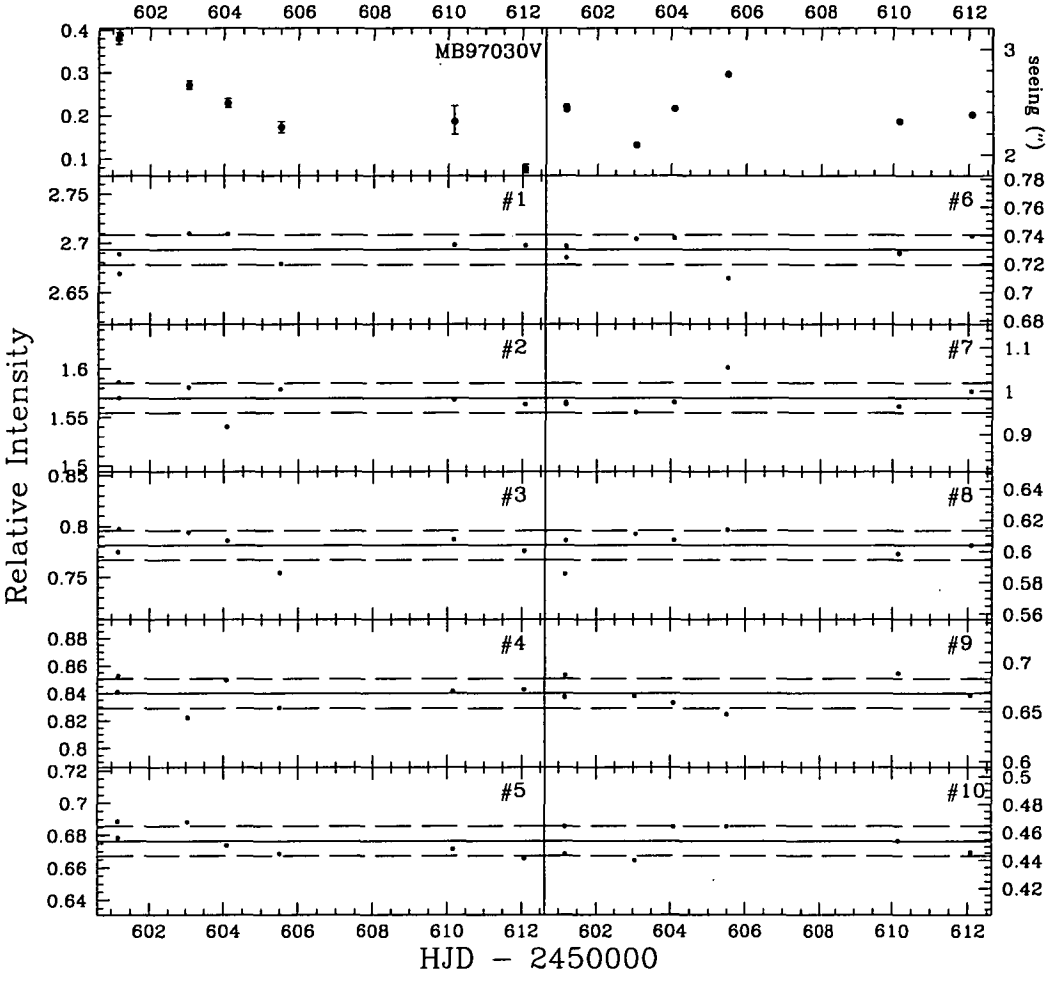

Figure 4.36: V band light curve for event MB97030. The relative intensity of the microlensed source with respect to the average flux of the reference stars is shown in the top left panel. The light curve includes a total of 7 data points. All 10 reference stars were used with an average scatter of 0.017.

MB97031

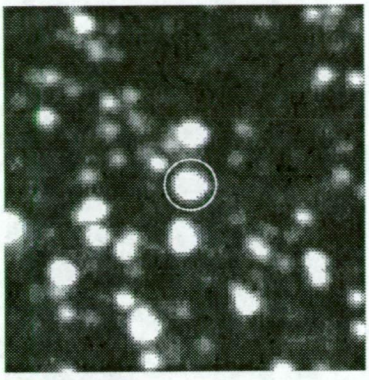

Figure 4.37: Bulge field MB97031. This bright event has a baseline magnitude of $V = 17.0$ and $R = 15.7$ and is relatively uncrowded.

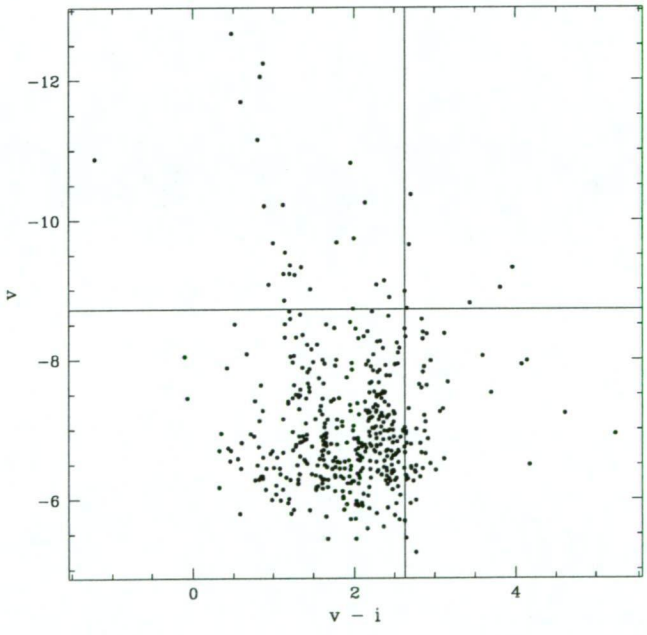

Figure 4.38: The colour-magnitude diagram of bulge field MB97031 is shown in which 473 stars are plotted. The location of the microlensed source at baseline is indicated by the cross-hairs where the DoPHOT fit magnitudes are $I = -11.3$ and $V = -8.7$.

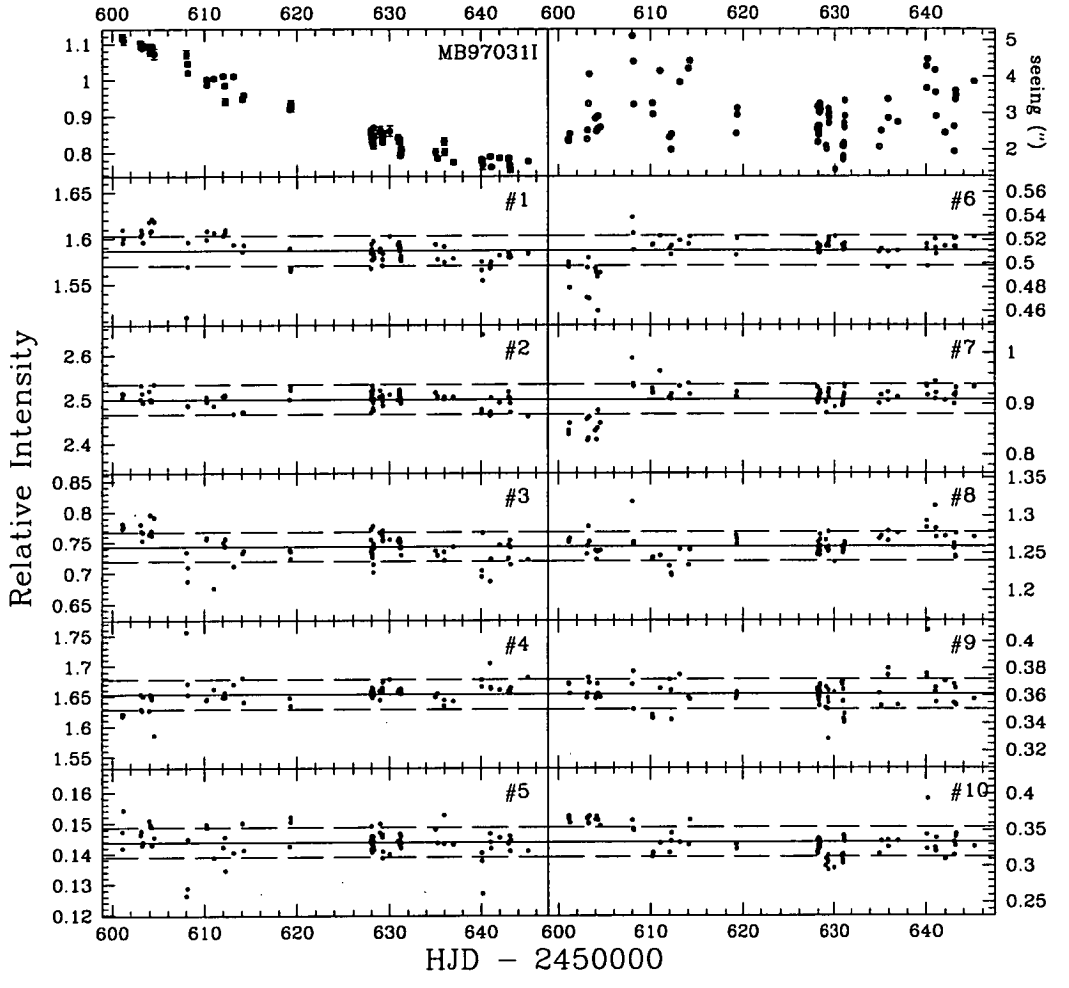

Figure 4.39: *I* band light curve for event MB97031. The relative intensity of the microlensed source with respect to the average flux of the reference stars is shown in the top left panel. The light curve includes a total of 78 data points. All 10 reference stars were used with an average scatter of 0.027.

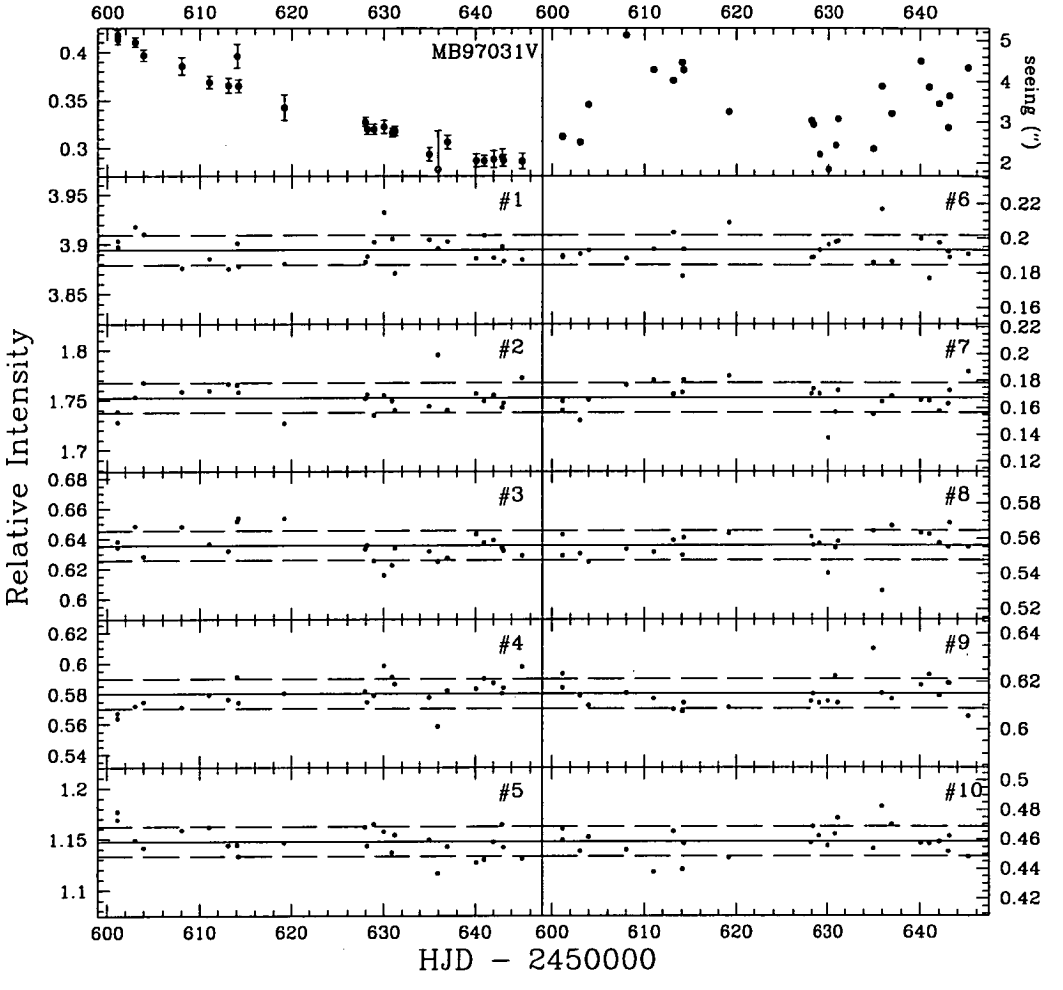

Figure 4.40: V band light curve for event MB97031. The relative intensity of the microlensed source with respect to the average flux of the reference stars is shown in the top left panel. The light curve includes a total of 25 data points. All 10 reference stars were used with an average scatter of 0.021.

MB97041

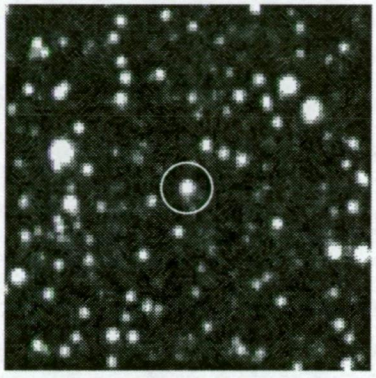

Figure 4.41: Bulge field MB97041. The event has a baseline magnitude of $V = 19.4$ and $R = 18.2$. This CTIO image shows the event to be relatively uncrowded.

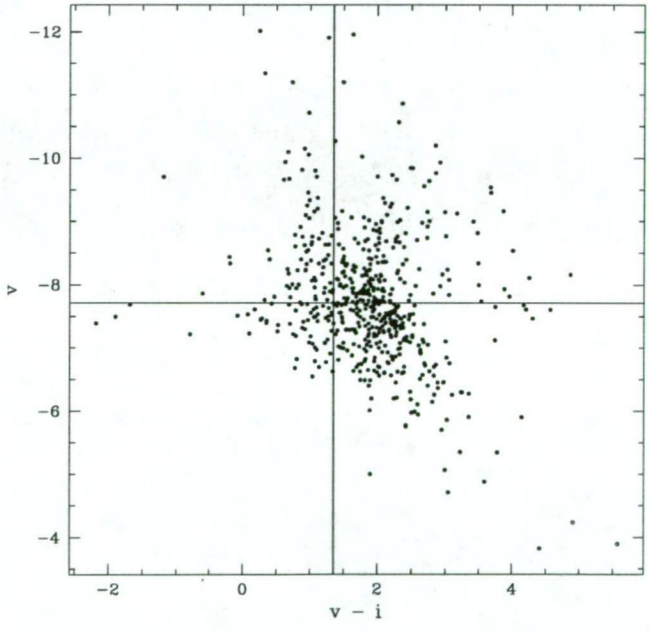

Figure 4.42: The colour-magnitude diagram of bulge field MB97041 is shown in which 582 stars are plotted. The location of the microlensed source at baseline is indicated by the cross-hairs where the DoPHOT fit magnitudes are $I = -9.1$ and $V = -7.7$.

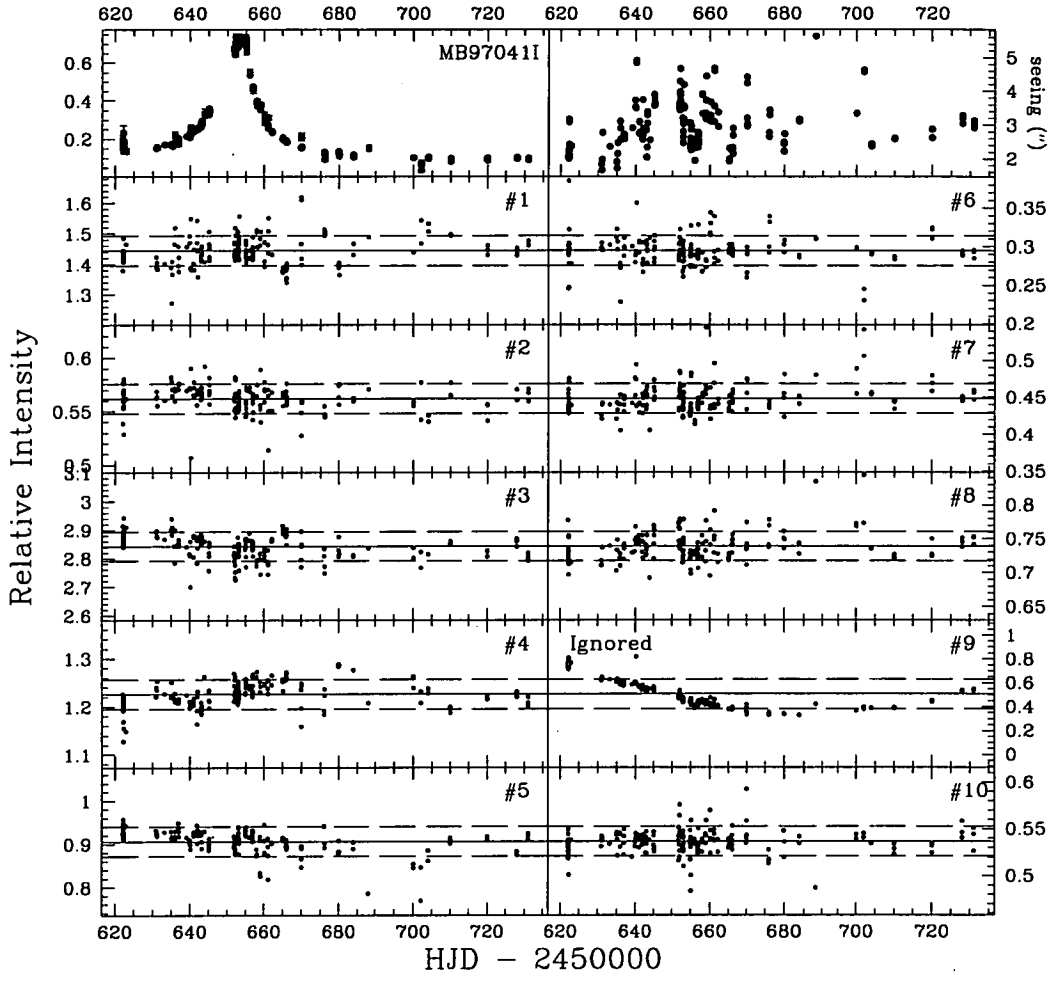

Figure 4.43: Canopus Observatory I band light curve for event MB97041. The relative intensity of the microlensed source with respect to the average flux of the reference stars is shown in the top left panel. The light curve includes a total of 171 data points. It is clear that reference star 9 is a variable star and so excluding this star results in an average scatter of 0.034. This event was the best sampled, and possibly the most intriguing event, of the 1997 bulge season. It has since been found by PLANET that the event can be well fit by a rotating binary lens model [10]

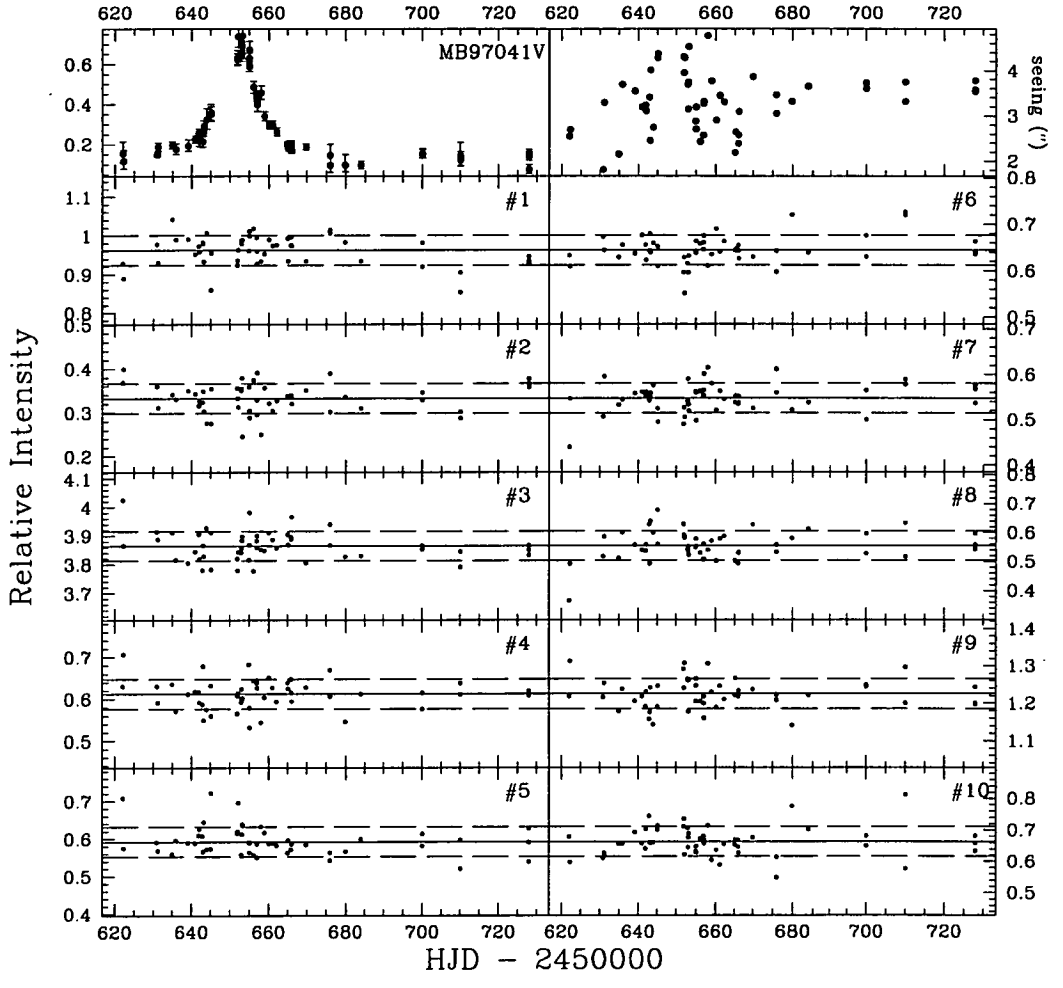

Figure 4.44: Canopus Observatory V band light curve for event MB97041. The relative intensity of the microlensed source with respect to the average flux of the reference stars is shown in the top left panel. The light curve includes a total of 52 data points. All 10 reference stars were used with an average scatter of 0.058.

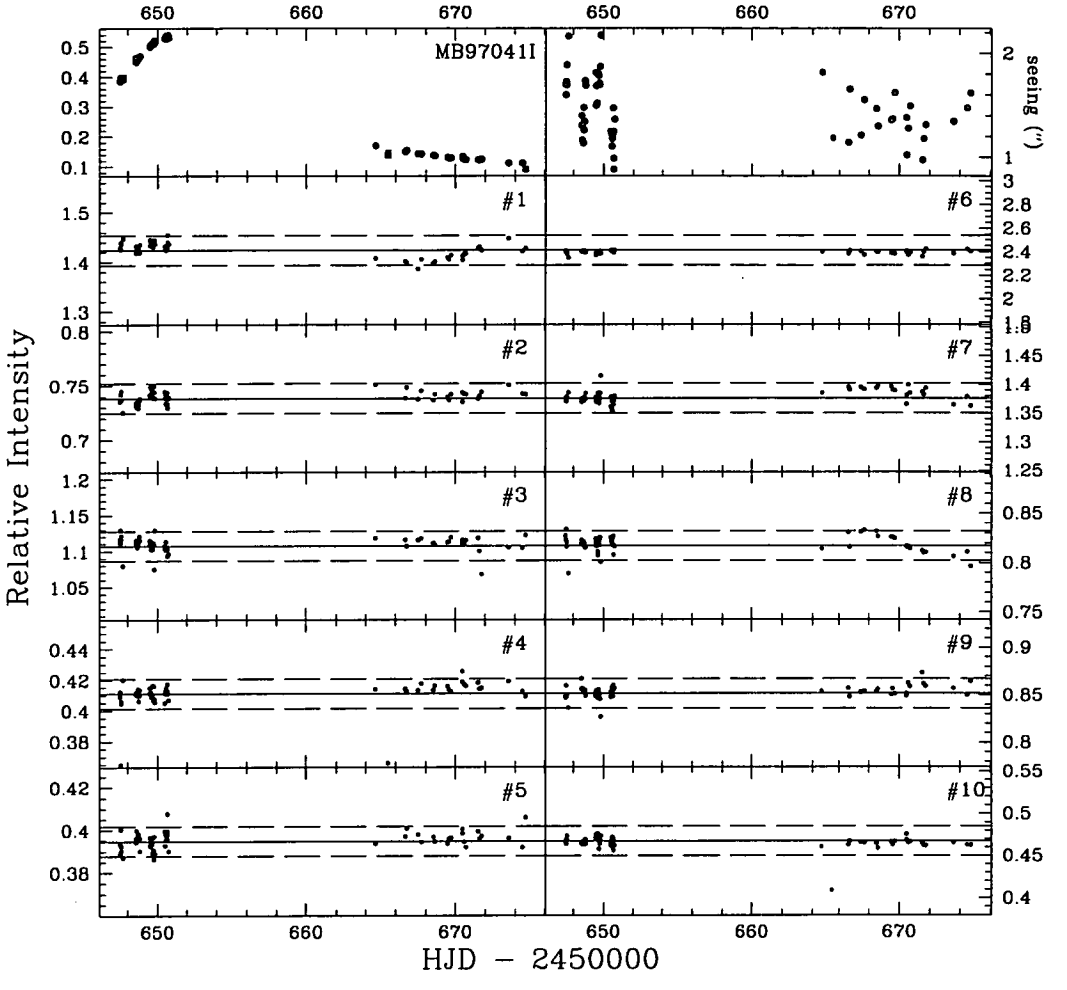

Figure 4.45: CTIO I band light curve for event MB97041. The relative intensity of the microlensed source with respect to the average flux of the reference stars is shown in the top left panel. The light curve includes a total of 58 data points. All 10 reference stars were used with an average scatter of 0.024.

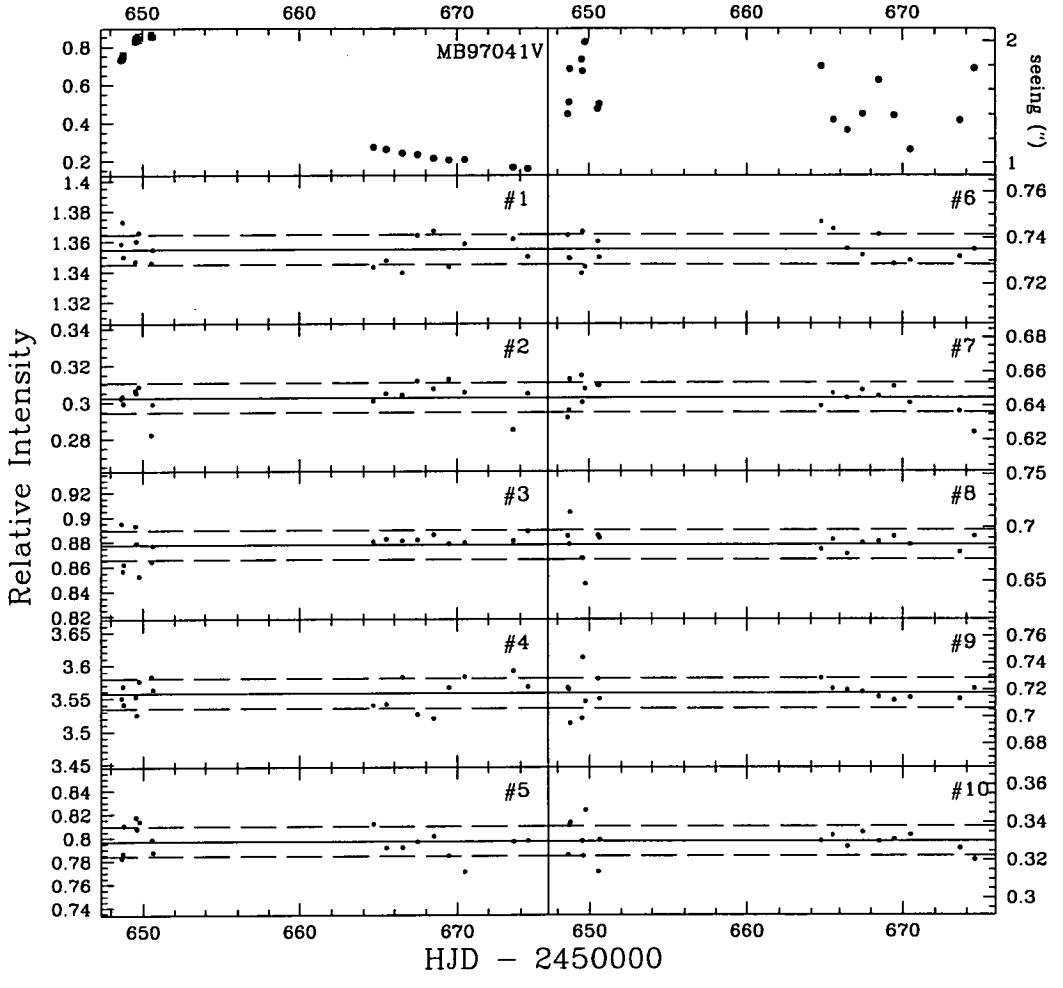

Figure 4.46: CTIO V band light curve for event MB97041. The relative intensity of the microlensed source with respect to the average flux of the reference stars is shown in the top left panel. The light curve includes a total of 17 data points. All 10 reference stars were used with an average scatter of 0.015.

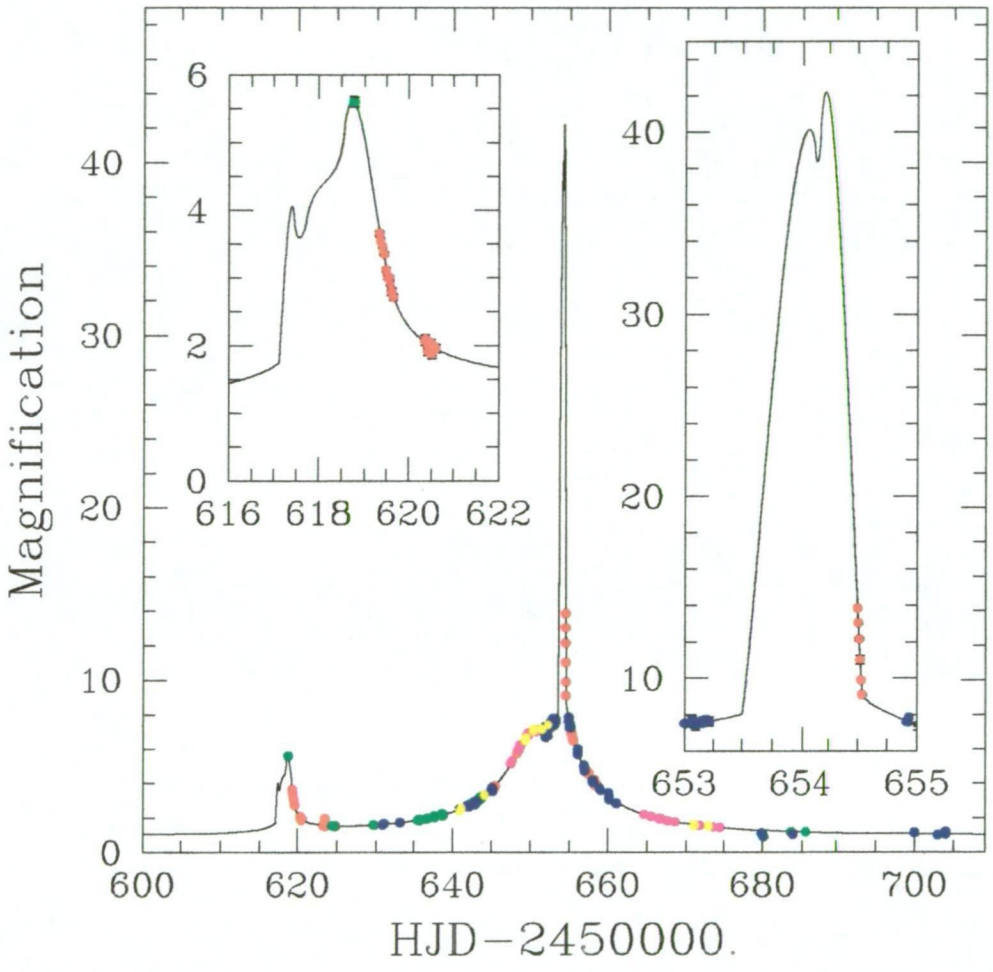

Figure 4.47: The MB97041 PLANET multi-site data in the I and V bands is shown along with fitted rotating binary model [10]. The data points consist of measurements from Canopus (blue), CTIO (yellow), SAAO (red), La Silla (green), and Perth (magenta). The error bars are shown, but are generally smaller than the size of the points. Insets are zooms on the two caustic crossing regions.

4.3 The 1998 Bulge Season

Event	Coordinates		# Frames	
	R.A. (J2000)	DEC. (J2000)	I	V
OB98014	17:53:09.3	-30:01:12	57	7
OB98018	17:54:21.8	-29:53:24	16	9

Table 4.3: Events observing during the 1998 bulge season.

1998 was the second year that the 0.9 m telescope at CTIO was used to monitor microlensing events with the PLANET collaboration. Two events, OB98014 and OB98018, were monitored during the 1998 bulge season, as shown in Table 4.3. A CTIO bulge field is shown for each of the events and the baseline I magnitude of the source indicated by the OGLE Early Warning System is also given.

OB98014

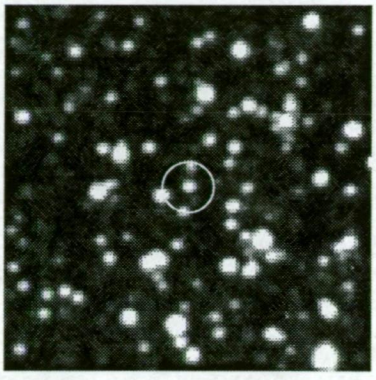

Figure 4.48: Bulge field OB98014. The event has a baseline magnitude of $I = 16.5$. This CTIO image shows the event to be relatively uncrowded.

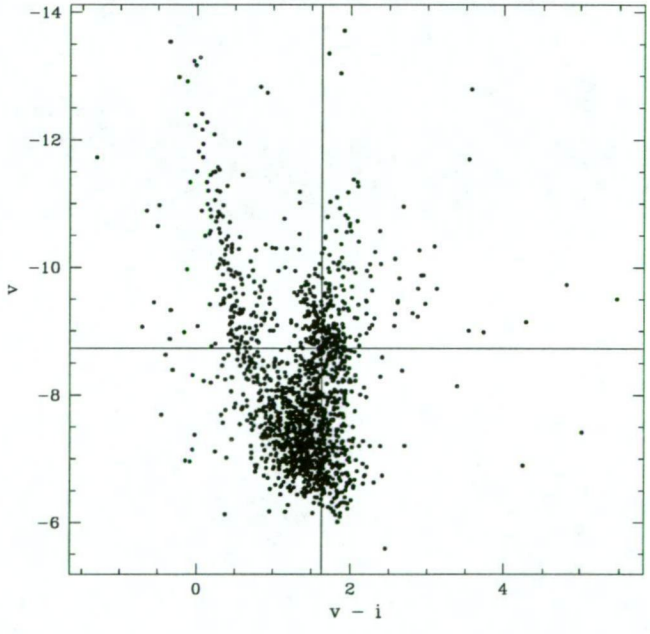

Figure 4.49: The colour-magnitude diagram of bulge field OB98014 is shown in which 1689 stars are plotted. The location of the microlensed source at baseline is indicated by the cross-hairs where the DoPHOT fit magnitudes are $I = -10.4$ and $V = -8.7$.

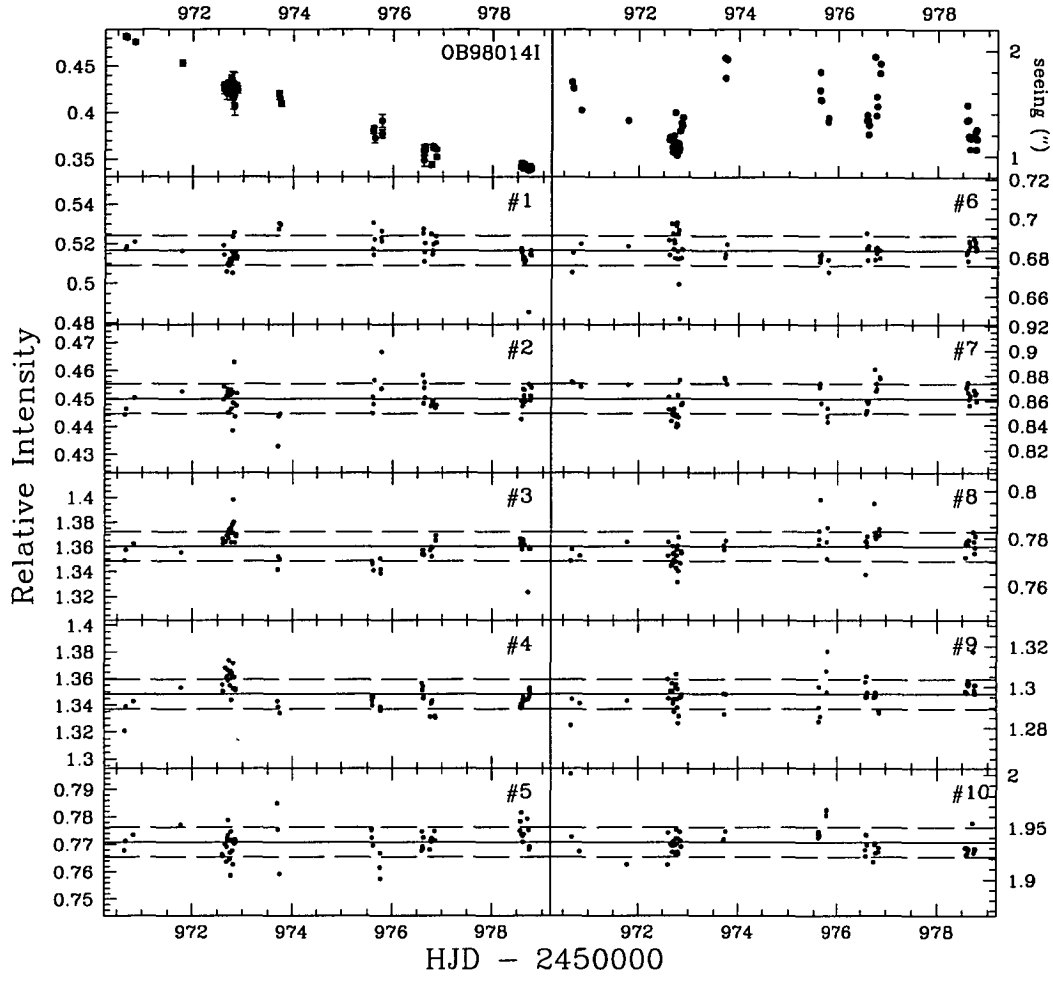

Figure 4.50: I band light curve for event OB98014. The relative intensity of the microlensed source with respect to the average flux of the reference stars is shown in the top left panel. The light curve includes a total of 58 data points. All 10 reference stars were used with an average scatter of 0.010. PLANET obtained about 600 data points for this high magnification event. This made it an ideal candidate to constrain the detection efficiency of the light curve to low amplitude perturbations that are signatures of a planetary companion orbiting the primary lens [9]. It was found that companions of mass ratio ≥ 0.01 are ruled out at the 95% level for projected separations between $0.4 - 2.4\,R_E$, where R_E is the Einstein ring radius of the primary lens.

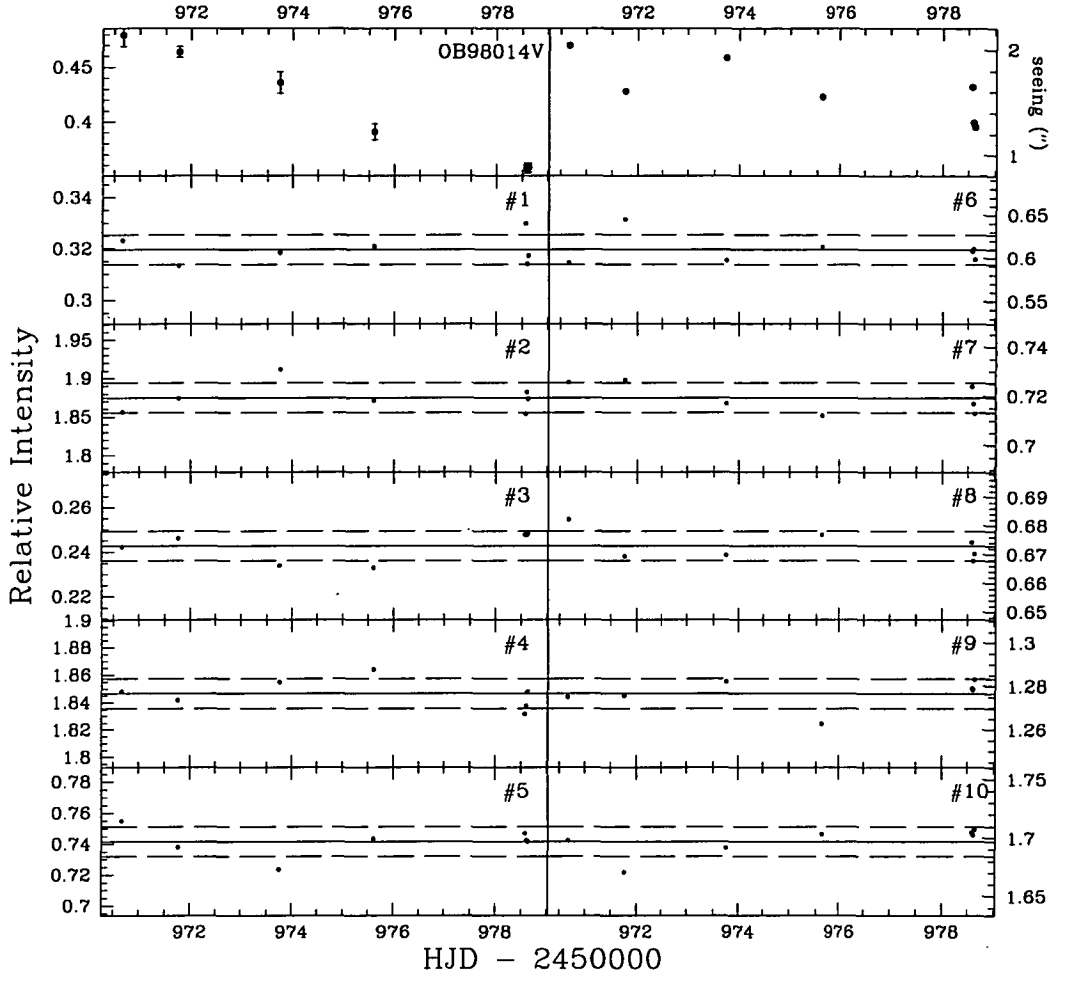

Figure 4.51: V band light curve for event OB98014. The relative intensity of the microlensed source with respect to the average flux of the reference stars is shown in the top left panel. The light curve includes a total of 7 data points. All 10 reference stars were used with an average scatter of 0.013.

OB98018

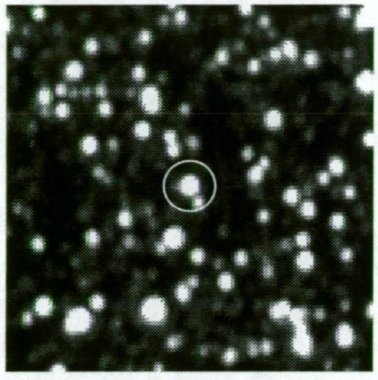

Figure 4.52: Bulge field OB98018. The event has a baseline magnitude of $I = 15.5$. This CTIO image shows the event to be relatively uncrowded.

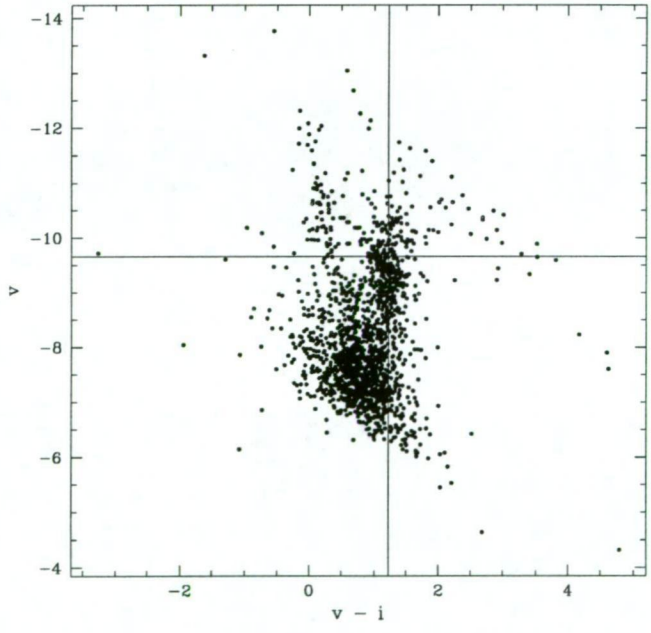

Figure 4.53: The colour-magnitude diagram of bulge field OB98018 is shown in which 1829 stars are plotted. The location of the microlensed source at baseline is indicated by the cross-hairs where the DoPHOT fit magnitudes are $I = -10.9$ and $V = -9.7$.

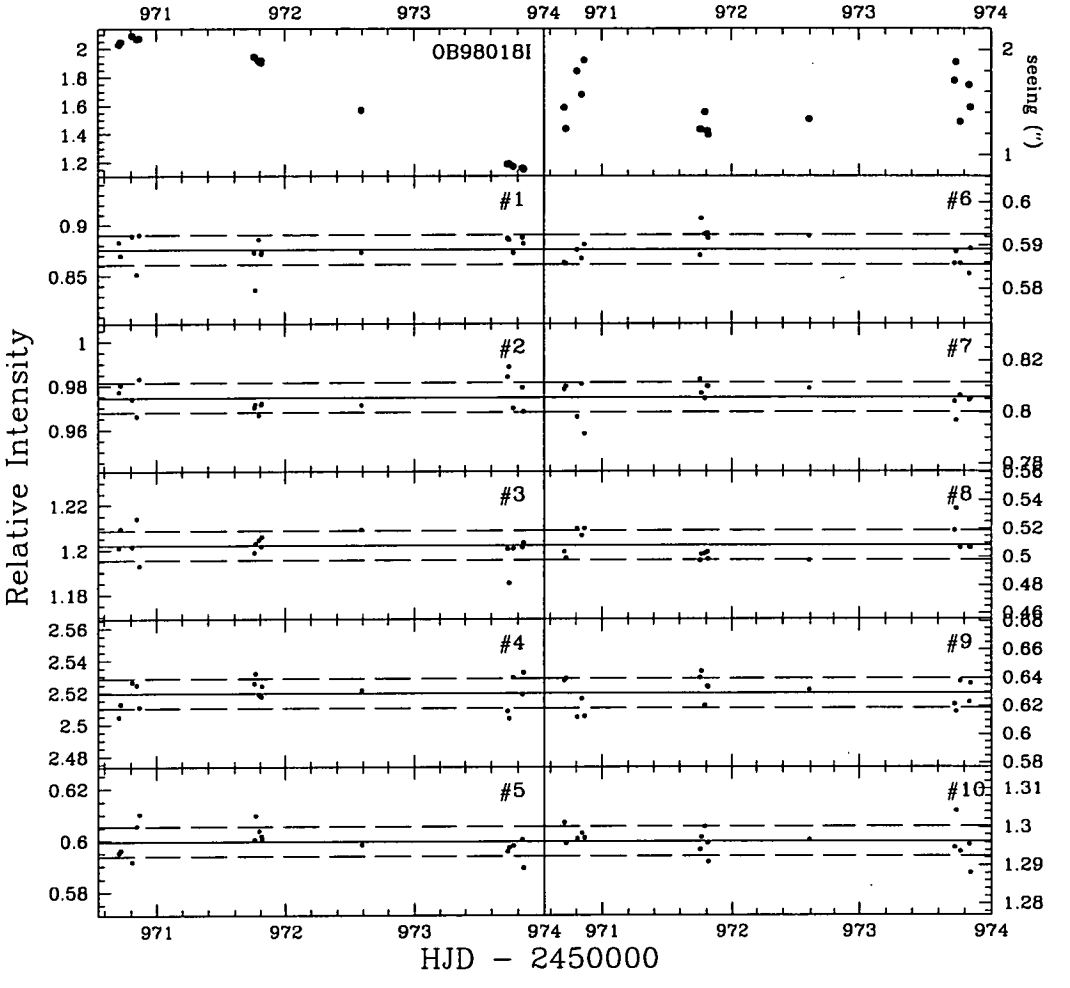

Figure 4.54: I band light curve for event OB98018. The relative intensity of the microlensed source with respect to the average flux of the reference stars is shown in the top left panel. The light curve includes a total of 16 data points. All 10 reference stars were used with an average scatter of 0.010.

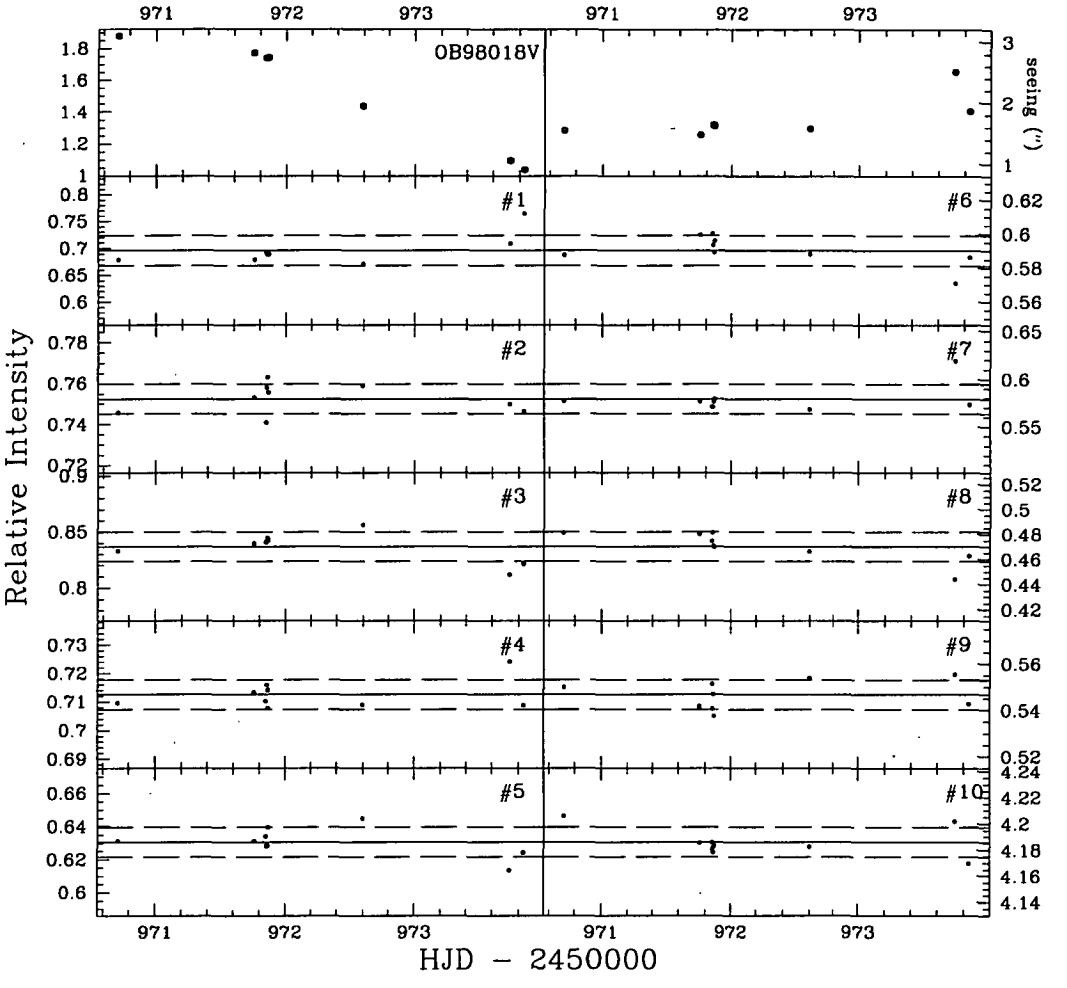

Figure 4.55: V band light curve for event OB98018. The relative intensity of the microlensed source with respect to the average flux of the reference stars is shown in the top left panel. The light curve includes a total of 9 data points. All 10 reference stars were used with an average scatter of 0.017.

4.4 Summary of Photometric Data

This chapter has presented the photometry results of observations of Galactic microlensing events from three consecutive bulge seasons. There is a large dependency of the accuracy of the photometry upon the scatter in the reference stars. For the data acquired at Canopus, the average scatter in the reference stars is $\sim 3.1\%$ for the 1996 season and $\sim 5.2\%$ for the 1997 season. The higher scatter for the 1997 season is partly due to the smaller fields restricting the choice of reference stars. For the data acquired at CTIO, the average scatter in the reference stars is $\sim 1.7\%$ for the 1997 season and $\sim 1.3\%$ for the 1998 season. It is worth noting that these figures include those events for which the microlensed source was extremely faint or highly blended with a nearby star.

The number of useful events amongst those monitored is determined by several factors including the baseline magnitude, the maximum amplification, and the crowding (and subsequent blending) of the event. The term "useful events" in this context simply means those events from which meaningful characteristics of the microlensing event could possibly be derived. The limiting magnitude for these observations depends upon the photometric conditions but has been estimated to be approximately 18.5 in I.

From the 1996 bulge season, a total of 737 (542 I and 195 V) frames were acquired at Canopus. The most useful of the events monitored in this season are events 11, 12, and 16 with the remainder being either too faint or too blended. From the 1997 bulge season, a total of 1021 (720 I and 301 V) frames were acquired at Canopus and a total of 193 (142 I and 51 V) frames were acquired at CTIO. The most useful of the events monitored in this season are events 18, 26, 28, 30, 31, and 41 with the remainder being either too faint or too blended. From the 1998 bulge season, a total of 89 (73 I and 16 V) frames were acquired at CTIO. Both of the events monitored in this season were quite bright and so both of the events are very useful.

The CMD shown for each of the events quite clearly shows the main sequence and the red giant branch, although the CMDs for the 1997 events contain much fewer stars due to a much smaller field of view. As one would expect, almost all of these microlensed sources are main sequence stars with a few appearing to lie amongst the red clump giants. In particular, the detailed CMDs from the OB98014 and OB98018 fields indicate that these bright OGLE events are red clump giants.

The data presented here has been archived and stored with the archives from the other PLANET observing sites. The majority of this data set will be published in data papers for each of the PLANET observing seasons. An important criterion for modelling an event is to obtain baseline points from at least one of the PLANET observing sites. A selection of these events have been modelled by the author and will be presented in the following chapter.

Chapter 5

Modelling the Data

This chapter describes results from fitting models to a selection of observed microlensing events. The first section describes the method used to minimize the χ^2 for a microlensing light curve by adjusting the free parameters. The second section applies this method to a selection of events incorporating available data from all PLANET observing sites. The third section discusses the results from these fits and their relevance to microlensing statistics.

5.1 Minimizing χ^2

Various methods have been developed to minimize the value of χ^2 (see Equation 2.52) for a given data set. The method adopted for this analysis is similar to the *downhill simplex method* [73, 82] which uses function evaluations rather than derivatives to numerically solve the minimization problem. In the 1-dimensional case, it is typically a simple matter to vary the one free parameter to locate the point where χ^2 reaches its minimum value. For multi-dimensional minimization, adjusting one of the f independent free parameters will change the location of the minimum χ^2 value for each of the other free parameters. In this case, an initial guess of the parameters is needed and the process of adjusting the parameters is repeated until convergence at a local minimum is attained.

The SuperMongo program `model.sm` written by the author (see Appendix D) allows n data sets to be used and the magnitude offsets between them can be adjusted. The data files were created from the output of the PLANET archiving software. For each observing site, the baseline points of a particular event are often stored in a separate archive from the main archive of the event. Since both of the archives used the same detector, the same template file, and the same reference stars, the offset between the resulting data sets was fixed at zero. The magnitude offsets between the data sets were treated as free parameters for the modelling and so the number of degrees of freedom is given as $d = N - n - f + 2$, where N is the total number of data points from all n data sets.

Once the magnitude offsets are satisfactorily estimated, the magnitudes are converted to amplifications and are normalized using the baseline points. The first guesses of the free parameters for the chosen model may then be entered until a reasonable first value of χ^2 is obtained. The program then begins a fitting procedure which continues to adjust the free parameters by pre-defined increments until convergence is achieved. Convergence is achieved when the calculated reduced χ^2 between successive iterations changes by less than 0.001. The program then plots the data along with the model using the final fit parameters.

Since DoPHOT underestimates photometric errors, the modelling program increases the magnitude errors by a factor of 2 (see Section 3.3.3) thereby reducing the chance of overestimating the significance of any anomalies being studied. However, there are several additional systematic effects which are not taken into account by the DoPHOT error estimation [9]. Firstly, there is a correlation between the residuals of constant stars and the seeing (and sometimes also the background). This correlation is dependant on the observing site and the detector, and can increase the scatter by a factor of 2. Secondly, the non-Gaussian nature of the photometric errors result in outliers that deviate by more than $> 3\sigma$. Hence, it was found that several of the fitted models produced a high reduced χ^2 despite the lack of high deviations from the data.

The `model.sm` script currently only allows the user to fit a standard PSPL model, a PSPL model with blending, or a BSPL model. Subroutines from the light curve generating program `curve.sm` (see Appendix A.3) could be incorporated into the modelling program for a more exhaustive study of microlensing anomalies.

5.2 Light Curve Fitting

A selection of microlensing events was chosen from Tables 4.1, 4.2, and 4.3 to be studied further. The events were selected based on the quantity and quality of the data, and on the availability of baseline points from the observing sites. Also a factor considered was whether or not the event had already been modelled in any of the PLANET publications, with preference being given to those that had not been previously analysed. The final events chosen to be modelled were the 1997 events MB97018, MB97026, MB97030, and MB97031. Various microlensing models are fitted to these events in this section and the data is plotted with the best-fit model. The residuals shown on these plots is the difference in amplification between the data and the model.

5.2.1 MB97018

The MACHO event MB97018 was alerted around the 28th of April, 1997. The PLANET collaboration acquired 179 I and 87 V data points on this event from 4 separate observing sites. The number of data points obtained at each observing site is shown in Table 5.1. Included in the data points obtained at SAAO are 4 I and 5 V baseline points.

Site	I	V
Canopus	56	38
CTIO	9	11
SAAO	28	11
La Silla	86	27

Table 5.1: Data points included in modelling for event MB97018.

An attempt to fit a BSPL model with 170 d.o.f. to the I data set resulted in convergence after 20 iterations of the minimization subroutine and fitted with a reduced χ^2 of 1.176. A blended PSPL model with 172 d.o.f. resulted in convergence after 9 iterations and fitted with a reduced χ^2 of 1.146. However, the best fit was achieved by a standard PSPL model resulting in a reduced χ^2 of 1.137.

Shown in Figure 5.1 is the I data from all 4 observing sites along with the best-fit model. The 1 σ scatter in the residuals shown is 5.9%. Using first guesses of $t_0 = 609$ days, $u_{min} = 0.4$, and $t_E = 80$ days, the standard PSPL model converged after 9 iterations. The resulting fit parameters for the event are $t_0 = 608.41 \pm 0.12$ days, $u_{min} = 0.390 \pm 0.023$, and $t_E = 89.20 \pm 5.26$ days. These parameters imply a maximum amplification of ≈ 2.7.

An attempt to fit a BSPL model with 78 d.o.f. to the V data set resulted in convergence after 28 iterations of the minimization subroutine and fitted with a reduced χ^2 of 2.129. A blended PSPL model with 80 d.o.f. resulted in convergence after 4 iterations and fitted with a reduced χ^2 of 2.065. As was the case for the I data, the best fit was achieved by a standard PSPL model resulting in a reduced χ^2 of 2.039.

Shown in Figure 5.2 is the V data from all 4 observing sites along with the best-fit model. The 1 σ scatter in the residuals shown is 12.7%. Using first guesses of $t_0 = 609$ days, $u_{min} = 0.4$, and $t_E = 80$ days, the standard PSPL model converged after 5 iterations. The resulting fit parameters for the event are $t_0 = 606.14 \pm 0.25$ days, $u_{min} = 0.425 \pm 0.054$, and $t_E = 89.62 \pm 11.38$ days. These parameters imply a maximum amplification of ≈ 2.5.

A summary of the fits for each model to the I and V data is shown in Table 5.2. The fit parameters are shown and the resulting reduced χ^2 is presented.

Figure 5.3 shows a plot of the best-fit V model divided by the best-fit I model. This clearly shows chromaticity over the peak of the light curve. However, the 1

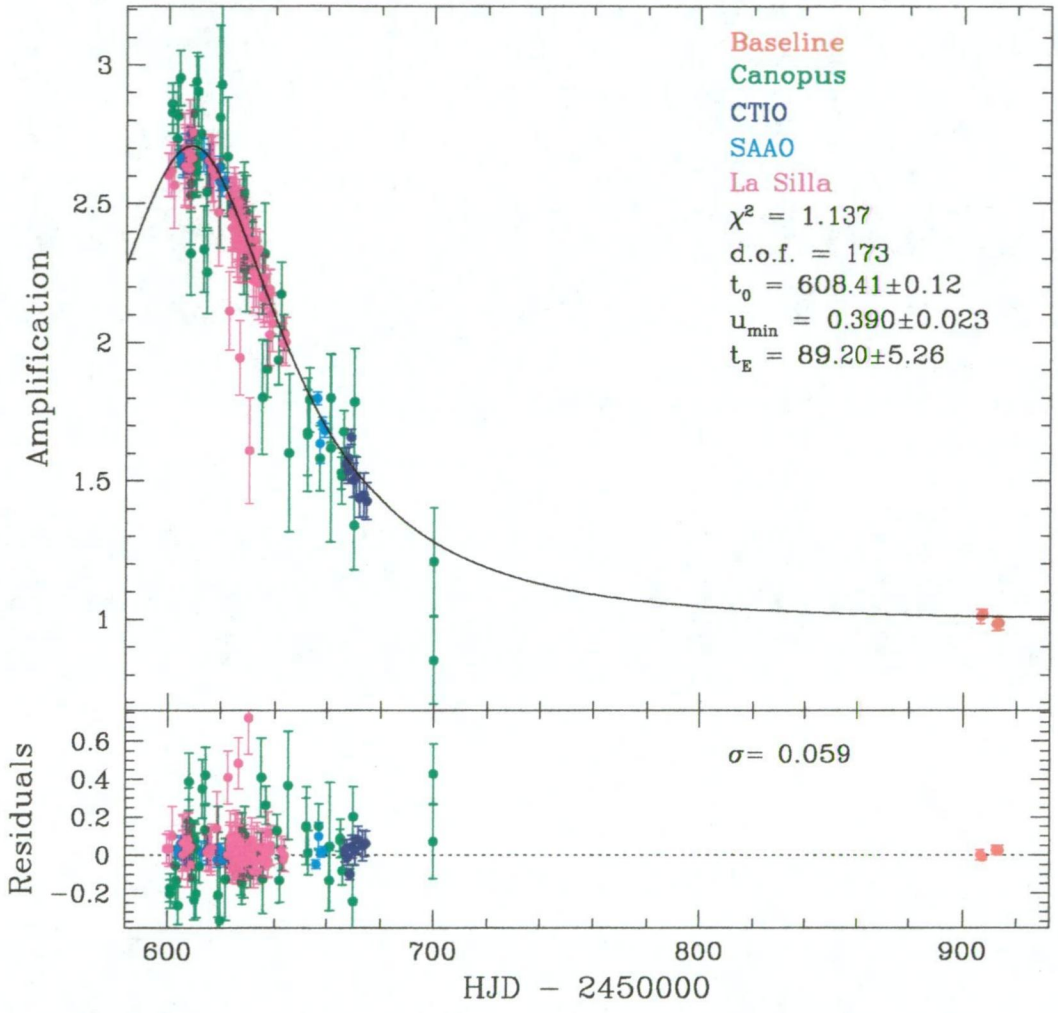

Figure 5.1: The best-fit light curve for the I band data of event MB97018 and the best-fit parameters. The data points consist of 179 measurements from Canopus (green), CTIO (blue), SAAO (red & cyan), and La Silla (magenta). Shown in the lower panel are the residuals from the best-fit model. The 1 σ scatter in the residuals is 5.9%.

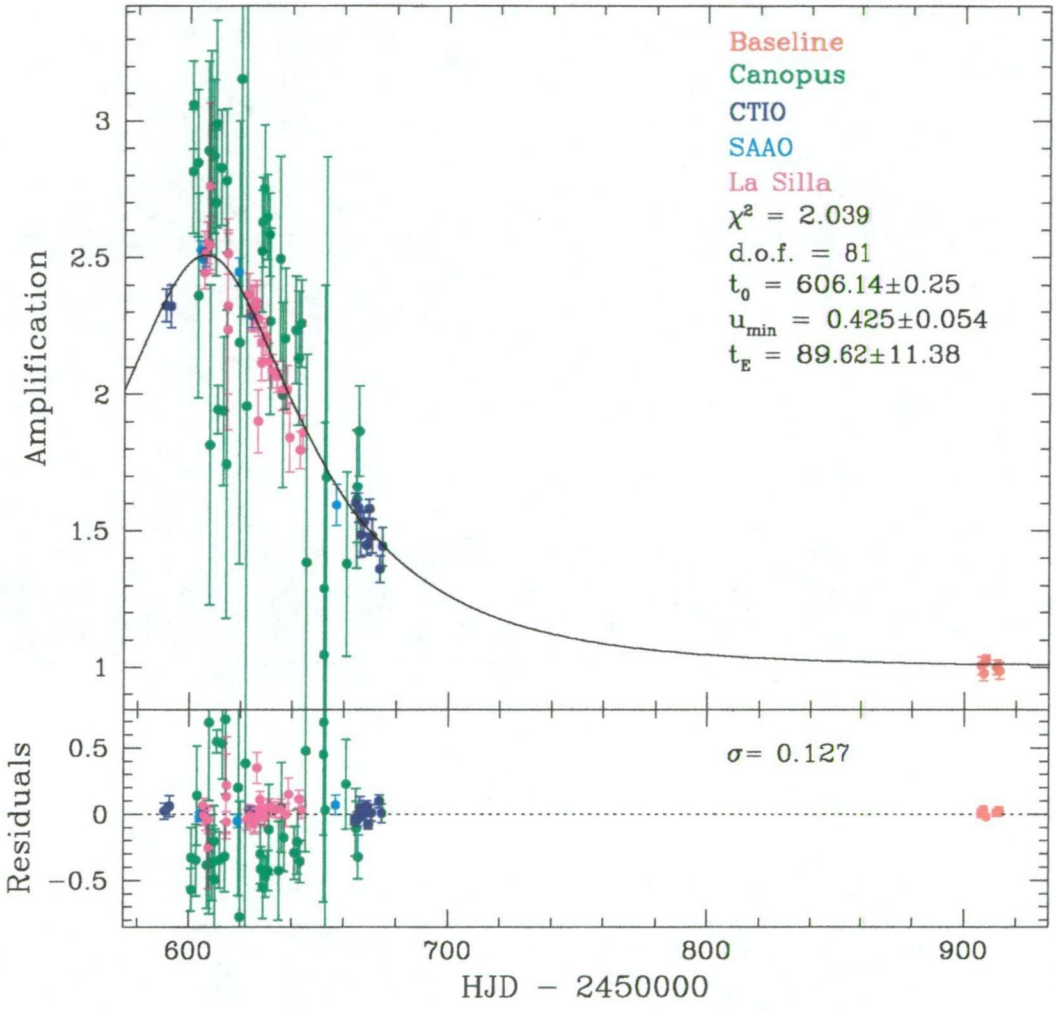

Figure 5.2: The best-fit light curve for the V band data of event MB97018 and the best-fit parameters. The data points consist of 87 measurements from Canopus (green), CTIO (blue), SAAO (red & cyan), and La Silla (magenta). Shown in the lower panel are the residuals from the best-fit model. The 1 σ scatter in the residuals is quite high at 12.7%.

PSPL		
Parameter	**I**	**V**
t_0 (days)	608.41 ± 0.12	606.14 ± 0.25
u_{min}	0.390 ± 0.023	0.425 ± 0.054
t_E (days)	89.20 ± 5.26	89.62 ± 11.38
reduced χ^2	1.137	2.039
Blended PSPL		
Parameter	**I**	**V**
t_0 (days)	608.66 ± 0.12	606.61 ± 0.25
u_{min}	0.344 ± 0.020	0.376 ± 0.048
t_E (days)	97.23 ± 5.74	96.77 ± 12.29
f	0.84 ± 0.05	0.84 ± 0.11
reduced χ^2	1.146	2.065
BSPL		
Parameter	**I**	**V**
$t_{0,1}$ (days)	596.38 ± 0.12	594.09 ± 0.25
$t_{0,2}$ (days)	617.23 ± 0.12	613.53 ± 0.25
$u_{min,1}$	0.259 ± 0.015	0.346 ± 0.044
$u_{min,2}$	0.421 ± 0.025	0.444 ± 0.058
t_E (days)	82.00 ± 4.84	85.60 ± 10.87
ω	0.77 ± 0.05	0.71 ± 0.09
reduced χ^2	1.176	2.129

Table 5.2: The fit parameters and reduced χ^2 for each model fitted to the MB97018 I and V data.

σ scatter in the plot is about 2.6% which places it within the experimental errors of the PLANET data residuals.

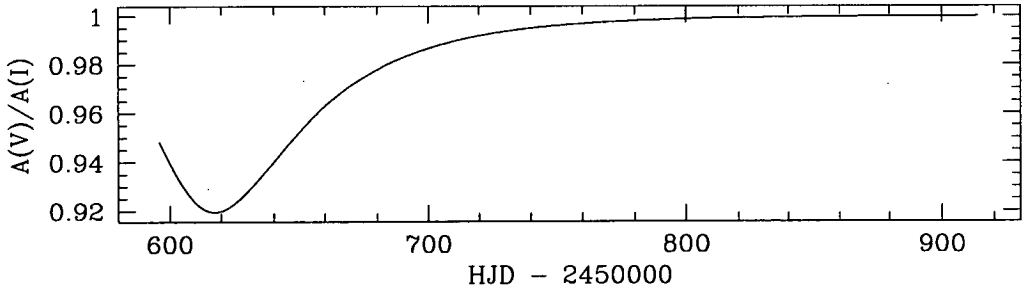

Figure 5.3: The best-fit V model divided by the best-fit I model. The $A(V)/A(I)$ curve shows the chromatic nature of the fitted models with a 1 σ scatter of 0.026.

5.2.2 MB97026

The MACHO event MB97026 was alerted around the 27th of May, 1997. The PLANET collaboration acquired 404 I and 173 V data points on this event from 4 separate observing sites. The number of data points obtained at each observing site is shown in Table 5.3. Included in the data points obtained at SAAO are 8 I and 6 V baseline points.

Site	I	V
Canopus	109	43
CTIO	24	12
SAAO	51	15
La Silla	220	103

Table 5.3: Data points included in modelling for event MB97026.

A standard PSPL model with 398 d.o.f. was fitted to the I data set and converged after 4 iterations of the minimization subroutine and fitted with a reduced χ^2 of 3.537. A blended PSPL model with 397 d.o.f. resulted in convergence after 4 iterations and fitted with a reduced χ^2 of 3.820. However, the best fit was achieved by a BSPL model resulting in a reduced χ^2 of 2.844.

Shown in Figure 5.4 is the I data from all 4 observing sites along with the best-fit model. Since there are no obvious deviations from the model, the relatively high χ^2 may indicate that the DoPHOT errors are an underestimation of the true error by a factor of ~ 2. The 1 σ scatter in the residuals shown is 2.9%. Using first guesses of $t_{0,1} = 630$ days, $t_{0,2} = 640$ days, $u_{min,1} = 0.15$, $u_{min,2} = 0.10$, $t_E = 50$ days, and $\omega = 0.6$, the BSPL model converged after 41 iterations. The resulting fit parameters for the event are $t_{0,1} = 633.76 \pm 0.06$ days, $t_{0,2} = 637.92 \pm 0.06$ days, $u_{min,1} = 0.100 \pm 0.003$, $u_{min,2} = 0.132 \pm 0.004$, $t_E = 57.03 \pm 1.65$ days, and $\omega = 0.80 \pm 0.02$.

A standard PSPL model with 167 d.o.f. was fitted to the V data set and converged after 6 iterations of the minimization subroutine and fitted with a reduced χ^2 of 1.407. A blended PSPL model with 166 d.o.f. resulted in convergence after 5 iterations and fitted with a reduced χ^2 of 1.489. As was the case for the I data, the best fit was achieved by a BSPL model resulting in a reduced χ^2 of 1.337.

Shown in Figure 5.5 is the V data from all 4 observing sites along with the best-fit model. The 1 σ scatter in the residuals shown is 5.4%. Using first guesses of $t_{0,1} = 633$ days, $t_{0,2} = 637$ days, $u_{min,1} = 0.10$, $u_{min,2} = 0.13$, $t_E = 57$ days, and $\omega = 0.8$, the BSPL model converged after 44 iterations. The resulting fit parameters for the event are $t_{0,1} = 630.00 \pm 0.11$ days, $t_{0,2} = 637.11 \pm 0.11$ days, $u_{min,1} = 0.165 \pm 0.009$, $u_{min,2} = 0.137 \pm 0.007$, $t_E = 51.56 \pm 2.78$ days, and $\omega = 0.90 \pm 0.05$.

A summary of the fits for each model to the I and V data is shown in Table 5.4. The fit parameters are shown and the resulting reduced χ^2 is presented.

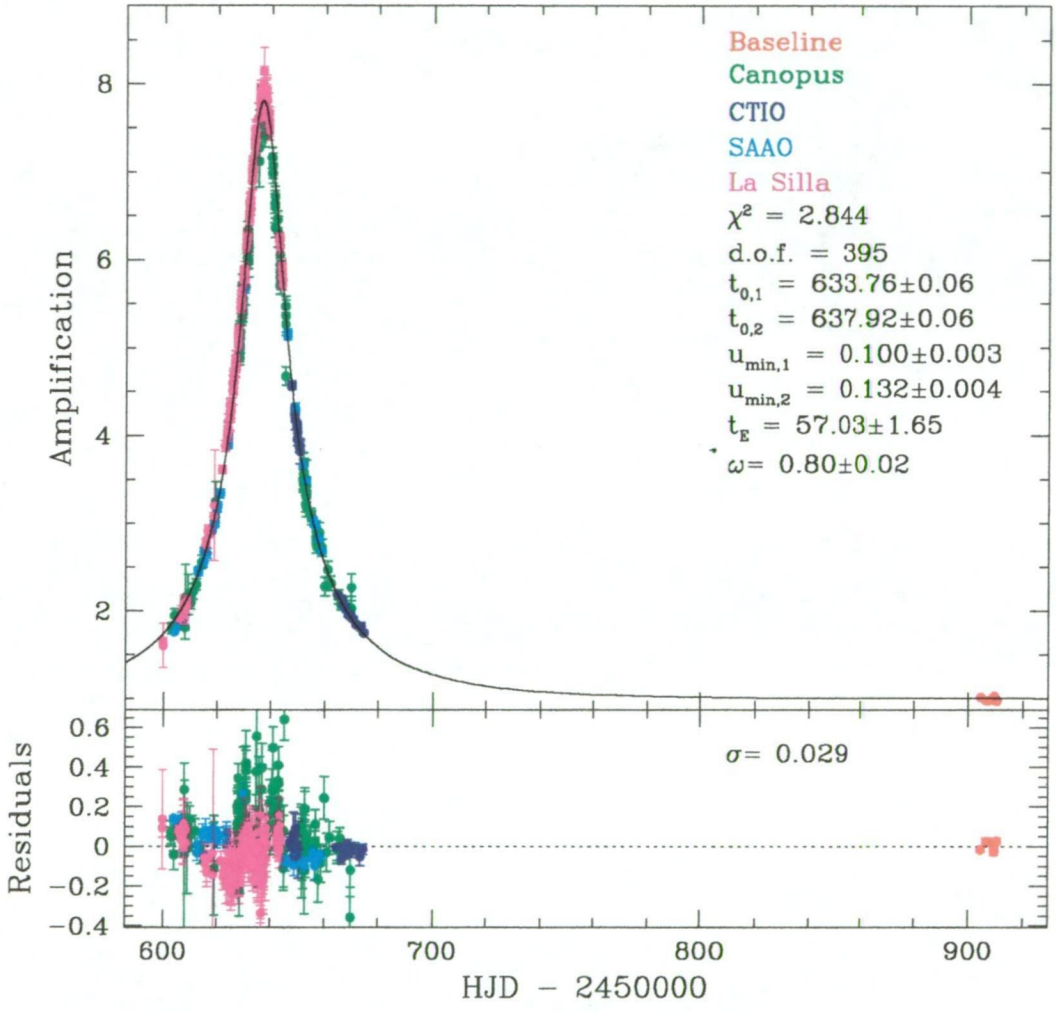

Figure 5.4: The best-fit light curve for the I band data of event MB97026 and the best-fit parameters. The data points consist of 404 measurements from Canopus (green), CTIO (blue), SAAO (red & cyan), and La Silla (magenta). Shown in the lower panel are the residuals from the best-fit model. The 1 σ scatter in the residuals is 2.9%.

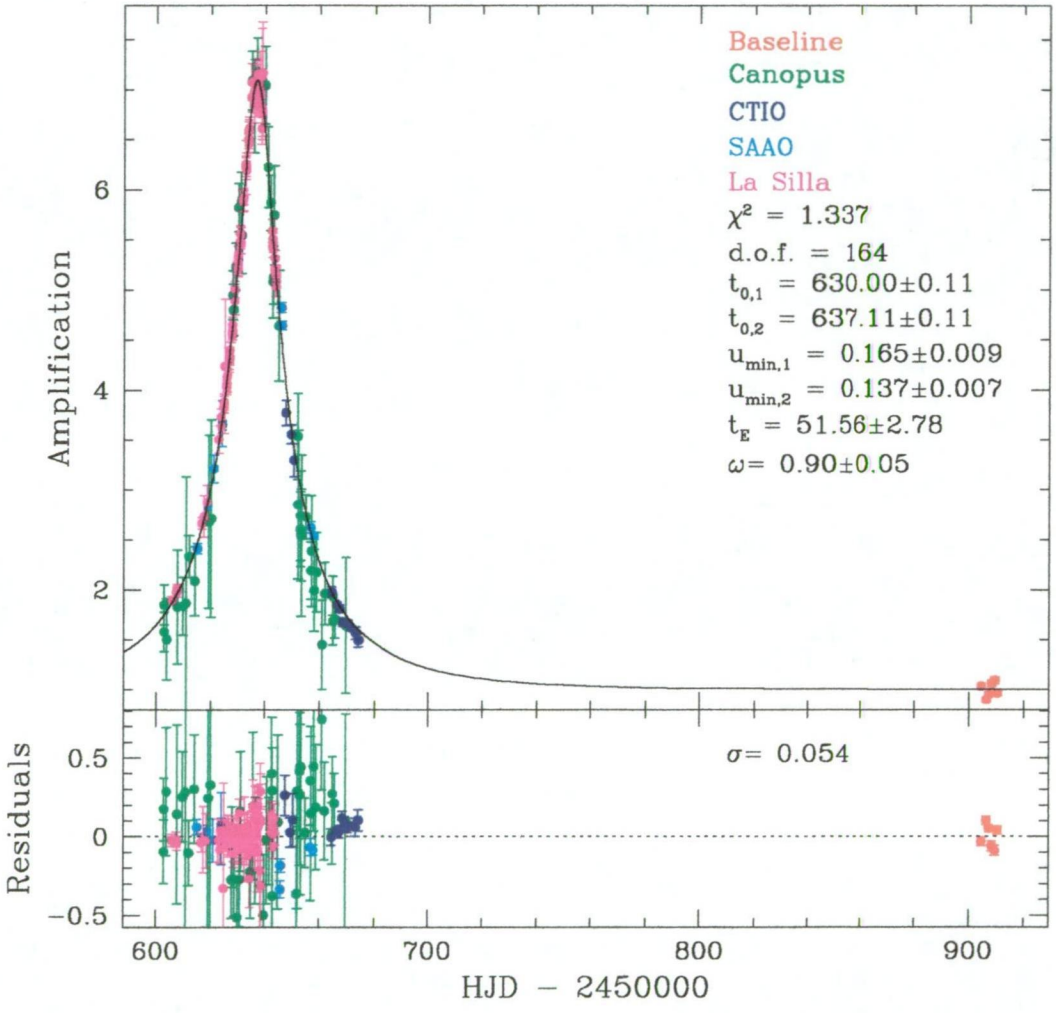

Figure 5.5: The best-fit light curve for the V band data of event MB97026 and the best-fit parameters. The data points consist of 173 measurements from Canopus (green), CTIO (blue), SAAO (red & cyan), and La Silla (magenta). Shown in the lower panel are the residuals from the best-fit model. The 1 σ scatter in the residuals is 5.4%.

PSPL		
Parameter	**I**	**V**
t_0 (days)	636.83 ± 0.06	636.64 ± 0.12
u_{min}	0.126 ± 0.004	0.143 ± 0.008
t_E (days)	57.76 ± 1.79	52.60 ± 3.05
reduced χ^2	3.537	1.407
Blended PSPL		
Parameter	**I**	**V**
t_0 (days)	636.82 ± 0.06	636.63 ± 0.12
u_{min}	0.119 ± 0.004	0.138 ± 0.008
t_E (days)	60.36 ± 1.93	54.16 ± 3.14
f	0.94 ± 0.03	0.96 ± 0.06
reduced χ^2	3.820	1.489
BSPL		
Parameter	**I**	**V**
$t_{0,1}$ (days)	633.76 ± 0.06	630.00 ± 0.11
$t_{0,2}$ (days)	637.92 ± 0.06	637.11 ± 0.11
$u_{min,1}$	0.100 ± 0.003	0.165 ± 0.009
$u_{min,2}$	0.132 ± 0.004	0.137 ± 0.007
t_E (days)	57.03 ± 1.65	51.56 ± 2.78
ω	0.80 ± 0.02	0.90 ± 0.05
reduced χ^2	2.844	1.337

Table 5.4: The fit parameters and reduced χ^2 for each model fitted to the MB97026 I and V data.

Figure 5.6 shows a plot of the best-fit V model divided by the best-fit I model. This clearly shows chromaticity over the peak of the light curve. The 1 σ scatter in the plot is about 3.8% but it would not be unreasonable for the light curve to be chromatic if it is a binary and the binary source components are different colours.

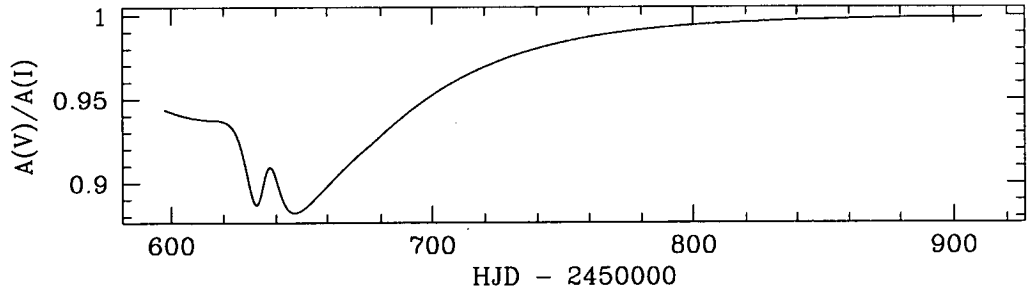

Figure 5.6: The best-fit V model divided by the best-fit I model. The $A(V)/A(I)$ curve shows the chromatic nature of the fitted models with a 1 σ scatter of 0.038.

5.2.3 MB97030

The MACHO event MB97030 was alerted around the 29th of May, 1997. The PLANET collaboration acquired 98 I and 30 V data points on this event from 3 separate observing sites. The number of data points obtained at each observing site is shown in Table 5.5. Included in the data points obtained at SAAO are 3 I and 4 V baseline points.

Site	I	V
Canopus	27	8
SAAO	29	9
La Silla	42	13

Table 5.5: Data points included in modelling for event MB97030.

An attempt to fit a BSPL model with 90 d.o.f. to the I data set resulted in convergence after 13 iterations of the minimization subroutine and fitted with a reduced χ^2 of 1.880. A blended PSPL model with 92 d.o.f. resulted in convergence after 23 iterations and fitted with a reduced χ^2 of 1.705. However, the best fit was achieved by a standard PSPL model resulting in a reduced χ^2 of 1.668.

Shown in Figure 5.7 is the I data from all 3 observing sites along with the best-fit model. The 1 σ scatter in the residuals shown is 7.1%. Using first guesses of $t_0 = 601$ days, $u_{min} = 0.2$, and $t_E = 12$ days, the standard PSPL model converged after 12 iterations. The resulting fit parameters for the event are $t_0 = 601.05 \pm 0.14$ days, $u_{min} = 0.200 \pm 0.014$, and $t_E = 10.90 \pm 0.77$ days. These parameters imply a maximum amplification of ≈ 5.1.

An attempt to fit a BSPL model with 22 d.o.f. to the V data set resulted in convergence after 83 iterations of the minimization subroutine and fitted with a reduced χ^2 of 2.639. A blended PSPL model with 24 d.o.f. resulted in convergence after 4 iterations and fitted with a reduced χ^2 of 2.470. Contrary to the I data fits, the best fit was achieved by the blended PSPL model. However, considering the high scatter in the residuals and the small difference in the reduced χ^2, the simpler standard PSPL model was adopted as the best-fit model which resulting in a reduced χ^2 of 2.486.

Shown in Figure 5.8 is the V data from all 3 observing sites along with the best-fit model. The 1 σ scatter in the residuals shown is 16.0%. Using first guesses of $t_0 = 601$ days, $u_{min} = 0.2$, and $t_E = 12$ days, the standard PSPL model converged after 32 iterations. The resulting fit parameters for the event are $t_0 = 600.88 \pm 0.32$ days, $u_{min} = 0.171 \pm 0.027$, and $t_E = 14.75 \pm 2.36$ days. These parameters imply a maximum amplification of ≈ 5.9.

A summary of the fits for each model to the I and V data is shown in Table 5.6. The fit parameters are shown and the resulting reduced χ^2 is presented.

Figure 5.9 shows a plot of the best-fit V model divided by the best-fit I model. This clearly shows chromaticity over the peak of the light curve. However, the 1

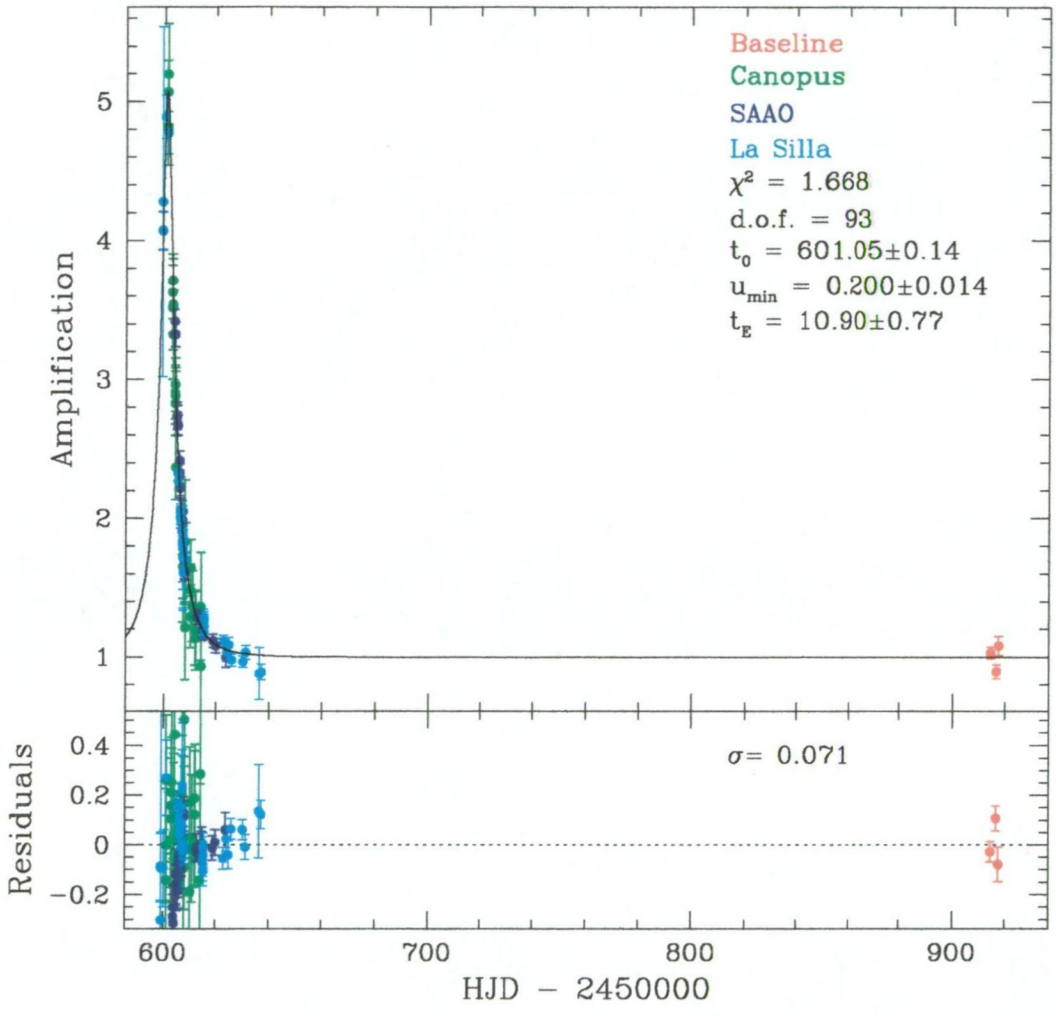

Figure 5.7: The best-fit light curve for the I band data of event MB97030 and the best-fit parameters. The data points consist of 98 measurements from Canopus (green), SAAO (red & blue), and La Silla (cyan). Shown in the lower panel are the residuals from the best-fit model. The 1 σ scatter in the residuals is 7.1%.

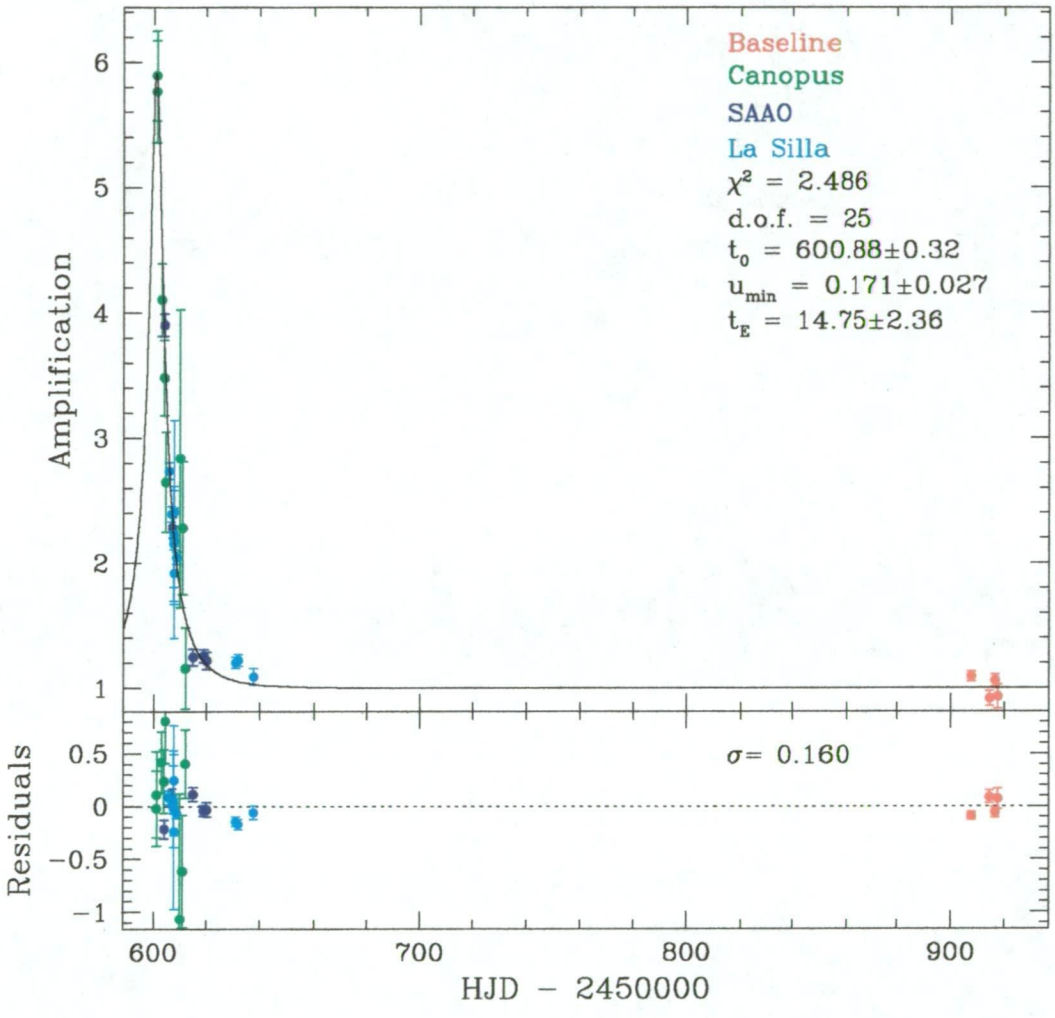

Figure 5.8: The best-fit light curve for the V band data of event MB97030 and the best-fit parameters. The data points consist of 30 measurements from Canopus (green), SAAO (red & blue), and La Silla (cyan). Shown in the lower panel are the residuals from the best-fit model. The 1 σ scatter in the residuals is quite high at 16.0%.

PSPL		
Parameter	**I**	**V**
t_0 (days)	601.05 ± 0.14	600.88 ± 0.32
u_{min}	0.200 ± 0.014	0.171 ± 0.027
t_E (days)	10.90 ± 0.77	14.75 ± 2.36
reduced χ^2	1.668	2.486
Blended PSPL		
Parameter	**I**	**V**
t_0 (days)	601.07 ± 0.14	601.00 ± 0.31
u_{min}	0.186 ± 0.013	0.142 ± 0.022
t_E (days)	11.42 ± 0.81	16.74 ± 2.63
f	0.92 ± 0.07	0.80 ± 0.13
reduced χ^2	1.705	2.470
BSPL		
Parameter	**I**	**V**
$t_{0,1}$ (days)	541.74 ± 0.15	598.64 ± 0.32
$t_{0,2}$ (days)	601.14 ± 0.15	602.56 ± 0.32
$u_{min,1}$	0.109 ± 0.008	0.089 ± 0.014
$u_{min,2}$	0.144 ± 0.011	0.126 ± 0.020
t_E (days)	13.34 ± 0.97	16.03 ± 2.55
ω	0.70 ± 0.05	0.23 ± 0.04
reduced χ^2	1.880	2.639

Table 5.6: The fit parameters and reduced χ^2 for each model fitted to the MB97030 I and V data.

σ scatter in the plot is about 5.0% which places it within the experimental errors of the PLANET data residuals.

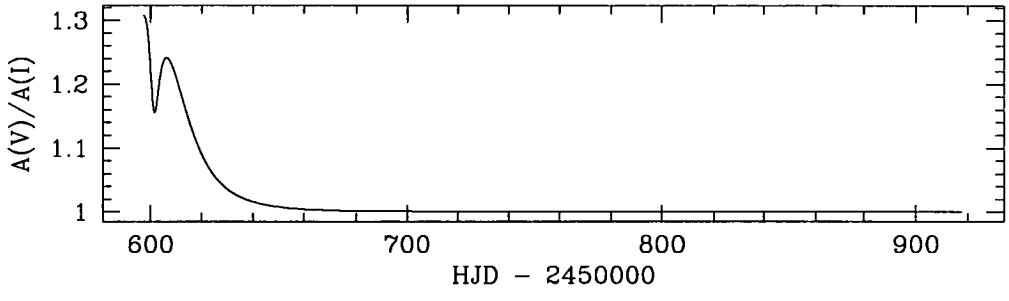

Figure 5.9: The best-fit V model divided by the best-fit I model. The $A(V)/A(I)$ curve shows the chromatic nature of the fitted models with a 1 σ scatter of 0.050.

5.2.4 MB97031

The MACHO event MB97031 was alerted around the 29th of May, 1997. The PLANET collaboration acquired 252 I and 86 V data points on this event from 3 separate observing sites. The number of data points obtained at each observing site is shown in Table 5.7. Included in the data points obtained at SAAO are 5 I and 3 V baseline points.

Site	I	V
Canopus	78	25
SAAO	36	15
La Silla	138	46

Table 5.7: Data points included in modelling for event MB97031.

An attempt to fit a BSPL model with 244 d.o.f. to the I data set resulted in convergence after 28 iterations of the minimization subroutine and fitted with a reduced χ^2 of 1.592. A blended PSPL model with 246 d.o.f. resulted in convergence after 6 iterations and fitted with a reduced χ^2 of 1.594. However, the best fit was achieved by a standard PSPL model resulting in a reduced χ^2 of 1.585.

Shown in Figure 5.10 is the I data from all 3 observing sites along with the best-fit model. The 1 σ scatter in the residuals shown is 1.2%. Using first guesses of $t_0 = 594$ days, $u_{min} = 0.7$, and $t_E = 41$ days, the standard PSPL model converged after 10 iterations. The resulting fit parameters for the event are $t_0 = 593.52 \pm 0.02$ days, $u_{min} = 0.676 \pm 0.008$, and $t_E = 39.39 \pm 0.47$ days. These parameters imply a maximum amplification of ≈ 1.7.

An attempt to fit a BSPL model with 78 d.o.f. to the V data set resulted in convergence after 32 iterations of the minimization subroutine and fitted with a reduced χ^2 of 0.513. A blended PSPL model with 80 d.o.f. resulted in convergence after 6 iterations and fitted with a reduced χ^2 of 0.517. As was the case for the I data, the best fit was achieved by a standard PSPL model resulting in a reduced χ^2 of 0.505.

The low reduced χ^2 in each of these fits indicates that the models are an over fit to the data and is probably caused by an overestimation of the errors. Exceptionally large error bars in several of the Canopus data points (see Figure 5.11) are the main cause of these over fits.

Shown in Figure 5.11 is the V data from all 3 observing sites along with the best-fit model. The 1 σ scatter in the residuals shown is 2.0%. Using first guesses of $t_0 = 594$ days, $u_{min} = 0.7$, and $t_E = 41$ days, the standard PSPL model converged after 5 iterations. The resulting fit parameters for the event are $t_0 = 593.66 \pm 0.04$ days, $u_{min} = 0.696 \pm 0.014$, and $t_E = 40.12 \pm 0.80$ days. These parameters imply a maximum amplification of ≈ 1.7.

A summary of the fits for each model to the I and V data is shown in Table 5.8. The fit parameters are shown and the resulting reduced χ^2 is presented.

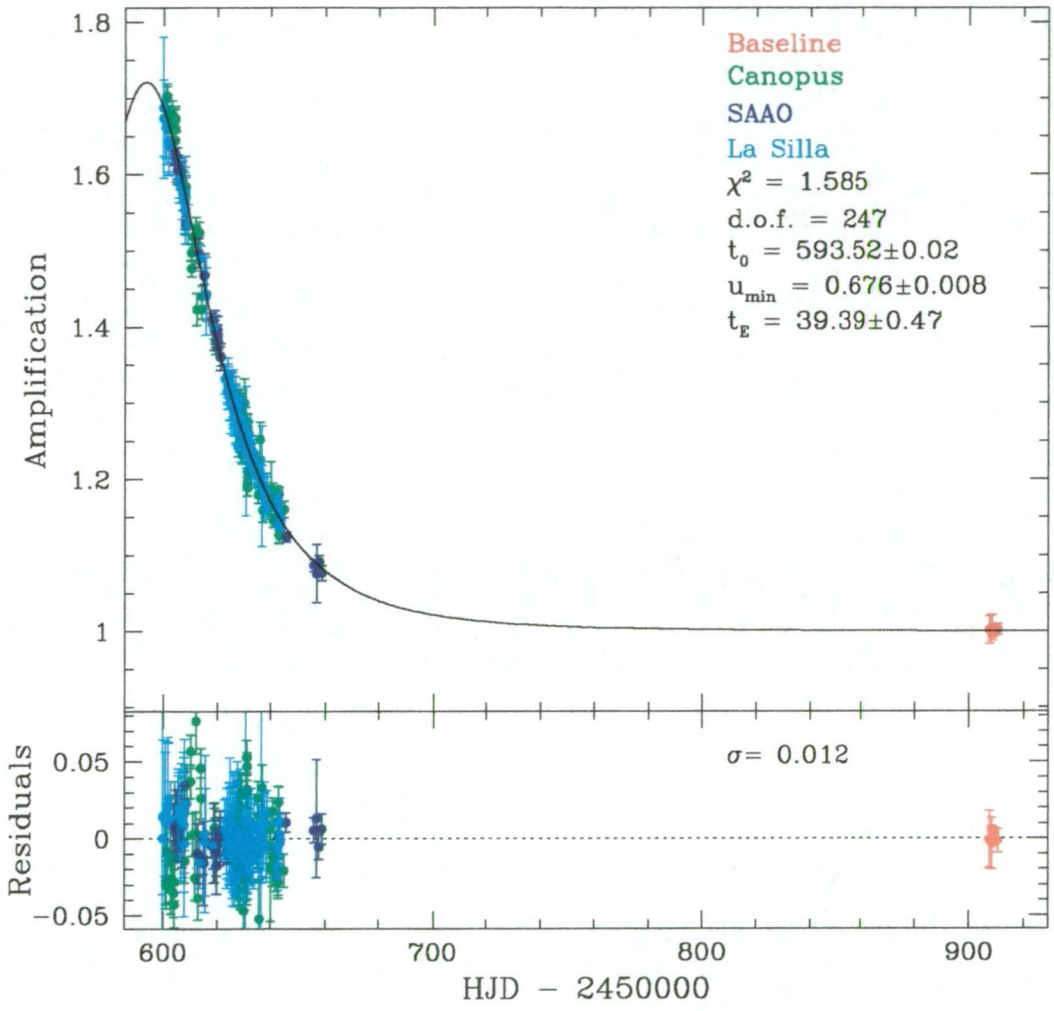

Figure 5.10: The best-fit light curve for the I band data of event MB97031 and the best-fit parameters. The data points consist of 252 measurements from Canopus (green), SAAO (red & blue), and La Silla (cyan). Shown in the lower panel are the residuals from the best-fit model. The 1 σ scatter in the residuals is 1.2%.

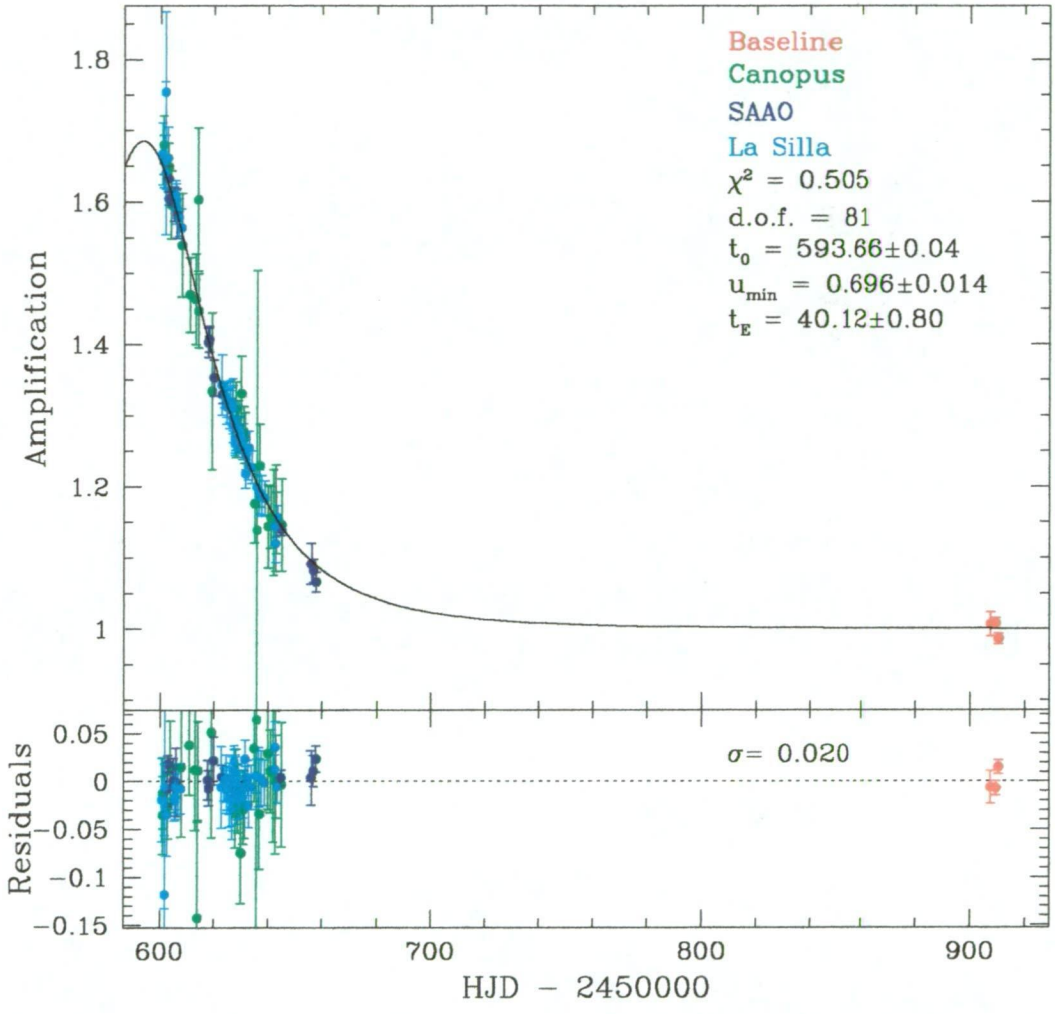

Figure 5.11: The best-fit light curve for the V band data of event MB97031 and the best-fit parameters. The data points consist of 86 measurements from Canopus (green), SAAO (red & blue), and La Silla (cyan). Shown in the lower panel are the residuals from the best-fit model. The 1 σ scatter in the residuals is 2.0%.

PSPL		
Parameter	**I**	**V**
t_0 (days)	593.52 ± 0.02	593.66 ± 0.04
u_{min}	0.676 ± 0.008	0.696 ± 0.014
t_E (days)	39.39 ± 0.47	40.12 ± 0.80
reduced χ^2	1.585	0.505
Blended PSPL		
Parameter	**I**	**V**
t_0 (days)	594.42 ± 0.02	594.95 ± 0.04
u_{min}	0.579 ± 0.007	0.594 ± 0.012
t_E (days)	42.93 ± 0.52	43.51 ± 0.87
f	0.76 ± 0.01	0.75 ± 0.02
reduced χ^2	1.594	0.517
BSPL		
Parameter	**I**	**V**
$t_{0,1}$ (days)	630.57 ± 0.02	610.05 ± 0.04
$t_{0,2}$ (days)	595.33 ± 0.02	595.60 ± 0.04
$u_{min,1}$	0.729 ± 0.009	0.701 ± 0.014
$u_{min,2}$	0.664 ± 0.008	0.707 ± 0.014
t_E (days)	34.47 ± 0.41	35.87 ± 0.72
ω	0.93 ± 0.01	0.88 ± 0.02
reduced χ^2	1.592	0.513

Table 5.8: The fit parameters and reduced χ^2 for each model fitted to the MB97031 I and V data.

Figure 5.12 shows a plot of the best-fit V model divided by the best-fit I model. This clearly shows chromaticity over the peak of the light curve. However, the 1 σ scatter in the plot is about 0.3% which places it within the experimental errors of the PLANET data residuals.

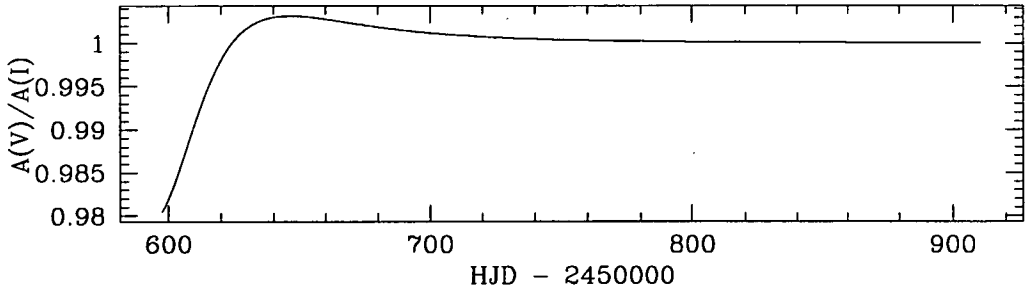

Figure 5.12: The best-fit V model divided by the best-fit I model. The $A(V)/A(I)$ curve shows the chromatic nature of the fitted models with a 1 σ scatter of 0.003.

5.3 Conclusions from Models

5.3.1 Event Fits and Parameters

In this chapter the results from modelling four microlensing events from the 1997 observing season have been presented. This modelling is certainly not intended to be an exhaustive study of these events but serves to narrow the event parameters such that definitive conclusions can be made or possible alternative explanations can be described. The events for which a standard PSPL model was found to provide the best fit (events MB97018, MB97030, and MB97031) appear to satisfy the requirements for being classified as microlensing events. However, the achromaticity of the events may not be well-constrained in the case of poor baseline measurements. A small amount of chromaticity may also arise from undetected blending, particularly in the case of MB97030 in which the scatter in the residuals is high and there is a relatively large difference in the derived characteristic time scale between the I and V band data.

The event parameters derived for the PSPL events agree within the error limits of those reported by the survey teams (see Table 5.9), although for some events (especially for those in which few or no data was acquired over the peak) the derived characteristic time scale differs somewhat. The modelling of events for which data over the peak of the light curve is not used, such as MB97031, are particularly sensitive to the initial guesses of the model parameters.

Event	A_{max}	t_0 (days)	u_{min}	t_E (days)
MB97018	2.5	609	0.43	79.5
MB97026	8.0	635	0.13	61.0
MB97030	5.1	601	0.20	13.5
MB97031	1.7	594	0.69	41.0

Table 5.9: Event parameters reported by the MACHO collaboration on the MACHO web site. The minimum impact parameter u_{min} was calculated from Equation 2.10. Although not mentioned, the uncertainty in t_0 would typically be on the order of a few days.

For the events MB97018, MB97030, and MB97031, the difference in the reduced χ^2 between models is relatively small. This difference is not significant since the purpose of the χ^2 test is to exclude those models which produce an excessively high χ^2. However, in most cases the PSPL model was found to provide the best χ^2 in both I and V bands and, since this is the simplest of the three models, it was adopted as the best-fit model.

In the case of event MB97026, the best fitting model was found to be that of a binary source with a point lens resulting in a $\Delta\chi^2 = \chi^2_{PSPL} - \chi^2_{BSPL} \approx 285$ for 395 degrees of freedom. This event appears to be an example of the type of binary source that may be erroneously identified as a standard PSPL or a blended PSPL

event, as outlined by Dominik [31] and further by Han & Jeong [50]. However, closer examination of the residuals for the PSPL fit and the BSPL fit (see Figure 5.13) indicate that there may be systematic and/or additional anomalous effects in the light curve.

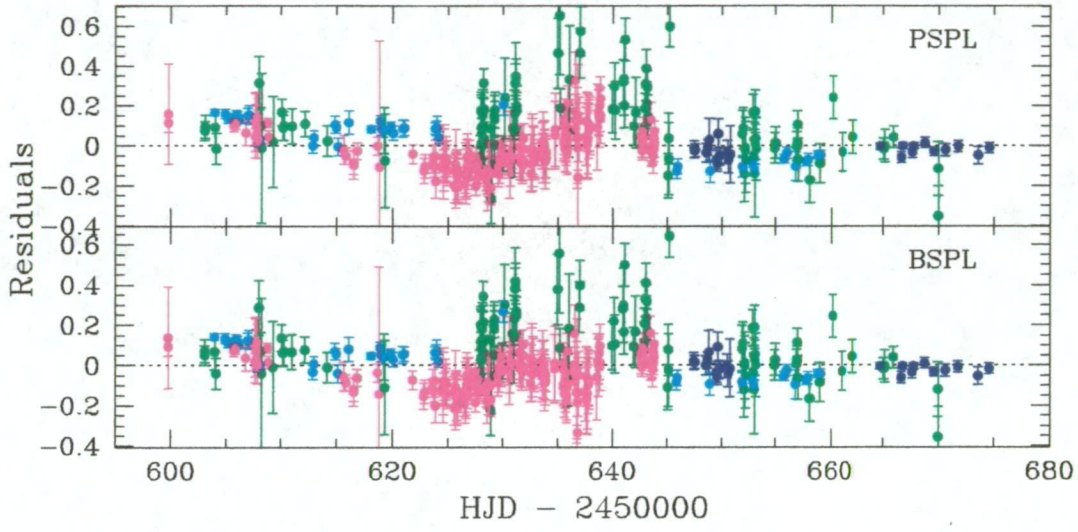

Figure 5.13: Residuals of the PSPL and BSPL models fitted to the I band data of event MB97026. The data points shown are from Canopus (green), CTIO (blue), SAAO (cyan), and La Silla (magenta).

The asymmetry in the residuals shown in Figure 5.13 can lead to several possible alternative explanations to a binary source event. Firstly, there appears to be a systematic deviation to one side of the zero point amongst the Canopus data between the dates 625 and 645. This could indicate that there is a blending factor in the Canopus data that is not present in the data from the other sites. It could also mean that the magnitude offset between Canopus and the other sites was not well determined. Secondly, the SAAO data appears to deviate from one side of the zero point to the other side, before and after the peak respectively. While difficult to tell from the scatter, this could be due to parallax, although parallax was not reported by any of the microlensing survey teams. In general, the PSPL residuals indicate some asymmetry, but the BSPL fit does not remove all of this asymmetry. Fitting more complex microlensing models to this data will further constrain the characteristics of this event. This study shows that a BSPL model is currently the most likely explanation for MB97026.

5.3.2 Planet Detection Efficiency

The probability of detecting a planet in a microlensing event has been estimated as 17% for a Jupiter-mass planet [42] and around 2% for an Earth-mass planet

[21]. Of course these estimates make certain assumptions regarding the distance to the lens, the characteristic time scale, and frequency of planetary companions. For the events modelled in this chapter, there appear to be no convincing deviations that are consistent with the presence of a planetary companion. However, it is useful to produce a rough estimate of the detection sensitivity to extrasolar planets for these 4 events, similar to the estimation for the 1995 pilot campaign of PLANET [7].

The sensitivity of a microlensing light curve to the presence of a planet will depend upon the portion of the light curve being monitored, as well as the projected separation of the planet from the primary lens. However, for events of moderate magnification, all portions of the light curve are approximately equally sensitive to the detection of planets that lie within the lensing zone. The mass ratio (as described in Section 2.5) may be expressed as $q \equiv m_p/M$, where m_p is the mass of the planet and M if the mass of the primary lens. As can be seen from Equations 2.5 and 2.11, this quantity will scale the duration of the anomaly with $q^{1/2}$ and will determine the frequency with which the anomaly will occur above a certain photometric threshold. Thus, a planetary anomaly will be detected if the photometric sampling interval Δt and the photometric precision of the data is sufficiently small for a given mass ratio. Therefore, the total length of light curve that is monitored with a given photometric precision can be used as a measure of the sensitivity to extrasolar planets.

In order to present this information in a meanful way, the monitoring period of each of the 4 light curves was normalized by $2(1 - u_{min}^2)^{1/2} t_E$. This represents the monitoring period as the fractional length of monitored light curve inside the Einstein ring radius. Summing this fractional length over all light curves for each value of a given normalized sampling time, $t_S = \Delta t / t_E$, results in the cumulative normalized light curve length η, as shown in Figure 5.14. The cumulative light curve length for both I and V band for all 4 microlensing events is shown, as well as the cumulative light curve length for only those data sets that have residuals less than 5% (I band for MB97026 and I and V band for MB97031).

The duration of a planetary anomaly may be approximately expressed as the time required to cross the diameter of the planetary Einstein ring $2t_p$. This may be expressed as

$$\begin{aligned} 2t_p &= 2q^{1/2} t_E \\ &= 2\left(\frac{m_p}{M}\right)^{1/2} t_E \\ &= 2\left(\frac{M_\odot}{M_\oplus}\right)^{1/2} \left(\frac{m_p}{M_\oplus}\right)^{1/2} \left(\frac{M}{M_\odot}\right)^{-1/2} t_E \end{aligned} \tag{5.1}$$

which, for a solar mass primary lens, becomes

$$2t_p = 0.0035 \left(\frac{m_p}{M_\oplus}\right)^{1/2} t_E \tag{5.2}$$

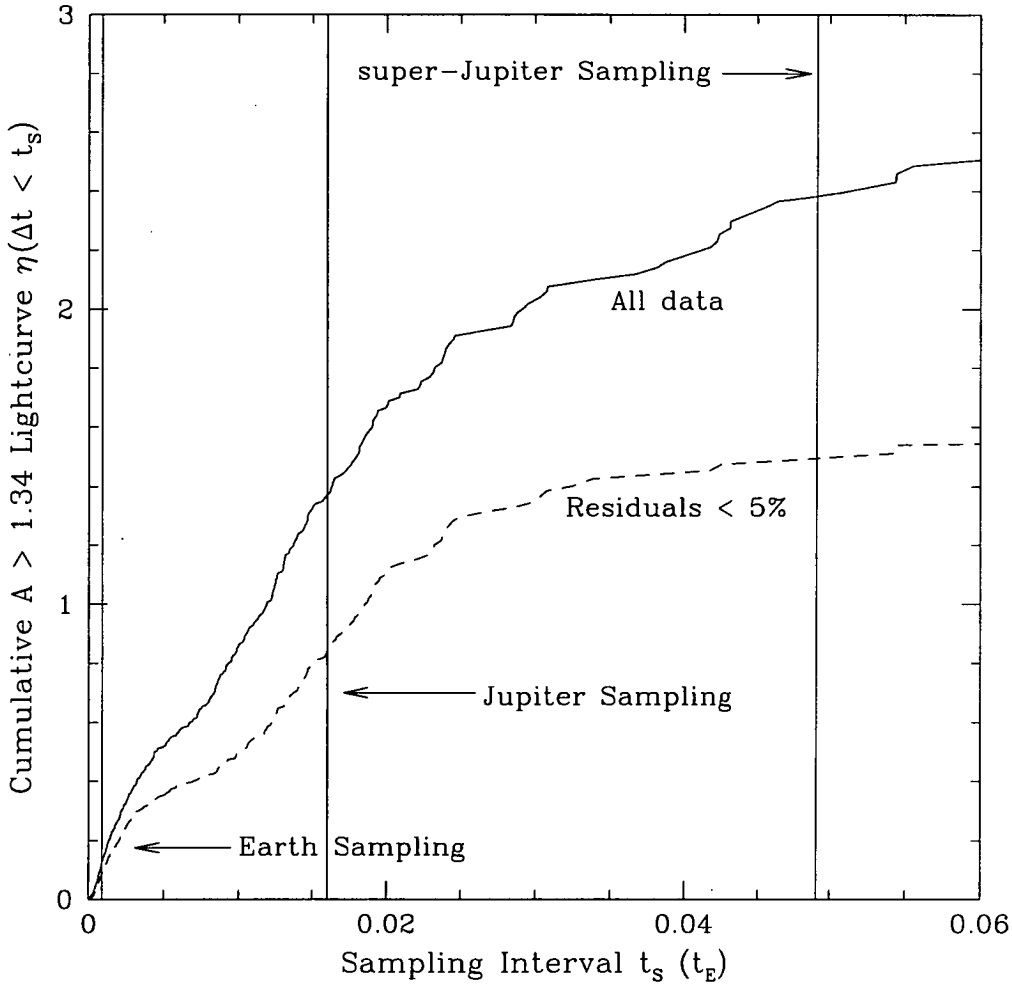

Figure 5.14: Estimate of the planet detection efficiency computed from the MACHO 1997 events 18, 26, 30, and 31. The cumulative normalized light curve length is shown as a function of the normalized sampling time. The solid curve includes all data and the dashed curve includes only those data sets for which the residuals are less than 5%. Also shown are the maximum sampling intervals required in order to be sensitive to planets of various mass ratios.

This results in event durations of $0.0035t_E$, $0.062t_E$, and $0.197t_E$ for Earth-mass, Jupiter-mass, and ten Jupiter-mass (super-Jupiter) planets respectively. In order to obtain 4 deviant points during the anomaly, the maximum sampling time should be $0.0009t_E$, $0.016t_E$, and $0.049t_E$ respectively. These sampling times are indicated by vertical lines in Figure 5.14.

Assuming that a deviation of 5% can be reliably detected, Figure 5.14 shows that a total normalized light curve length of $\eta \sim 1.5$ has been monitored frequently enough in order to detect super-Jupiters , $\eta \sim 0.8$ has been monitored frequently enough in order to detect Jupiters, and almost none of the normalized light curve length has been monitored frequently enough in order to detect Earth-mass planets. The detection sensitivity estimate of 17% by Gould & Loeb [42] means that a total normalized light curve length of $\eta \sim 6$ must be monitored for a single detection of a Jupiter-mass planet. This means that the monitoring of the 4 events included in this rough estimate is insufficient by about a factor of 7.5 for detecting a Jupiter-mass planet.

This approximate calculation of the detection efficiency is only meant as a guide for showing the capabilities of a microlensing search for planets. A comparison of Figure 5.14 with the similar figure shown in the paper describing the 1995 pilot campaign of PLANET [7] shows that the detection sensitivity of the PLANET monitoring has increased dramatically, considering that this sample only includes four of the events monitored during the 1997 bulge season. Inclusion of the remainder of the 1997 events, particularly events MB97028 and MB97041, will greatly improve this estimate and be useful in placing constraints on the frequency of extrasolar planets.

A limitation of this calculation is that it is just based on the total length of light curve inside the Einstein ring radius sampled at a given rate relative to t_E, and does not take into account the impact parameter dependence. A small impact parameter implies that the source is closer to the central caustic and thus the event is more sensitive. Hence, it is expected that this approximation underestimates the detection efficiency, especially for the MB97026 light curve. The method developed by Gaudi & Sackett [39] is currently being used to determine the detection efficiency of the entire PLANET data set. Early results, which includes a subset of the 1998 and 1999 events observed by PLANET, show that the non-detection of Jupiter-mass planets in the PLANET data indicates that Jupiter-mass planets with separations of 1.5–3.0 AU occur in less than one third of systems.

Chapter 6

Extinction in Spectroscopy

This chapter explores the effects of interstellar extinction on the microlensing optical depth and the spectra of microlensed sources. The contribution of bulge stars to the observed microlensing optical depth towards the Galactic bulge was estimated to be approximately 60%, the other 40% being due to the stars in the Galactic disk [54]. The optical depth to gravitational microlensing, as estimated from the observed microlensing events by OGLE [105] and MACHO [14], is significantly larger than the values predicted by theoretical models [75]. It has been argued [77] that the observed optical depth can be best explained if the effect of the Galactic bar and its inclination are correctly taken into account. A consequence of the fact that a large fraction of the events are due to bulge-bulge lensing is, as it shall be shown later, that the lensed stars will preferentially be located on the far side of the bulge in order that there be sufficient stars along the line of sight to cause microlensing. It was suggested by Stanek [95] that this would mean that there should be a systematic offset in the apparent magnitude between observed stars and lensed stars. This chapter presents a similar discussion by examining the model spectra of different spectral classes and investigating the effects of extinction on stars located on the far side of the bulge.

The first section adopts various models of the Galactic bulge to calculate the contributions of the different layers in the bulge to the microlensing optical depth, as has previously been calculated by Kiraga & Paczyński [54]. This method, however, takes the effect of extinction into account. The second section proceeds with a discussion on how the spectra of the microlensed sources can be used as a measure of the extinction which, in turn, can be used as a statistical measure of the contribution of the disk lenses and bulge lenses at different depths. It is shown that the spectra of the microlensed sources can be a useful probe for the 3-dimensional structure of the Galactic bulge.

6.1 Calculating the Probability of Microlensing

The aim here is to calculate the microlensing probability for sources at various depths within the Galactic bulge and to see how the microlensing optical depth varies for sources at various depths taking the effect of extinction into account. For these calculations, the formalism used by Sahu [84, 85] shall be adopted.

6.1.1 Constant Density Between Observer and Source

Firstly, the number of sources observed at various depths shall be estimated. One of the effects of extinction is the reduction of the observed number of stars at larger depths in the Galactic bulge. Extinction and the distance modulus increase as one goes deeper into the bulge, and both these effects make the sources fainter. So, in a magnitude limited survey (such as the current ones), the observed stellar density decreases as we go from the nearest to the farthest region in a line of sight. Let the ratio of observed stellar number density in the nearest and the farthest region in a given line of sight due to this effect be x.

Let N_{tot} be the number of stars being monitored in a region. For the analysis presented here, it will be assumed that *all* the sources are located within the Galactic bulge. Assuming the extinction to be uniform in depth, the number of observed stars at any layer dz, at a depth of z (as measured from the observer), may be expressed as

$$N_{obs}(z) = N_z x^{-z/d} \tag{6.1}$$

where N_z is the observed number of stars per unit depth in the absence of extinction and d is the physical depth of the region being monitored. Integrating this expression yields

$$N_{tot} = \int_0^d N_z x^{-z/d}\, dz = N_z d \left(\frac{1 - 1/x}{\ln x} \right) \tag{6.2}$$

Substituting Equation 6.2 into Equation 6.1 gives the following

$$N_{obs}(z) = \frac{N_{tot}}{d} \left(\frac{\ln x}{1 - 1/x} \right) x^{-z/d} \tag{6.3}$$

The fraction of area covered by the Einstein rings of all the individual stars lying in front of a source at distance D_s may be expressed as

$$A_f(D_s) = \int_0^{D_s} \pi R_E^2(D_d) n(D_d)\, dD_d \tag{6.4}$$

where D_d is the distance to the lens and $n(D_d)$ is the stellar number density at distance D_d. If we define $\rho(D_d)$ as the average mass density at depth D_d then we

see that $n(D_d) = \rho(D_d)/M$. Since the Einstein ring radius for a lens of mass M in this case is given by

$$R_E = \sqrt{\frac{4GM}{c^2}\frac{D_d(D_s - D_d)}{D_s}} \tag{6.5}$$

Equation 6.4 can be rewritten as

$$A_f(D_s) = \frac{4\pi G}{c^2}\int_0^{D_s} \rho(D_d)\frac{D_d(D_s - D_d)}{D_s}\, dD_d \tag{6.6}$$

If we assume a constant density of matter between the observer and the source and make the substitution $y = D_d/D_s$ then Equation 6.6 becomes

$$\begin{aligned} A_f(D_s) &= \frac{4\pi G D_s^2}{c^2}\int_0^1 \rho(D_d) y(1-y)\, dy \\ &= \frac{2\pi G \rho D_s^2}{3c^2} \end{aligned} \tag{6.7}$$

The instantaneous probability that an observed star at a given distance D_s is microlensed, can be written as

$$p = \frac{A_f(D_s) N_{obs}(D_s)}{N_{tot}} \tag{6.8}$$

Substituting Equation 6.7 and Equation 6.3 into Equation 6.8 yields

$$p = \frac{2\pi G \rho D_s^2}{3c^2 d}\left(\frac{\ln x}{1 - 1/x}\right) x^{-D_s/d} \tag{6.9}$$

This probability p is plotted in Figure 6.1 as a function of D_s assuming a density of $\rho = 0.20\, M_\odot \mathrm{pc}^{-3}$.

As seen in Figure 6.1, in the case of zero extinction the fractional area covered by the Einstein rings of the lenses increases dramatically with distance. However, the number of observed stars decreases with distance if there is internal extinction. As seen in Equation 6.8, the probability is a multiplication of these two functions which, as demonstrated in Figure 6.1, is dominated by the first effect for a reasonable value of extinction. Table 6.1 shows the difference in probability of microlensing for stars located at a distance of $D_s = 7.0\,\mathrm{kpc}$ and stars located at a distance of $D_s = 9.0\,\mathrm{kpc}$.

The total microlensing optical depth τ can now be calculated. If N_{tot} stars within the bulge are being monitored, then the instantaneous probability of observing a lensing event with an amplification of $A > 1.34$ is given by

$$P = \int_0^d N_{obs}(D_s) A_f(D_s)\, dD_s \tag{6.10}$$

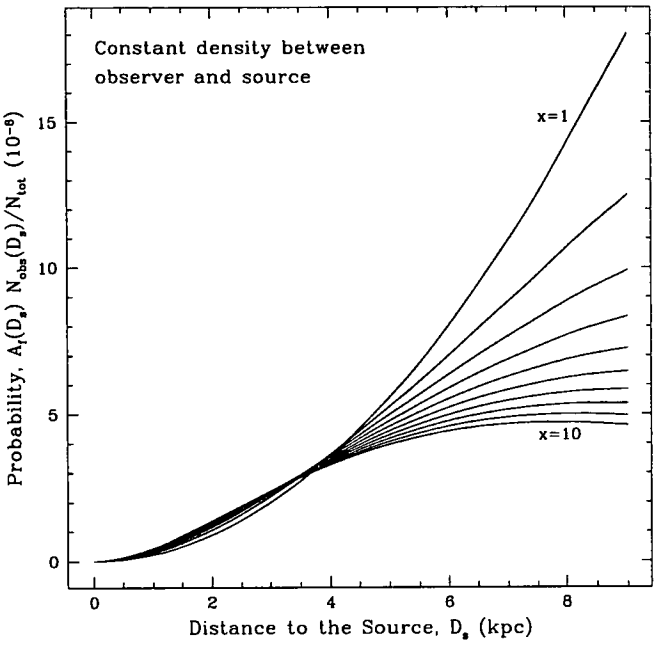

Figure 6.1: Probability as a function of distance to the source for increasing levels of extinction from $x = 1$ (zero extinction) to $x = 10$.

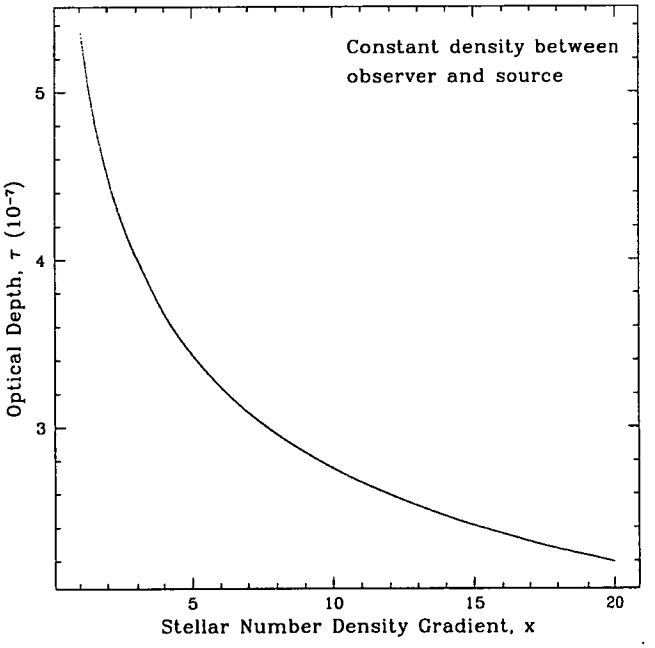

Figure 6.2: Optical depth as a function of the stellar number density gradient.

x	$A_f(7)N_{obs}(7)/N_{tot}(10^{-8})$	$A_f(9)N_{obs}(9)/N_{tot}(10^{-8})$
1.0	10.92	18.04
2.0	8.83	12.51
3.0	7.66	9.91
4.0	6.87	8.34
5.0	6.28	7.26
6.0	5.83	6.47
7.0	5.46	5.85

Table 6.1: Variation of instantaneous probability of microlensing with extinction x for a constant density between the observer and the source.

Substituting Equation 6.3 and Equation 6.7 into Equation 6.10 gives

$$P = \frac{2\pi G\rho}{3c^2}\frac{N_{tot}}{d}\left(\frac{\ln x}{1-1/x}\right)\int_0^d x^{-D_s/d}D_s^2\,dD_s \tag{6.11}$$

where the integrand can be solved analytically via repeated integration by parts (see Appendix E.1). Dividing the result by N_{tot} yields an expression for the optical depth for gravitational microlensing

$$\tau = \frac{2\pi G\rho d^2}{3c^2}\frac{x}{x-1}\left(\frac{2}{(\ln x)^2} - \frac{1}{x} - \frac{2}{x\ln x} - \frac{2}{x(\ln x)^2}\right) \tag{6.12}$$

The value of τ as given in Equation 6.12 is plotted in Figure 6.2 as a function of x, which shows the variation of optical depth with increasing extinction.

6.1.2 Constant Density for Disk and Bulge

If a constant density of matter for the disk ρ_d and for the bulge ρ_b is assumed (see Figure 6.3), Equation 6.6 becomes

$$A_f(D_s) = \frac{4\pi G}{c^2}\left(\int_0^b \rho_d\frac{D_d(D_s-D_d)}{D_s}\,dD_d + \int_b^{D_s}\rho_b\frac{D_d(D_s-D_d)}{D_s}\,dD_d\right) \tag{6.13}$$

where b is the distance from the observer to the near side of the bulge. Note that this expression assumes that the sources are within the bulge, where $D_s > b$, otherwise Equation 6.6 must be used. Making the substitution $y = D_d/D_s$, Equation 6.13 simplifies to

$$A_f(D_s) = \frac{4\pi G D_s^2}{c^2}\left(\rho_d\int_0^{b/D_s} y(1-y)\,dy + \rho_b\int_{b/D_s}^1 y(1-y)\,dy\right) \tag{6.14}$$

Solving this yields the following expression for the fractional area covered by the Einstein rings, which is the same as the probability that a given star at a distance

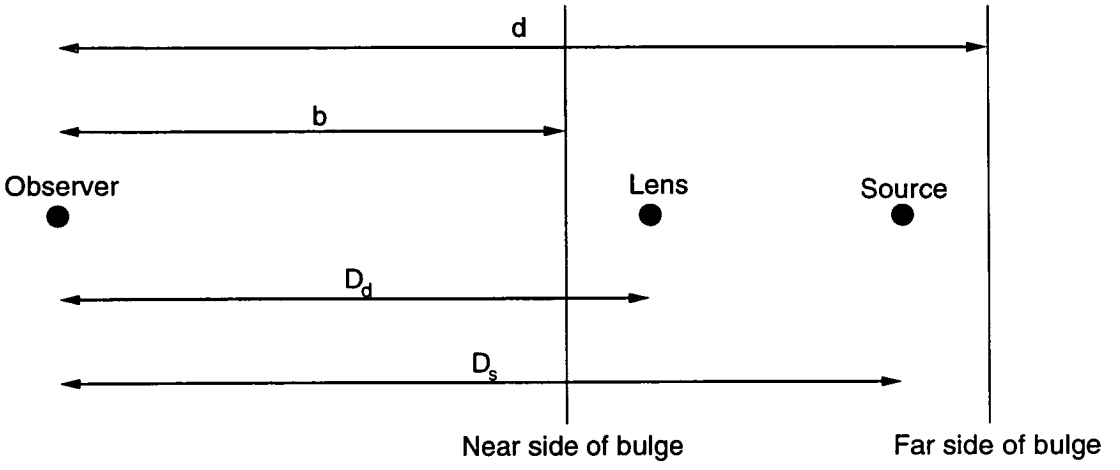

Figure 6.3: Galactic model using a constant density for the disk and a constant density for the bulge.

D_s is microlensed at any given time:

$$A_f(D_s) = \frac{4\pi G}{c^2}\left(\rho_d\left(\frac{b^2}{2} - \frac{b^3}{3D_s}\right) + \rho_b\left(\frac{D_s^2}{6} - \frac{b^2}{2} + \frac{b^3}{3D_s}\right)\right) \tag{6.15}$$

The first term is the contribution of the disk lenses and the second term is that of the bulge lenses.

Let $b = 7.0\,\mathrm{kpc}$, $d = 9.0\,\mathrm{kpc}$, $\rho_d = 0.07\,M_\odot\mathrm{pc}^{-3}$, and $\rho_b = 0.50\,M_\odot\mathrm{pc}^{-3}$. Substituting Equation 6.15 and Equation 6.3 into Equation 6.8 yields the instantaneous probability that an observed star at a given distance D_s is microlensed

$$p = \frac{4\pi G}{c^2 d}\left(\frac{\ln x}{1-1/x}\right)x^{-D_s/d}\left(\rho_d\left(\frac{b^2}{2} - \frac{b^3}{3D_s}\right) + \rho_b\left(\frac{D_s^2}{6} - \frac{b^2}{2} + \frac{b^3}{3D_s}\right)\right) \tag{6.16}$$

This probability p is plotted in Figure 6.4 as a function of D_s using the above parameters for the bulge.

Figure 6.4 shows that the probability is still dominated by the fractional area covered by the Einstein rings of the lenses for a reasonable value of extinction. Indeed the stars located at the far side of the bulge ($D_s = 9.0\,\mathrm{kpc}$) have a much larger probability of being microlensed than those located at the near side of the bulge ($D_s = 7.0\,\mathrm{kpc}$), as shown in Table 6.2.

For completeness, the total microlensing optical depth will now be calculated. Substituting Equation 6.3 and Equation 6.15 into Equation 6.10 and dividing by N_{tot} yields an expression for the optical depth for gravitational microlensing

$$\tau = \frac{4\pi G}{c^2 d}\left(\frac{\ln x}{1-1/x}\right)\int_b^d\left((\rho_b - \rho_d)x^{-D_s/d}\left(\frac{b^3}{3D_s} - \frac{b^2}{2}\right) + \frac{\rho_b}{6}x^{-D_s/d}D_s^2\right)dD_s \tag{6.17}$$

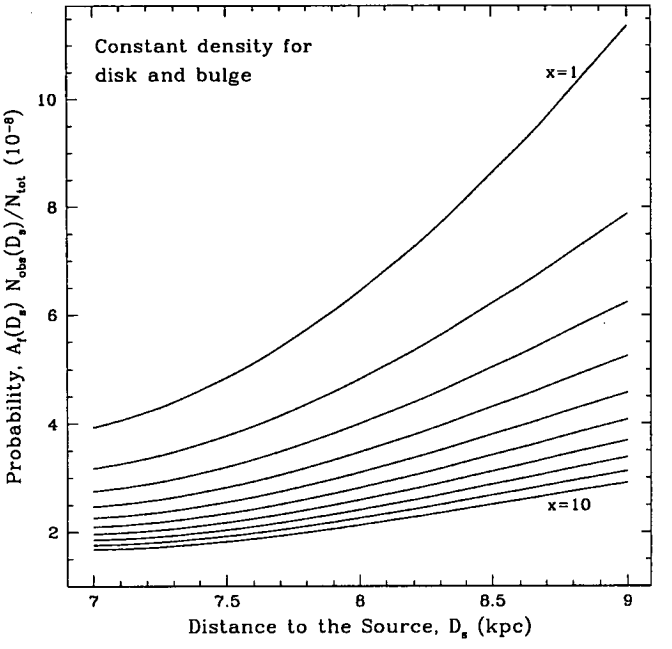

Figure 6.4: Probability as a function of distance to the source for increasing levels of extinction from $x = 1$ (zero extinction) to $x = 10$.

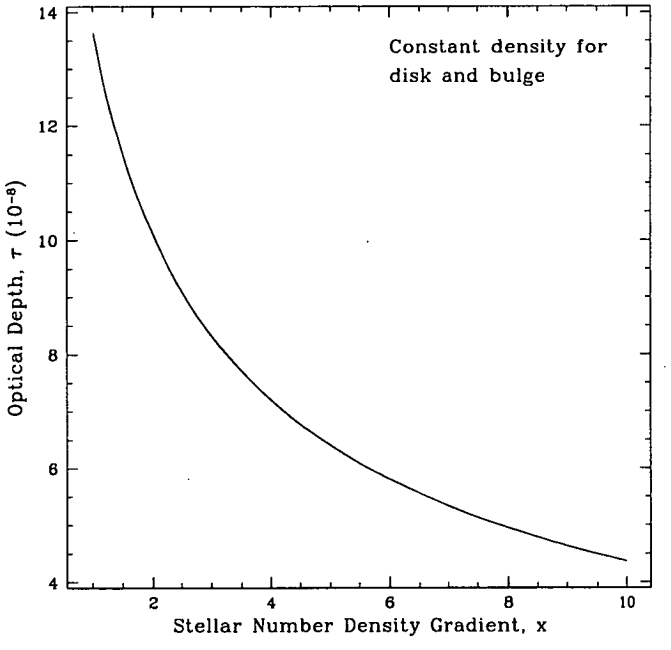

Figure 6.5: Optical depth as a function of the stellar number density gradient.

x	$A_f(7)N_{obs}(7)/N_{tot}(10^{-8})$	$A_f(9)N_{obs}(9)/N_{tot}(10^{-8})$
1.0	3.93	11.37
2.0	3.18	7.88
3.0	2.76	6.25
4.0	2.47	5.25
5.0	2.26	4.58
6.0	2.10	4.08
7.0	1.96	3.69

Table 6.2: Variation of instantaneous probability of microlensing with extinction x for a constant density for the disk and bulge.

The value of τ as given in Equation 6.17 is plotted in Figure 6.5 as a function of x, which shows the variation of optical depth with increasing extinction. For $x = 3.0$ the optical depth is $\approx 8.33 \times 10^{-8}$ and for $x = 7.0$ the optical depth is $\approx 5.34 \times 10^{-8}$. These values are significantly lower than an optical depth of $\approx 8.5 \times 10^{-7}$ estimated by Kiraga & Paczyński [54] using a similar Galactic model but without taking extinction into account. However, this calculation is dependent upon the choice of ρ_d and ρ_b which, given the nature of the model, will be crude estimates at best.

6.1.3 Exponential Density Model for Bulge

An even better approximation of the distribution of matter between the observer and the source is to use an exponential-type function to represent the density profile over the Galactic bulge. The model used to do this is a simplified version of the E2 triaxial Galactic bulge model fitted by Dwek *et al* [35] with an exponential cutoff at 2.4 kpc. This model is defined as

$$\rho_{E2}(i,j,k) = \rho_0 \exp(-r) \tag{6.18}$$

where

$$r = \left[\left(\frac{i}{i_0}\right)^2 + \left(\frac{j}{j_0}\right)^2 + \left(\frac{k}{k_0}\right)^2\right]^{1/2} \tag{6.19}$$

is the distance from the Galactic centre. Treating this from a purely radial perspective and centering the coordinate system on the observer results in the density profile given by

$$\rho(D_d) = \rho_0 \exp\left[-\frac{|R_0 - D_d|}{i_0}\right] \tag{6.20}$$

where the normalisation constant is given by

$$\rho_0 = \frac{M}{8\pi i_0 j_0 k_0} \tag{6.21}$$

The value of ρ_0 shall be calculated by adopting the total bulge mass estimated by Dwek *et al* [35] of $M = 1.3 \times 10^{10}\, M_\odot$ and using the scale lengths of $i_0 = 0.71$, $j_0 = 0.18$, and $k_0 = 0.25\,\mathrm{kpc}$ for a Galactocentric distance of $R_0 = 8.0\,\mathrm{kpc}$.

Using this model, Equation 6.6 becomes

$$A_f(D_s) = \frac{4\pi G\rho_0}{c^2} \int_0^{D_s} \exp\left[-\frac{|R_0 - D_d|}{i_0}\right] \frac{D_d(D_s - D_d)}{D_s}\, dD_d \tag{6.22}$$

Solving this equation (see Appendix E.2) yields the following expression for the fractional area covered by the Einstein rings:

$$A_f(D_s) = \begin{cases} \frac{4\pi G\rho_0}{c^2} \frac{i_0^2 e^{-R_0/i_0}\alpha}{D_s} & \text{for } D_s < R_0 \\ \frac{4\pi G\rho_0}{c^2} \frac{i_0(2i_0^2\beta - 2R_0^2 + D_s\gamma)}{D_s} & \text{for } D_s > R_0 \end{cases} \tag{6.23}$$

where

$$\begin{aligned} \alpha &= D_s(1 + e^{D_s/i_0}) + 2i_0(1 - e^{D_s/i_0}) \\ \beta &= e^{-(D_s - R_0)/i_0} + e^{-R_0/i_0} - 2 \\ \gamma &= i_0 e^{-(D_s - R_0)/i_0} + i_0 e^{-R_0/i_0} + 2R_0 \end{aligned}$$

Substituting Equation 6.23 and Equation 6.3 into Equation 6.8 yields the instantaneous probability that an observed star at a given distance D_s is microlensed

$$p = \begin{cases} \frac{4\pi G\rho_0}{c^2 d} \left(\frac{\ln x}{1 - 1/x}\right) x^{-D_s/d} \left(\frac{i_0^2 e^{-R_0/i_0}\alpha}{D_s}\right) & \text{for } D_s < R_0 \\ \frac{4\pi G\rho_0}{c^2 d} \left(\frac{\ln x}{1 - 1/x}\right) x^{-D_s/d} \left(\frac{i_0(2i_0^2\beta - 2R_0^2 + D_s\gamma)}{D_s}\right) & \text{for } D_s > R_0 \end{cases} \tag{6.24}$$

This probability p is plotted in Figure 6.6 as a function of D_s using the above model.

Figure 6.6 shows that an exponential density model dramatically increases the domination of the fractional area in the probability of microlensing. for stars located at the far side of the bulge ($D_s = 9.0\,\mathrm{kpc}$) the probability of being microlensed is much larger than those located at the near side of the bulge ($D_s = 7.0\,\mathrm{kpc}$), as shown in Table 6.3.

The total microlensing optical depth can now be calculated. Substituting Equation 6.3 and Equation 6.23 into Equation 6.10 and dividing by N_{tot} yields an expression for the optical depth for gravitational microlensing

$$\tau = \begin{cases} \frac{4\pi G\rho_0}{c^2 d} \left(\frac{\ln x}{1 - 1/x}\right) i_0^2 e^{-R_0/i_0} \int_0^d \frac{\alpha}{D_s} & \text{for } D_s < R_0 \\ \frac{4\pi G\rho_0}{c^2 d} \left(\frac{\ln x}{1 - 1/x}\right) i_0 \int_0^d \frac{2i_0^2\beta - 2R_0^2 + D_s\gamma}{D_s} & \text{for } D_s > R_0 \end{cases} \tag{6.25}$$

The value of τ as given in Equation 6.25 is plotted in Figure 6.7 as a function of x, which shows the variation of optical depth with increasing extinction. For

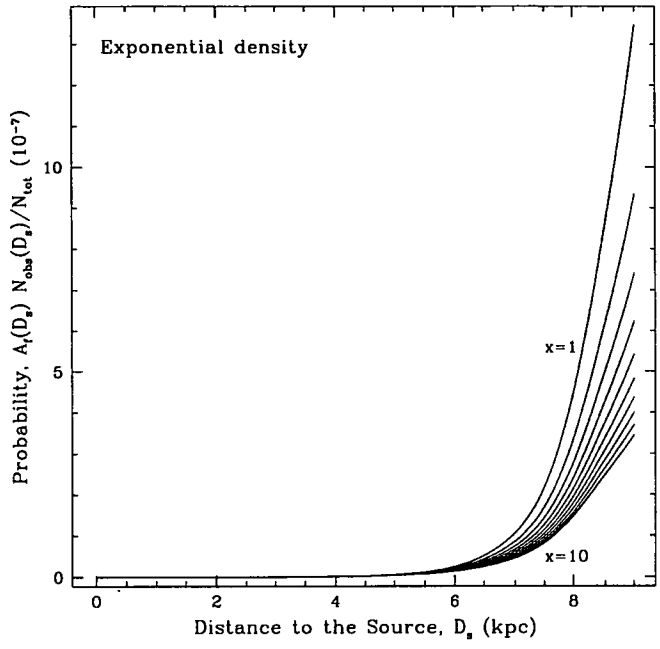

Figure 6.6: Probability as a function of distance to the source for increasing levels of extinction from $x = 1$ (zero extinction) to $x = 10$.

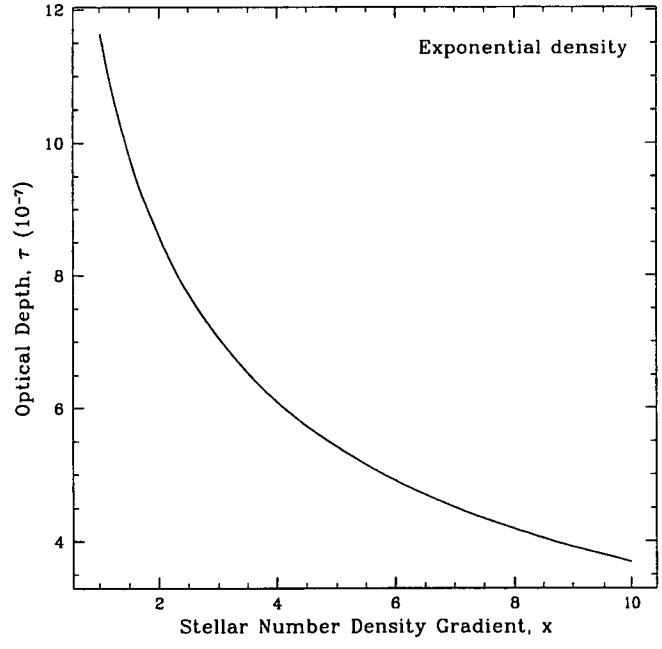

Figure 6.7: Optical depth as a function of the stellar number density gradient.

x	$A_f(7)N_{obs}(7)/N_{tot}(10^{-7})$	$A_f(9)N_{obs}(9)/N_{tot}(10^{-7})$
1.0	1.06	13.48
2.0	0.86	9.34
3.0	0.75	7.41
4.0	0.67	6.23
5.0	0.61	5.43
6.0	0.57	4.83
7.0	0.53	4.37

Table 6.3: Variation of instantaneous probability of microlensing with extinction x for an exponential density model.

$x = 3.0$ the optical depth is $\approx 7.06 \times 10^{-7}$ and for $x = 7.0$ the optical depth is $\approx 4.51 \times 10^{-7}$. These values are only slightly lower than an optical depth of $\approx 8.5 \times 10^{-7}$ estimated by Kiraga & Paczyński [54]. This is the result one would expect when extinction is added to the optical depth calculations. However, since the theoretical calculations of the optical depth already fall below those measured by the MACHO and OGLE collaborations, this means that more emphasis must be placed on factors which raise the optical depth, such as the inclination of the bar.

The limiting apparent magnitude of the current surveys is about $m_V = 20$ which at the near side of the bulge would correspond to an absolute magnitude of $M_V = 5.8$ and an absolute magnitude of $M_V = 5.3$ at the far side of the bulge were there no extinction. However, the estimated foreground extinction within 7 kpc is about 2.1 magnitudes (taking 0.3 magnitudes/kpc [18]). The additional extinction within Baade's window has been estimated by Stanek [96] to lie in the range of 1.26 to 2.79 magnitudes, depending on the line of sight. Hence, the limiting magnitude of the stars at the near side of the bulge is about $M_V = (5.8 - 2.1) = 3.7$ and the limiting magnitude of the stars at the far side about is 1.3–2.8 magnitudes brighter (including the 0.5 magnitudes because of the larger distance). If the distribution of stars amongst different spectral types is assumed to be similar to what is observed in the solar neighbourhood [55, 113] then the stellar number density is relatively flat in this region. This distribution shows that the ratio in the observed stellar number density from the near to far side of the bulge is between 3.8 to 6.3.

For $x = 4.0$ the fractional area at the far side of the bulge is ≈ 9.3 times that at the near side of the bulge. For $x = 6.0$ the fractional area at the far side of the bulge is ≈ 8.5 times that at the near side of the bulge. This means that, on average, stars that are lensed in Baade's window are almost ten times more likely to be at the far side of the bulge than the near side.

If lensed stars are indeed predominantly on the far side of the bulge then this provides us with a useful tool for studying the Galactic structure at the far side

of the bulge. Radial velocity measurements from spectra of microlensed sources combined with the measured time scale of the events may be used as a unique probe into the 3-dimensional kinematics of the far side of the bulge.

6.1.4 Blending Effects

We have so far ignored the effect of blending. However, as the recent HST images towards the LMC and the Galactic bulge show, blending can be an important effect. In the case of the microlensing events towards the LMC, each 'microlensed star' typically splits into 2 or more sources in the high spatial-resolution HST image [17]. Towards the Galactic bulge, however, for which the distance is about 7 times smaller than the LMC, blending is less severe.

The effect of blending is discussed in detail by Di Stefano & Esin [28], including the effects of blending when inferring properties of underlying populations through the statistical study of lensing events [33, 117]. The effect of blending can be summarized as follows: (i) Blending makes it more difficult to observe a microlensing event since the observed amplification is smaller than the actual amplification. This decreases the efficiency of the detection of a microlensing event. (ii) Blending enables some stars which are otherwise invisible in the sample to be included in the sample of the monitored events. This increases the efficiency of detection. (iii) The effect of blending is to increase the number of monitored stars, thus increasing the net efficiency of detection.

The first effect tends to offset the latter two. The net effect depends on the brightness of the source/lens, and the crowding of the field. So far as our analysis of extinction is concerned, since the blending star is expected to be preferentially closer than the microlensed source, blending dilutes the effect of extinction. As Di Stefano & Esin point out, the effect of blending is more important for fainter sources. A full analysis of blending is beyond the scope of this work. However, but our preliminary estimate suggests that, if the microlensed star is brighter than $m_v \sim 18$, the contribution of the blended star is about 10%. This contribution increases to more than 50% for stars with $m_V \sim 20$. Thus, if the analysis is confined to brighter sources (as is the case for the sources presented in Chapter 8), the effect of blending is expected to be small, and is ignored in our subsequent analysis.

6.2 Effects of Extinction on Spectra

It has been shown that a predominant fraction of microlensed sources are located on the far side of the Galactic bulge. If this is true then it can be shown experimentally by observing the extinction effects in the spectra of the lensed stars.

To simulate the effects of extinction on various spectral types, the spectral

models used were those from the Kurucz database (Dr. R. Kurucz, CD-ROM No. 13 [57]). Each of the Kurucz models used have been normalized for a solar metallicity and a distance of $D_s = 9.0\,\mathrm{kpc}$. Each of the model spectra are recalculated for E_{B-V} values of 0.0, 0.2, 0.4, 0.6, 0.8 where the extinction corrected spectrum, s_c, is calculated from the raw spectrum, s_r, via

$$(s_c)_\lambda = (s_r)_\lambda \times 10^{-(E_{B-V} \times e_g)/2.5} \tag{6.26}$$

where

$$e_g = \frac{A_\lambda}{E_{B-V}} \tag{6.27}$$

The data for the Galactic extinction, e_g, was taken from Seaton [93].

Spectral Type	T_{eff}	log g	m_V
M0III	3800	+1.34	14.4
G0V	6030	+4.39	19.2
F0V	7200	+4.34	17.4
B5III	15000	+3.49	12.4

Table 6.4: Characteristics of example spectral types

Table 6.4 shows the stellar parameters used for the model spectra, where T_{eff} is the effective temperature, $\log g$ is the log gravity, and m_V is the apparent magnitude of the star. Then varying E_{B-V} from 0.4 to 0.8 is fairly representative of the levels of extinction that exist within Baade's window, suggested by Stanek [96] to be in the range of 1.26 to 2.79 magnitudes.

Figures 6.8, 6.9, 6.10, and 6.11 show the effect of extinction on observed spectra of various types of stars given in Table 6.4. There is a significant change in spectral features, such as slope and line strength, from an E_{B-V} value of 0.0 to 0.8. The slope and the features can be used to quantitatively estimate the extinction of the microlensed stars in comparison to the general sample in the Galactic bulge. It is apparent from the model spectra that, although blue stars in the main sequence will always be brighter than red main-sequence stars at all wavelengths, the effects of extinction will cause the stellar population at the far side of the bulge to discriminate against blue stars as source stars in microlensing.

From our previous arguments, we expect a majority of the microlensed sources to show an extinction value between $E_{B-V} = 0.4$ and $E_{B-V} = 0.8$. Clearly, a collection of microlensed source spectra bearing this characteristic would become statistically significant when estimating the contribution of bulge-bulge lensing to the microlensing optical depth. If this is shown to statistically be the case then this simple method can be used as a statistical distance indicator for microlensed sources.

A knowledge of the distance to the source enables the distance to the lens to be estimated. To demonstrate this, the Galactic bulge model outlined in Section

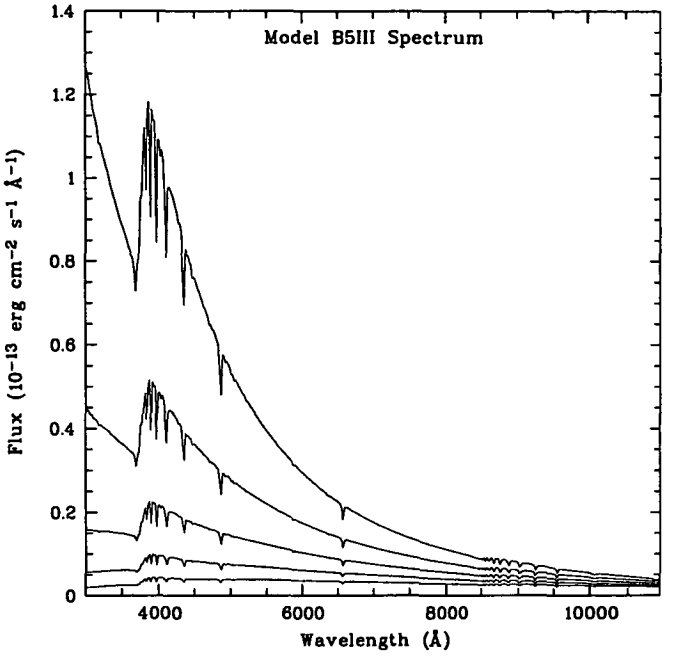

Figure 6.8: Model spectra of a spectral type B5III star showing the effect of increasing levels of extinction from E_{B-V} of 0.0 to 0.8 in steps of 0.2.

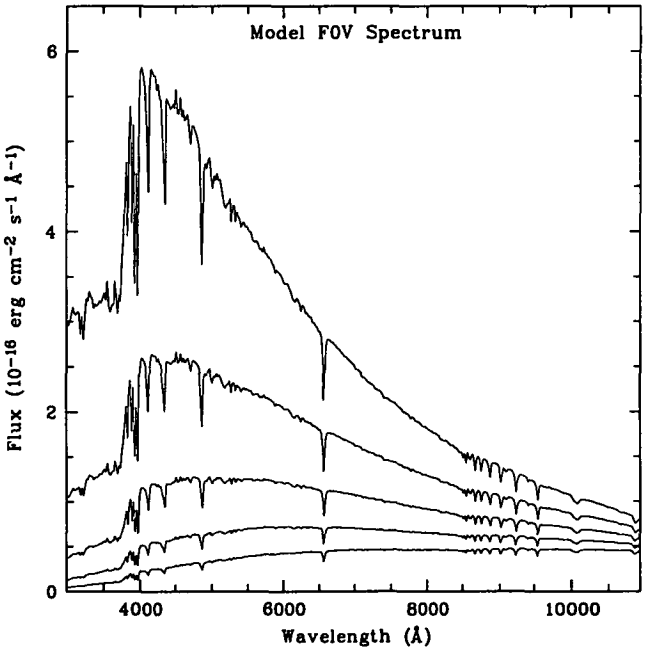

Figure 6.9: Model spectra of a spectral type F0V star showing the effect of increasing levels of extinction from E_{B-V} of 0.0 to 0.8 in steps of 0.2.

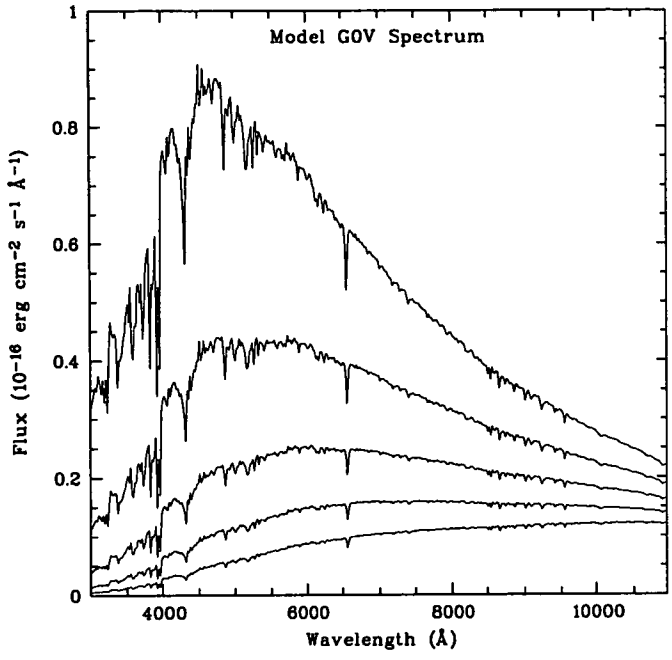

Figure 6.10: Model spectra of a spectral type G0V star showing the effect of increasing levels of extinction from E_{B-V} of 0.0 to 0.8 in steps of 0.2.

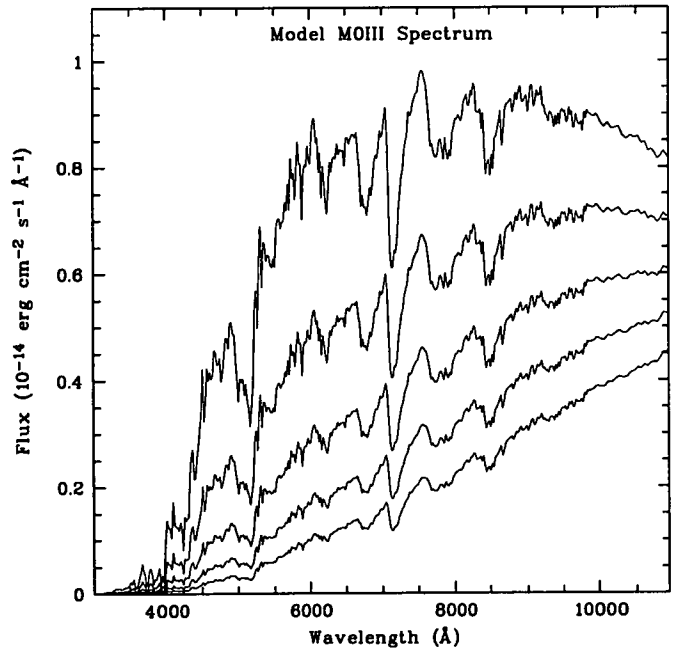

Figure 6.11: Model spectra of a spectral type M0III star showing the effect of increasing levels of extinction from E_{B-V} of 0.0 to 0.8 in steps of 0.2.

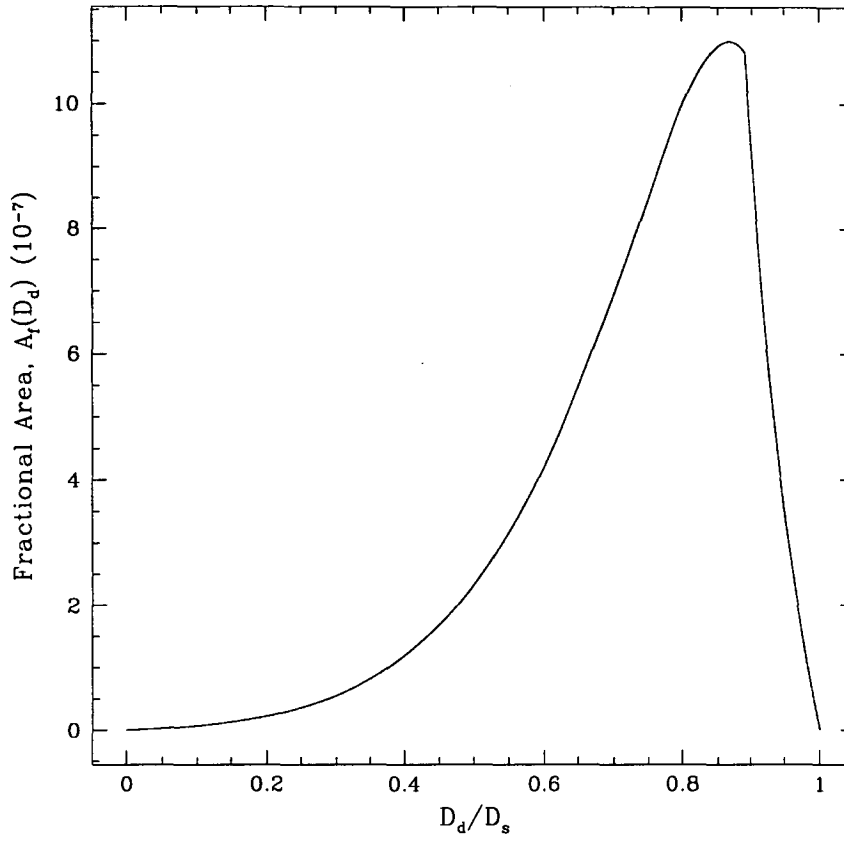

Figure 6.12: A probability distribution for lenses given a source located at a distance of $D_s = 9.0\,\mathrm{kpc}$. In this case, it is most probable that the lens will be located at a distance of $D_d = 7.8\,\mathrm{kpc}$.

6.1.3 shall be used. For a source located at a distance D_s, the fractional area covered by the Einstein rings of the intervening stars at a distance D_d is

$$A_f(D_d) = \frac{4\pi G}{c^2}\rho_0 \exp\left[-\frac{|R_0 - D_d|}{i_0}\right]\frac{D_d(D_s - D_d)}{D_s} \tag{6.28}$$

As discussed earlier, the probability distribution of the distance to the source peaks at 9.0 kpc. The probability distribution of the location of the lenses (in units of the distance to the source) is shown in Figure 6.12, which shows that the probability peaks at a distance of $D_d = 0.85D_s$ which, for $D_s = 9.0\,\mathrm{kpc}$, corresponds to $D_d = 7.8\,\mathrm{kpc}$. It is worth noting that this does not imply that most of the lenses are at $D_d = 7.8\,\mathrm{kpc}$. This only implies that a lens distance of 0.85 D_s is twice more likely than a lens distance of 0.6 D_s.

Since the angular Einstein ring radius is known from the characteristic time scale of the event, the extinction exhibited in the spectra of microlensed sources

can be used as a means to estimate the size of the Einstein ring radius in terms of AU. Detectable deviations in microlensing light curves due to planetary masses depend highly upon the star-planet distance in the lensing system [21], making this method a useful technique to constrain calculations of planet detection efficiencies.

It is of interest to compare the extinction effects and the radial velocity measurements from the spectra of microlensed sources. There may be a statistical correlation between the radial velocity and the extinction of microlensed sources which, given enough samples, will provide useful information regarding the 3-dimensional velocity structure of the far side of the Galactic bulge. Given the variation in extinction through the Galactic bulge, the sample would require $\sim$ 100 spectra of microlensed sources in order to clearly show the described effects.

Chapter 7

Reduction of Spectral Data

This chapter describes the method used to reduce the spectral data acquired using the ESO 3.6 m telescope. The first section breifly outlines the design of the spectrometer used to obtain the spectroscopic data. The second section describes the initial steps in the data reduction in preparing the observed image for wavelength calibration. The third section describes the method used for wavelength calibration of the spectra and the fourth section details the flux calibration of the data. The final section describes how the final spectra of the microlensed stars and various other stars in the field were produced.

7.1 Observations at ESO

Observations were made using the European Southern Observatory (ESO) 3.6 m telescope located at La Silla, Chile at an altitude of 2400 m. The data were obtained by Dr. Kailash Sahu during two separate observing runs which utilized the ESO Faint Object Spectrograph and Camera (EFOSC). The first observing run took place during June 28 – July 1, 1995 and the second observing run took place during the night of June 14, 1996. The spectra of almost 20 different microlensed sources were obtained during these observing runs.

7.1.1 The Use of Grisms

From the nineteenth century well into the twentieth century, the dispersing element used in astronomical spectrographs was a prism. In most cases this has been replaced with a reflection grating due to the convenience of use, higher throughput, and higher resolution. Transmission gratings that are used in conjunction with a prism are known as a *grism*. The basic arrangement is a slit placed in the focal plane of the telescope, usually at the Cassegrain focus, so that the image is focused onto the slit and as much light as possible passes through. The diverging beam is made parallel by a collimating lens, directed onto a prism or grating, and

then brought via a camera to a focus again on a detector. It is the slit that is re-imaged onto the CCD by the camera, the slit projection factor being the ratio of the f/ratio of the collimator to the f/ratio of the camera.

Grism	Wavelength Range (Å)	Dispersion (Å/pixel)
B150	3780–5510	3.3
B300	3740–6950	6.3
O150	5220–6980	3.4
R300	5890–9920	7.9

Table 7.1: Grisms used and their characteristics.

Table 7.1 shows the grisms that were used for the observations. The resolution of the spectra will depend upon the chosen slit width. For a pixel size of 0.61″ and a 1.5″ slit, the true resolution will be approximately the dispersion as shown in Table 7.1 multiplied by a factor of 2.46 [88].

7.1.2 EFOSC

The optical system of EFOSC incorporates a collimator which produces a beam with a diameter of 40 mm. This beam passes through a grism mounted in the grism wheel and is focused onto the CCD. The CCD has an array of 512 × 512 pixels and a pixel scale of 0.61 arcsec/pixel. At the time of observations, the camera was set to have a gain of 3.8 electrons/count for which the read-out noise is 8.5 electrons/pixel.

As shown in Figure 7.1, approximately 80% of the energy in the range 3500–10000 Å from an on-axis star is transmitted. There is a sharp decrease in efficiency of transmission below 4000 Å due to transmission losses in the camera and collimator lenses.

There are a variety of slits available to the observer for EFOSC on two aperture wheels. These include 5 fixed long slits, one movable long slit, one echelle slit, and a single coronograph single spot. For these observations, a long slit of width 1.5″ was typically used to match the typical seeing during these observations.

7.2 Photometric Corrections

First, it is necessary to correct the observed images for the detector noise and flat field the images to correct for the detector response function. Bias frames were averaged in groups of 5 and then subtracted from the science images to take out the electronic bias. Exposure times for the spectra typically exceeded 20 minutes and so resulted in a large number of cosmic ray hits. These cosmic ray hits were removed by hand towards the end of the reduction procedure (see Section 7.5.3).

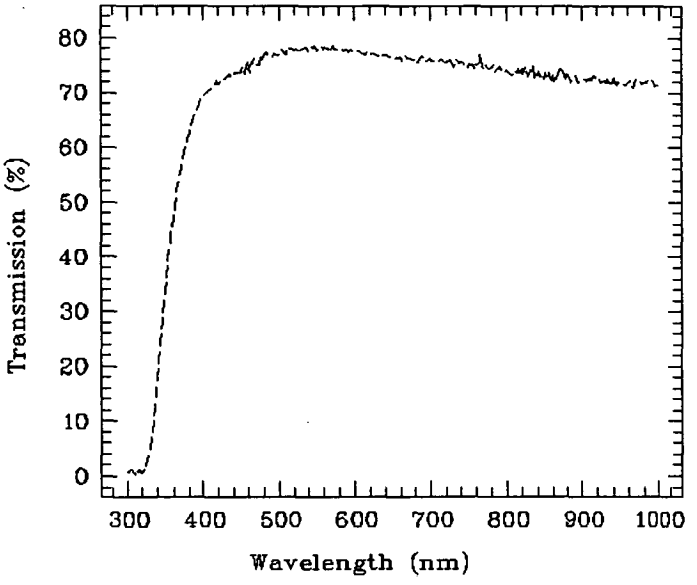

Figure 7.1: The optical transmission of EFOSC. [88]

Flat fields are used to correct for the pixel-to-pixel variations in response on the CCD as well as for a first order correction of the wavelength response of the CCD. In the case of spectroscopy, the wavelength response is taken into account by the flux calibrator which is used to calculate the instrumental response curve. In principle, this is all that is needed to correct for these variations in the rest of the spectral data. However, the response curve is calculated by integrating over spectral intervals of small but finite width. This means large spurious behaviour may be introduced in the case of strong gradients.

If the flat field is relatively smooth and the pixel-to-pixel response variation is small then it becomes unnecessary to apply the flat field to the spectroscopic data. Shown in Figure 7.2 is a plot of the normalized gradient in one of the flat fields from the observing run of June 14, 1995. This relatively smooth gradient was typical of the flat fields contained in the set of data and so the the flat fields were not applied.

7.3 Wavelength Calibration

The data reduction described in the following sections was performed using the long-slit reduction package contained in MIDAS. Further information on the capabilities and characteristics of this package may be found in Chapter 6 of the MIDAS User Guide, Volume B.

Wavelength calibration involves an accurate geometrical correction over the entire frame. The importance of an accurate wavelength calibration becomes

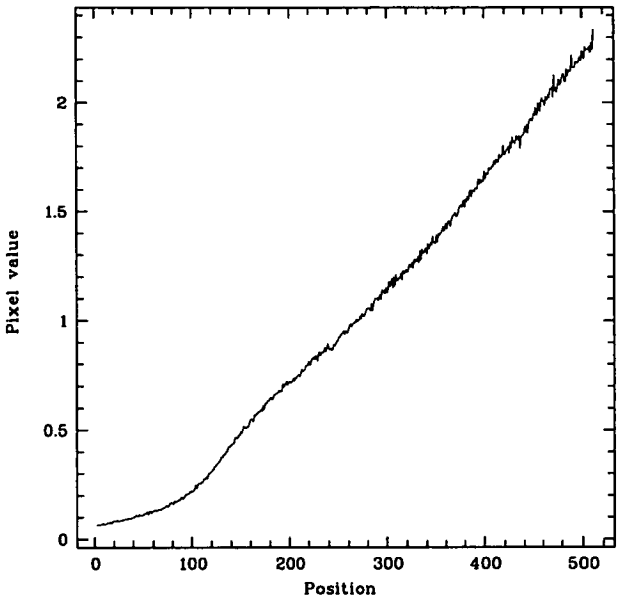

Figure 7.2: Normalized gradient of a typical flat field.

evident when one tries to make radial velocity measurements. The wavelength calibration is a transformation from the pixel coordinates (X, Y) to the sampling space (λ, θ), where λ is the wavelength and θ is the angular direction in the sky.

The wavelength calibration of these observations used helium and argon lamps (HEAR) to illuminate the slit, which have lines in the blue and red part of the spectrum respectively. These lamps tend to be rather faint and require a long exposure to obtain enough signal. Furthermore, the helium and argon lamps are two physically separate lamps in this particular spectrograph. The lines in the helium lamp are typically stronger by a factor of 100 compared to the argon lines. To take a HEAR lamp exposure, the helium lamp was switched on for 1 minute and the argon lamp was switched on for 15 minutes during the same exposure so that all the lines have similar intensity. If sufficient signal is achieved then an accuracy of about one tenth of the comparison lines can be obtained.

The first step in wavelength calibration is to detect and identify lines in the arc spectrum. The MIDAS command `SEARCH/LONG` detects reference lines whose strength exceeds a specified threshold. The positions of the reference lines are then estimated by fitting gaussians to the lines and the results are stored in a table. The command `IDENTIFY/LONG` allows the user to manually identify and specify the wavelength of major lines in the spectrum.

The second step is to obtain the dispersion solution of the arc spectrum. The command `CALIBRATE/LONG` performs this operation using the lines identified by the user and outputs the coefficients of the dispersion relation, the starting wavelength, the final wavelength, and the average step in wavelength. These

values can be saved in a table and recalled later to continue the session. The data can now be resampled to a constant step in wavelength using the command REBIN/LONG.

In order to visualize the results of the calibration process, the commands PLOT/CALIBRATE and PLOT/RESIDUAL are provided. PLOT/CALIBRATE plots the central row of the lines identified by CALIBRATE/LONG and adds the line identifications obtained. PLOT/RESIDUAL plots the residuals and is used to test the quality of the calibration.

7.3.1 B150

Presented here are the results of the B150 wavelength calibration.

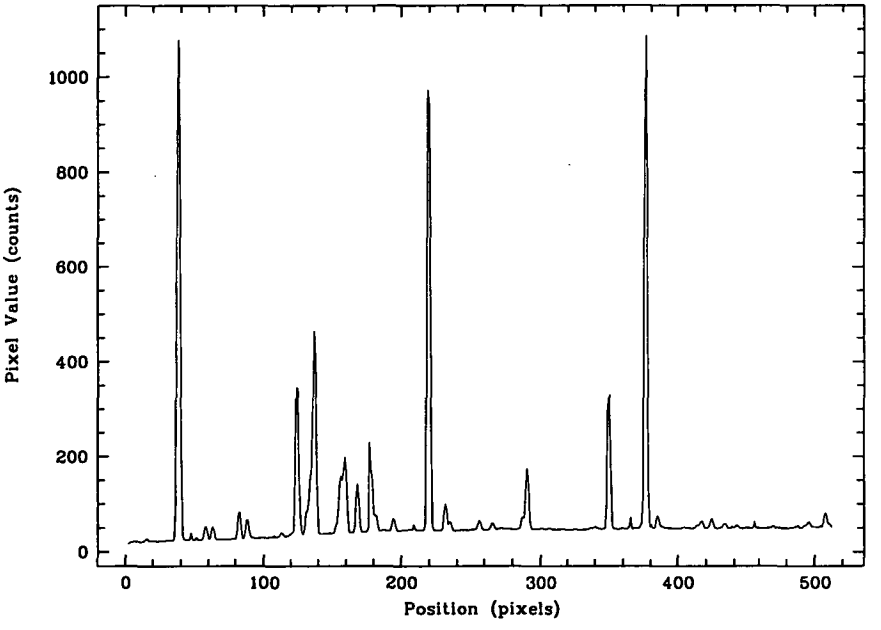

Figure 7.3: HEAR spectrum for the B150 grism.

Shown in Figure 7.3 is the spectrum obtained from the HEAR lamp using the B150 grism. The exposure time for this observation was about 30 minutes and the command SEARCH/LONG detected 3677 spectral features, considering the features in each row to be different. The results of fitting the dispersion solution is shown in Figure 7.4 along with the lines identified by IDENTIFY/LONG. In this figure the position in pixels is shown as a function of the pixel value in counts. The plot of the residuals in Figure 7.5 shows that the polynomial used gives a good fit to the dispersion relation with a rms deviation of about 0.18 pixels.

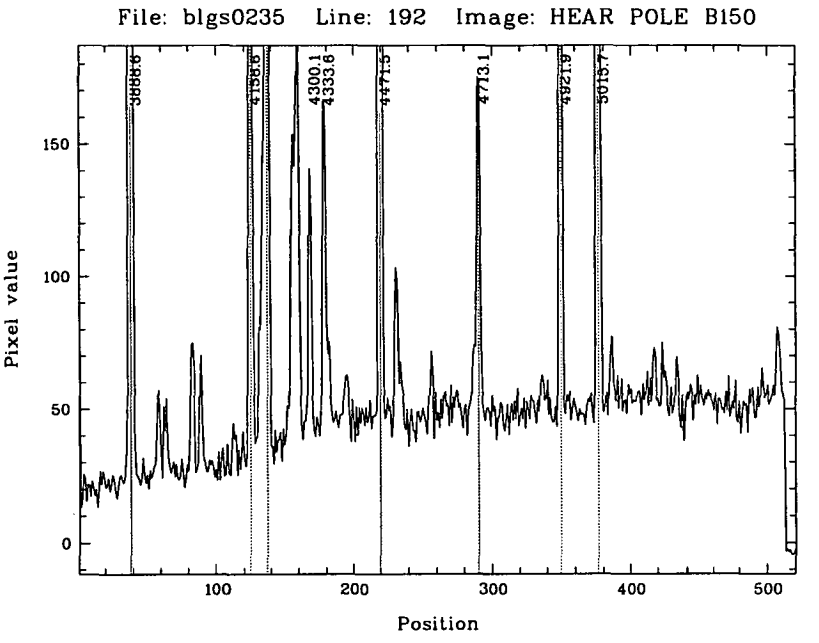

Figure 7.4: PLOT/CALIBRATE for B150.

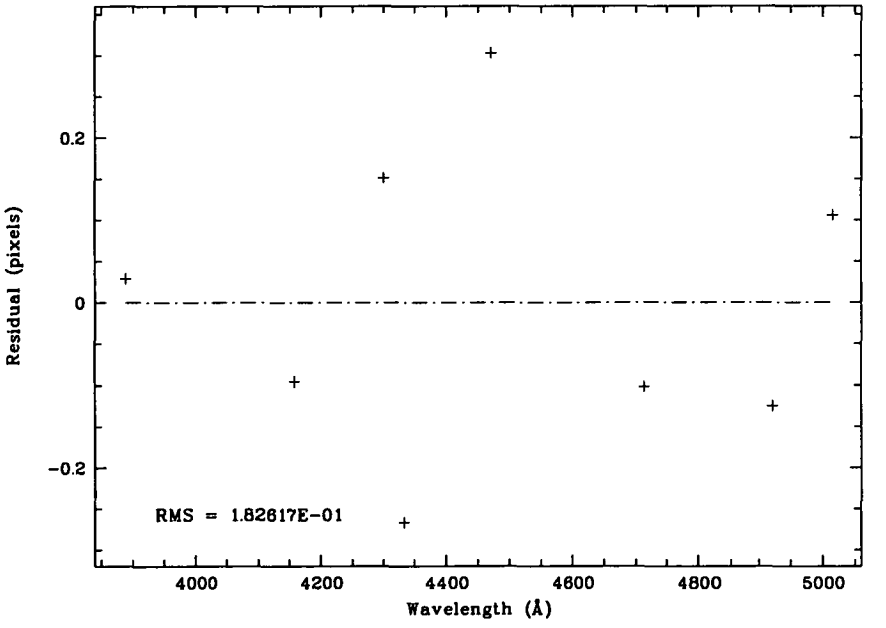

Figure 7.5: PLOT/RESIDUAL for B150.

7.3.2 B300

Presented here are the results of the B300 wavelength calibration.

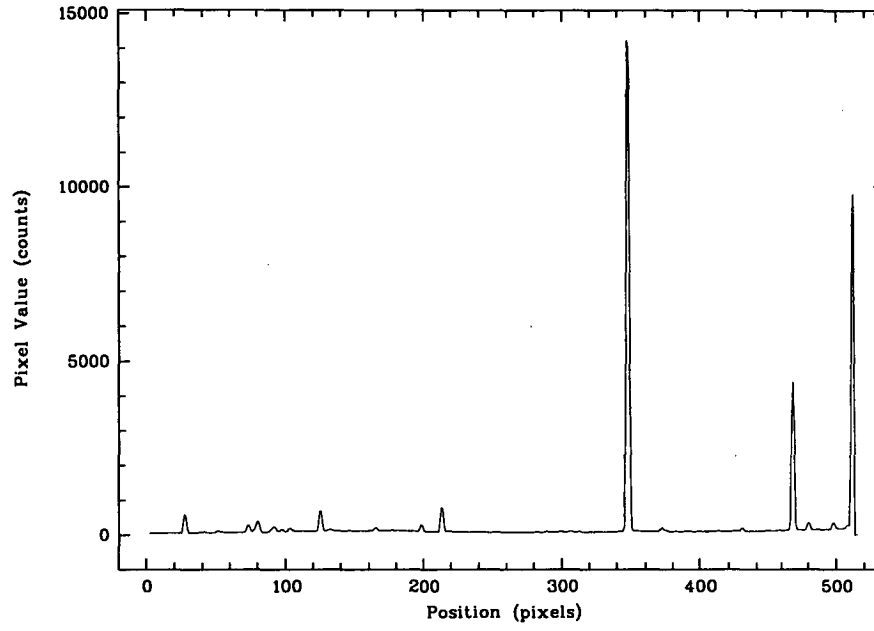

Figure 7.6: HEAR spectrum for the B300 grism.

Shown in Figure 7.6 is the spectrum obtained from the HEAR lamp using the B300 grism. The exposure time for this observation was about 10 minutes and the command `SEARCH/LONG` detected 327 spectral features. The results of fitting the dispersion solution is shown in Figure 7.7 along with the lines identified by `IDENTIFY/LONG`. In this figure the position in pixels is shown as a function of the pixel value in counts. The plot of the residuals in Figure 7.8 shows that the polynomial used gives a good fit to the dispersion relation with a rms deviation of about 0.31 pixels.

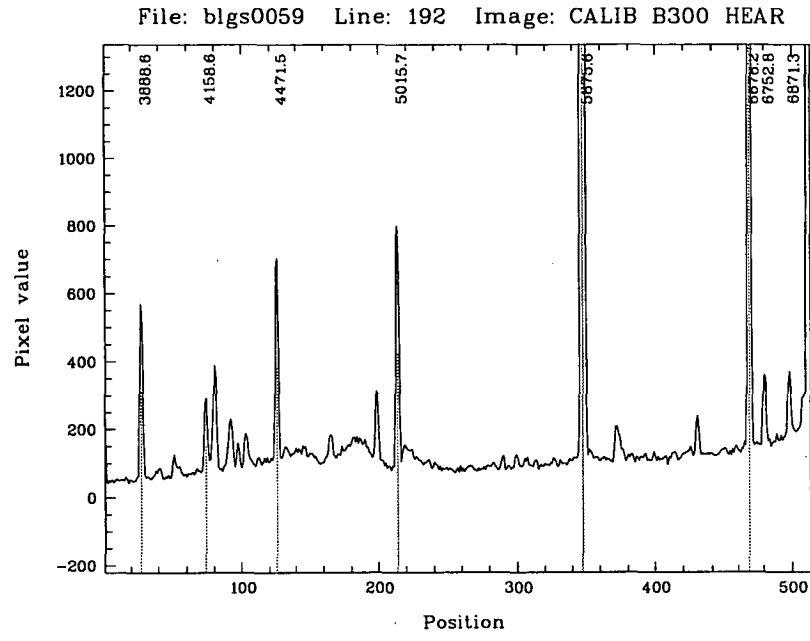

Figure 7.7: PLOT/CALIBRATE for B300.

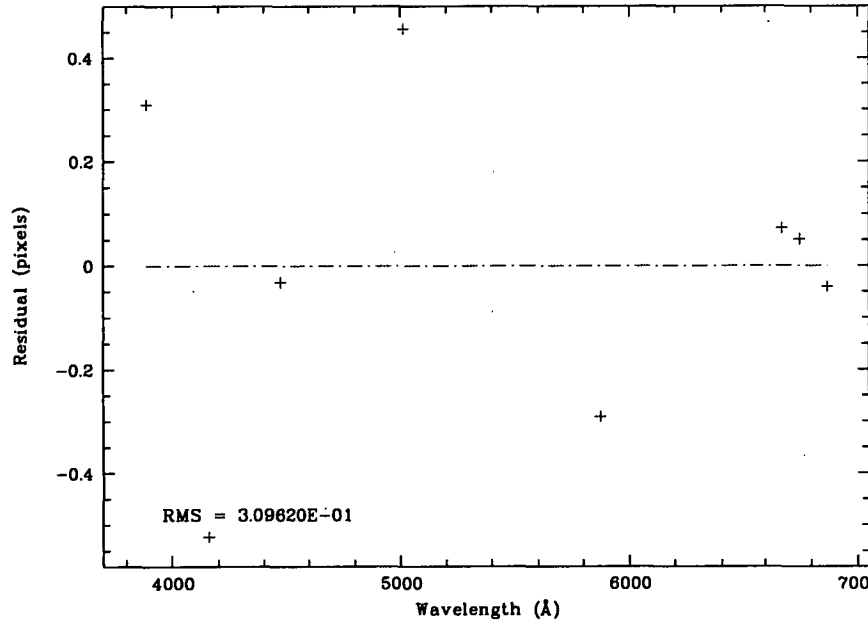

Figure 7.8: PLOT/RESIDUAL for B300.

7.3.3 O150

Presented here are the results of the O150 wavelength calibration.

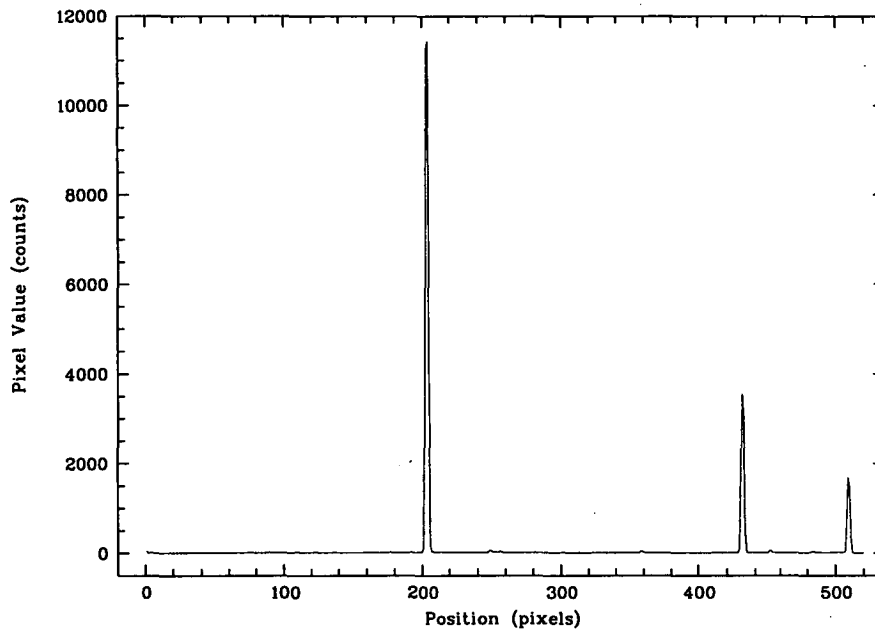

Figure 7.9: HEAR spectrum for the O150 grism.

Shown in Figure 7.9 is the spectrum obtained from the HEAR lamp using the O150 grism. The exposure time for this observation was about 10 minutes and the command `SEARCH/LONG` detected 2355 spectral features, considering the features in each row to be different. The results of fitting the dispersion solution is shown in Figure 7.10 along with the lines identified by `IDENTIFY/LONG`. In this figure the position in pixels is shown as a function of the pixel value in counts. The plot of the residuals in Figure 7.11 shows that the polynomial used gives a good fit to the dispersion relation with a rms deviation of about 0.19 pixels.

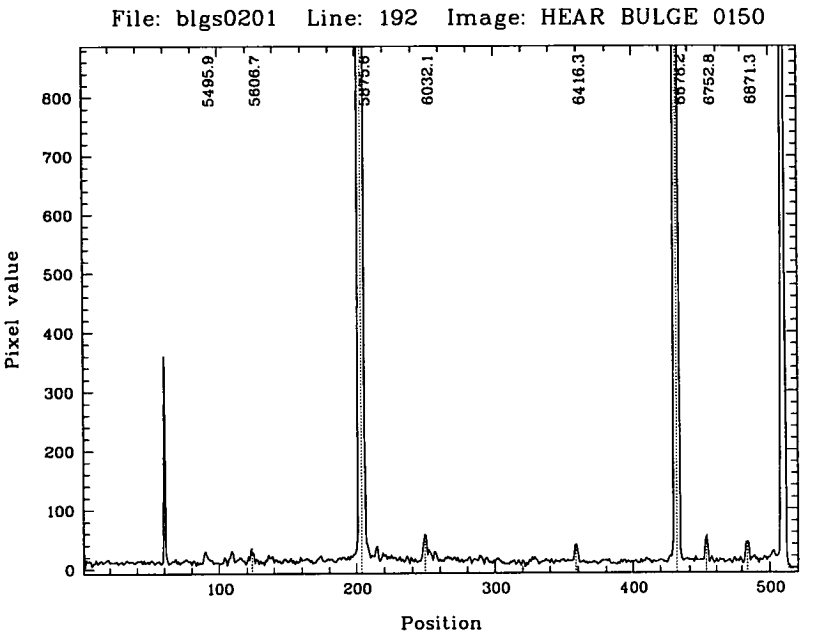

Figure 7.10: PLOT/CALIBRATE for O150.

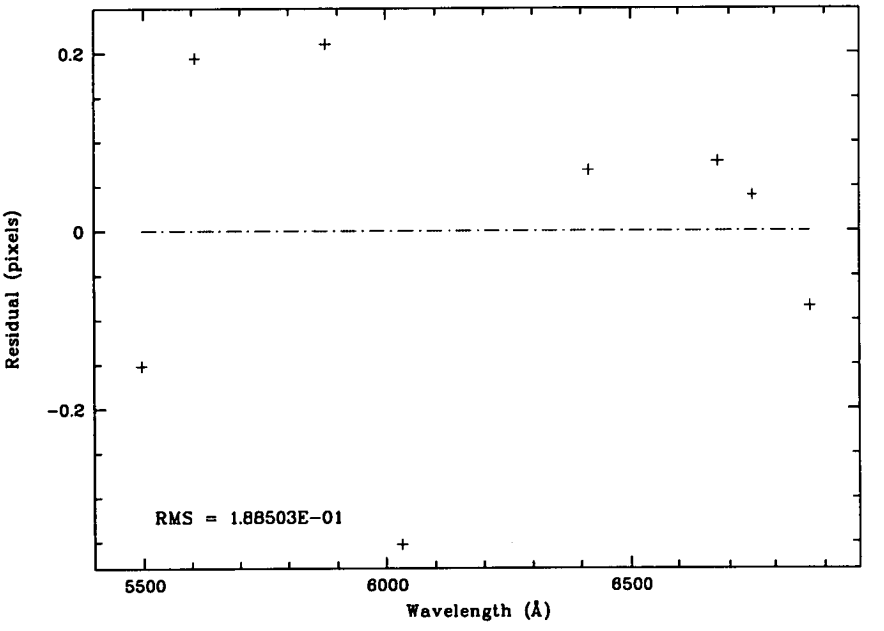

Figure 7.11: PLOT/RESIDUAL for O150.

7.3.4 R300

Presented here are the results of the R300 wavelength calibration.

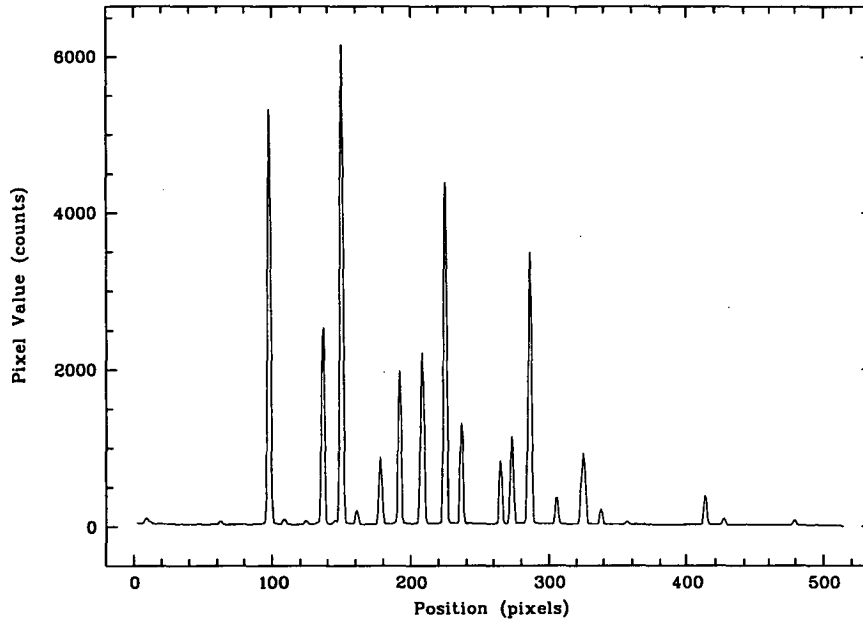

Figure 7.12: HEAR spectrum for the R300 grism.

Shown in Figure 7.12 is the spectrum obtained from the HEAR lamp using the R300 grism. The exposure time for this observation was about 10 minutes and the command `SEARCH/LONG` detected 6495 spectral features, considering the features in each row to be different. The results of fitting the dispersion solution is shown in Figure 7.13 along with the lines identified by `IDENTIFY/LONG`. In this figure the position in pixels is shown as a function of the pixel value in counts. The plot of the residuals in Figure 7.14 shows that the polynomial used gives a good fit to the dispersion relation with a rms deviation of about 0.20 pixels.

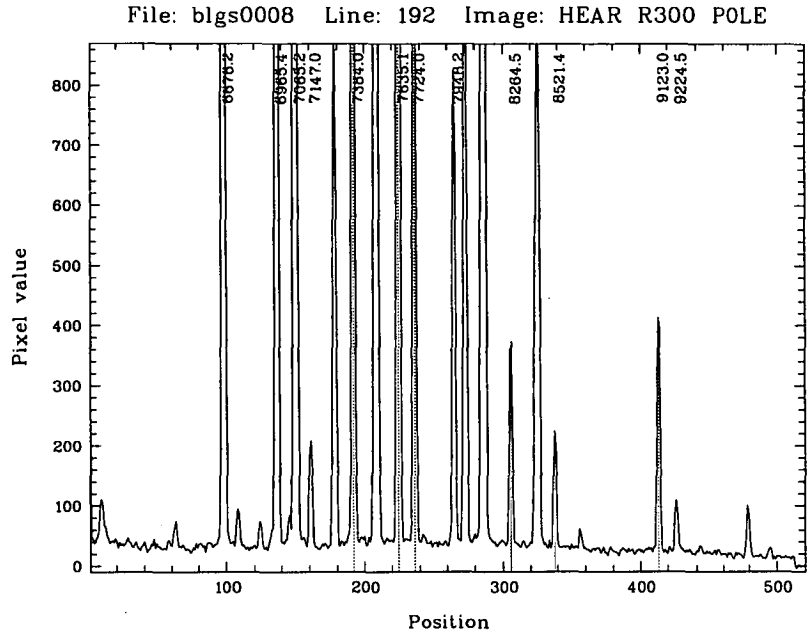

Figure 7.13: PLOT/CALIBRATE for R300.

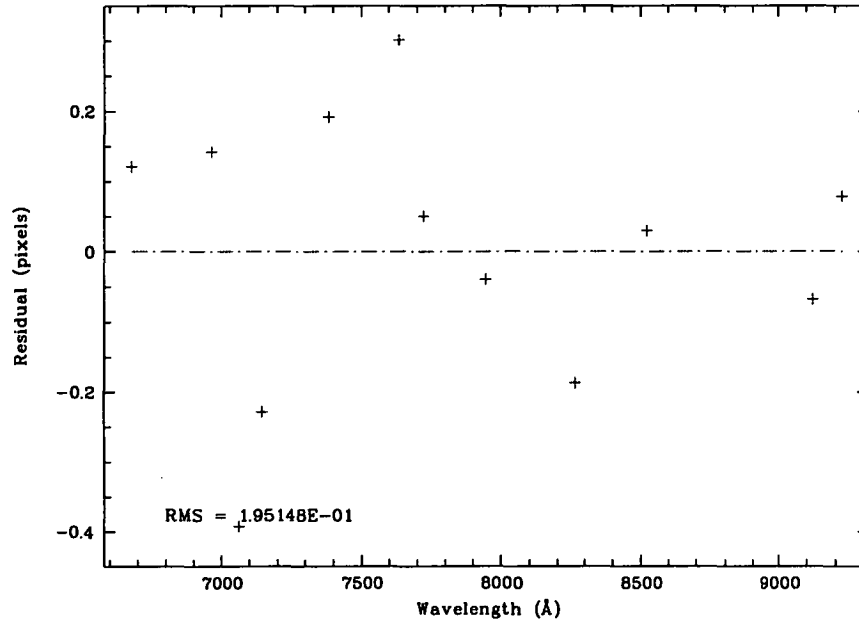

Figure 7.14: PLOT/RESIDUAL for R300.

7.4 Flux Calibration

The purpose of flux calibration is to place astrophysical measurements in fundamental units. This is often referred to as *absolute calibration*, as opposed to *relative calibration* where the flux of the source is compared with another source. Absolute flux calibration in spectroscopy is, in general, extremely difficult since it depends on the fraction of light in the slit which changes with seeing conditions, particularly if the slit is narrow as was the case for these observations. For accurate absolute flux calibration it is often suggested that several observations be made during the night, typically at the beginning and end. However, if the seeing is different during the source star and standard star observations then the fraction of light in the slit for the two standard star observations can be different, introducing a major source of uncertainty. It is worth noting that this can be overcome in many cases by calculating the percentage flux lost due to the slit when comparing a slit-limited exposure to an exposure with the slit at maximum width. Since this study is mostly interested in the relative line strengths rather than the absolute line strengths, a single standard star per night was deemed sufficient. The uncertainty in absolute flux would normally be in the range of 10–20% in clear sky conditions and worse if the sky is not photometric, however the relative absolute fluxes will be more accurate.

The images were rotated such that the spectra were oriented perpendicular to the y-axis. The standard star could then be extracted from the image using the command `AVERAGE/ROW` which calculates the average row in a selected range of rows but optionally outputs the sum of the rows. The number of rows summed to obtain the standard star spectrum was typically 8–14 and an equal amount of rows were summed in a region of low intensity to extract an estimate for the sky.

After the spectrum of the standard star has been extracted from the rebinned image and the sky has been subtracted, the MIDAS command `EXTINCTION/LONG` can be used to correct the spectrum for atmospheric extinction. The command `INTEGRATE/LONG` then divides the spectrum of the standard star by a flux table for that star and generates a table of response values. These response values are then interpolated by a polynomial of specified degree using the command `RESPONSE/LONG`. The resulting response curve can be applied to wavelength calibrated and extinction corrected spectra using the command `CALIBRATE/FLUX`.

The standard star LTT 9239 was used for the 1995 observations and the standard star LTT 8702 was used for the 1996 observations. Figures 7.15 and 7.16 show the results for the standard star LTT 9239 observed through the O150 grism. Shown in Figure 7.15 is the result of fitting an eighth-order polynomial to the response values which are the ratio of the standard star spectrum to the MIDAS flux table. This response curve was used to calibrate the observed standard star. Shown in Figure 7.16 is the flux calibrated standard star spectrum plotted over the top of the MIDAS flux table for that star.

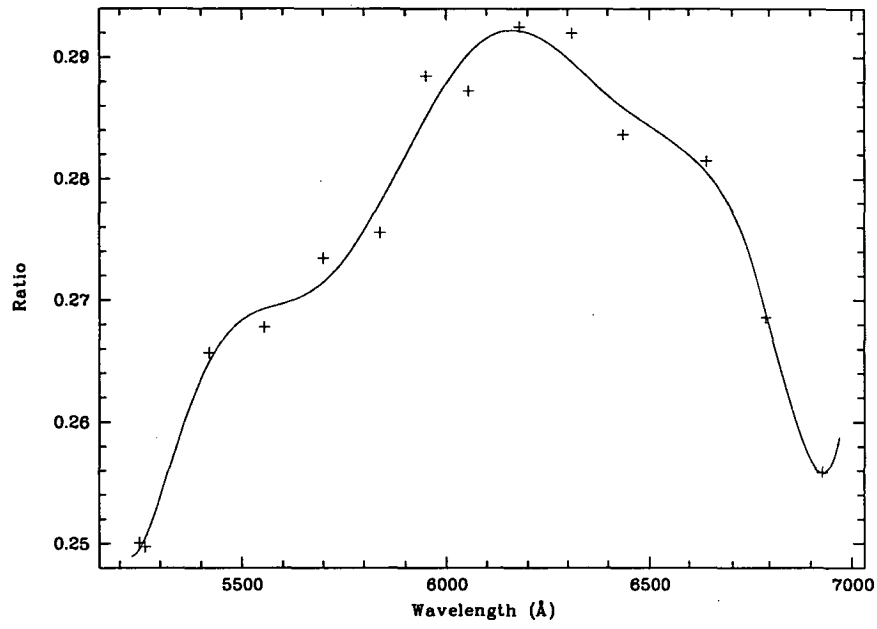

Figure 7.15: Response curve fitted using the command RESPONSE/LONG.

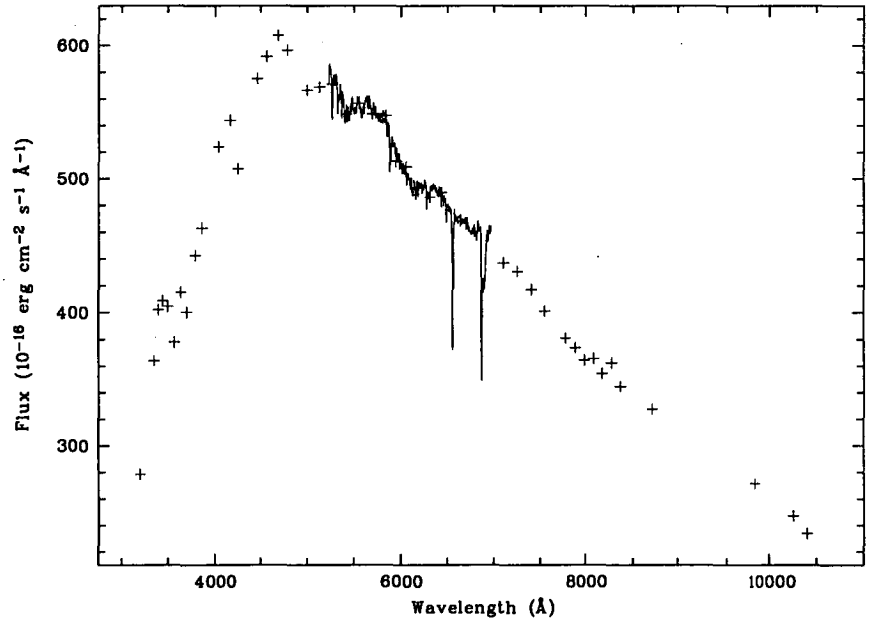

Figure 7.16: Flux calibrated standard star (solid line) plotted over the fluxes read from the MIDAS flux table (crosses).

7.5 Spectral Analysis

7.5.1 Microlensed Stars

The first step to reducing the science frames was to wavelength calibrate them using the command `REBIN/LONG`. The spectra of the microlensed sources were obtained by summing the rows of the source spectra in the image. An equal amount of rows (typically 3–6) of sky were summed and then subtracted from the source spectra. Atmospheric extinction was taken into account using the command `EXTINCTION/LONG` and finally the flux was calibrated using the command `CALIBRATE/FLUX`. These results are presented in the next chapter.

7.5.2 Non-Microlensed Stars in the Field

Since the purpose of this study is to compare the spectra of microlensed sources with various other stars, up to 10 stars were chosen at random from each field and were reduced in the same way as the microlensed sources described above. These results are presented in the next chapter.

7.5.3 Removing Cosmic Ray Hits

Cosmic ray hits were generally removed during and after the reduction procedure. This was done using the MIDAS command `MODIFY/GCURSOR`.

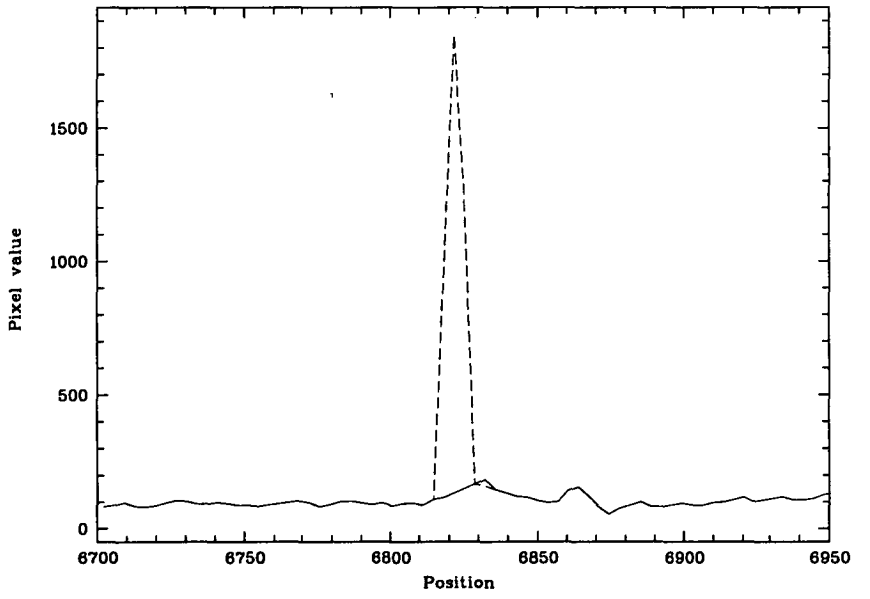

Figure 7.17: The removal of a cosmic ray. The dashed line shows the cosmic ray as it existed prior to removal.

Shown in Figure 7.17 is a typical cosmic ray (dashed line) removal. The cosmic ray is removed by means of a cursor and so particular care must be taken to in order to modify only the few pixels affected by the cosmic rays.

Chapter 8

Spectroscopy of Microlensed Sources

This chapter presents the spectra of microlensed sources that were observed using the ESO 3.6 m telescope. The first section describes the methods that were developed and used to estimate the spectral type and the radial velocity of the observed sources, and the interstellar extinction towards them. The reduced spectra and the results derived from them are presented in the second section. The third section provides an analysis of the extinction features of the spectra, particularly with respect to the spectra of other random stars in the field. These results are used to reach conclusions regarding the extinction bias and kinematics of the microlensed sources.

8.1 Estimating Extinction, Spectral Type, and Radial Velocity

In order to process the large number of spectra that were obtained for analysis, a MIDAS script was written which estimates both the extinction and the spectral type for each individual spectrum. This script is able to achieve this by using a large library of model spectra that was constructed from the Kurucz database. An additional script was written to determine the radial velocities of the microlensed and non-microlensed sources using the cross-correlation technique.

8.1.1 Calculation of Model Spectra

The 1993 Kurucz stellar atmospheres atlas [57] covers a wide range of metallicities, effective temperatures, and gravities. The models were first developed by Kurucz in 1970 using the stellar atmosphere modelling program ATLAS [56]. The 1993 atlas contains about 7600 models which are convenient to access using the IRAF (Image Reduction Analysis Facility) task *synphot*, which is available in

the *stsdas* package developed at the Space Telescope Science Institute. Synphot allows a model spectrum to be extracted from the atlas by specifying a temperature, metallicity, and surface gravity. The model spectra in the atlas are in surface flux units which can be renormalized to the absolute flux calculated for a given distance.

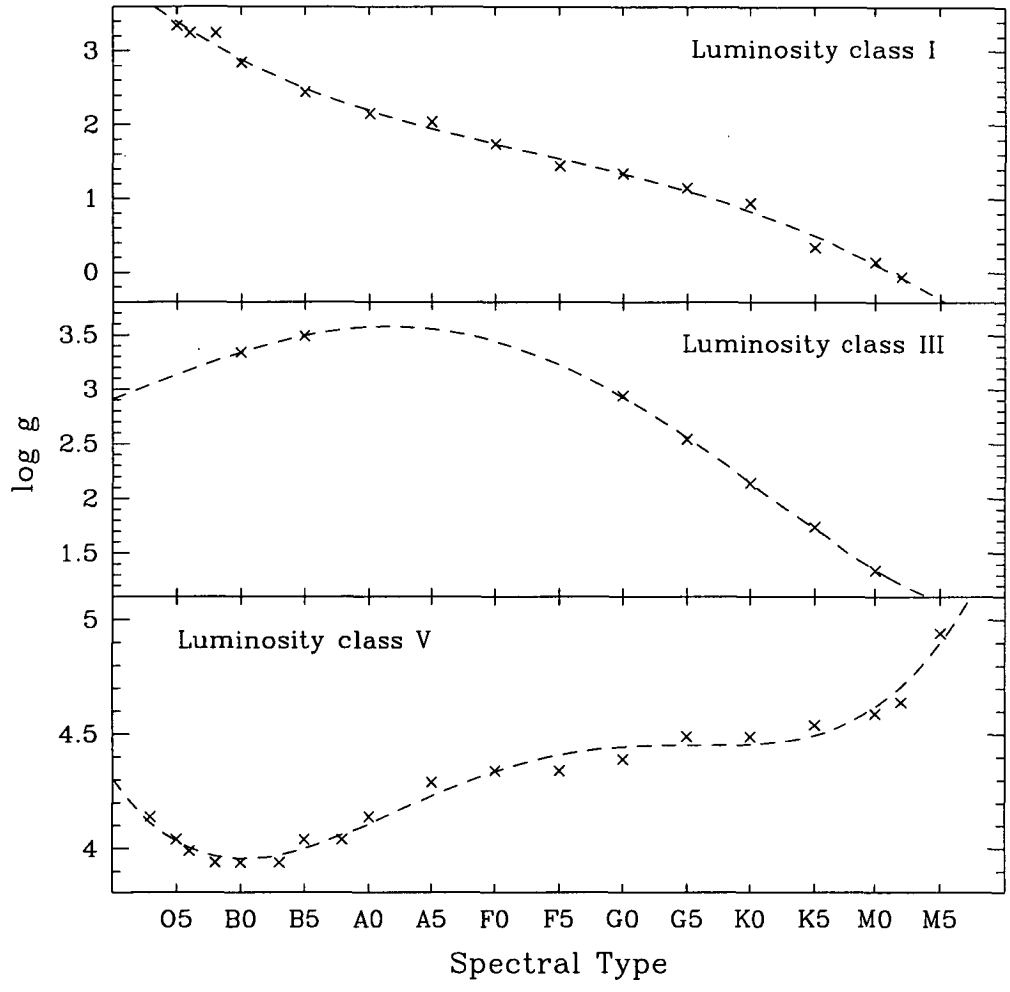

Figure 8.1: Surface gravity $\log g$ for luminosity classes I, III, and V.

To extract the model spectra from the atlas, an exhaustive list of stellar parameters was needed for each of the stellar sub-types and luminosity classes. The values for the effective temperature T_{eff}, the surface gravity $\log g$, and the absolute magnitude M_V characterizing each star were obtained from Schmidt-Kaler's compilation of physical parameters of stars [90]. However, the values of $\log g$ were found to be severely lacking in their coverage of the stellar sub-types and so the remaining values were determined from the interpolation of the values

given in Schmidt-Kaler. As shown in Figure 8.1, a fourth-order polynomial of the form $y = ax^4 + bx^3 + cx^2 + dx + e$ was fitted to the available data for each luminosity class. The coefficients for the polynomial fitted to each luminosity class are shown in Table 8.1. The estimates obtained for the required values of $\log g$ by this method were sufficient to create the desired spectral models since spectral classification within a luminosity class has a weak dependence on surface gravity. It is worth mentioning that the grids of theoretical isocrones calculated by Bertelli *et al* [22] also provide a useful set of stellar parameters. Although there are slight differences in the model parameters between these two references, they are unlikely to affect the main goals of this study.

Class	a	b	c	d	e
I	1.71×10^{-3}	-0.05	0.37	-1.50	4.05
III	5.75×10^{-3}	-0.06	0.04	0.44	2.91
V	9.30×10^{-3}	-0.13	0.56	-0.80	4.30

Table 8.1: Coefficients for polynomial fits to $\log g$ values.

A total of 226 model spectra were produced for this analysis. The absolute magnitude of each stellar type was used to normalize the spectra to a distance of 8 kpc. Galactic bulge stars tend to have a large range of metallicity with most being more metal poor than solar. Initially only spectra with solar metallicity were used in the analysis but the library of model spectra was eventually expanded to a range of metallicities including metallicity of 0.1 times solar corresponding to population II stars.

8.1.2 The Fitting Routine

Spectral classification is based on the strength of various spectral features in the spectra which are compared with those of a set of standard stars defining the classification system. Although the classification of the observed spectra is not the primary goal of this analysis, it served as a tool for providing the necessary information. The main purpose of the MIDAS fitting routine (see Appendix F) was to provide a reasonable estimate of the extinction present in each of the measured spectra. This was achieved by comparing the real spectrum to model spectra to which varying amounts of extinction were applied by the fitting routine. The fitting routine combines spectra of a star observed through multiple grisms into one complete spectrum to increase the reliability of the spectral classification.

The extinction for each stellar model was estimated by dividing the observed spectrum by the model spectrum and then using linear regression to calculate the slope of the resulting image. Interstellar extinction (Equations 6.26 and 6.27, Galactic extinction data from Seaton [93]) was increasingly applied to the model spectrum until the slope was approximately equal to zero. The current value of E_{B-V} was then adopted as the extinction value for that model spectrum.

Once the extinction was estimated for the model spectrum, the extincted model was fitted to the observed spectrum. A fitting parameter was calculated by measuring the mean flux for each 10 pixels along the entire wavelength range for both the observed spectrum and the model. The square of the difference of these two values was added to a cumulative value and the final result became the fit parameter for that spectral model, similar to that which is obtained in a χ^2 analysis. Thus, the model spectrum that best fitted the real spectrum was the one with the lowest fit parameter and the associated extinction value was then known. The error in the extinction is not necessarily a reflection of the error in the fit but rather it is a reflection of the difference in fitted extinction between models.

It should be noted that the spectral classification of stars using the fitting routine was accompanied by a comparison with standard stars from libraries of stellar spectra [27, 51, 101]. The MK classification of stellar spectra [70] provides a complete and detailed 2-dimensional classification system for the classification of stars of almost the entire spectral sequence. This method consists of estimating intensity ratios of suitable pairs of lines, one more sensitive to temperature and the other more sensitive to luminosity. The luminosity and temperature dependence of many of the main spectral lines have been conveniently summarized by Torres-Dodgen & Weaver [101]. The combination of analysis of lines ratios and the slope of the continuum allow unique determinations of the temperature and extinction to be made. This method uses the information contained in the continuum as well as the lines and hence should be at least as reliable as the MK classification method. An example of this reliability is from the use of this method to classify the spectrum of MB95030, as presented later in this chapter. The method described here provides a classification of M2III, a close match to the result of M4III derived by the MACHO collaboration [16].

The limitations of this method turn out to be limitations in the model spectra. The model spectra cover a wavelength range from the ultra-violet (1000 Å) to the infra-red (10 μm). However, the model spectra are particularly unreliable for wavelengths greater than 9000 Å, largely due to very strong atmospheric water band extinction, and indeed spectral information in this region has only been obtained in recent years (after the models were created). To account for this, wavelengths greater than 9200 Å were ignored for spectra obtained through the R300 grism.

There is a truncation error in the stellar parameters used for each model due to the limitations in the grid of models available from the Kurucz stellar atmospheres atlas. This resulted in a limitation in the number of models that were able to be produced and consequently a limitation in the resolution of the fitting procedure. The lower threshold in the grid of temperatures of 3500 K meant that stars cooler than spectral types of about M2 could not be created. This consideration led to an estimated uncertainty in the classification of about two spectral subtypes if it is M2 or later. However, the expected number of stars

later than M2 is small, and hence this in unlikely to have a significant effect on this analysis.

Further limitations were found when the fitting routine attempted to fit models for late K and early M-type stars, particularly for stars which were only observed using the O150 grism. The spectral bands (such as the TiO band that is characteristic of M-type stars) that tend to dominate these stellar types created problems which in some cases caused a mis-classification of the spectra. In these cases, special care was taken to identify the spectra through the use of the previously mentioned libraries of stellar spectra. The spectra were then reprocessed with the correct model spectrum.

8.1.3 Radial Velocity Determination

In general, the radial velocity of a star may be measured from the Doppler shift of stellar spectral lines. The radial velocity is then given by $v_r = (\Delta\lambda/\lambda_0)c$ where $\Delta\lambda = \lambda - \lambda_0$ is the Doppler shift of the line from its rest wavelength λ_0. However, there are factors intrinsic to stellar structure, such as surface convection and magnetic fields, which can affect the symmetry and wavelength of line profiles [34]. An approximate value of the radial velocity may still be determined from one of the few lines, such as Hα (6563 Å), which are not sensitive to the velocity structure of the photosphere.

A more reliable and accurate method for measuring the radial velocity of a star is to cross-correlate the stellar spectrum with a template spectrum. The correlation between them may be analysed using the cross-correlation function from which the location of the main peak is used to determine the wavelength shift. Cross-correlation techniques and the theory of correlation analysis have been described in detail by Tonry & Davis [100].

To obtain absolute radial velocities (radial velocities relative to the barycentre of the solar system) it is often necessary to cross-correlate the stellar spectrum with that of a radial velocity standard star, such as those monitored by CORAVEL [109]. No such standard stars were observed to carry out such an analysis but radial velocities measured relative to a bright star are adequate for this analysis. As noticed earlier by Morse *et al* [71], when a large number of spectral lines are used for the radial velocity determination, the systematic errors caused by lines formed at different regions of the stellar atmosphere average out, and the resultant radial velocity determination is insensitive to the choice of template for late-type stars. The template used for these measurements (see Figure 8.2) was a bright star with high S/N selected from the MB95012 field. By fitting a gaussian to the Hα line, the absolute radial velocity of the template star was found to be $-98.5 \pm 18.0\,\mathrm{km\,s^{-1}}$. Taking into account the wavelength calibration residuals, the absolute radial velocity is correctly stated as $-98.5 \pm 37.3\,\mathrm{km\,s^{-1}}$.

A MIDAS script was written to perform the cross-correlation and extract the radial velocity information. Prior to correlation, it is important to prepare a

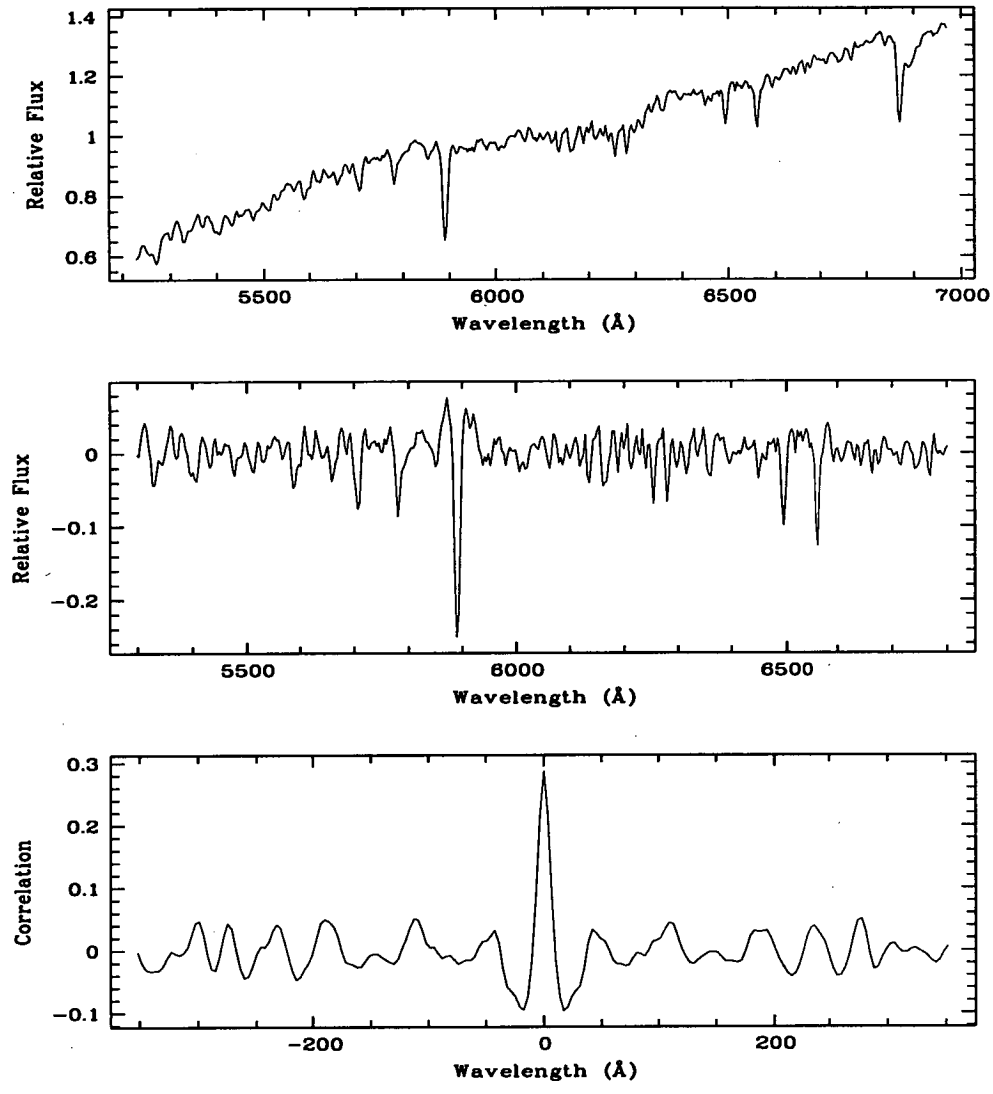

Figure 8.2: **Top:** Normalized spectrum of the star to be used as the cross-correlation template for the sources studied spectroscopically in this chapter. **Middle:** The result of subtracting the continuum, applying a bandpass filter, and extracting the region of the spectrum that excludes atmospheric lines. **Bottom:** The cross-correlation function that results from correlating the template with itself. The shift of the central peak is approximately zero as expected.

spectrum to reduce noise in the cross-correlation function. The first step in this process is to normalize the spectrum. Next an eighth-order polynomial is fitted to the continuum and the continuum is subtracted. A bandpass filter is applied to the spectrum which excises both high and low spatial frequency components. The final step is to extract a large segment of the spectrum which excludes atmospheric absorption lines. These steps are shown in Figure 8.2 in which the template spectrum is cross-correlated with itself.

After cross-correlating the stellar spectrum with the template spectrum, the wavelength shift was determined from the position of the peak of the cross-correlation function. The central position of this peak was determined by fitting a gaussian which has an associated error. The error in the gaussian fit was used to estimate the error in the radial velocity. The MIDAS cross-correlation script was successfully tested by simulating line shifts in various spectra and by performing correlations on restricted wavelength ranges within a spectrum.

8.2 Spectroscopy Results

As was the case for the photometric studies presented in this thesis, the majority of microlensing events observed were alerted by the MACHO collaboration with the remainder being discovered by the OGLE and DUO collaborations. In order to distinguish between these, the prefixes "MB", "OB", and "DB" have been chosen to signify a MACHO, OGLE, or DUO bulge event respectively. The microlensing events observed are summarized in Table 8.2 with binary events having an undetermined characteristic time scale. This information has been extracted from the MACHO alerts and from the OGLE and DUO publications [2, 118].

Event	R.A. (J2000)	DEC. (J2000)	V	R	t_E (days)
DB95002	18:10:17.2	-27:28:49	-	18.6	binary
MB95002	18:08:25.2	-27:58:38	19.0	17.9	61.0
MB95003	18:02:37.5	-29:39:36	18.7	17.6	1.0
MB95004	18:00:03.4	-29:11:04	18.1	17.1	3.5
MB95008	18:16:46.0	-26:11:43	17.1	16.3	15.5
MB95009	18:06:32.3	-30:55:55	17.2	16.2	12.0
MB95010	17:58:16.0	-29:32:11	18.9	18.0	47.5
MB95012	18:06:04.8	-29:52:38	18.6	17.7	binary
MB95013	18:08:47.0	-27:40:47	16.6	15.6	73.5
MB95014	18:01:26.3	-28:31:14	17.4	16.5	9.0
MB95017	18:03:01.1	-28:21:09	18.8	18.0	18.5
MB95018	18:07:20.6	-28:36:51	18.7	17.8	39.5
MB95019	18:11:32.5	-27:45:27	18.6	17.9	31.5
MB95030	18:07:04.3	-27:22:06	16.1	14.7	33.5
OB95003	18:04:43.5	-30:14:11	17.7	-	11.5
OB95007	18:03:35.8	-29:47:06	19.3	-	binary
OB95016	18:02:07.6	-30:01:12	20.0	-	26.2

Table 8.2: Microlensing event information provided by the MACHO alerts and the OGLE and DUO publications. Information includes the coordinates of the sources, the baseline V and R magnitudes, and the characteristic time scales of the events.

A summary of the observations of these events is shown in Table 8.3, including the date of observation, the grisms used, the exposure times, and the time after the peak (TAC) measured in units of days and in units of the characteristic time scales of the events. Single observations were made of each of the events with the exception of the event MB95017 for which two separate observations were made.

Shown in Figure 8.4 is a $45'' \times 45''$ image for each of the observed microlensing events. The images are centred on the event and a circle indicates the location

Event	Date	Grisms Used	Exposure	TAP (days,t_E)
DB95002	899.64	B150,O150	1800,2220	binary
MB95002	899.89	O150	2280	67, 1.10
MB95003	899.86	O150	1200	91, 91.00
MB95004	899.84	O150	1800	110, 31.43
MB95008	899.71	O150	2700	54, 3.48
MB95009	899.78	O150	1800	61, 5.08
MB95010	897.79	B150,O150	1800,1800	28, 0.59
MB95012	897.74	B150,O150	1500,1200	binary
MB95013	897.70	B150,O150,R300	900,600,120	0, 0.00
MB95014	899.81	O150	1800	45, 5.00
MB95017	897.90	B150,O150	1500,1110	16, 0.86
MB95017	898.69	B150,O150	1200,1800	17, 0.92
MB95018	898.73	B150,O150	1800,1800	−10, −0.25
MB95019	897.85	B150,O150	1800,1800	−8, −0.25
MB95030	1251.75	B150,B300	1200,900	307, 9.16
OB95003	899.75	O150	1800	1069, 92.96
OB95007	898.84	O150	2700	binary
OB95016	898.79	B150,O150	1800,1800	14, 0.53

Table 8.3: Summary of microlensing events observed. Information includes the date of observation (HJD - 2449000), the grisms used, the respective exposure times (seconds), and the time after the peak of the events (TAP) in units of days and in units of the characteristic time scales of the events.

of the microlensed source. The orientation of the fields is such that east is left and north is up. These images were created from observations of the bulge fields at the time of the spectroscopic observations. The orientation of the slit relative to these fields is in a horizontal direction and is centred on the microlensed source. At the time of observations, the spectrograph did not have an atmospheric dispersion corrector but the observations were almost always performed at very low zenith angles and so the atmospheric correction is minimal. Furthermore, the microlensed sources are expected to be affected in the same way as other observed stars in the field, so the effect on the results should be minimal.

For each event an estimate of the spectral type, extinction, and relative radial velocity is made. It is important to remember that these measurements apply to the microlensed source rather than the lens itself. The contribution of the lens is assumed to be small because the stellar mass function is biased towards lower masses and hence it is likely that the lens is less massive and considerably fainter than the source [63]. Low luminosity stars do not contribute significantly as sources since these would not normally be detected by the magnitude limited microlensing surveys.

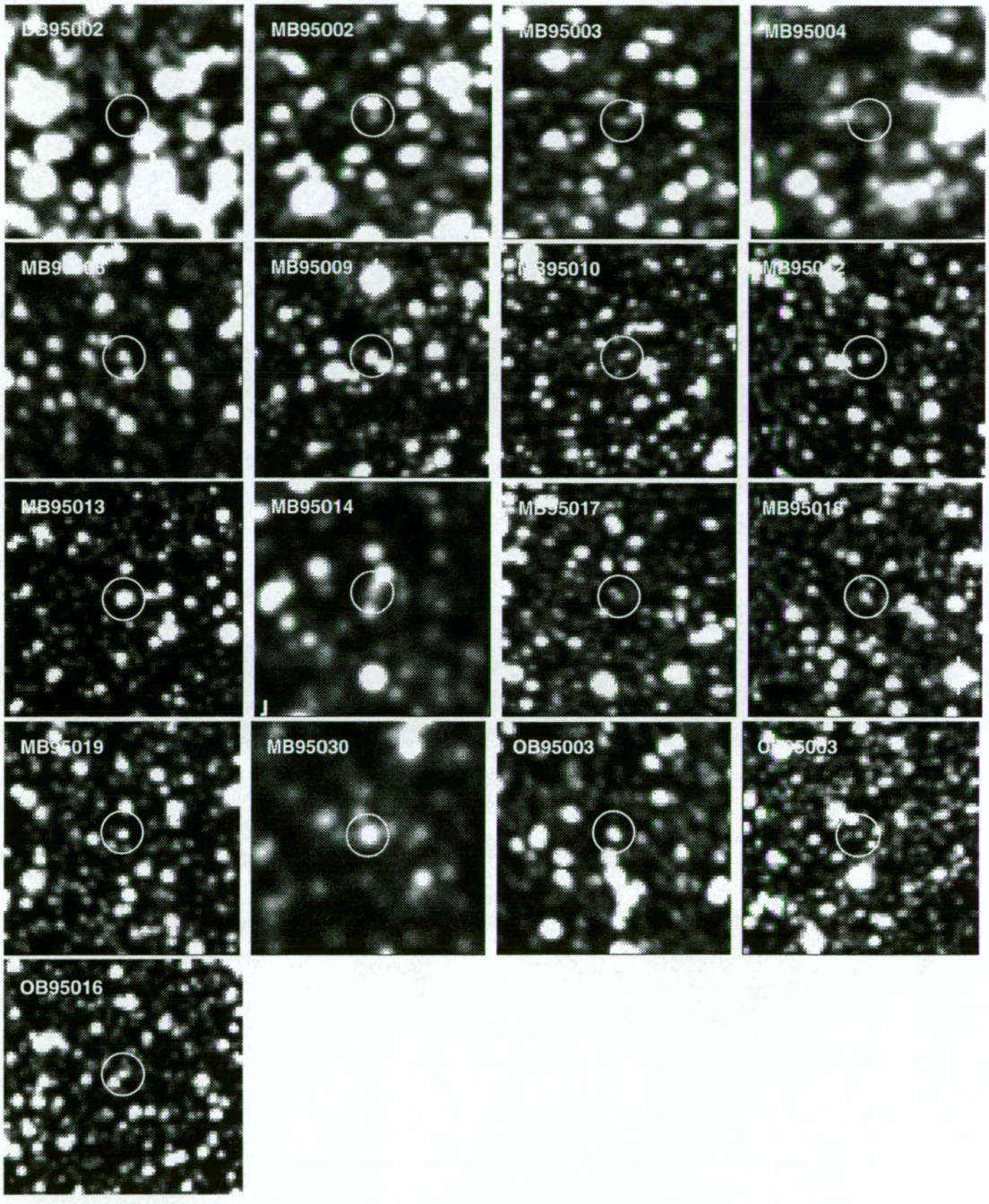

Figure 8.3: A 45″ × 45″ field for each of the 1995 microlensing events for which spectra was obtained. The images are centred on the event and a circle indicates the location of the microlensed source. North is up and east is left.

DB95002

The event DB95002 was observed using the B150 and O150 grisms giving a total wavelength coverage of 3790–6970 Å. The spectra of the microlensed source and five other stars in the field with their associated models are shown in Figure 8.5. The microlensed source proved to have a very low S/N which produced unreliable results for the event and a few of the stars. The results from fitting models to the spectra are given in Table 8.4. Shown in Figure 8.4 is the cross-correlation function for the event DB95002. The radial velocities measured relative to the selected bright star are included in Table 8.4.

Spectrum	Classification	E_{B-V}	v_r (km s^{-1})
DB95002	K2III	0.22 ± 0.09	-97.3 ± 11.6
Star 1	G0III	0.35 ± 0.05	-23.3 ± 14.8
Star 2	K0III	0.26 ± 0.10	-216.7 ± 9.3
Star 3	K0V	0.40 ± 0.01	-33.1 ± 9.6
Star 4	K2I	0.16 ± 0.04	-177.0 ± 19.6
Star 5	K1I	0.23 ± 0.09	-138.4 ± 13.8

Table 8.4: Classification, extinction, and relative radial velocity results for the DB95002 field.

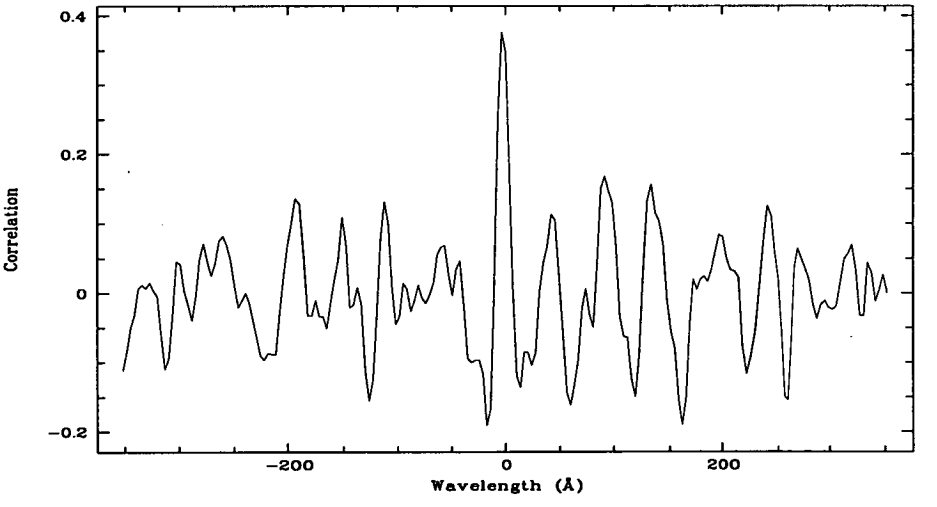

Figure 8.4: Cross-correlation function for event DB95002.

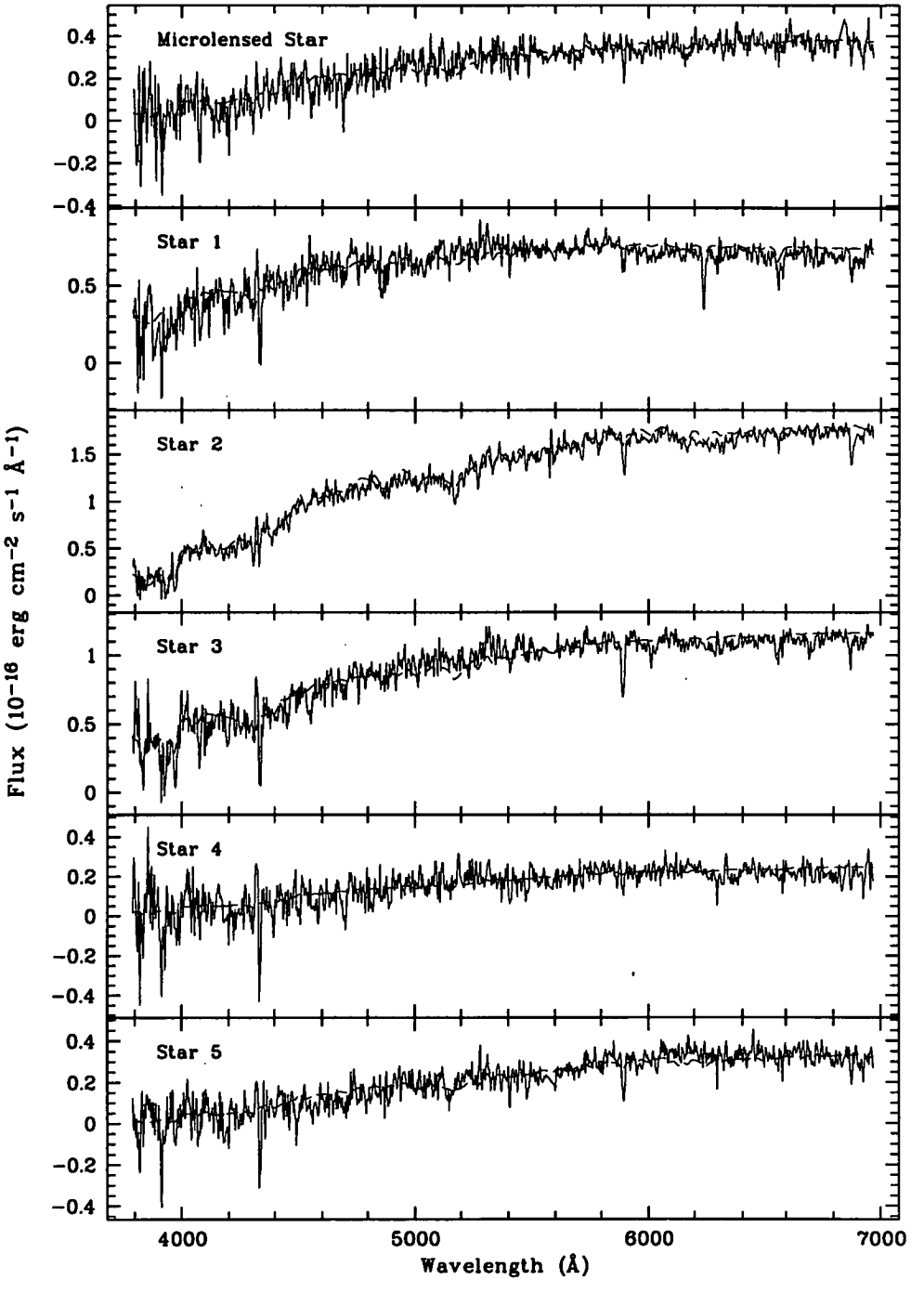

Figure 8.5: Spectra (solid line) and fitted models (dashed line) for event DB95002 and five non-microlensed stars in the field.

MB95002

The event MB95002 was observed using the O150 grism giving a total wavelength coverage of 5230–6970 Å. The spectra of the microlensed source and five other stars in the field with their associated models are shown in Figure 8.7. The results from fitting models to the spectra are given in Table 8.5. Shown in Figure 8.6 is the cross-correlation function for the event MB95002. The radial velocities measured relative to the selected bright star are included in Table 8.5.

Spectrum	Classification	E_{B-V}	v_r (km s^{-1})
MB95002	G2III	1.19 ± 0.01	-210.7 ± 6.2
Star 1	K0III	0.70 ± 0.07	-112.7 ± 4.4
Star 2	K0III	0.36 ± 0.08	-103.1 ± 1.4
Star 3	K4III	0.63 ± 0.18	-116.4 ± 3.9
Star 4	M0III	0.60 ± 0.05	-33.2 ± 4.6
Star 5	K4III	0.00 ± 0.01	-154.1 ± 6.5

Table 8.5: Classification, extinction, and relative radial velocity results for the MB95002 field.

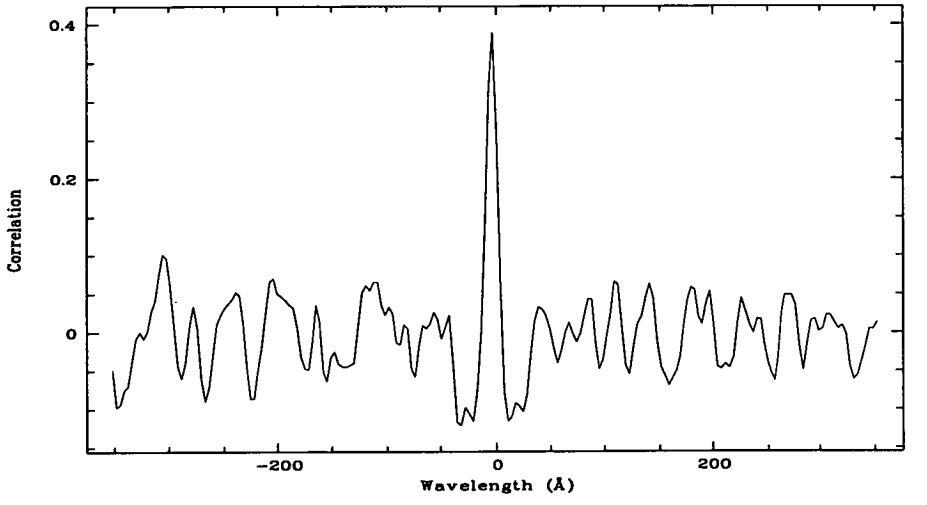

Figure 8.6: Cross-correlation function for event MB95002.

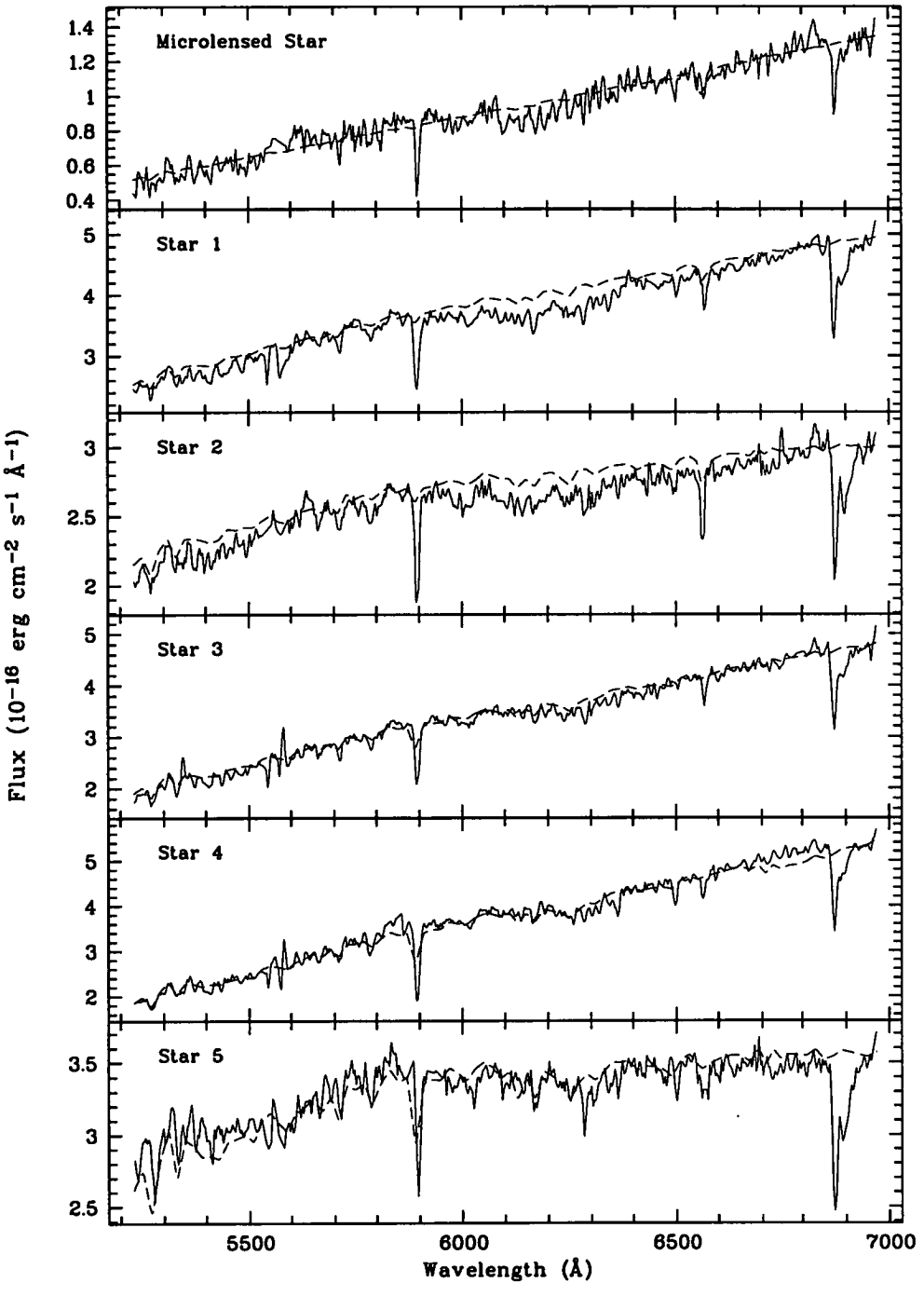

Figure 8.7: Spectra (solid line) and fitted models (dashed line) for event MB95002 and five non-microlensed stars in the field.

MB95003

The event MB95003 was observed using the O150 grism giving a total wavelength coverage of 5230–6970 Å. The spectra of the microlensed source and five other stars in the field with their associated models are shown in Figure 8.9. The results from fitting models to the spectra are given in Table 8.6. Shown in Figure 8.8 is the cross-correlation function for the event MB95003. The radial velocities measured relative to the selected bright star are included in Table 8.6.

Spectrum	Classification	E_{B-V}	v_r (km s^{-1})
MB95003	GOIII	1.31 ± 0.01	-37.6 ± 14.0
Star 1	MOIII	0.89 ± 0.18	-51.3 ± 4.1
Star 2	G0V	1.10 ± 0.03	-4.2 ± 24.2
Star 3	M2III	0.39 ± 0.03	118.8 ± 28.3
Star 4	G8V	1.37 ± 0.05	-77.1 ± 15.4
Star 5	MOIII	0.80 ± 0.18	-42.25 ± 13.0

Table 8.6: Classification, extinction, and relative radial velocity results for the MB95003 field.

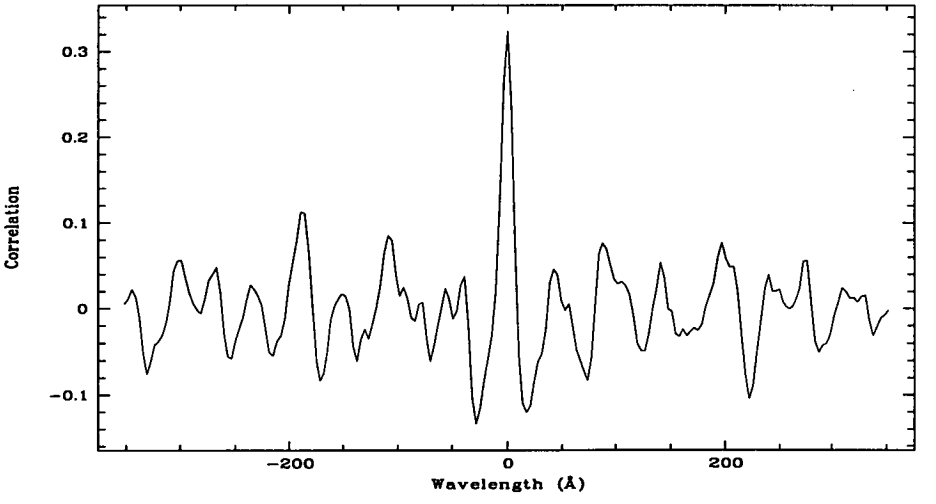

Figure 8.8: Cross-correlation function for event MB95003.

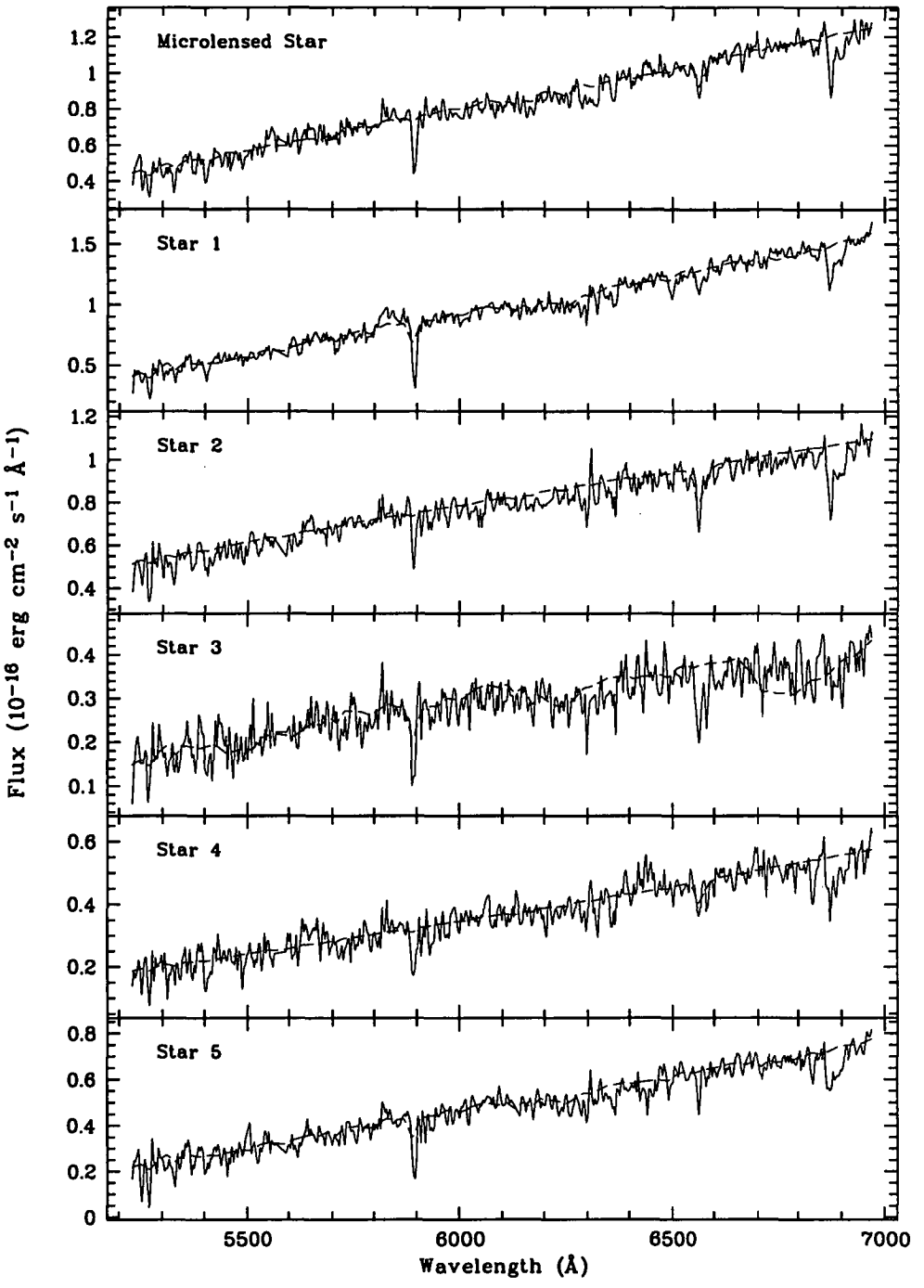

Figure 8.9: Spectra (solid line) and fitted models (dashed line) for event MB95003 and five non-microlensed stars in the field.

MB95004

The event MB95004 was observed using the O150 grism giving a total wavelength coverage of 5230–6970 Å. The spectra of the microlensed source and five other stars in the field with their associated models are shown in Figure 8.11. The results from fitting models to the spectra are given in Table 8.7. Shown in Figure 8.10 is the cross-correlation function for the event MB95004. The radial velocities measured relative to the selected bright star are included in Table 8.7.

Spectrum	Classification	E_{B-V}	v_r (km s^{-1})
MB95004	K0III	0.63 ± 0.03	-46.7 ± 5.0
Star 1	K0V	0.73 ± 0.01	-16.1 ± 3.2
Star 2	M0III	0.00 ± 0.01	-52.4 ± 4.7
Star 3	K4V	0.00 ± 0.01	-94.5 ± 1.6
Star 4	K4III	0.23 ± 0.16	-114.3 ± 5.8
Star 5	K4III	0.31 ± 0.05	22.1 ± 2.1

Table 8.7: Classification, extinction, and relative radial velocity results for the MB95004 field.

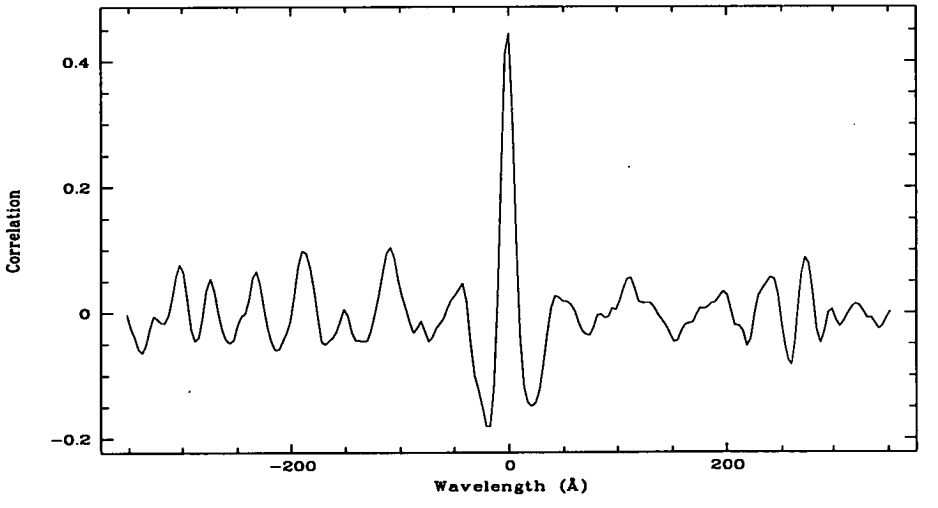

Figure 8.10: Cross-correlation function for event MB95004.

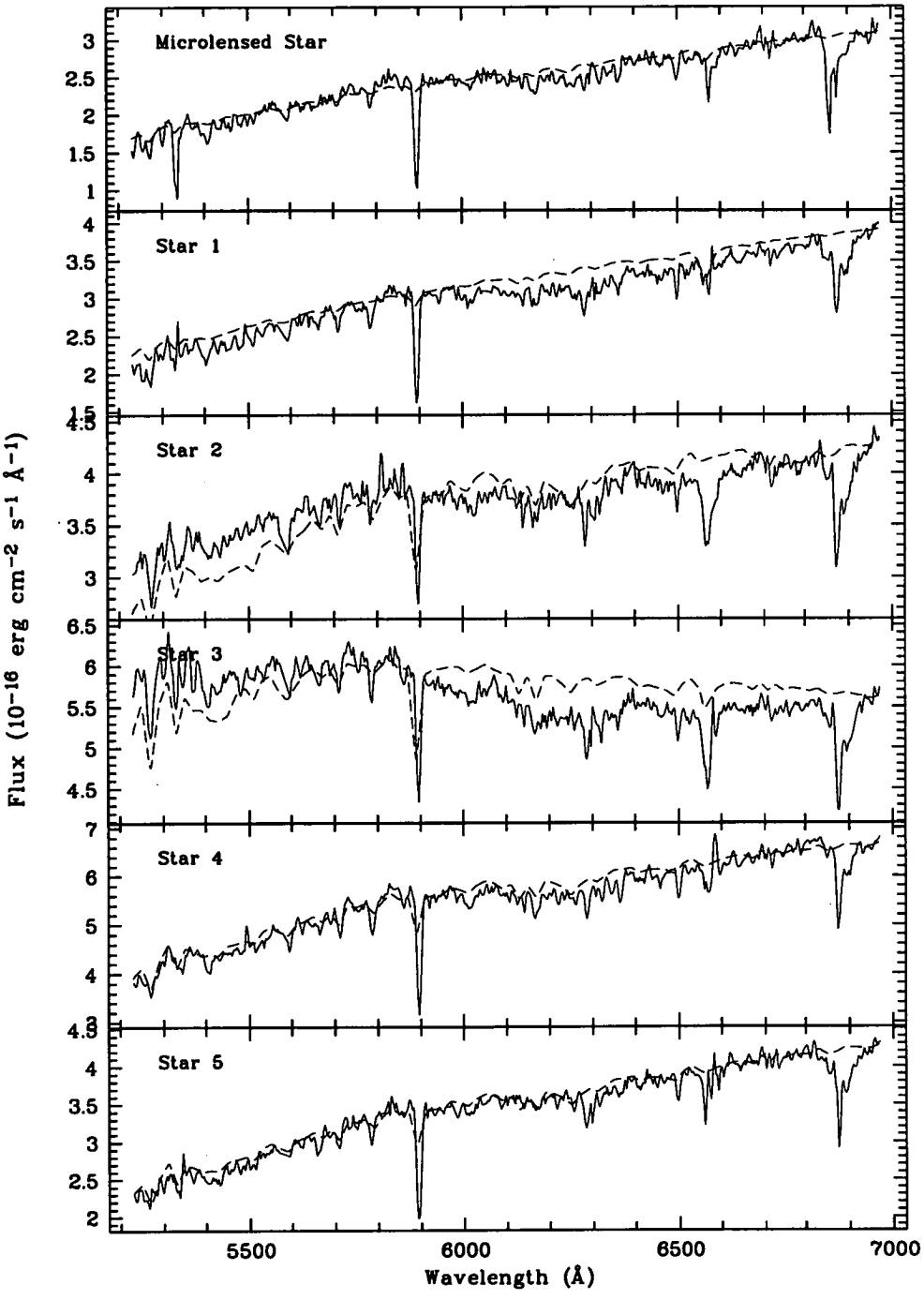

Figure 8.11: Spectra (solid line) and fitted models (dashed line) for event MB95004 and five non-microlensed stars in the field.

MB95008

The event MB95008 was observed using the O150 grism giving a total wavelength coverage of 5230–6970 Å. The spectra of the microlensed source and five other stars in the field with their associated models are shown in Figure 8.13. The results from fitting models to the spectra are given in Table 8.8. Shown in Figure 8.12 is the cross-correlation function for the event MB95008. The radial velocities measured relative to the selected bright star are included in Table 8.8.

Spectrum	Classification	E_{B-V}	v_r (km s^{-1})
MB95008	G0III	0.61 ± 0.03	-21.9 ± 6.2
Star 1	K5V	0.00 ± 0.01	-66.2 ± 10.8
Star 2	K5III	0.00 ± 0.01	-18.6 ± 3.1
Star 3	K4V	0.39 ± 0.25	-101.4 ± 4.0
Star 4	M0III	0.00 ± 0.25	-10.1 ± 7.4
Star 5	K3I	0.11 ± 0.06	-104.0 ± 5.0

Table 8.8: Classification, extinction, and relative radial velocity results for the MB95008 field.

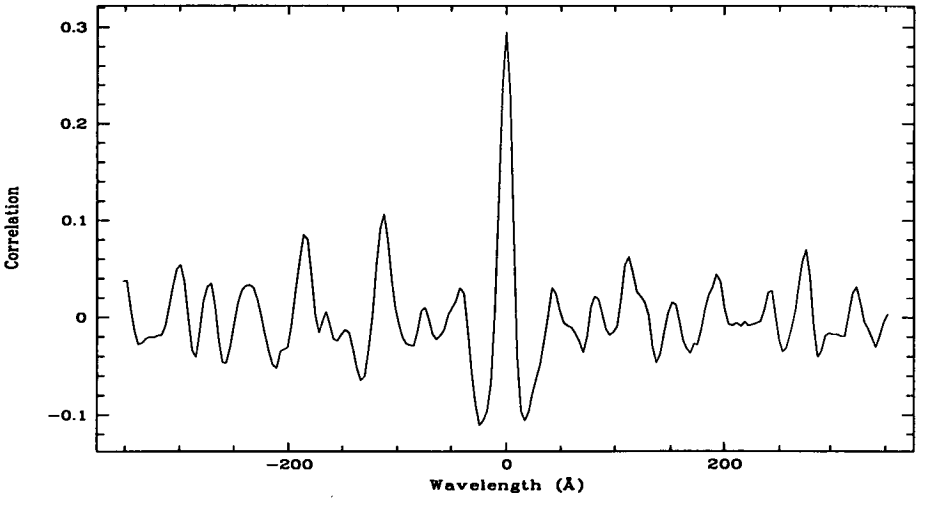

Figure 8.12: Cross-correlation function for event MB95008.

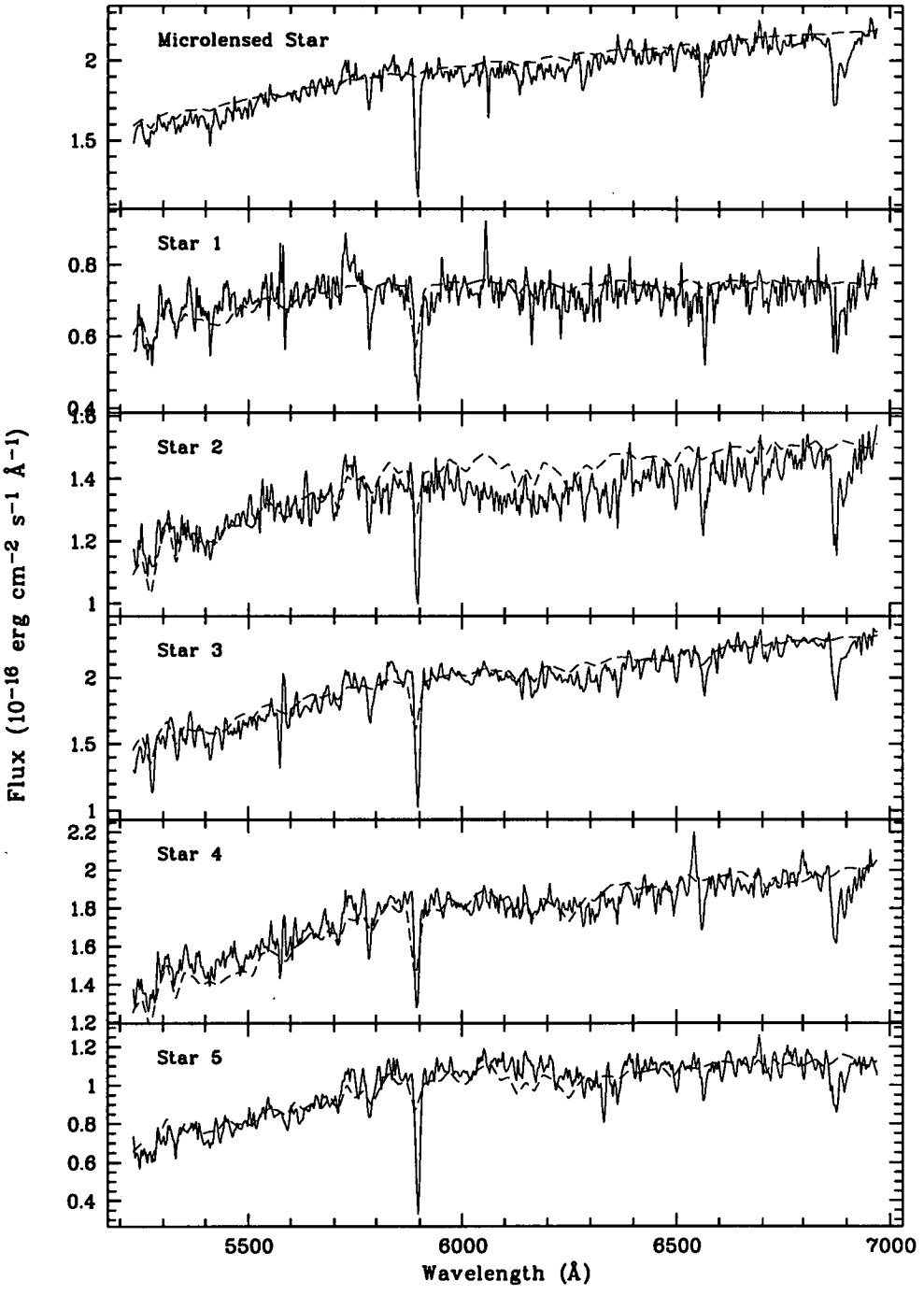

Figure 8.13: Spectra (solid line) and fitted models (dashed line) for event MB95008 and five non-microlensed stars in the field.

MB95009

The event MB95009 was observed using the O150 grism giving a total wavelength coverage of 5230–6970 Å. The spectra of the microlensed source and five other stars in the field with their associated models are shown in Figure 8.15. The results from fitting models to the spectra are given in Table 8.9. Shown in Figure 8.14 is the cross-correlation function for the event MB95009. The radial velocities measured relative to the selected bright star are included in Table 8.9.

Spectrum	Classification	E_{B-V}	v_r (km s^{-1})
MB95009	K4III	0.39 ± 0.21	-34.2 ± 2.8
Star 1	K4III	0.37 ± 0.03	-108.6 ± 3.6
Star 2	K5I	0.00 ± 0.35	-98.2 ± 12.9
Star 3	K4V	0.43 ± 0.05	-124.3 ± 6.2
Star 4	K4III	0.27 ± 0.02	22.3 ± 15.1
Star 5	M0III	0.00 ± 0.01	-90.4 ± 15.8

Table 8.9: Classification, extinction, and relative radial velocity results for the MB95009 field.

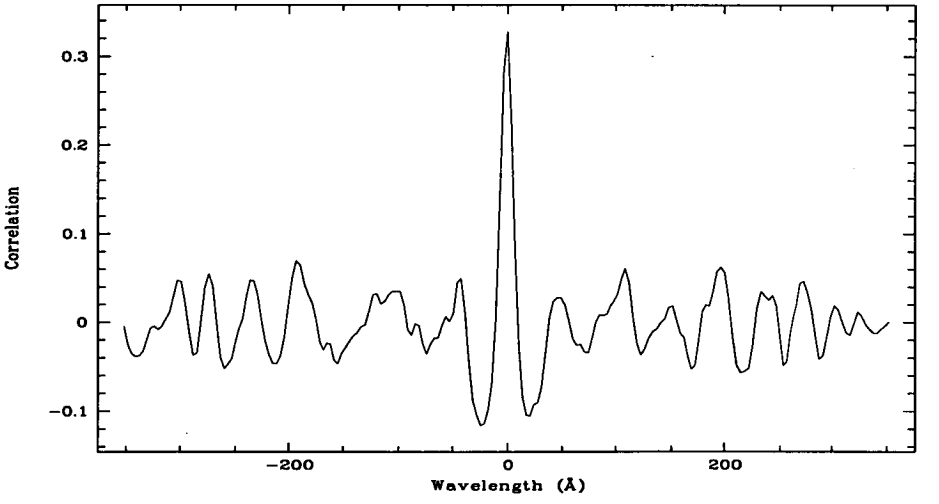

Figure 8.14: Cross-correlation function for event MB95009.

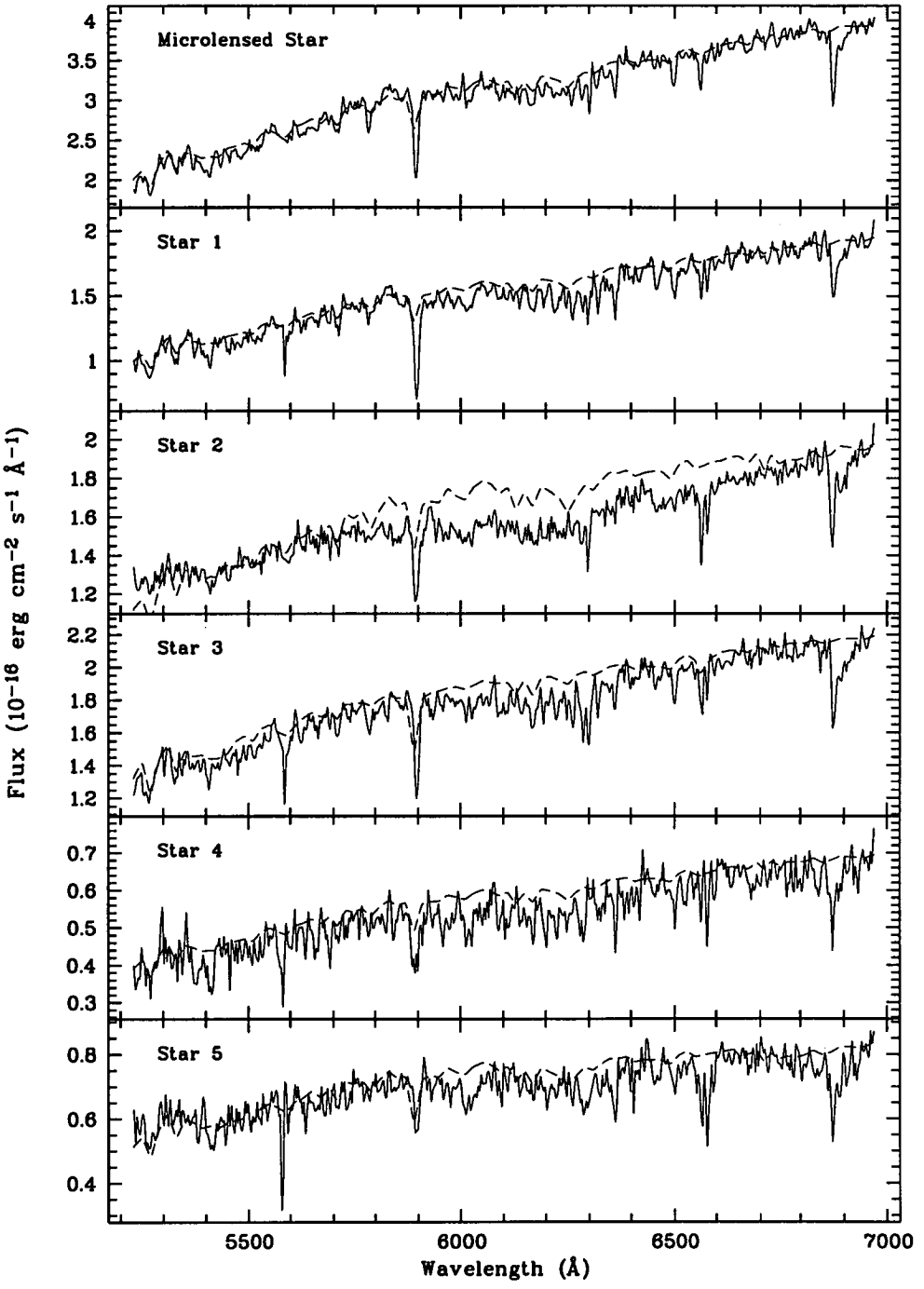

Figure 8.15: Spectra (solid line) and fitted models (dashed line) for event MB95009 and five non-microlensed stars in the field.

MB95010

The event MB95010 was observed using the B150 and O150 grisms giving a total wavelength coverage of 3790–6970 Å. The spectra of the microlensed source and five other stars in the field with their associated models are shown in Figure 8.17. The results from fitting models to the spectra are given in Table 8.10. Shown in Figure 8.16 is the cross-correlation function for the event MB95010. The radial velocities measured relative to the selected bright star are included in Table 8.10.

Spectrum	Classification	E_{B-V}	v_r (km s^{-1})
MB95010	G2III	0.99 ± 0.01	-41.1 ± 2.9
Star 1	G0III	0.68 ± 0.01	-79.5 ± 7.5
Star 2	K5III	0.99 ± 0.10	-197.3 ± 7.0
Star 3	K2V	0.88 ± 0.01	-97.4 ± 1.5
Star 4	K5III	0.78 ± 0.03	35.0 ± 6.8
Star 5	K3III	0.86 ± 0.15	-36.3 ± 4.1

Table 8.10: Classification, extinction, and relative radial velocity results for the MB95010 field.

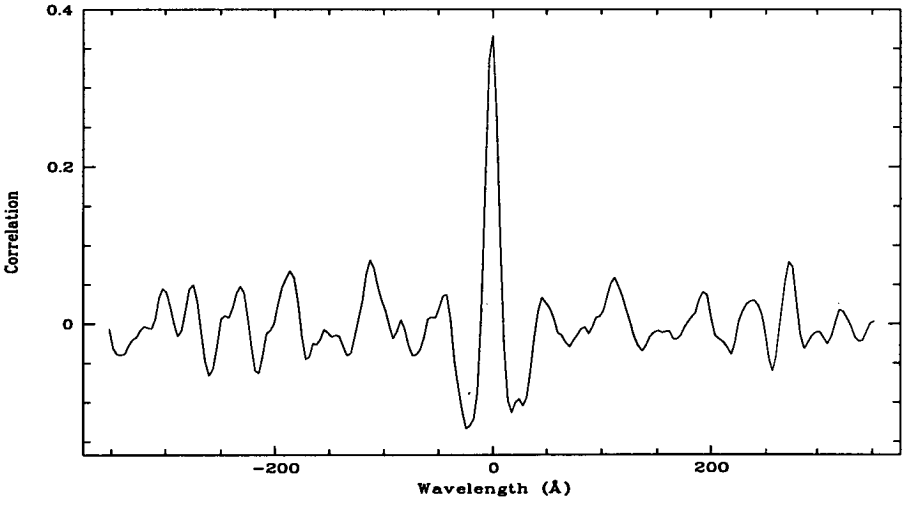

Figure 8.16: Cross-correlation function for event MB95010.

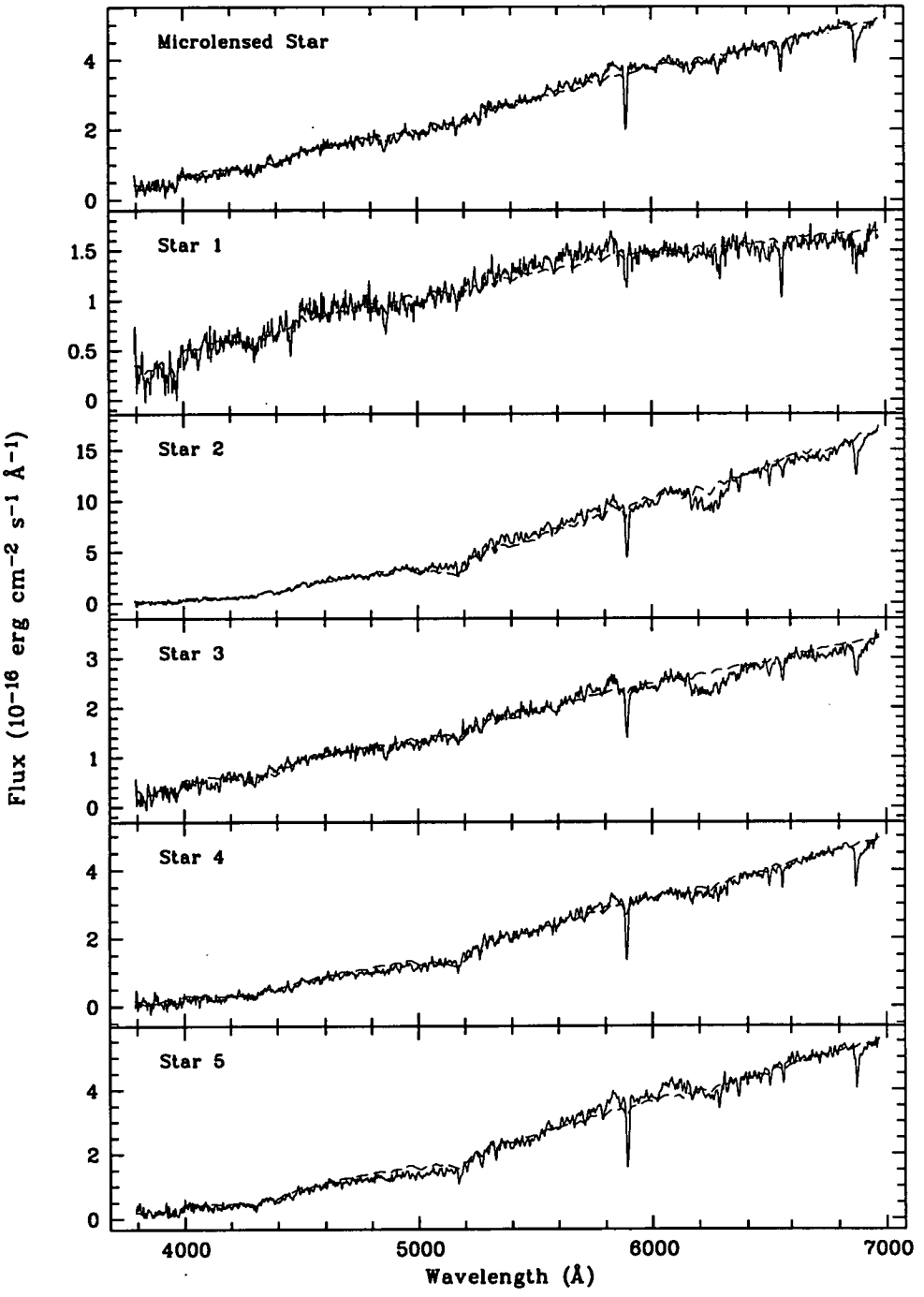

Figure 8.17: Spectra (solid line) and fitted models (dashed line) for event MB95010 and five non-microlensed stars in the field.

MB95012

The event MB95012 was observed using the B150 and O150 grisms giving a total wavelength coverage of 3790–6970 Å. The spectra of the microlensed source and five other stars in the field with their associated models are shown in Figure 8.19. The results from fitting models to the spectra are given in Table 8.11. Shown in Figure 8.18 is the cross-correlation function for the event MB95012. The radial velocities measured relative to the selected bright star are included in Table 8.11.

Spectrum	Classification	E_{B-V}	v_r (km s^{-1})
MB95012	K0III	0.58 ± 0.16	9.5 ± 3.0
Star 1	G2III	0.55 ± 0.09	-179.5 ± 7.3
Star 2	K2III	0.57 ± 0.03	-71.5 ± 2.9
Star 3	K3III	0.30 ± 0.10	109.7 ± 2.9
Star 4	G5V	0.44 ± 0.03	-40.0 ± 2.9
Star 5	G2III	0.28 ± 0.09	-146.9 ± 2.0

Table 8.11: Classification, extinction, and relative radial velocity results for the MB95012 field.

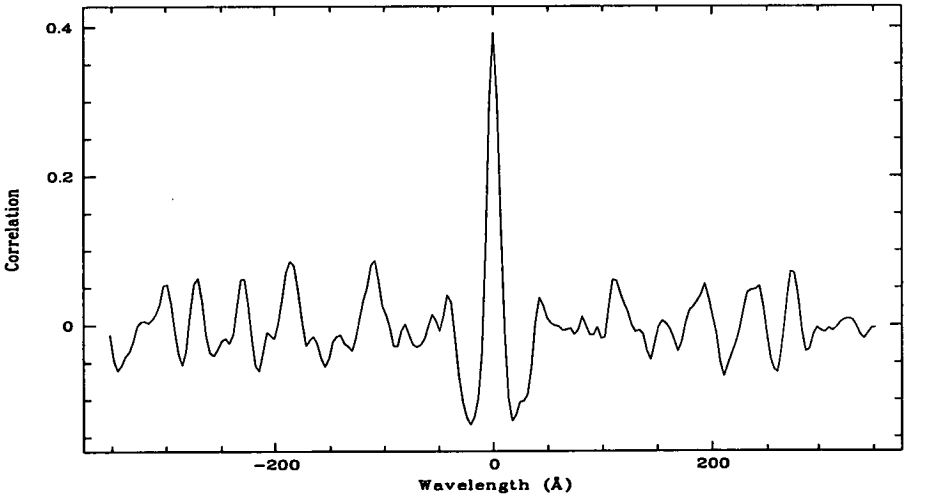

Figure 8.18: Cross-correlation function for event MB95012.

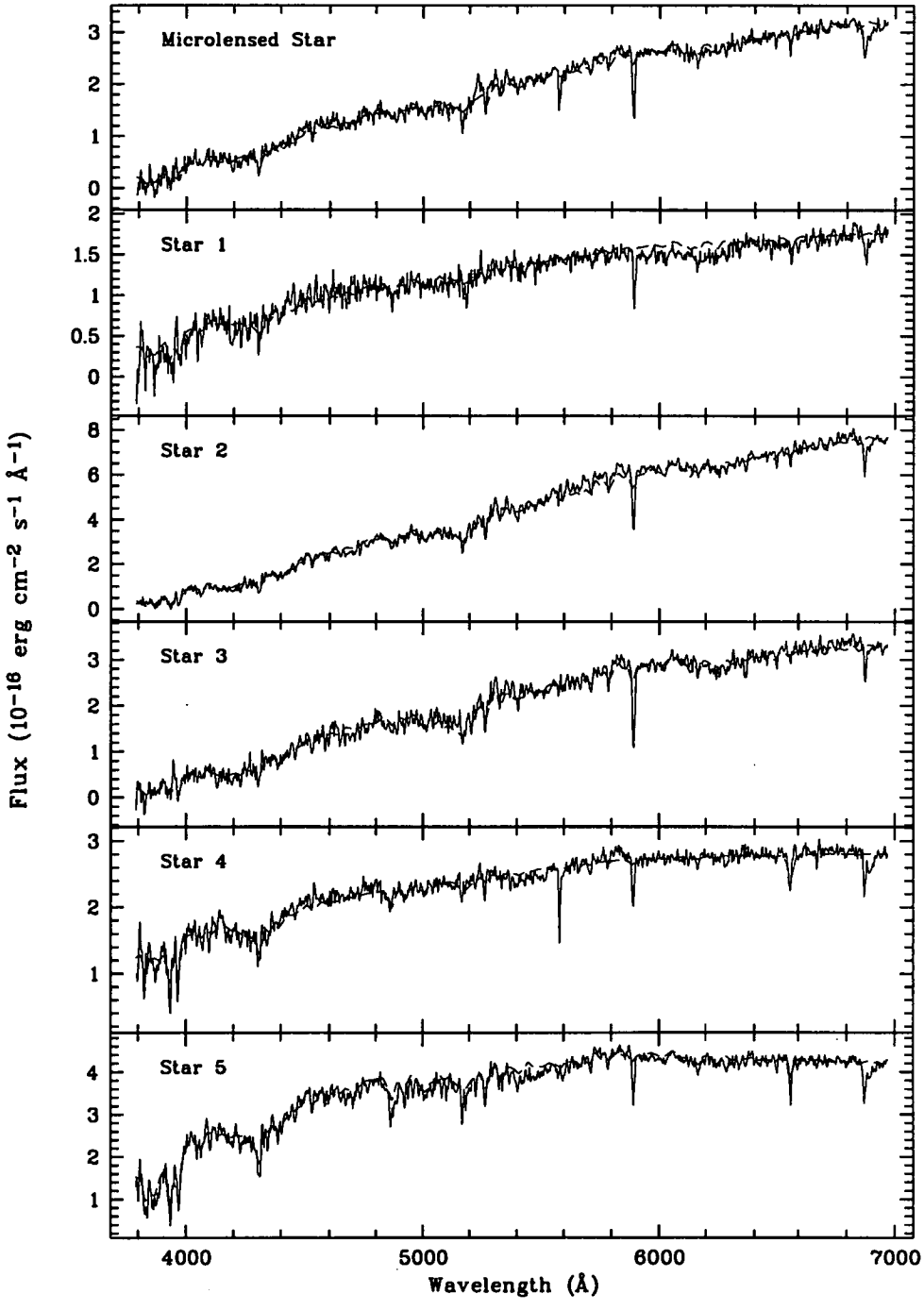

Figure 8.19: Spectra (solid line) and fitted models (dashed line) for event MB95012 and five non-microlensed stars in the field.

MB95013

The event MB95013 was observed using the B150, O150, and R300 grisms giving a total wavelength coverage of 3790–9920 Å, although only wavelengths up to 9200 Å were used in the modelling due to limitations in the model spectra (see Section 8.1.2). The spectra of the microlensed source and five other stars in the field with their associated models are shown in Figure 8.21. The results from fitting models to the spectra are given in Table 8.12. Shown in Figure 8.20 is the cross-correlation function for the event MB95013. The radial velocities measured relative to the selected bright star are included in Table 8.12.

Spectrum	Classification	E_{B-V}	v_r (km s^{-1})
MB95013	K1I	0.48 ± 0.07	-65.9 ± 4.1
Star 1	K5III	0.43 ± 0.04	-14.1 ± 4.3
Star 2	G2III	0.81 ± 0.01	-138.6 ± 2.7
Star 3	K5III	0.33 ± 0.10	-79.1 ± 6.8
Star 4	K5III	0.53 ± 0.04	72.4 ± 6.6
Star 5	K3III	0.46 ± 0.01	-98.9 ± 8.6

Table 8.12: Classification, extinction, and relative radial velocity results for the MB95013 field.

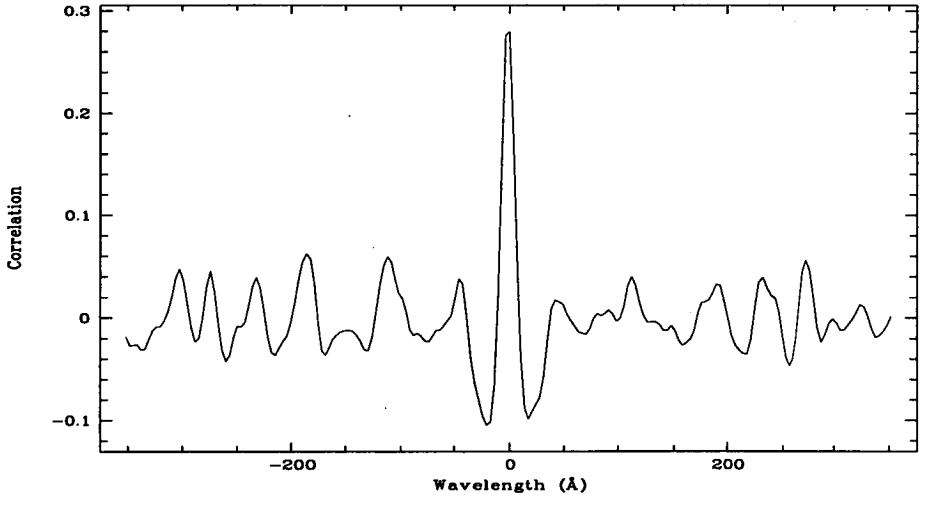

Figure 8.20: Cross-correlation function for event MB95013.

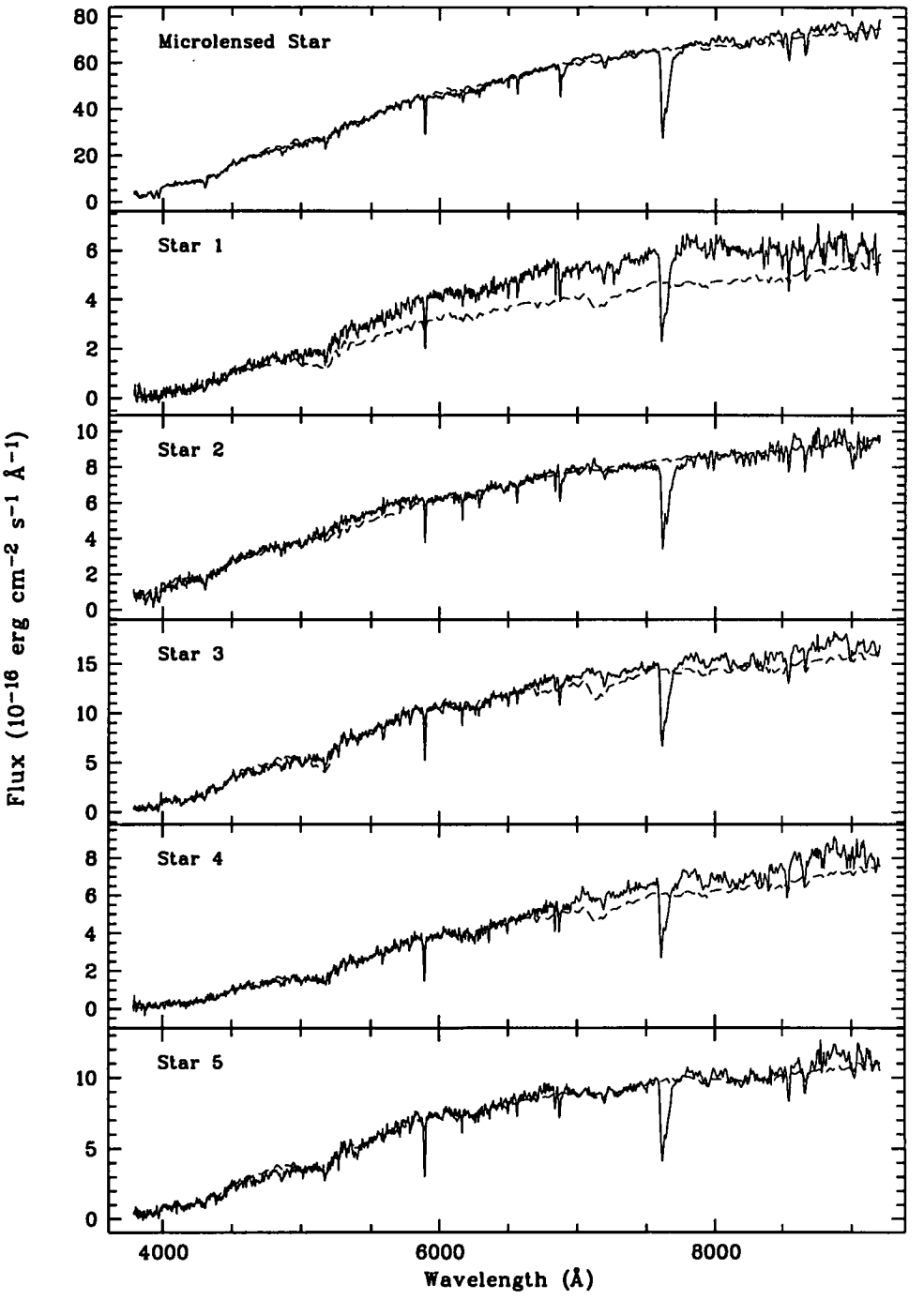

Figure 8.21: Spectra (solid line) and fitted models (dashed line) for event MB95013 and five non-microlensed stars in the field.

MB95014

The event MB95014 was observed using the O150 grism giving a total wavelength coverage of 5230–6970 Å. The spectra of the microlensed source and five other stars in the field with their associated models are shown in Figure 8.23. The results from fitting models to the spectra are given in Table 8.13. Shown in Figure 8.22 is the cross-correlation function for the event MB95014. The radial velocities measured relative to the selected bright star are included in Table 8.13.

Spectrum	Classification	E_{B-V}	v_r (km s^{-1})
MB95014	K4III	0.32 ± 0.04	-181.0 ± 6.4
Star 1	G8III	0.00 ± 0.01	-39.1 ± 6.1
Star 2	M0I	0.00 ± 0.01	-10.2 ± 3.0
Star 3	M0III	0.37 ± 0.07	-12.8 ± 1.7
Star 4	K4III	0.60 ± 0.06	6.4 ± 3.3
Star 5	K0III	0.47 ± 0.03	-32.2 ± 2.9

Table 8.13: Classification, extinction, and relative radial velocity results for the MB95014 field.

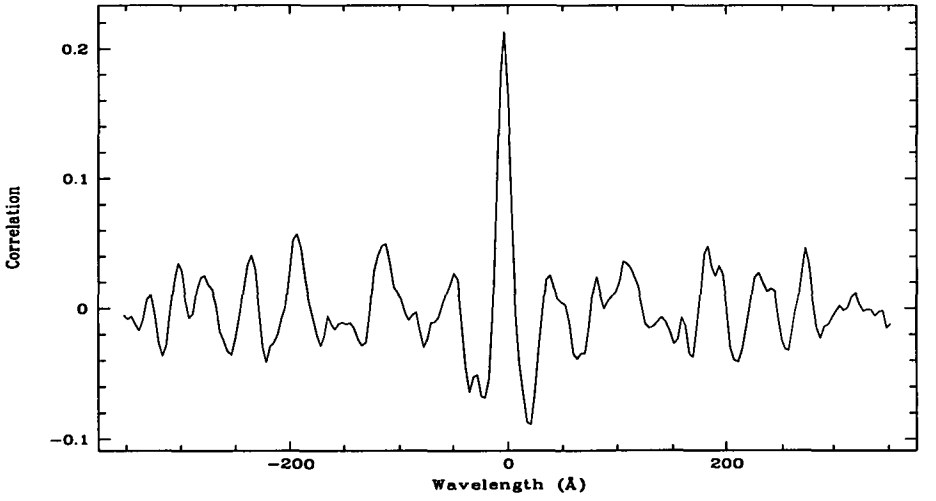

Figure 8.22: Cross-correlation function for event MB95014.

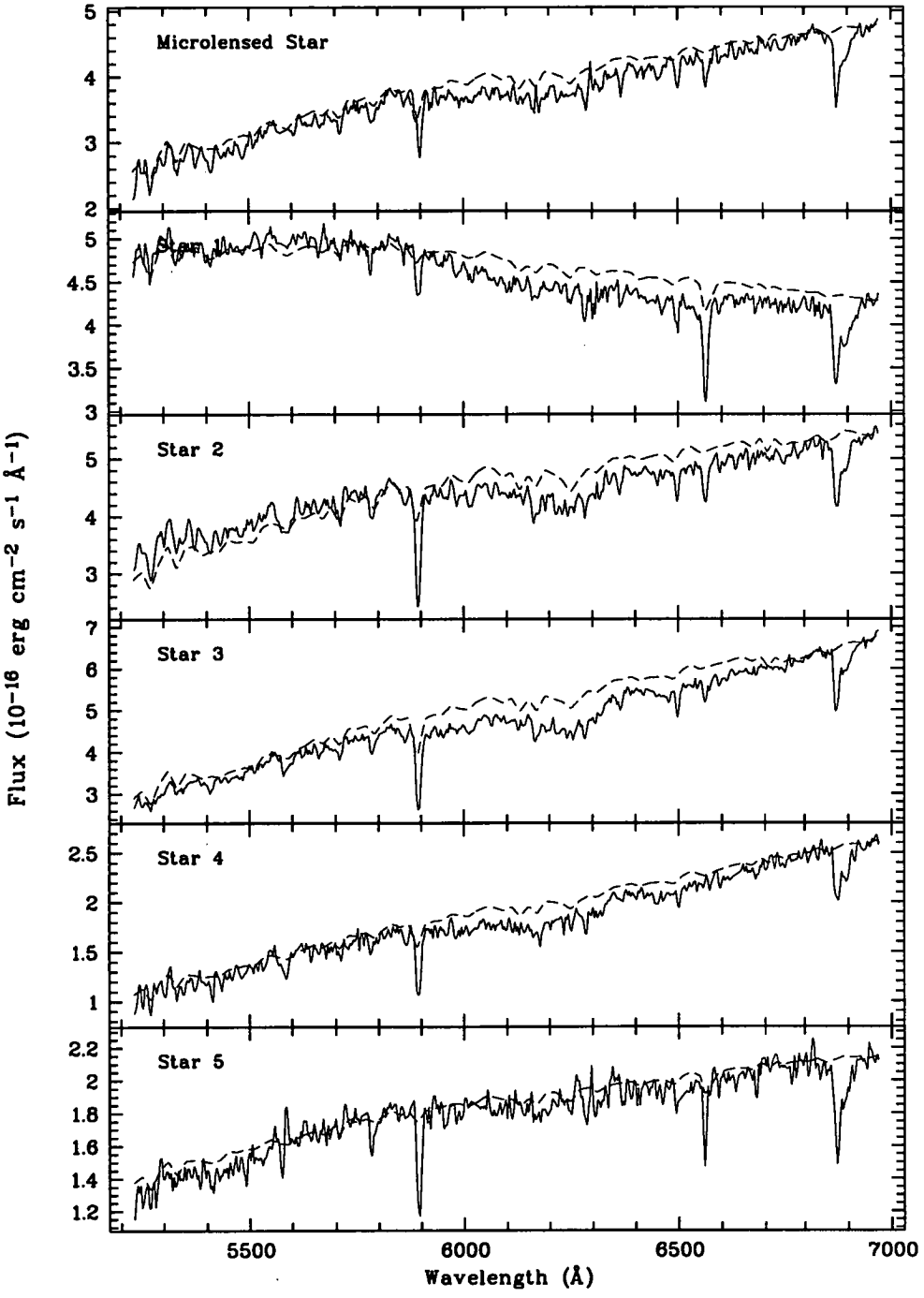

Figure 8.23: Spectra (solid line) and fitted models (dashed line) for event MB95014 and five non-microlensed stars in the field.

MB95017

The event MB95017 was observed using the B150 and O150 grisms giving a total wavelength coverage of 3790–6970 Å. Two observations of this event were made and five separate stars were chosen for each observation. The spectra of the microlensed source and five other stars in the field with their associated models for each observation are shown in Figures 8.25 and 8.27. The corresponding results from fitting models to the spectra are given in Tables 8.14 and 8.15 respectively. Shown in Figures 8.24 and 8.26 are the cross-correlation functions for the first and second observations of the event MB95017 respectively. The radial velocities measured relative to the selected bright star are included in Tables 8.14 and 8.15.

Spectrum	Classification	E_{B-V}	v_r (km s^{-1})
MB95017	G2III	0.56 ± 0.01	-71.0 ± 10.4
Star 1	G5III	0.19 ± 0.08	-74.8 ± 4.3
Star 2	K2III	0.10 ± 0.03	-134.3 ± 6.5
Star 3	G5III	0.25 ± 0.01	-46.9 ± 6.0
Star 4	G5III	0.61 ± 0.01	18.8 ± 4.2
Star 5	K2III	0.24 ± 0.07	-146.2 ± 2.5

Table 8.14: Classification, extinction, and relative radial velocity results for the first observation of the MB95017 field.

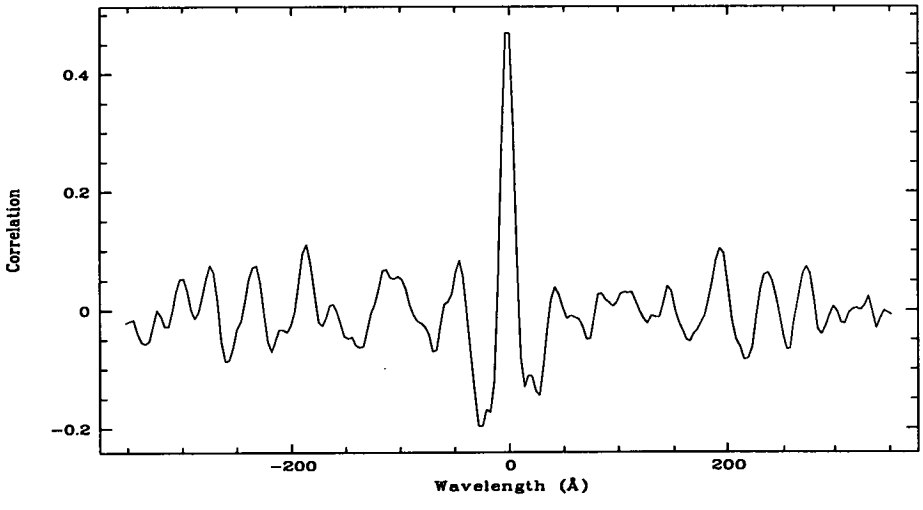

Figure 8.24: Cross-correlation function for the first observation of event MB95017.

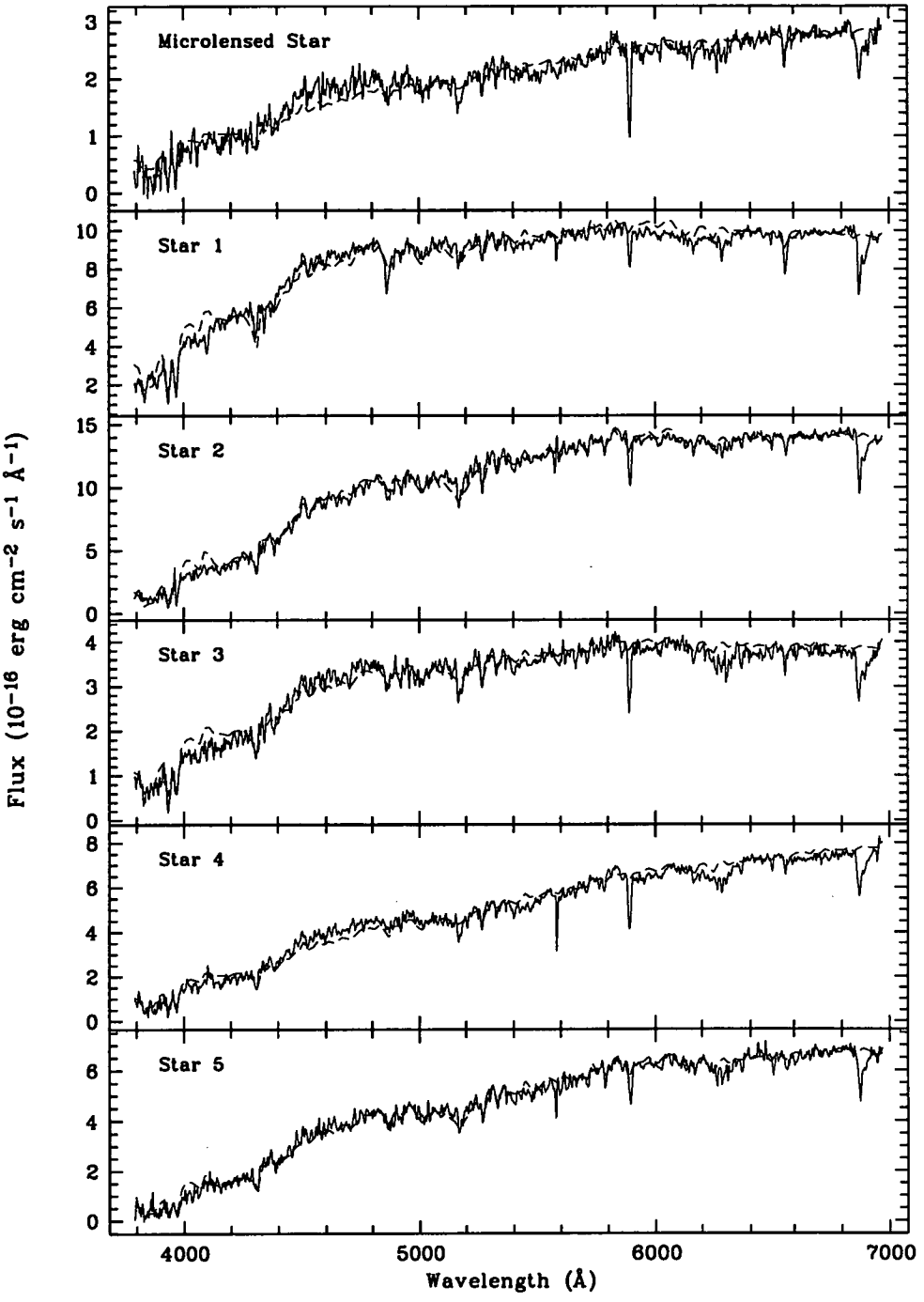

Figure 8.25: Spectra (solid line) and fitted models (dashed line) for the first observation of event MB95017 and five non-microlensed stars in the field.

The second observation of MB95017 has much better S/N than the first observation which was observed during a period of bad seeing. Hence, the results from the second observation were used in preference to the first in the final analysis. Although the estimation of the spectral type and extinction are in excellent agreement between the two observations, the estimation of the radial velocity differ by almost $50\,\mathrm{km\,s^{-1}}$. This is largely due to a cosmic ray incident upon the Hα line in the first observation.

Spectrum	Classification	E_{B-V}	$v_r\,(\mathrm{km\,s^{-1}})$
MB95017	G5III	0.55 ± 0.04	-21.3 ± 1.6
Star 1	K3III	0.42 ± 0.13	-72.1 ± 5.4
Star 2	K5III	0.33 ± 0.03	-150.1 ± 5.3
Star 3	K2III	0.64 ± 0.09	-72.1 ± 4.4
Star 4	G2III	0.29 ± 0.03	-182.1 ± 12.4
Star 5	K2III	0.46 ± 0.07	-180.9 ± 7.5

Table 8.15: Classification, extinction, and relative radial velocity results for the second observation of the MB95017 field.

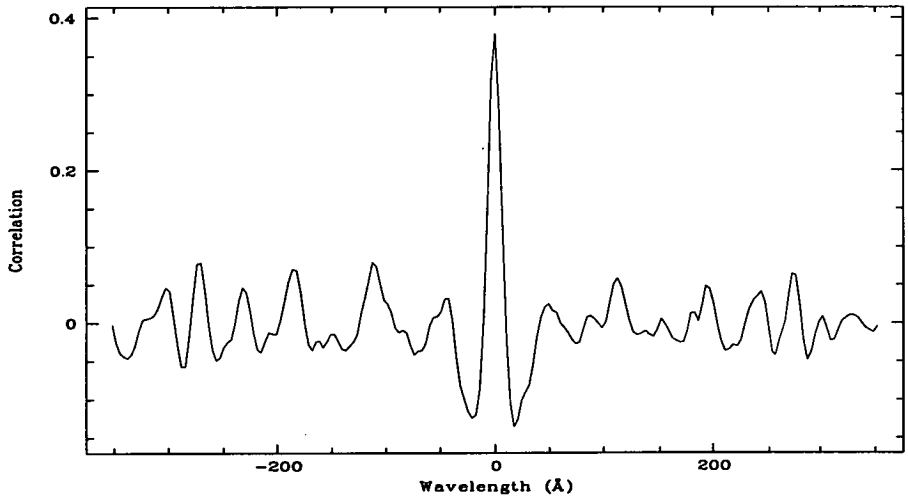

Figure 8.26: Cross-correlation function for the second observation of event MB95017.

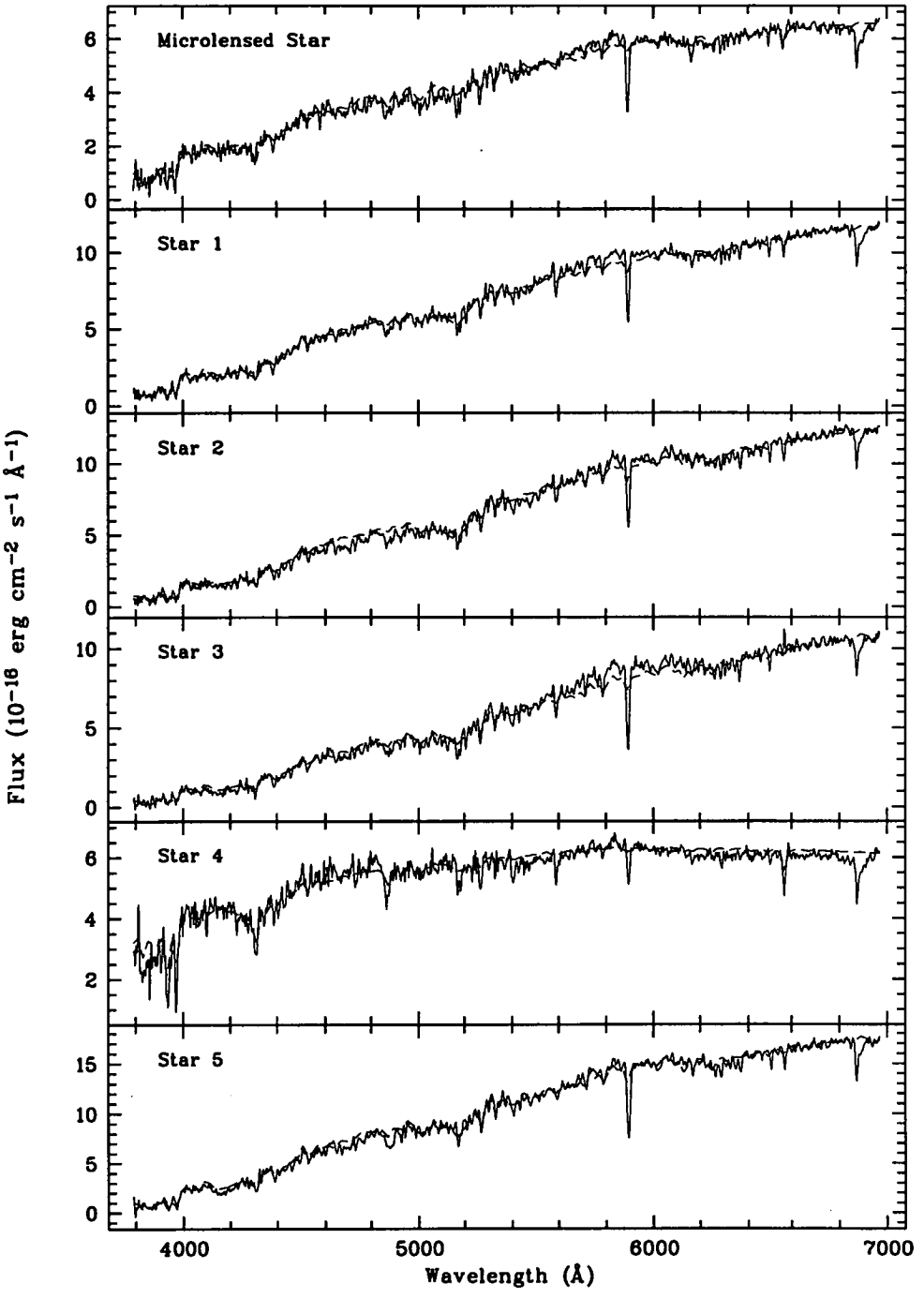

Figure 8.27: Spectra (solid line) and fitted models (dashed line) for the second observation of event MB95017 and five non-microlensed stars in the field.

MB95018

The event MB95018 was observed using the B150 and O150 grisms giving a total wavelength coverage of 3790–6970 Å. The spectra of the microlensed source and five other stars in the field with their associated models are shown in Figure 8.29. The results from fitting models to the spectra are given in Table 8.16. Shown in Figure 8.28 is the cross-correlation function for the event MB95018. The radial velocities measured relative to the selected bright star are included in Table 8.16.

Spectrum	Classification	E_{B-V}	v_r (km s^{-1})
MB95018	K0III	0.66 ± 0.09	-102.6 ± 1.9
Star 1	K4III	0.38 ± 0.09	42.1 ± 1.8
Star 2	K2III	0.64 ± 0.11	28.6 ± 1.6
Star 3	K4III	0.42 ± 0.07	-140.1 ± 8.9
Star 4	G5III	0.53 ± 0.01	-22.3 ± 3.1
Star 5	K5III	0.66 ± 0.09	-133.9 ± 3.7

Table 8.16: Classification, extinction, and relative radial velocity results for the MB95018 field.

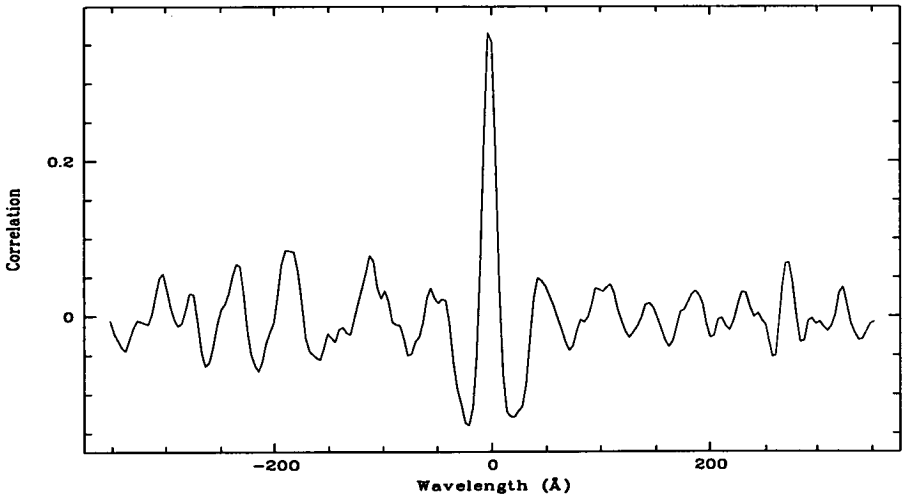

Figure 8.28: Cross-correlation function for event MB95018.

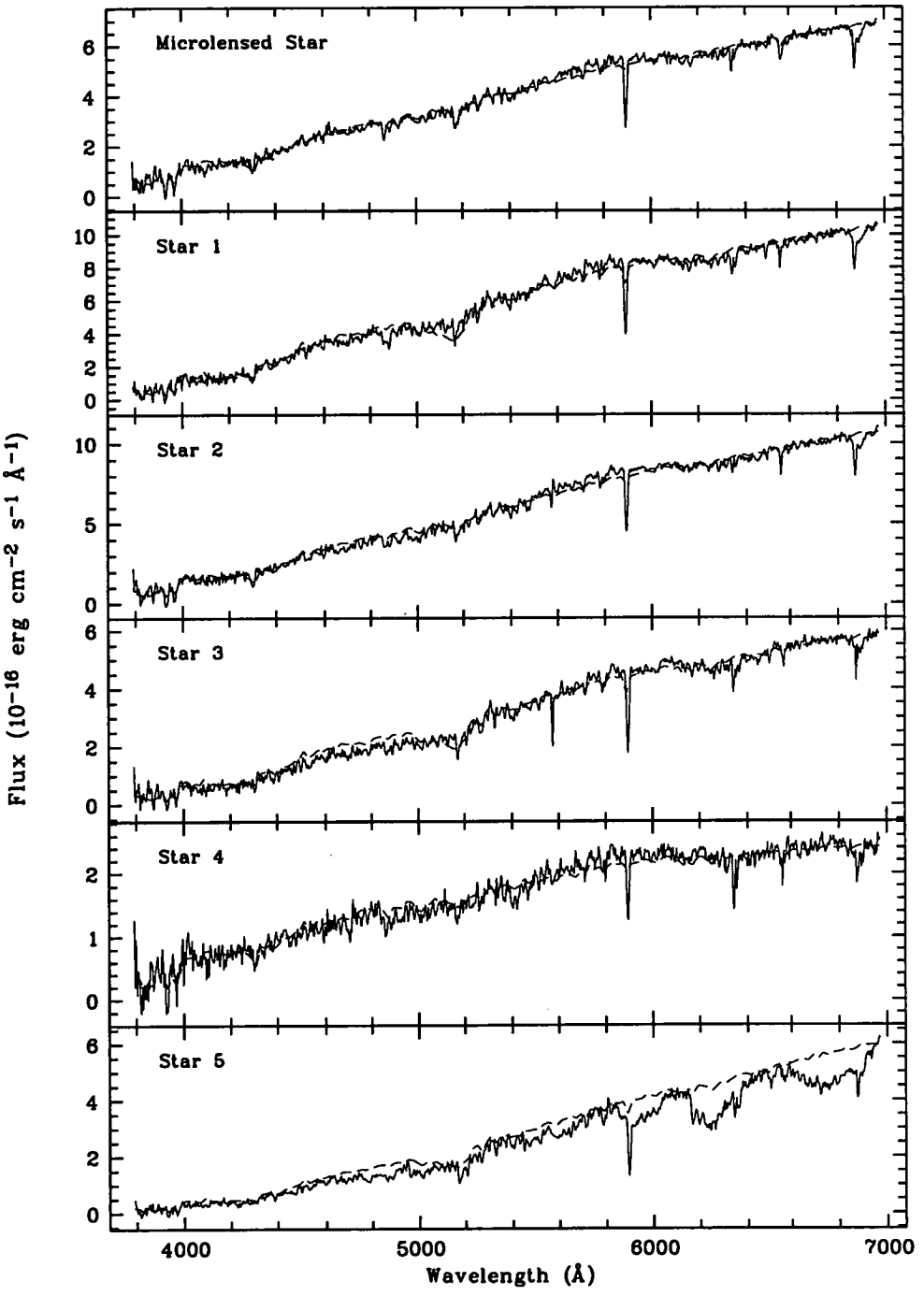

Figure 8.29: Spectra (solid line) and fitted models (dashed line) for event MB95018 and five non-microlensed stars in the field.

MB95019

The event MB95019 was observed using the B150 and O150 grisms giving a total wavelength coverage of 3790–6970 Å. The spectra of the microlensed source and five other stars in the field with their associated models are shown in Figure 8.31. The results from fitting models to the spectra are given in Table 8.17. Shown in Figure 8.30 is the cross-correlation function for the event MB95019. The radial velocities measured relative to the selected bright star are included in Table 8.17.

Spectrum	Classification	E_{B-V}	v_r (km s^{-1})
MB95019	G2III	0.47 ± 0.11	-62.3 ± 3.8
Star 1	G5III	0.43 ± 0.01	-3.9 ± 3.1
Star 2	G5III	0.30 ± 0.04	-112.7 ± 4.6
Star 3	G8III	0.52 ± 0.06	-39.9 ± 7.4
Star 4	K3III	0.35 ± 0.07	-89.9 ± 2.3
Star 5	G8III	0.21 ± 0.08	-101.7 ± 3.7

Table 8.17: Classification, extinction, and relative radial velocity results for the MB95019 field.

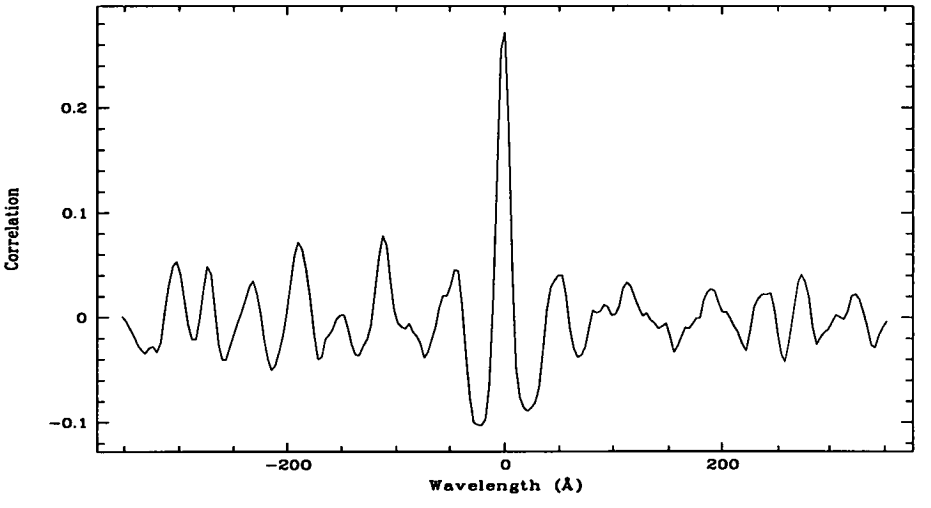

Figure 8.30: Cross-correlation function for event MB95019.

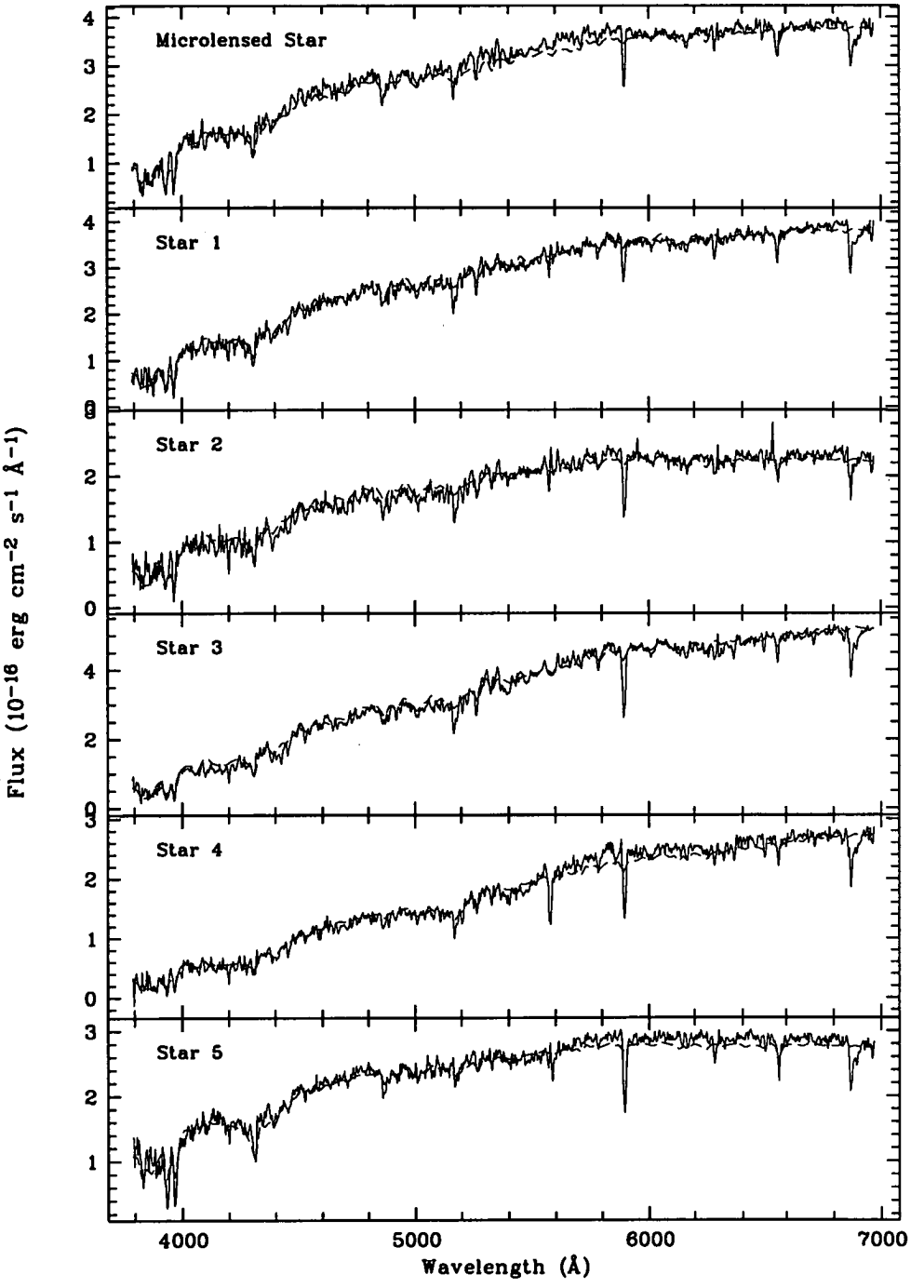

Figure 8.31: Spectra (solid line) and fitted models (dashed line) for event MB95019 and five non-microlensed stars in the field.

MB95030

The event MB95030 was observed using the B150 and B300 grisms giving a total wavelength coverage of 3750–6950 Å. The spectra of the microlensed source and five other stars in the field with their associated models are shown in Figure 8.34. The results from fitting models to the spectra are given in Table 8.18. The radial velocities measured relative to the selected bright star are included in Table 8.18.

Spectrum	Classification	E_{B-V}	v_r (km s^{-1})
MB95030	M2III	0.56 ± 0.02	-162.0 ± 17.7
Star 1	G8III	0.46 ± 0.07	-93.5 ± 11.7
Star 2	K3I	0.31 ± 0.20	-106.0 ± 7.2
Star 3	K1I	0.62 ± 0.22	-399.8 ± 9.1
Star 4	G5III	0.58 ± 0.07	-174.3 ± 12.3
Star 5	K0III	0.83 ± 0.09	-198.8 ± 6.5

Table 8.18: Classification, extinction, and relative radial velocity results for the MB95030 field.

The B150 spectrum (see Figure 8.32) was not used in the fitting procedure since the wavelength coverage of the B300 spectrum completely encompasses that of the B150 spectrum. The B150 spectrum was only used to measure the relative radial velocities for the MB95030 field since it has a much higher resolution than the B300 spectrum. The cross-correlation function for the event MB95030 is shown in Figure 8.33.

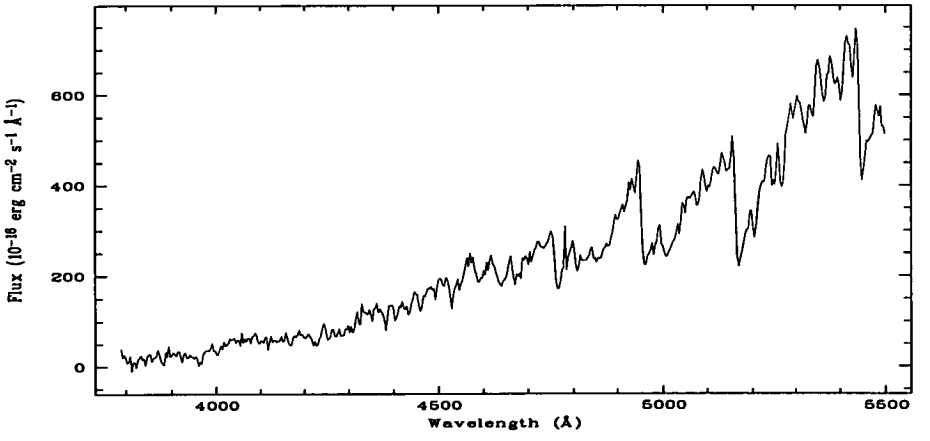

Figure 8.32: The B150 spectrum of event MB95030.

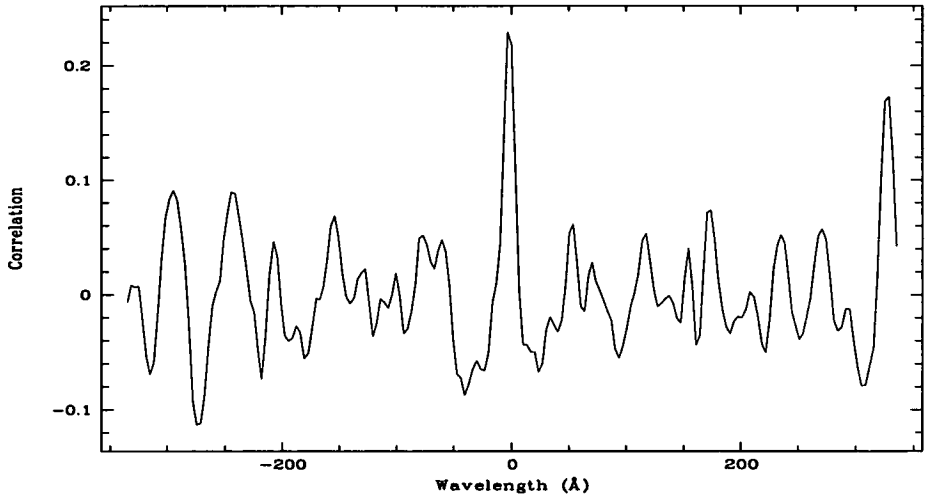

Figure 8.33: Cross-correlation function for event MB95030.

The event MB95030 has been studied in detail by the MACHO collaboration [16] who obtained spectra with a wavelength coverage of 6230–9340 Å. From this they were able to estimate a spectral type of M4III and a radial velocity of $v_r = 80 \pm 5\,\mathrm{km\,s^{-1}}$.

Comparison with the results presented here show that they are in agreement. Unfortunately limitations in the model spectra prevented an adequate fit to the spectrum for MB95030 (see Section 8.1.2). However, the result of M2III shows that an improvement in the resolution of the fitting procedure would allow greater accuracy for cooler stars. Combining the relative radial velocity of the MB95030 source with the estimated absolute velocity of the template star yields a radial velocity of $v_r = -63.5 \pm 41.3\,\mathrm{km\,s^{-1}}$. This places the MACHO measurement within the experimental errors of the value obtained in this study.

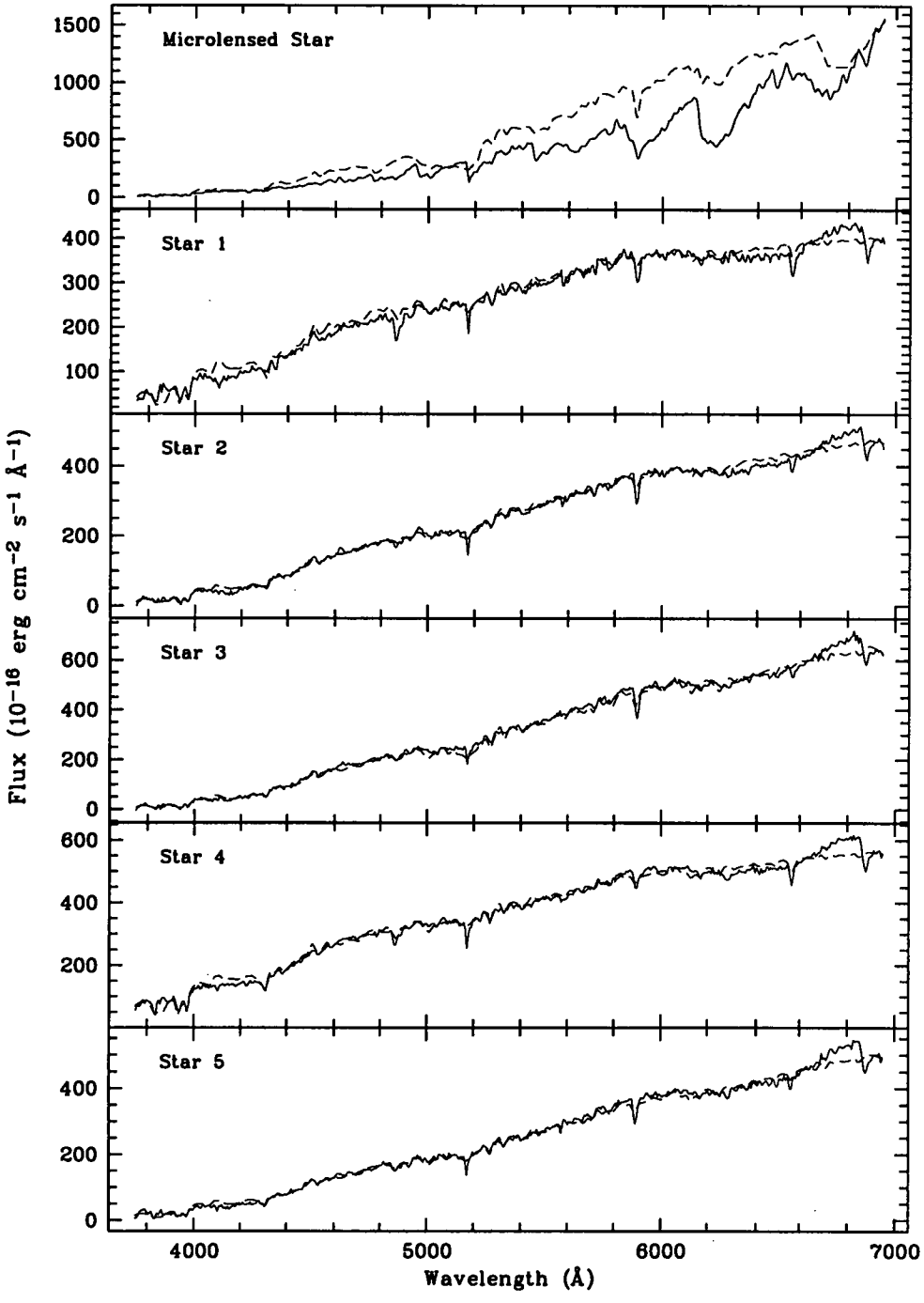

Figure 8.34: Spectra (solid line) and fitted models (dashed line) for event MB95030 and five non-microlensed stars in the field.

OB95003

The event OB95003 was observed using the O150 grism giving a total wavelength coverage of 5230–6970 Å. The spectra of the microlensed source and five other stars in the field with their associated models are shown in Figure 8.36. The microlensed source proved to have a very low S/N which produced unreliable results for the event and a few of the stars. The results from fitting models to the spectra are given in Table 8.19. Shown in Figure 8.35 is the cross-correlation function for the event OB95003. The radial velocities measured relative to the selected bright star are included in Table 8.19.

Spectrum	Classification	E_{B-V}	v_r (km s^{-1})
OB95003	K2I	0.08 ± 0.01	-63.1 ± 6.3
Star 1	K5V	0.00 ± 0.01	-374.2 ± 25.2
Star 2	K2III	0.55 ± 0.01	-11.3 ± 4.1
Star 3	G0V	0.00 ± 0.01	-34.6 ± 2.4
Star 4	K4III	0.42 ± 0.11	-9.6 ± 7.2
Star 5	M2III	0.43 ± 0.11	-83.8 ± 2.7

Table 8.19: Classification, extinction, and relative radial velocity results for the OB95003 field.

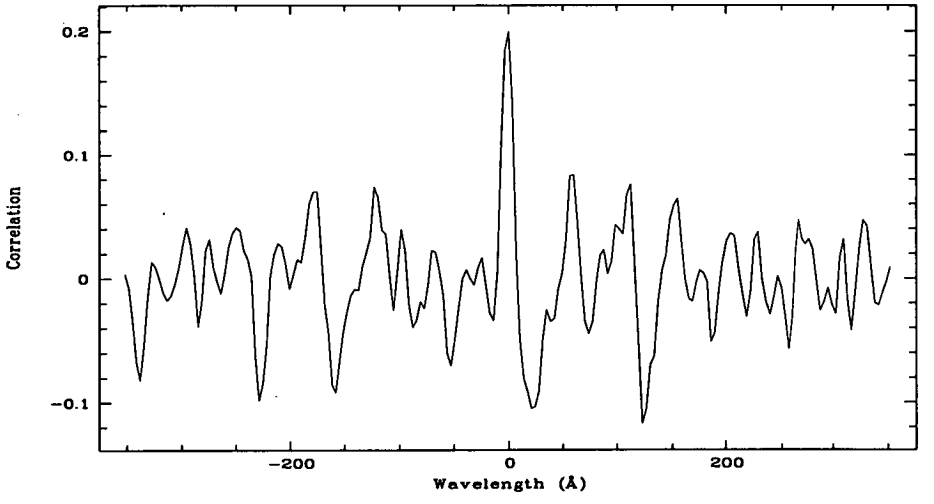

Figure 8.35: Cross-correlation function for event OB95003.

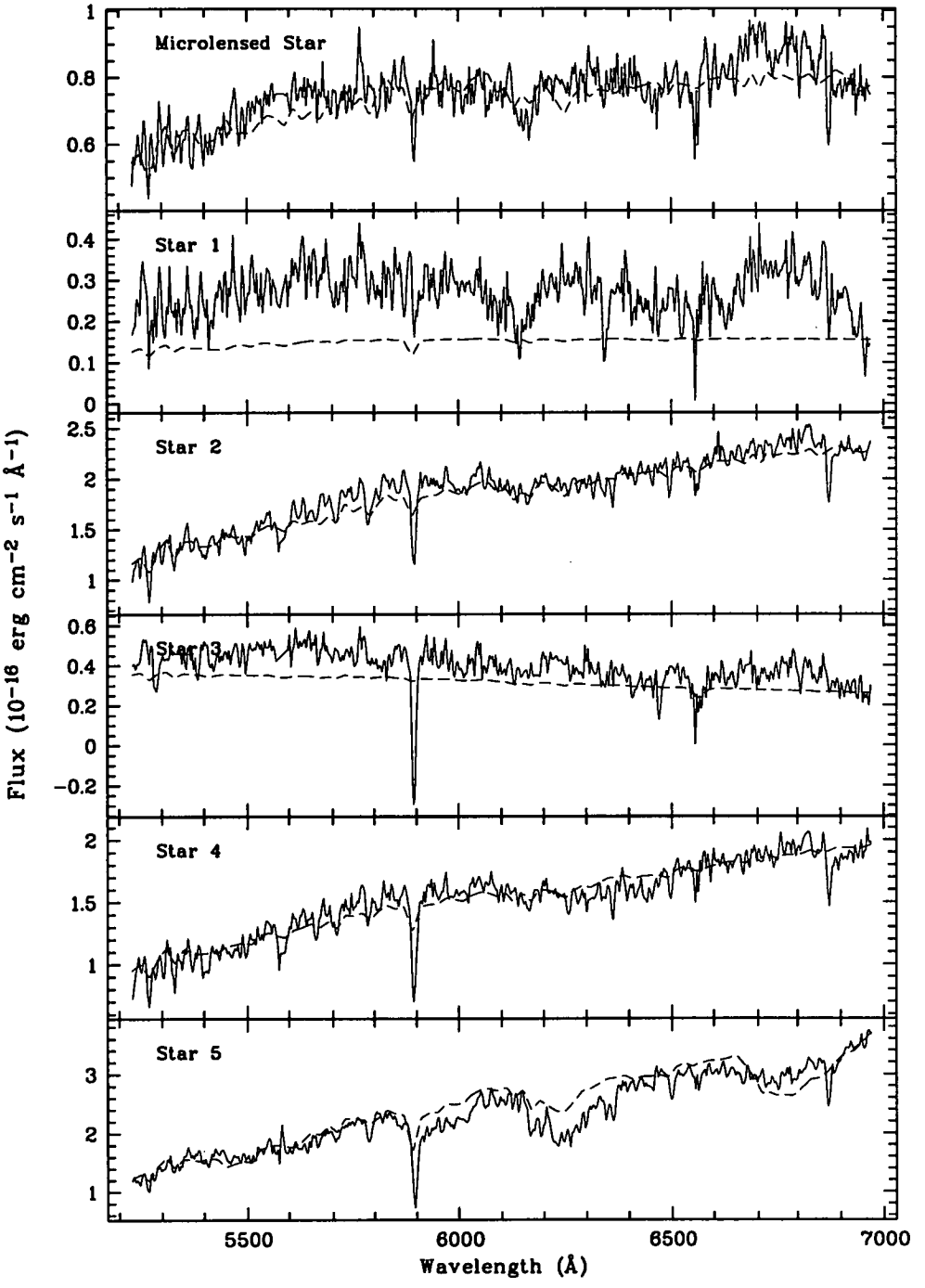

Figure 8.36: Spectra (solid line) and fitted models (dashed line) for event OB95003 and five non-microlensed stars in the field.

OB95007

The event OB95007 was observed using the O150 grism giving a total wavelength coverage of 5230–6970 Å. The spectra of the microlensed source and five other stars in the field with their associated models are shown in Figure 8.38. The results from fitting models to the spectra are given in Table 8.20. Shown in Figure 8.37 is the cross-correlation function for the event OB95007. The radial velocities measured relative to the selected bright star are included in Table 8.20.

Spectrum	Classification	E_{B-V}	v_r (km s^{-1})
OB95007	GOIII	0.79 ± 0.02	-137.9 ± 6.5
Star 1	KOIII	0.51 ± 0.01	-111.4 ± 3.5
Star 2	MOIII	0.00 ± 0.33	-94.7 ± 2.8
Star 3	K5III	0.15 ± 0.01	-150.5 ± 2.7
Star 4	K4III	0.20 ± 0.08	-100.2 ± 14.5
Star 5	MOIII	0.00 ± 0.25	-57.0 ± 2.2

Table 8.20: Classification, extinction, and relative radial velocity results for the OB95007 field.

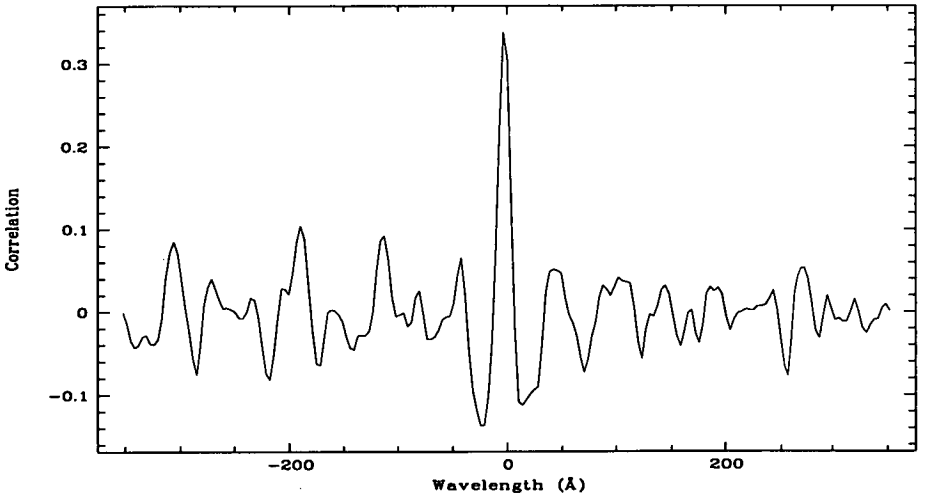

Figure 8.37: Cross-correlation function for event OB95007.

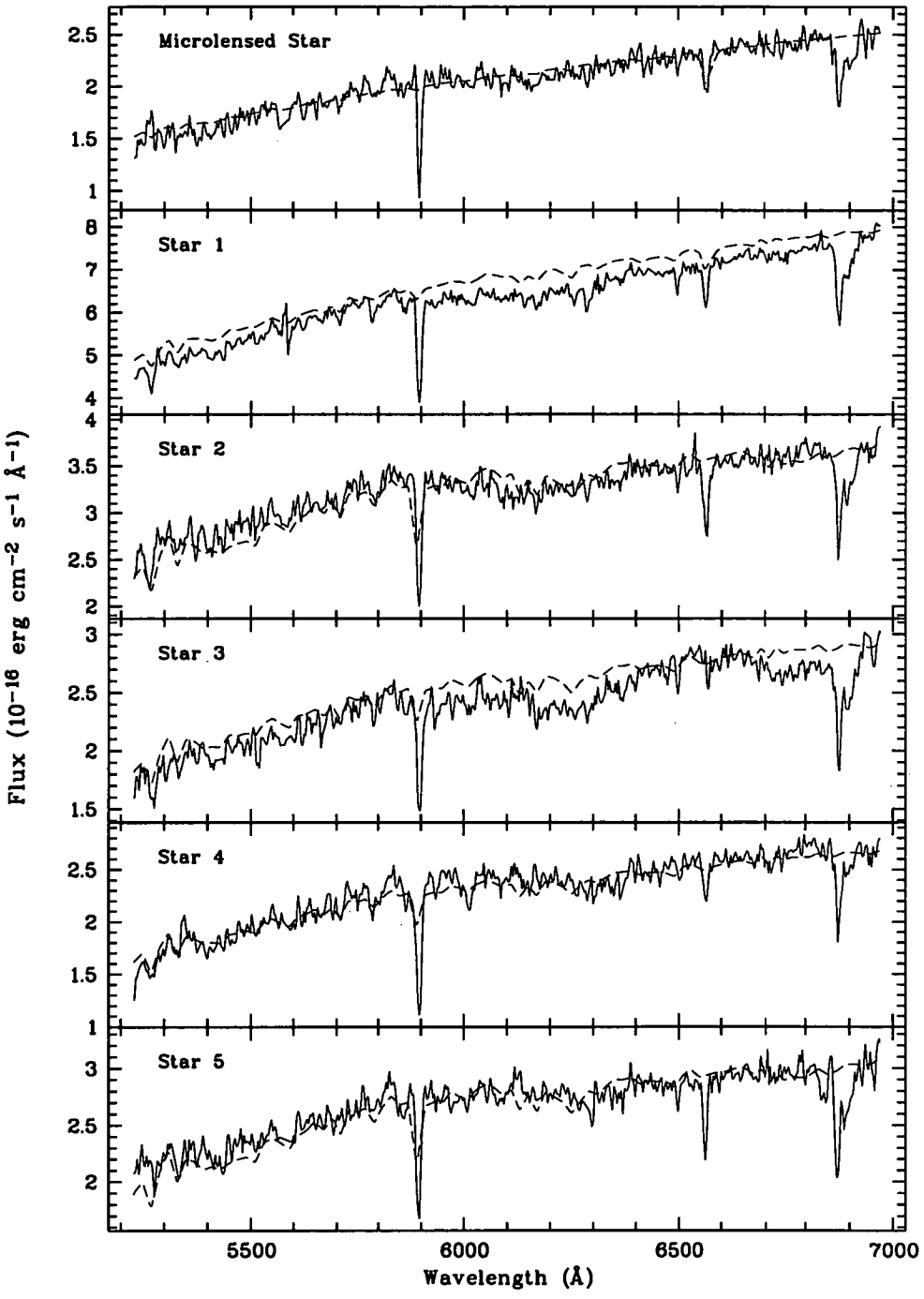

Figure 8.38: Spectra (solid line) and fitted models (dashed line) for event OB95007 and five non-microlensed stars in the field.

OB95016

The event OB95016 was observed using the B150 and O150 grisms giving a total wavelength coverage of 3790–6970 Å. The spectra of the microlensed source and five other stars in the field with their associated models are shown in Figure 8.40. The results from fitting models to the spectra are given in Table 8.21. Shown in Figure 8.39 is the cross-correlation function for the event OB95016. The radial velocities measured relative to the selected bright star are included in Table 8.21.

Spectrum	Classification	E_{B-V}	v_r (km s^{-1})
OB95016	G5III	0.60 ± 0.01	-102.9 ± 5.0
Star 1	M0III	0.68 ± 0.11	-47.9 ± 12.6
Star 2	K4III	0.56 ± 0.09	55.7 ± 4.1
Star 3	K4III	0.38 ± 0.10	-35.6 ± 15.1
Star 4	G0III	0.43 ± 0.01	0.6 ± 6.6
Star 5	K0III	0.55 ± 0.04	-123.3 ± 3.0

Table 8.21: Classification, extinction, and relative radial velocity results for the OB95016 field.

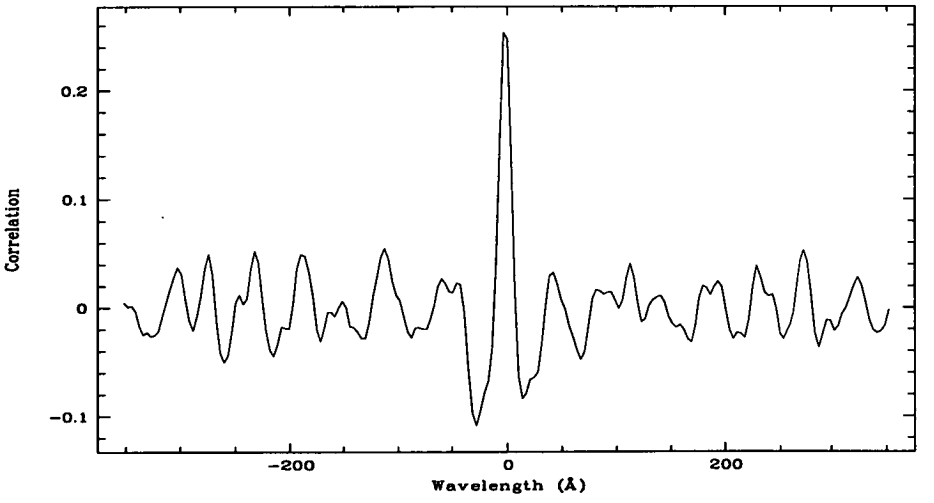

Figure 8.39: Cross-correlation function for event OB95016.

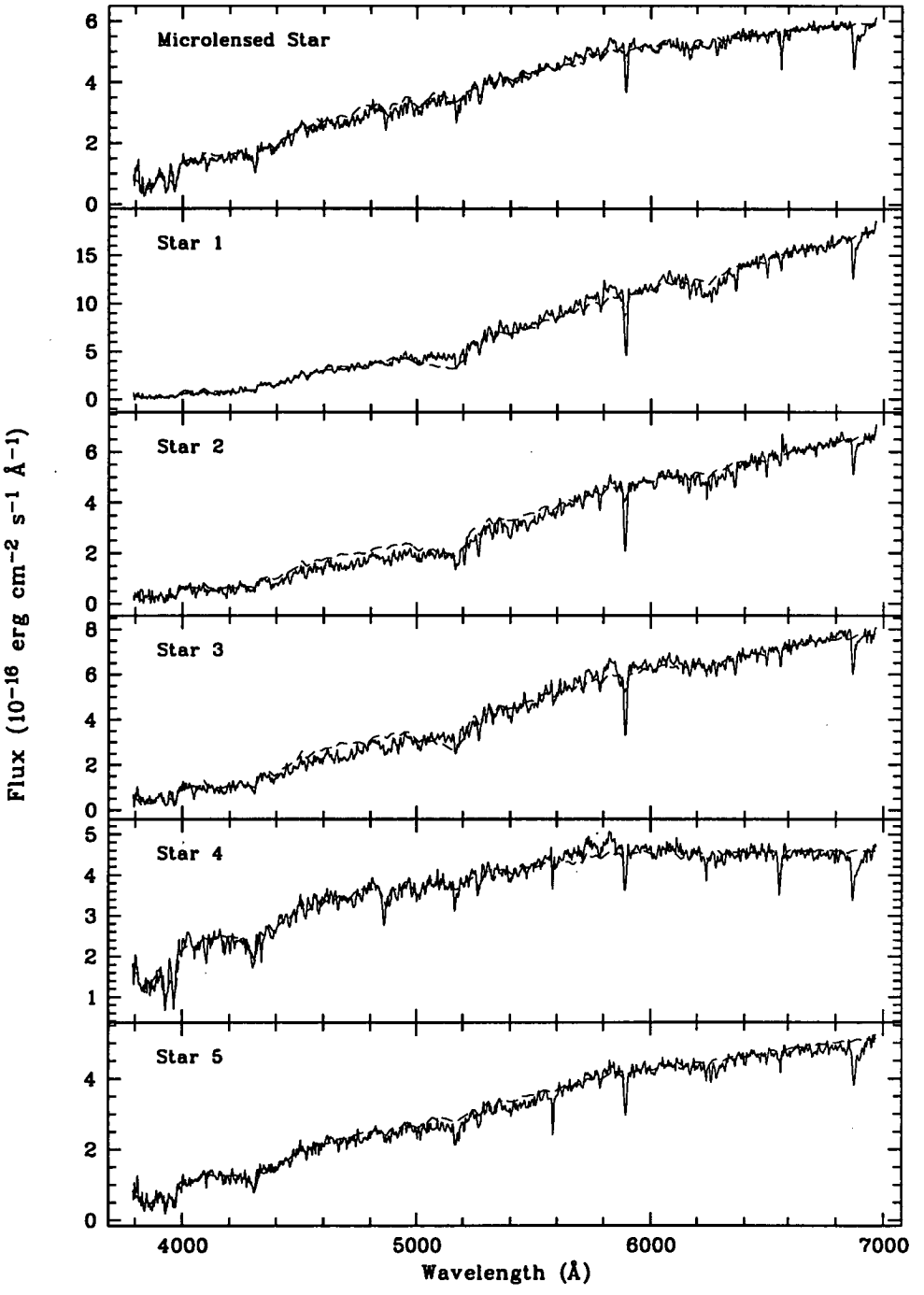

Figure 8.40: Spectra (solid line) and fitted models (dashed line) for event OB95016 and five non-microlensed stars in the field.

8.3 Conclusions from Spectra

In this chapter the results from determining the extinction and radial velocity properties exhibited in numerous spectra have been presented. For 8 of the 17 observed events, spectra were only obtained through the O150 grism. The limited wavelength range in these spectra (5230–6970 Å) made the fitting of an adequate model a more challenging task and may have introduced additional uncertainty into the outcome of these fits. Most stars were fitted better by the lower metallicity models. This is an expected result since the Galactic bulge tends to be dominated by population II stars. Due to the considerably low S/N in the spectra of events DB95002 and OB95003, these events and their associated non-microlensed stars are not included in the following analysis.

8.3.1 Colour-Magnitude Diagram Analysis

There have been several studies performed on Galactic bulge CMDs, such as Terndrup [99] who was the first to use a CCD in this analysis. The OGLE collaboration has since presented CMDs of 14 fields surveyed in the direction of the Galactic bulge [103]. Some of the features common to these CMDs have been further studied, such as the well-defined red clump branch [94] and the distribution of disk stars [76].

During the 1995 PLANET observing season [7], photometric data from 7 of the 17 fields studied in this chapter were obtained. The CMDs for the individual fields were constructed by Dr. Penny Sackett and were then combined into a single CMD by the author, as shown in Figure 8.41. The combined CMD contains almost 22000 stars from the MACHO fields 10, 12, 13, 17, 18, 19, and 30. Since the distribution of stars in the individual CMDs was almost identical, the colours and magnitudes were calibrated by adopting the position for the bulge red clump giants as estimated by Paczyński & Stanek [80], who found an average $(V - I)$ for the red clump region of 1.22 and an average I magnitude of 14.34. The microlensed sources are shown in blue in the CMD and the non-microlensed sources are shown in red.

The combined CMD is in good agreement with the CMDs published by OGLE and also with those presented in Chapter 4. As expected, the CMD is dominated by bulge stars contained is a wide main sequence turnoff point and the red giant branch. Also visible in the diagram is a high concentration of stars in the blue part of the CMD, suggested to be dominated by disk stars [76]. The non-microlensed stars chosen for the study in this chapter are of similar brightness to the microlensed sources. The combined CMD shows that these stars lie within the same sample as the microlensed sources and are generally located in the recognisable main sequence or red giant branch. Hence, the non-microlensed stars are fairly typical of the population towards the Galactic bulge and are suitable for use in this study.

Star	Classification	m_V	V − I	M_V
MB95010	G2III	16.25	0.65	1.63
Star 1	G0III	16.13	0.67	1.51
Star 2	K5III	14.28	1.69	-0.34
Star 4	K5III	15.67	1.40	1.05
Star 5	K3III	15.63	1.41	1.01
MB95012	K0III	16.27	1.18	1.65
Star 1	G2III	17.15	0.94	2.52
Star 2	K2III	15.86	1.29	1.24
Star 3	K3III	15.45	1.38	0.83
Star 4	G5V	16.82	0.66	2.20
Star 5	G2III	16.02	0.59	1.40
MB95013	K1I	13.38	1.24	-1.24
Star 1	K5III	15.40	1.39	1.78
Star 2	G2III	14.96	1.18	0.34
Star 3	K5III	15.38	1.25	0.76
Star 4	K5III	15.46	1.42	0.84
Star 5	K3III	15.43	1.25	0.81
MB95017	G5III	16.58	0.88	1.94
Star 1	G5III	14.57	0.52	-0.05
Star 3	G5III	15.70	0.58	1.08
MB95018	K0III	15.78	1.13	1.16
Star 1	K4III	14.66	1.21	0.04
Star 2	K2III	14.98	1.22	0.36
Star 3	K4III	15.79	1.41	1.17
Star 4	G5III	16.64	0.84	2.02
Star 5	K5III	14.20	2.04	-0.42
MB95019	G2III	15.96	0.75	1.34
Star 1	G5III	15.66	0.96	1.04
Star 2	G5III	17.45	1.06	2.83
Star 3	G8III	16.17	1.14	1.55
Star 4	K3III	16.66	1.18	2.04
Star 5	G8III	16.26	1.01	1.64
MB95030	M2III	14.28	2.55	-0.34
Star 1	G8III	14.80	0.54	0.28
Star 2	K3I	12.73	1.00	-1.89
Star 3	K1I	14.20	1.21	-0.42
Star 4	G5III	14.55	0.57	-0.07

Table 8.22: Classifications derived from spectra, dereddened apparent magnitudes and colours, and an estimate of the absolute magnitude for each of the microlensed and non-microlensed sources of interest included in the CMD.

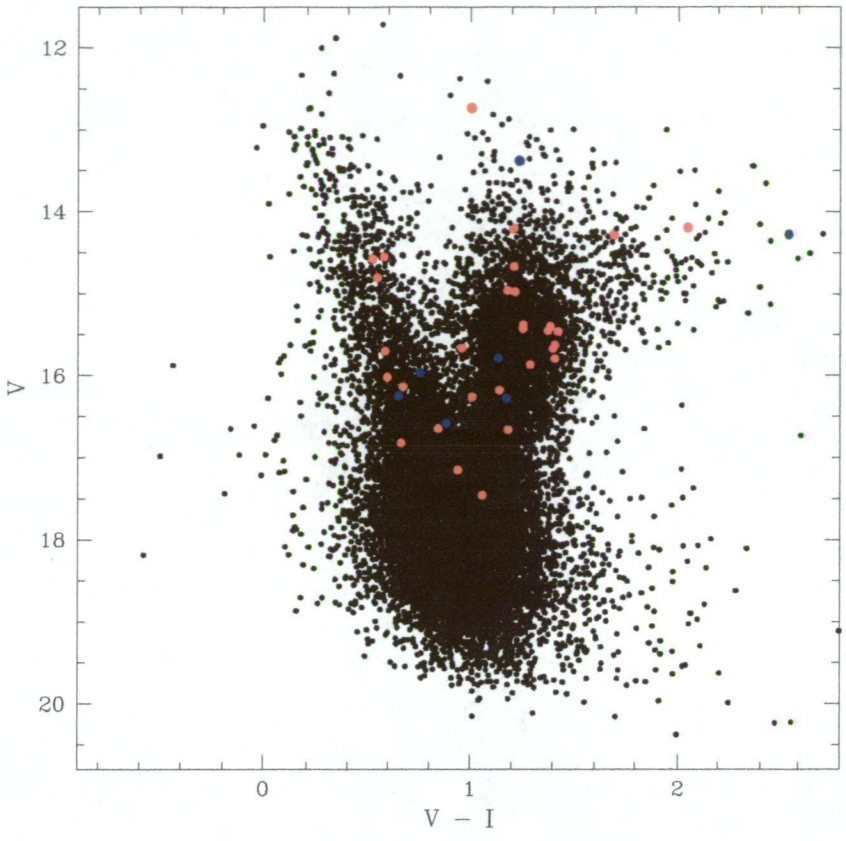

Figure 8.41: Combined colour-magnitude disgrams for the MACHO fields 10, 12, 13, 17, 18, 19, and 30. The microlensed sources are shown in blue and the non-microlensed sources are shown in red.

It is of interest to compare the magnitudes and colours of the sources of interest contained in the CMD with the spectral classifications derived from the spectra in Section 8.2. Shown in Table 8.22 are these results along with an estimate of the absolute magnitude M_V. The value of M_V derived here assumes that the peak of the red clump is at $m_I = 14.34$ and $(V - I) = 1.22$, as found by Paczyński & Stanek [80]. This is equivalent to assuming that the star is in the middle of the bulge (corresponding to a distance modulus of 14.62). The error in M_V is dominated by the intrinsic dispersion of the bulge stars, which is $\sigma_V \sim 1.5$ magnitudes. These results show that the luminosities measured from the CMD are roughly consistent with the classifications derived from the spectra and that giant stars have been preferentially selected since they are most likely to be in the Galactic bulge. Note that the magnitudes and colours shown in Table 8.22 are not the calibrated values but they are the expected dereddened magnitudes and colours if the sources were at the middle of the Galactic bulge.

8.3.2 Extinction Bias

From the discussion in Chapter 6, it is expected that the microlensed sources will show an extinction offset relative to the unlensed stars. It was shown that the mean extinction for microlensed sources should lie between $E_{B-V} = 0.4$ and $E_{B-V} = 0.8$. It has been found by Stanek [95] that the expected offset in apparent magnitudes between lensed and unlensed stars may be as large as 0.2 magnitudes. However, this offset is due largely to the distance modulus. The magnitude offset due to extinction will be an additional factor.

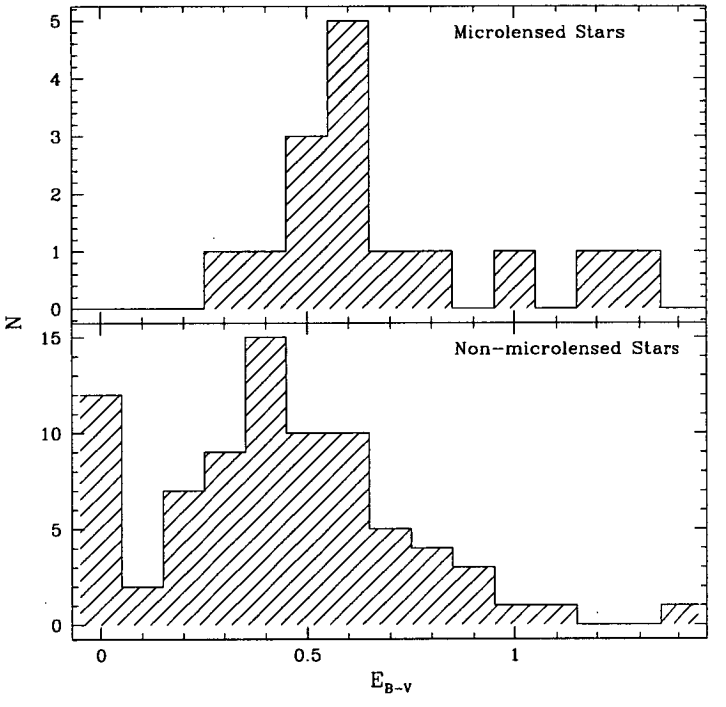

Figure 8.42: Histogram of extinction values for microlensed and non-microlensed stars.

Shown in Figure 8.42 is a histogram of the extinction for microlensed and non-microlensed stars. There is a surprisingly large number of stars with little or no extinction amongst the non-microlensed stars which is most likely due to disk stars of low mass. This could be explained in part by the findings of Paczyński *et al* [76] that indicate that there is an excess of disk stars by a factor of ~ 2 between us and a distance of 2.5 kpc towards the Galactic bulge, and a rapid drop by a factor of ~ 10 beyond that distance. The average extinction for the microlensed sources is $E_{B-V} = 0.68$ and is $E_{B-V} = 0.43$ for the non-microlensed stars. As expected, the distributions peak at these average values. The offset between the two mean values of $\Delta E_{B-V} = 0.25$ is equivalent to a magnitude offset of ≈ 0.80.

To investigate the significance between the two mean values, a *t-test* was performed on the histogram data. A value of $t = 3.07$ was obtained for 93 degrees of freedom which results in a probability of $p = 0.01$. In other words, the difference in the mean values of the two distributions is significantly different at the 99% confidence level. To test how much weight is held by the unlensed stars with zero extinction, the t-test was performed again after removing these stars from the sample. This reduced the values to $t = 2.42$ for 81 degrees of freedom which results in a probablility of ≈ 0.02, or significance at the 98% confidence level.

This test assumes a normal distribution for the data sets which is difficult to determine given the relatively small number of microlensed sources included in this sample. These results appear to agree with the previous discussions regarding the extinction bias of microlensed sources and a clear trend is seen in the presented histogram. However, as was suggested by Stanek [95], in order to unambiguously show this extinction bias then it is estimated that ~ 100 sources would be required in the sample. However, it is easier to observe the extinction bias than the magnitude bias since the intrinsic magnitudes of the sources and the lenses have a much larger spread which overlap with each other.

From the extinction distribution for microlensed sources it is possible to make an estimate of the fraction of bulge-bulge lensing. If we assume that microlensed sources with an extinction greater than $E_{B-V} = 0.4$ are on the far side of the bulge then it is also probable that the lens is located in the bulge (see Figure 6.12). Using this method, a simple estimate of the fraction of bulge-bulge lensing is found to be $\sim 70\%$. This value is slightly higher than the 60% predicted by Kiraga & Paczyński [54].

For self-lensing within the bulge, the Einstein ring size increases if the distance between the lens and the source is larger. Since the microlensed sources are preferentially located on the far side of the bulge, it is expected that the characteristic time scale should be longer for events exhibiting larger extinction. However, the time scale of an event is also a function of the velocities of the lens and the source and so the time scale may depend upon the Galactic kinematics. If the velocity dispersion is the dominant component and is relatively constant then the time scale should be larger for a higher value of extinction. On the other hand, if rotation is the dominant component then the time scale may show a behaviour which is only a small function of the extinction value.

Shown in Figure 8.43 is a plot of the extinction of the microlensed sources as a function of their characteristic time scales. The top frame uses the abbreviated names of the events to show their positions on the plot and the bottom frame shows the corresponding data points with error bars. There is a trend visible in the data if one excludes the points corresponding to MB95003 and MB95013. MB95013 is excluded because it is a very bright event and, since it has relatively low extinction, is probably a disk star. MB95003 is excluded on the basis of its extremely short time scale which could mean that the source and the lens are very

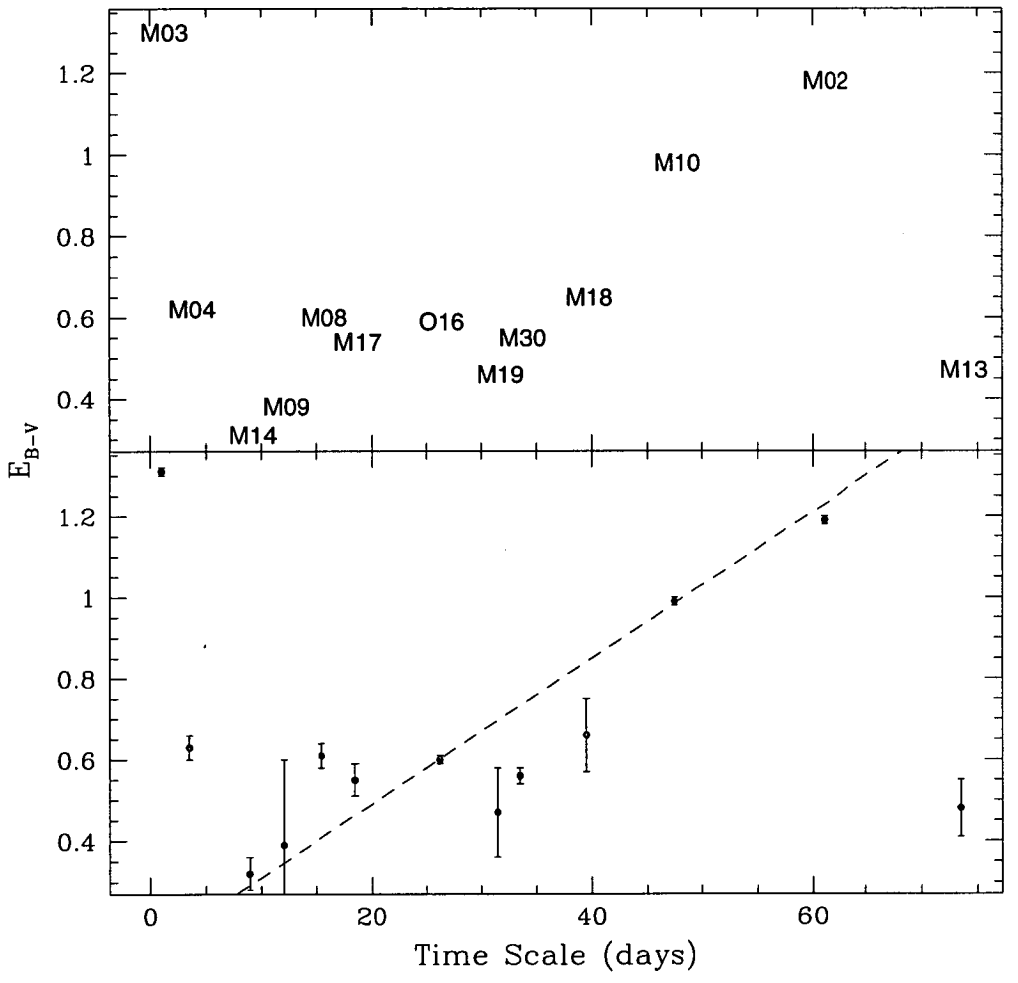

Figure 8.43: Plot of the extinction of microlensed sources as a function of their characteristic time scales. Events exhibiting binary behaviour are not included in this plot. **Top:** An abbreviated version of the event names is used to indicate the source positions. **Bottom:** A line of best fit to the points excluding events MB95003 and MB95013.

close to each other (both at the far side of the bulge), rather than a very small mass of the lens or a very high relative velocity. As indicated in Figure 6.12, this would make the event quite unusual and not typical of Galactic microlensing.

Rejecting these two anomalous points, a line was fitted to the data using linear regression. This fit is shown in the bottom panel of Figure 8.43. The trend in this data shows that the velocity dispersion component of the Galactic kinematics is strong enough such that there is a correlation between the extinction and the characteristic time scale of the event. Linear regression was used to obtain a linear fit which produces the following equation for this trend

$$E_{B-V} = 0.018 t_E + 0.13 \tag{8.1}$$

Of course contamination due to disk lensing will cause greater scatter in this result.

8.3.3 Kinematics of Microlensed Sources

The location of the microlensed sources allows a unique opportunity to investigate the kinematic properties in this region. The kinematic properties of our Galaxy have been studied and used with microlensing to construct consistent models of the Galaxy [68]. It was suggested by Walker [111] that one could use the kinematic properties of microlensed sources to distinguish between a lens population in the disk and a lens population in the bulge. It was found in this study that there should be a substantially different distribution of tranverse velocities between these two populations. It was also found that the radial velocity distributions between the two populations should not be substantially different for an axisymmetric bulge model but may exhibit a relative shift if the bulge is non-axisymmetric (barred), depending upon the kinematics of the bar.

Shown in Figure 8.44 is a histogram of the relative radial velocities for microlensed and non-microlensed stars. This histogram excludes Star 3 from the MB95030 field which has a relative radial velocity of $v_r = -399.8 \pm 9.1$. The average relative radial velocity for the microlensed sources is $v_r = -81.2$ and is $v_r = -75.6$ for the non-microlensed stars. There appears to be a slight shift between the peak values of these two distributions but, given the small number of samples, this may not be statistically significant.

To investigate the significance between the two mean values, a t-test was performed on the histogram data. A value of $t = 0.27$ was obtained for 93 degrees of freedom which results in a very high probability that the difference in the mean values of the two distributions is not significantly different. To test how much weight is held by the value at $v_r = -399.8 \pm 9.1$, the t-test was performed again after removing this data point from the sample. This increased the value of t to $t = 0.52$ for 92 degrees of freedom which still results in the conclusion that the two distributions are not significantly different.

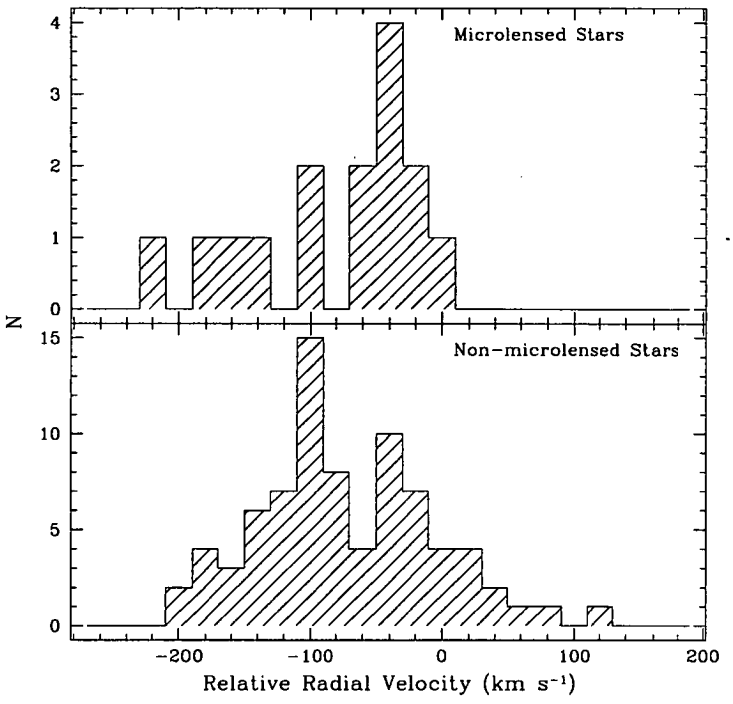

Figure 8.44: Histogram of relative radial velocities for microlensed and non-microlensed stars.

It has been shown that there is a significant difference between the extinction distributions for the microlensed and non-microlensed stars. Since there is no such difference between the radial velocity distributions, it is not expected that there will be a correlation between the extinction and radial velocity of the observed sources.

Shown in Figure 8.45 is a plot of the extinction of the microlensed and non-microlensed stars as a function of their relative radial velocities. This figure excludes Star 3 from the MB95030 field which has a relative radial velocity of $v_r = -399.8 \pm 9.1$. The microlensed sources are shown as black triangles and the non-microlensed sources are shown as red circles. As expected, there is an extinction shift between the microlensed population and the non-microlensed population but there is no apparent correlation between the extinction and the radial velocity. These results appear to agree with the postulates made by Walker [111]. These results are also expected since the total extinction varies depending upon the line of sight.

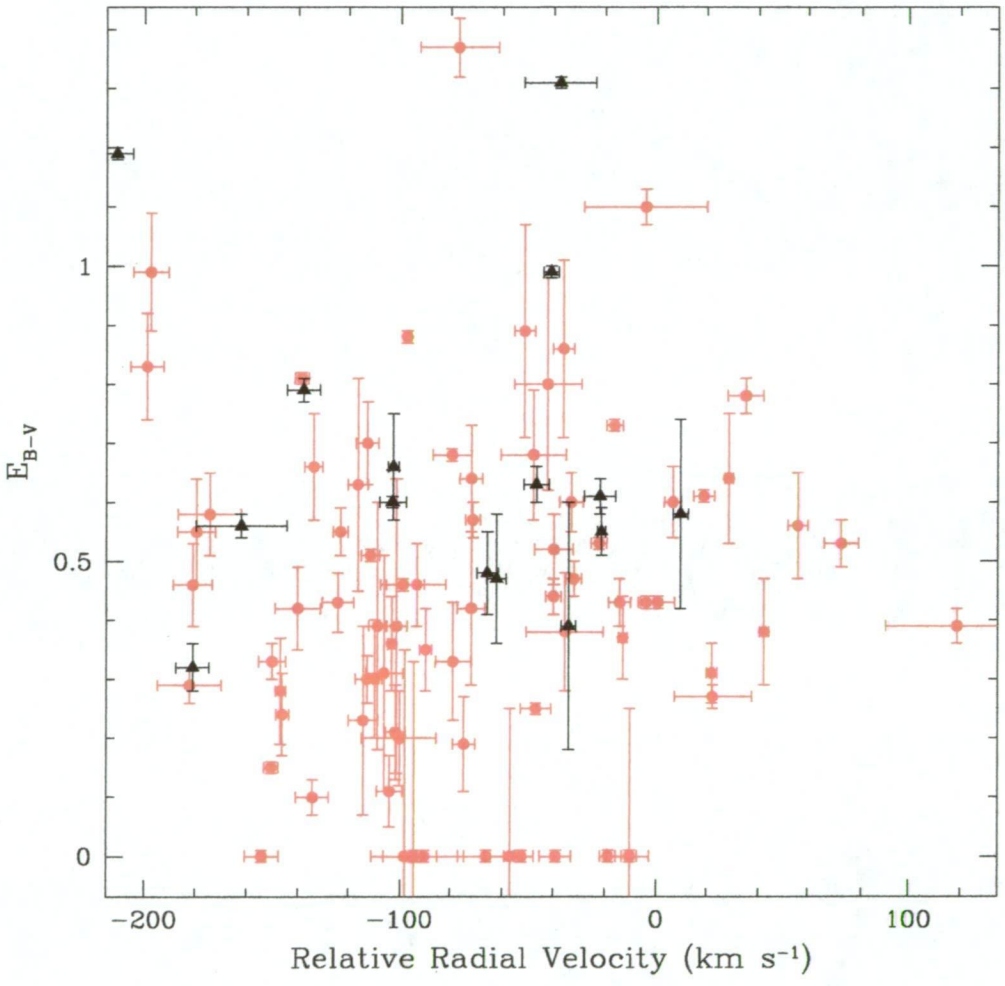

Figure 8.45: Plot of the extinction of all observed sources as a function of their relative radial velocities. The microlensed sources are shown as black triangles and the non-microlensed sources are shown as red circles.

Chapter 9

Summary of Conclusions

This chapter summarizes the main results from the work presented in this thesis. The first section describes the results from the photometric studies, including the photometric observations and data, and the modelling of a selection of these events. The second section describes the results from the spectroscopic work that was undertaken and the conclusions that were obtained from the analysis of the spectroscopic data.

9.1 Microlensing Photometry

The photometric studies in this project were conducted as a member of the PLANET collaboration. The acquisition of the data involved over 5 months using the 1.0 m telescope at Canopus Observatory in Australia, and 3 separate observing runs using the 0.9 m telescope at the Cerro Tololo Inter-American Observatory (CTIO) in Chile. The photometric results presented in this thesis are from observations of 34 microlensing events over three consecutive bulge seasons.

9.1.1 Photometric Data

From the 1996 bulge season, a total of 737 (542 I and 195 V) frames were acquired. From the 1997 bulge season, a total of 1021 (720 I and 301 V) frames were acquired from Canopus and a total of 193 (142 I and 51 V) frames were acquired from CTIO. From the 1998 bulge season, a total of 89 (73 I and 16 V) frames were acquired. The limiting magnitude for these observations depends upon the photometric conditions but has been estimated to be approximately 18.5 in I.

For the data acquired at Canopus, the average scatter in the reference stars is $\sim$ 3.1% for the 1996 season and $\sim$ 5.2% for the 1997 season. For the data acquired at CTIO, the average scatter in the reference stars is $\sim$ 1.7% for the 1997 season and $\sim$ 1.3% for the 1998 season. These figures include those events for which the microlensed source was extremely faint or highly blended with a

nearby star.

The CMDs show that almost all of these microlensed sources are main sequence stars with a few appearing to lie amongst the red clump giants. In particular, the detailed CMDs from the OB98014 and OB98018 fields indicate that these bright OGLE events are red clump giants. These diagrams will be useful in determining some properties of the source star, although scatter will be introduced due to interstellar reddening.

9.1.2 Light Curve Modelling

Most of the microlensing events that have been observed appear to exhibit standard Paczyński point source - point lens curves whilst a few, such as MB97028 and MB97041, deviate significantly from the standard model. These have already been studied in great detail by the PLANET collaboration [8, 10]. Four events are modelled from the data set which had not yet been previously studied. This modelling incorporates all available data from all PLANET observing sites.

Various microlensing models that include anomalous structure are fitted to the selected events resulting in the discovery of a possible binary source event. Analysis of the residuals for this event shows that there is additional asymmetry that may be explained by the inclusion of parallax in the modelling. The BSPL model results in a $\Delta\chi^2 \approx 285$ for 395 degrees of freedom and this study shows that this is currently the most likely explanation for MB97026. The remaining three events are fitted quite adequately using a point source - point lens model. These fitted events are used to estimate the sensitivity to extra-solar planets and it is found that the sampling rate for these events was insufficient by about a factor of 7.5 for detecting a Jupiter-mass planet. This sensitivity will be improved by including the remainder of the events observed during the 1997 season and by increasing the sampling rate in future seasons. This result assumes that deviations of 5% can be reliably detected.

9.2 Microlensing Spectroscopy

The spectroscopic studies in this project involved investigations of the effects of extinction on the microlensing event rate. These effects were then tested using Kurucz model spectra and real spectra of microlensed sources observed using the 3.6 m ESO telescope.

9.2.1 Theoretical Extinction Effects

Various Galactic models have been used to demonstrate the theoretical effects of extinction upon the microlensing optical depth. As expected, including extinction in the calculations results in a lower optical depth than those estimates made

without taking extinction into account. For the exponential model, it is shown that stars that are lensed within Baade's window are almost ten times more likely to be at the far side of the bulge than the near side.

The effects of extinction on spectra of microlensed sources have been simulated using Kurucz model spectra. It is shown that the majority of microlensed sources should exhibit extinction between $E_{B-V} = 0.4$ and $E_{B-V} = 0.8$. It is also shown that using extinction as a distance indicator for microlensed sources may be used to estimate the distance to the lens from the probability distribution corresponding to the appropriate Galactic model.

9.2.2 Modelling of Spectra

In order to process the large number of spectra that were obtained for analysis, MIDAS scripts were written to provide estimates of the extinction, spectral type, and radial velocity for each individual spectrum. A large library of Kurucz model spectra was constructed to model the spectra and the radial velocities were measured relative to a bright star using the cross-correlation technique. These results are presented so that a comparison between microlensed and non-microlensed stars can be made.

9.2.3 Consistency with Photometry

A combined CMD for 7 of the 17 fields studied was constructed using photometry from the 1995 PLANET observing season. The combined CMD is in good agreement with the CMDs published by OGLE and also with those presented in Chapter 4. Although the non-microlensed stars chosen for the spectroscopic study are almost certainly relatively bright, the combined CMD shows that these stars lie within the same sample as the microlensed sources and are therefore suitable for use in the study. Apparent magnitudes, colours, and absolute magnitudes derived from the CMD show that the luminosities measured from the CMD are roughly consistent with the classifications derived from the spectra and that giant stars have been preferentially selected since they are most likely to be in the Galactic bulge.

9.2.4 Extinction and Velocity Bias in Microlensing

A comparison of the extinction distributions for microlensed and non-microlensed stars is presented and the results analysed statistically. The average extinction for the microlensed sources is $E_{B-V} = 0.68$ and is $E_{B-V} = 0.43$ for the non-microlensed stars. The offset between the two mean values of $E_{B-V} = 0.25$ is equivalent to a magnitude offset of ≈ 0.80. A t-test performed on these distributions showed that the difference in the mean values of the two distributions are significantly different at the 99% confidence level.

By plotting the extinction of the microlensed sources as a function of their characteristic time scales, it is shown that there is a visible trend in the data. The trend in these data shows that the velocity dispersion component of the Galactic kinematics is strong enough such that there is a correlation between the extinction and the characteristic time scale of the event. This trend was fitted using linear regression and an equation describing the trend was obtained.

The histogram presenting the relative radial velocities for microlensed and non-microlensed stars shows that the difference between the two distributions is not significantly different. This is confirmed using a t-test, thus confirming the postulates made by Walker regarding the radial velocity bias of microlensed sources [111]. A further investigation uses a plot of the extinction of the microlensed and non-microlensed stars as a function of their relative radial velocities. This shows that there is an extinction shift between the microlensed population and the non-microlensed population but there is no apparent correlation between the extinction and the radial velocity. This result experimentally confirms the suggestion made by Walker [111] that there should not be a substantial difference in the radial velocity distributions between a disk lens population and a bulge lens population. It is also a consequence of the variation of total extinction with the line of sight to the source stars.

9.2.5 Fraction of Bulge-Bulge Lensing

An estimate of the fraction of bulge-bulge lensing was made from the extinction distribution for microlensed sources and the probability distribution of the lenses as shown in Figure 6.12. This simple method provided a crude estimate of the fraction of bulge-bulge lensing and is found to be $\sim$ 70%. This value is slightly higher than the 60% predicted by Kiraga & Paczyński [54]. This difference is due to a higher number of source stars estimated to be at the far side of the bulge.

9.3 Further Studies

The spectroscopic and photometric studies presented in this thesis build upon previous microlensing research and also serve as a starting point for future work. Most of the suggestions presented here were not included in this study due to either time constraints or not being able to access the proper facilities.

9.3.1 Additional Photometric Work

The photometric work performed in this project is a continuing process with much scope for future work. The PLANET collaboration is continuing observations of alerted microlensing events and obtaining good coverage of most events. The data reduction procedure still needs some improvements in the automation and

the treatment of image descriptors. Camera upgrades are frequently occurring at the PLANET observing sites which can lead to complications in combining the data sets.

Various methods can be used to improve the modelling of the events studied in this project. Baseline measurements are still needed for many past events in order to correctly model the data. It is also apparent from a few of the events presented in Chapter 4 that the mean value of a constant star is often correlated with seeing. This correlation depends upon the site and the detector and may increase the scatter in the light curves, thus obscuring small deviations from a standard light curve. This effect could be removed by determining the slope of the seeing correlation and correcting the photometric data prior to modelling, as described in a PLANET publication [9]. Performing a seeing correction of this kind could correct a number of MB97018 data points which lie beneath the fitted PSPL model (see Figure 5.1). In addition to this, the error bars may be rescaled based on a comparison of how well DoPHOT errors reflect the scatter for each observing site independently. The modelling presented in this thesis could also be improved by taking more models into account and hence provide a more exhaustive study of microlensing anomalies. However, it is likely that inclusion of more complex models would require a more advanced minimization routine, such as that developed by Dominik [29].

A crude estimate of the detection efficiency to extra-solar planets is presented in this thesis. The method used was that followed in the paper describing the 1995 pilot campaign of PLANET [7]. The data sets modelled in this project will eventually be combined with the data being used by Gaudi to determine the detection efficiency of the entire PLANET data set using the method developed by Gaudi & Sackett [39].

Although the PLANET collaboration has had much success in the scientific returns from the monitoring of microlensing events, no detections of extra-solar planets have yet been made. Several suggested observing strategies have been proposed, such as those by Gould & Loeb [42], Bennett & Rhie [21], and Peale [81]. In particular, Tytler [102] has suggested an ambitious microlensing planet search using four 2.0 m telescopes scattered in longitude, one serving to provide microlensing alerts and the other three providing follow-up monitoring.

There a number of ways PLANET can increase the sensitivity of its monitoring to extra-solar planet detection, several of which are mentioned here. During the course of a PLANET observing season, many events are monitored which turn out to be low amplification events, confused with nearby stars, and uninteresting. To avoid wasted observing time on these events, further analysis is required in developing a sophisticated 'early modelling' routine which can more accurately predict the future behaviour of events at an early stage. This will ensure that the higher amplification events will be monitored and thus increase the sensitivity to planets.

A further improvement to the detection sensitivity will be made when the

OGLE collaboration upgrades from its current OGLE-II phase [108] to its OGLE-III phase, scheduled to begin in early 2001. The major upgrade will be a new CCD which will result in a 5–8 times larger area being monitored. It is expected that the number of microlensing events detected in this phase will scale similarly and will thus provide a larger selection of brighter events for the PLANET collaboration to monitor. More information regarding the OGLE-III phase is available at the OGLE web site located at:
http://www.astrouw.edu.pl/ ftp/ogle/index.html

9.3.2 Additional Spectroscopic Work

The spectroscopic work performed in this project also present much opportunity for future work. The Galactic models used for calculating the optical depth in Chapter 6 contain a number of approximations. Incorporating the extinction effects into an improved model of the density profile of our Galaxy would further refine the optical depth estimates. In particular, the axisymmetric model of the Galaxy should be modified to take the bar of the Galaxy into account.

A large library of model spectra was constructed in order to process the large number of spectra that were obtained for analysis. The limitations in using these models was mostly due to the limited number of models available. However, the library could be improved by including a greater range of metallicities. The Kurucz stellar atmospheres atlas is being regularly updated and future versions may enhance the resolution of the grid of models and also increase the temperature range available. This would greatly increase the accuracy of the spectral classification method used in this project.

This project has presented the results from determining the extinction and radial velocity properties exhibited in numerous spectra. These have been used to determine if there are visible trends in the relationship between various microlensing parameters. However, it is difficult to show these effects with the limited number of spectra available in this analysis. It has been suggested by Stanek [95] that $\sim$ 100 sources would be required in order to show these effects unambiguously. As more spectra are obtained of microlensed sources, the statistics presented in this thesis will be greatly improved and will become more useful to modelling the kinematics of the Galactic center.

As expected, there appears to be no apparent correlation between the radial velocity of microlensed and non-microlensed sources. It is expected, however, that there should be an observable correlation between the transverse velocity of these two populations [111]. Hence, it would be of great interest to determine the transverse velocities of the microlensed sources as these would, when combined with the radial velocities, contribute significantly to the knowledge of the kinematics of the far side of the Galactic bulge. It is possible that such measurements could be made with the Hubble Space Telescope or with future space telescopes, such as NGST.

Appendix A

Microlensing Theory

A.1 Calculation of PSPL Magnification

From Equation 2.6 we can calculate

$$\frac{d\theta_{1,2}}{d\theta_s} = \frac{1}{2}\left(1 \pm \frac{\theta_s}{\sqrt{\theta_s^2 + 4\theta_E^2}}\right)$$

Substituting this result into Equation 2.7 gives

$$\begin{aligned}
A_{1,2} &= \left|\frac{\theta_{1,2}}{\theta_s}\frac{d\theta_{1,2}}{d\theta_s}\right| \\
&= \left|\frac{1}{2\theta_s}\left(\theta_s \pm \sqrt{\theta_s^2 + 4\theta_E^2}\right)\frac{1}{2}\left(1 \pm \frac{\theta_s}{\sqrt{\theta_s^2 + 4\theta_E^2}}\right)\right| \\
&= \left|\frac{1}{4\theta_s}\left(\theta_s \pm \frac{\theta_s^2}{\sqrt{\theta_s^2 + 4\theta_E^2}} \pm \sqrt{\theta_s^2 + 4\theta_E^2} + \theta_s\right)\right| \\
&= \left|\frac{1}{4\theta_s}\left(2\theta_s \pm \frac{\theta_s^2 + \theta_s^2 + 4\theta_E^2}{\sqrt{\theta_s^2 + 4\theta_E^2}}\right)\right| \\
&= \left|0.5 \pm \frac{\theta_s^2 + 2\theta_E^2}{2\theta_s\sqrt{\theta_s^2 + 4\theta_E^2}}\right| \\
&= \left|0.5 \pm \frac{\frac{\theta_s^2}{\theta_E^2} + 2}{2\frac{\theta_s}{\theta_E}\sqrt{\frac{\theta_s^2}{\theta_E^2} + 4}}\right|
\end{aligned}$$

Defining $u \equiv \theta_s/\theta_E$ simplifies the magnification to

$$A_{1,2} = \frac{u^2 + 2}{2u\sqrt{u^2 + 4}} \pm 0.5$$

A.2 Determination of PSPL Impact Parameter

From Equation 2.9

$$\begin{aligned} A &= \frac{u^2+2}{u\sqrt{u^2+4}} \\ u^2+2 &= Au\sqrt{u^2+4} \\ u^4+4u^2+4 &= A^2u^2(u^2+4) \\ &= A^2(u^4+4u^2) \end{aligned}$$

$$\begin{aligned} (u^4+4u^2)+4-A^2(u^4+4u^2) &= 0 \\ (1-A^2)(u^2+4u^2)+4 &= 0 \end{aligned}$$

$$\begin{aligned} u^4+4u^2 &= \frac{4}{A^2-1} \\ u^4+4u^2+4 &= \frac{4}{A^2-1}+4 \\ (u^2+2)^2 &= \frac{4}{A^2-1}+4 \\ u^2+2 &= \sqrt{\frac{4}{A^2-1}+4} \\ u^2 &= \sqrt{\frac{4}{A^2-1}+4}-2 \\ &= \sqrt{\frac{4+A^2-4}{A^2-1}}-2 \\ &= \frac{2A}{\sqrt{A^2-1}}-2 \\ u &= \sqrt{\frac{2A}{\sqrt{A^2-1}}-2} \end{aligned}$$

Hence, the instantaneous impact parameter can be determined from the magnification at any one time.

A.3 The curve.sm program

```
#
#  @@@   @   @  @@@@   @   @  @@@@@      @@@   @     @
# @   @  @   @  @   @  @   @  @         @   @  @@   @@
# @      @   @  @   @  @   @  @         @      @ @ @ @
# @      @   @  @@@@   @   @  @@@@@      @@@   @  @  @
# @      @   @  @   @  @   @  @             @  @     @
# @   @  @   @  @   @   @ @   @         @   @  @     @
#  @@@    @@@   @   @    @    @@@@@  @   @@@   @     @
#
# Type "curve" to begin
#

curve   # Script designed to produce light curves for various
        # models of microlensing events.

        echo [1] Point Source - Point Lens
        echo [2] Blended Point Source - Point Lens
        echo [3] Point Source - Point Lens (Parallax)
        echo [4] Extended (Uniformly Bright) Source - Point Lens
        echo [5] Extended (Limb-darkened) Source - Point Lens
        echo [6] Binary Source - Point Lens
        echo [7] Point Source - Binary Lens
        define model ? <Which model would you like to use?>
        if ($model==1) {pspl}
        if ($model==2) {blend}
        if ($model==3) {para}
        if ($model==4) {espl}
        if ($model==5) {limb}
        if ($model==6) {bspl}
        if ($model==7) {psbl}


pspl    define n 1
        define tE 20
        define t0 0
        define umin 0.4
        define tEf 1.0
        define format 0

        echo Additional plots increment u_min by 0.1
        define n ? <Number of plots?>
        echo Set t_E to zero to plot against p(t)
        define tE ? <Characteristic time scale?>
        if ($tE>0) {define t0 ? <Time of maximum amplification?>}
        define umin ? <Minimum impact parameter?>
        if ($tE==0) {define tEf ? <Characteristic time scale factor?>}
        define format ? <Create postscript file? (Yes 1 No 0)>
        if ($format==1) {device postencap pspl.ps}
```

```
if ($format==0) {device x11}
erase

define ii ($umin*10)  # This is used for labelling the plot

# The time of maximum amplification is taken to be zero.
# If the characteristic time scale is set to zero then
# the amplification is plotted against p(t)=(t-t0)/tE
# instead of t. The characteristic time scale factor
# effectively changes the value of tE.

do i=1,$n {
  if ($tE==0) {
    set p = -2,2,0.01
    set u = sqrt($umin**2+(p/$tEf)**2)
  } else {
    set t = -50,50,0.01
    set u = sqrt($umin**2+((t-$t0)/$tE)**2)
  }
  set A = (u**2+2)/(u*sqrt(u**2+4))
  define Amax (($umin**2+2)/($umin*sqrt($umin**2+4)))
  if ($i==1) {
    limits u A
    define ymax ($fy2*1.05)
    if ($tE==0) {limits p $fy1 $ymax} else {limits t $fy1 $ymax}
    expand 1.1
    ctype black
    if ($n==1) {window 1 3 1 2} else {window 1 2 1 2}
    box
    if ($tE==0) {xlabel p(t)} else {xlabel Time (t)}
    ylabel Amplification
  }
  ctype red
  if ($tE==0) {connect p A} else {connect t A}
  if ($n>1) {
    define iii ($Amax*1.01)
    relocate 0 $iii
    expand 0.7
    ctype black
    if ($ii>9) {
      define iii ($ii-10)
      putlabel 8 u_{min}=1.$iii
    } else {
      putlabel 8 u_{min}=0.$ii
    }
  }
  echo "@@@
```

```
blend   define umin1 0.4
        define tEf1 1.0
        define umin2 0.36
        define tEf2 1.1
        define f 0.85
        define format 0

        echo Unblended source parameters
        define umin1 ? <Minimum impact parameter?>
        define tEf1 ? <Characteristic time scale factor?>
        echo Blended source parameters
        define umin2 ? <Minimum impact parameter?>
        define tEf2 ? <Characteristic time scale factor?>
        define f ? <Blending parameter?>
        define format ? <Create postscript file? (Yes 1 No 0)>
        if ($format==1) {device postencap blend.ps}
        if ($format==0) {device x11}
        erase

        # Calculate the PSPL light curve without blending
        set p = -2,2,0.01
        set u = sqrt($umin1**2+(p/$tEf1)**2)
        set A = (u**2+2)/(u*sqrt(u**2+4))

        # Plot the PSPL light curve without blending
        stand

        # Calculate the PSPL light curve with blended source
        set u = sqrt($umin2**2+(p/$tEf2)**2)
        set A = (u**2+2)/(u*sqrt(u**2+4))
        set A = $f*A+1-$f

        # Plot the PSPL light curve with blended source
        connect p A


para    define umin 0.24
        define tE 118.1
        define v 75
        define th -0.7
        define be -0.08
        define res 1
        define format 0

        define umin ? <Minimum impact parameter?>
        define tE ? <Characteristic time scale?>
        define v ? <Relative velocity of lens? (km/s)>
        define th ? <Angle theta?>
        define be ? <Ecliptical latitude?>
```

```
        define res ? <Plot residuals? (Yes 1 No 0)>
        define format ? <Create postscript file? (Yes 1 No 0)>
        if ($format==1) {device postencap parallax.ps}
        if ($format==0) {device x11}
        erase

        define w (1/$tE)
        define a 1.0  # Semimajor axis of Earth's orbit
        define e 0.0167  # Earth's orbital eccentricity
        define W0 (2*pi/365.26)
        define tc -212  # time Earth is closest to Sun-source line
        define tp 0  # time of perihelion

        # Calculate the PSPL light curve without parallax
        set t = -150,150,0.05
        set u1 = sqrt(0.19**2+(t/89.8)**2)
        set A1 = (u1**2+2)/(u1*sqrt(u1**2+4))

        if ($res==0) {
          # Plot the PSPL light curve without parallax
          stand
        }

        # In the "alpha" equation, the factor 1731.4572 comes from
        # converting $v and $a to kilometres and days and dividing
        # one by the other.

        # Calculate the PSPL light curve with parallax
        set al = ($w*$a*1731.4572/$v)*(1-$e*cos($W0*(t-$tp)))
        set W = $W0*(t-$tc)+2*$e*sin($W0*(t-$tp))

        set u2 = sqrt($umin**2 + $w**2*t**2 + al**2*sin(W)**2\
+ 2*al*sin(W)*($w*t*sin($th)+$umin*cos($th)) + al**2*sin($be)**2*cos(W)**2\
+ 2*al*sin($be)*cos(W)*($w*t*cos($th)-$umin*sin($th)))
        set A2 = (u2**2+2)/(u2*sqrt(u2**2+4))

        if ($res==1) {
          # Plot the residuals
          set r = A2 - A1
          limits t r
          expand 0.9
          ctype black
          window -1 -6 1 4
          box
          xlabel Time (t)
          ylabel A_{PF}-A_{SF}
          ctype red
          connect t r
          ctype black
          # Plot the PSPL light curve without parallex
          limits t A1
```

```
    window -1 -3 1 3
    box 0 2 0 0
    ylabel Amplification
    ctype red
    ltype 2
    connect t A1
    ltype 0
  }
  # Plot the PSPL light curve with parallex
  connect t A2


espl  define umin 0.2
  define tEf 1.0
  define R 0.4
  define redo 0
  define format 0

  define umin ? <Minimum impact parameter?>
  define tEf ? <Characteristic time scale factor?>
  define R ? <Radius of source?>
  define redo ? <Recalculate data? (Yes 1 No 0)>
  define format ? <Create postscript file? (Yes 1 No 0)>
  if ($format==1) {device postencap extended.ps}
  if ($format==0) {device x11}
  erase

  # Calculate the PSPL light curve with source radius = 0
  set p = -2,2,0.01
  set u = sqrt($umin**2+(p/$tEf)**2)
  set A = (u**2+2)/(u*sqrt(u**2+4))

  # Plot the PSPL light curve with source radius = 0
  stand

  if ($redo==0) {eshow return}

  ecalc
  eshow

ecalc  # Calculate the PSPL light curve with source radius = R

  echo @@  Calculating light curve for a   @@
  echo @@ uniformly bright extended source @@

  !rm curve_espl.dat

  set p = -2,2,0.01

  set dimen(u)=dimen(p)
  do i=0,dimen(u)-1 {
```

```
          set u[$i] = sqrt($umin**2+(p[$i]/$tEf)**2)
        }

        do l=0,dimen(u)-1 {
          set upper = u[$l] + $R
          if (u[$l]>=$R) {set lower = u[$l] - $R}
          if (u[$l]<$R) {set lower = $R - u[$l]}
          define inc ((upper-lower)/101)
          set dimen(r)=101
          define limit lower
          set dimen(y)=101
          do i=0,100 {
            set r[$i] = $limit
            define limit ($limit+$inc)
            # A factor of 1.000001 was added to the expression
            # y[$l] to minimize attempts at calculating acos(1).
            set y[$i] = (r[$i]**2+2)/(sqrt(r[$i]**2+4))*acos((u[$l]**2
+r[$i]**2-$R**2)/(2*u[$l]*r[$i]*1.000001))
          }
          simp answer r y
          define answer ($answer*2/(pi*$R**2))
          if (u[$l]<$R) {define answer ($answer+(($R-u[$l])/$R**2)
*sqrt(($R-u[$l])**2+4))}
          write curve_espl.dat $(sprintf('%1.2f',p[$l]))
$(sprintf('%5.7f',$answer))
          define q (($l+1)/40)
          if ($q==int($q)) {define q ($q*10) echo $q"% complete ..."}
        }

eshow   # Plot the PSPL light curve with source radius = R
        data curve_espl.dat
        read {p 1 A 2}
        connect p A


limb    define umin 0.2
        define tEf 1.0
        define R 0.3
        define k1 0.567
        define k2 0.114
        define which 1
        define redo 1
        define format 0

        define umin ? <Minimum impact parameter?>
        define tEf ? <Characteristic time scale factor?>
        define R ? <Radius of source?>
        define k1 ? <Limb-darkening coefficient 1?>
        define k2 ? <Limb-darkening coefficient 2?>
        define which ? <Plot with PSPL (0) or ESPL(1)?>
        define redo ? <Recalculate data? (Yes 1 No 0)>
```

```
        define format ? <Create postscript file? (Yes 1 No 0)>
        if ($format==1) {device postencap limb.ps}
        if ($format==0) {device x11}
        erase

        if ($which==1) {
          if ($redo==0) {
            data curve_espl.dat
            read {p 1 A 2}
            stand
            lshow
          } else {
            ecalc
            data curve_espl.dat
            read {p 1 A 2}
            stand
            lcalc
            lshow
          }
          return
        }

        # Calculate the PSPL light curve with source radius = 0
        set p = -2,2,0.01
        set u = sqrt($umin**2+(p/$tEf)**2)
        set A = (u**2+2)/(u*sqrt(u**2+4))

        # Plot the PSPL light curve with source radius = 0
        stand

        if ($redo==0) {lshow return}

        lcalc
        lshow

lcalc   # Calculate the PSPL light curve with source radius = R

        echo @@ Calculating light curve for a @@
        echo @@ limb-darkened extended source @@

        !rm curve_limb.dat

        set p = -2,2,0.01

        set dimen(u)=dimen(p)
        do i=0,dimen(u)-1 {
          write curve_limb1.dat $(sprintf('%1.2f',p[$i]))
          set u[$i] = sqrt($umin**2+(p[$i]/$tEf)**2)
        }

        do l=0,dimen(u)-1 {
```

```
          write curve_limb_temp $(sprintf('%1.3f',u[$l]))
$(sprintf('%1.3f',$R)) $(sprintf('%1.3f',$k1)) $(sprintf('%1.3f',$k2))
          # The following line calls a FORTRAN program which utilises
          # the "Numerical Recipes" subroutines qgaus, midsql, and
          # midsqu.
          !curve_limb
          !cat curve_limb_temp >> curve_limb2.dat
          !rm curve_limb_temp
          define q (($l+1)/40)
          if ($q==int($q)) {define q ($q*10) echo $q"% complete ..."}
        }
        !paste curve_limb1.dat curve_limb2.dat > curve_limb.dat
        !rm curve_limb1.dat curve_limb2.dat

lshow   # Plot the PSPL light curve with source radius = R
        data curve_limb.dat
        read {p 1 A 2}
        connect p A


bspl    define w 0.3
        define rho 0.3
        define umin1 0.1
        define umin2 0.1
        define format 0

        define w ? <Luminosity offset ratio?>
        define rho ? <Distance between peaks?>
        define umin1 ? <Minimum impact parameter 1?>
        define umin2 ? <Minimum impact parameter 2?>
        define format ? <Create postscript file? (Yes 1 No 0)>
        if ($format==1) {device postencap bspl.ps}
        if ($format==0) {device x11}
        erase

        set p = -2,2,0.01
        set p1 = p + $rho
        set p2 = p - $rho
        set u1 = sqrt($umin1**2+p1**2)
        set u2 = sqrt($umin2**2+p2**2)
        set A1 = (u1**2+2)/(u1*sqrt(u1**2+4))
        set A2 = (u2**2+2)/(u2*sqrt(u2**2+4))
        set A = (1-$w)*A1+$w*A2

        limits p A
        expand 1.1
        ctype black
        window 1 2 1 2
        box
        xlabel p(t)
        ylabel Amplification
```

```
        ctype red
        connect p A


psbl    define old 1
        define rmu1 0.5
        define X 0.5
        define f 1.0
        define r 0.05
        define xs1 -1.5
        define xs2 -0.6
        define xf1 1.5
        define xf2 0.6
        define ts -2.0
        define tf 2.0
        define np 200
        define nint 100
        define which 1
        define path 0
        define squ 1
        define format 0

        define old ? <Plot old data? (Yes 1 No 0)>
        if ($old==1) {pold return}
        define rmu1 ? <Mass ratio of one lens?>
        define X ? <Location of lenses (-X,X)?>
        define f ? <Blending parameter?>
        define r ? <Source radius?>
        define xs1 ? <Source starting position (xs1)?>
        define xs2 ? <Source starting position (xs2)?>
        define xf1 ? <Source finishing position (xf1)?>
        define xf2 ? <Source finishing position (xf2)?>
        define ts ? <Starting time?>
        define tf ? <Finishing time?>
        define np ? <Number of points to compute?>
        define nint ? <Number of points in the integration?>
        define ident ? <Choose a number to save as (1-9)?>
        pcont

pold    echo These files are available for plotting:
        !ls curve_psbl*.dat
        define ident ? <Choose a number to plot (1-9)?>
        define which ? <Plot with source radius = 0? (Yes 1 No 0)>
        define path ? <Plot the source path? (Yes 1 No 0)>
        if ($path==0) {
          define squ ? <Make a square plot? (Yes 1 No 0)>
        }
        pcont

pcont   define format ? <Create postscript file? (Yes 1 No 0)>
        if ($format==1) {device postencap psbl.ps}
```

```
        if ($format==0) {device x11}
        erase

        if ($old==1) {pshow return}

        pcalc
        pshow

pcalc   # Calculate the PSBL light curve

        echo @@ Go away and have a break! @@
        echo @@   This may take a while   @@

        write curve_psbl_input.dat $(sprintf('%1.3f',$rmu1))
$(sprintf('%1.3f',$X)) $(sprintf('%1.3f',$f)) $(sprintf('%1.3f',$r))
$(sprintf('%1.2f',$xs1)) $(sprintf('%1.2f',$xs2)) $(sprintf('%1.2f',$xf1))
$(sprintf('%1.2f',$xf2)) $(sprintf('%1.2f',$ts)) $(sprintf('%1.2f',$tf))
$(sprintf('%3.0f',$np)) $(sprintf('%3.0f',$nint))
        !cp curve_psbl_input.dat curve_psbl$ident.par
        # The following line calls a FORTRAN program which utilises
        # the "Numerical Recipes" subroutines laguer and zroots.
        !curve_psbl
        !rm curve_psbl_input.dat
        !mv curve_psbl_output.dat curve_psbl$ident.dat

pshow   # Plot the PSBL light curve
        echo The parameters for this model are:
        echo rmu1  X  f  r  xs1  xs2  xf1  xf2  ts  tf  np  nint
        !cat curve_psbl$ident.par
        if ($path==1) {
          data curve_psbl$ident.par
          read {X 2 r 4 xs1 5 xs2 6 xf1 7 xf2 8}
          define l1 (abs(xs1[0]))
          define l2 (abs(xs2[0]))
          limits -$l2 $l2 -$l2 $l2
          if ($l1>$l2) {limits -$l1 $l1 -$l1 $l1}
          expand 1.1
          ctype black
          window 1 1 1 1
          box
          expand 1.5
          xlabel \xi
          ylabel \eta
          ptype 10 3
          expand 1.6
          define x (X[0])
          relocate -$x 0
          dot
          relocate $x 0
          dot
          expand 1.4
```

```
        define x ($x*1.3)
        relocate -$x 0
        putlabel 2 m_1
        relocate $x 0
        putlabel 2 m_2
        ltype 1
        grid 1
        ltype 0
        ctype red
        define r (r[0])
        if ($which==1) {define r 0}
        if ($l1>$l2) {
          define x1 (xs1[0])
          define x2 (xf1[0])
          define y1 (xs2[0]-$r)
          define y2 (xf2[0]-$r)
        } else {
          define x1 (xs1[0]-$r)
          define x2 (xf1[0]-$r)
          define y1 (xs2[0])
          define y2 (xf2[0])
        }
        do a=1,3,1 {
          relocate $x1 $y1
          draw $x2 $y2
          if ($l1>$l2) {
            define y1 ($y1+$r)
            define y2 ($y2+$r)
          } else {
            define x1 ($x1+$r)
            define x2 ($x2+$r)
          }
        }
        return
      }
      data curve_psbl$ident.dat
      if ($which==1) {read {p 3 A 5}} else {read {p 3 A 4}}
      if ($squ==1) {square} else {stand}


stand  # Plots a standard PSPL light curve
      if ($model==3) {limits t A1} else {limits p A}
      expand 1.1
      ctype black
      window 1 2 1 2
      box
      if ($model==3) {xlabel Time (t)} else {xlabel p(t)}
      ylabel Amplification
      ctype red
      if ($model==7) {connect p A return}
      ltype 2
```

```
        if ($model==3) {connect t A1} else {connect p A}
        ltype 0


square  # Plot the PSBL light curve using a square box
        limits p 0 8
        expand 1.1
        ctype black
        window 1 1 1 1
        box
        expand 1.3
        xlabel p(t)
        ylabel Amplification
        ctype red
        connect p A
```

Appendix B

Photometric Data Reduction

B.1 DoPHOT Parameter Files

Shown are all the parameters that are accepted by DoPHOT along with example values.

```
FWHM = 2.0              Approx FWHM of objects (pixels) along major axis.
AXIS_RATIO = 1.0        For star objects.  AR=b/a; b=minor axis.
TILT = 0.0              Angle of major axis in degrees; +x=0; +y=90.
SKY = 10.0              Approximate mean sky value in data numbers.
NFITBOX_X = 7           Size of fit box in the x-direction.
NFITBOX_Y = 7           Size of fit box in the y-direction.
MASKBOX_X = 5           Size of mask box size in x.
MASKBOX_Y = 5           Size of mask box size in y.
APBOX_X = 13.0          Size of aperture photometry box in x.
APBOX_Y = 13.0          Size of aperture photometry box in y.
IBOTTOM = -50           Lowest allowed data value in data numbers.
ITOP = 16384            Maximum allowed data value in data numbers.
THRESHMIN = 20.0        Value of lowest threshold.
THRESHMAX = 10000.0     Value of maximum threshold.
THRESHDEC = 1.0         Threshold decrement in powers-of-2.
EPERDN = 2.0            Electrons per data number.
RDNOISE = 15.0          Readout noise in electrons.
AUTOSCALE = 'NO'        Auto-scaling of sizes by FWHM.
AUTOTHRESH = 'NO'       Auto-scaling of thresholds.
FIXPOS = 'NO'           Fix star positions?
PARAMS_DEFAULT = 'param_default2_0'  Default parameters file name.
PARAMS_OUT = 'param_out'            Output parameters file name.
IMAGE_IN = 'image_in'               Input image name.
IMAGE_OUT = 'image_out'             Output image name.
OBJECTS_IN = ' '                    Input object list file name.
OBJECTS_OUT = 'objects_out'         Output object list file name.
SHADOWFILE_IN = ' '                 Input shadow file name.
SHADOWFILE_OUT = 'shadowfile_out'   Output shadow file name.
LOGFILE = 'TERM'                    Log file name.  TERM for screen.
```

```
LOGVERBOSITY = 1                    Verbosity of log file; (0-4).
RESIDNOISE = 0.3          Fraction of noise to ADD to noise file.
FOOTPRINT_NOISE = 1.3     Expand stars in noise file by this amount.
NPHSUB = 1                Limiting surface brightness for subtractions.
NPHOB = 1                 Limiting surface brightness for obliterations.
ICRIT = 10                Obliterate if # of pixels > ITOP exceeds this.
CENTINTMAX = 20000.0      Obliterate if central intensity exceeds this.
CTPERSAT = 1.0e4          Assumed intensity for saturated pixels.
STARGALKNOB = 1.0         Star/galaxy discriminator.
STARCOSKNOB = 1.0         Object/cosmic-ray discriminator.
SNLIM7 = 7.0              Minimum S/N for 7-parameter fit.
SNLIM = 0.5               Minimum S/N for a pixel to be in fit subraster.
SNLIMMASK = 4.0           Minimum S/N through mask to identify an object.
SNLIMCOS  = 3.0           Minimum S/N to be called a cosmic ray.
NBADLEFT = 0              Ignore pixels closer to the left edge than this.
NBADRIGHT = 0             Ignore pixels closer to the right edge than this.
NBADTOP = 0               Ignore pixels closer to the top edge than this.
NBADBOT = 0               Ignore pixels closer to the bottom edge than this.
PSFTYPE = 'PGAUSS'          PSF type: (PGAUSS)
SKYTYPE = 'PLANE'           SKY type: (PLANE, HUBBLE, MEDIAN)
JHXWID = 0                 X Half-size of median box (.le. 0 -> autoscale)
JHYWID = 0                 Y (same as above)
MPREC = 1                  Median precision in DN (use .le. 0 for autocalc)
NTHPIX = 0                 Frequency of sky updates in pixels for 1st pass
OBJTYPE_IN = 'COMPLETE'    Input format: (COMPLETE, INTERNAL)
OBJTYPE_OUT = 'COMPLETE'  Output format: (COMPLETE, INCOMPLETE, INTERNAL)
NFITITER = 10             Maximum number of iterations.
NPARAM = 7                Maximum number of PSF fit parameters.
NFITMAG = 4               No. of PSF parameters to get magnitudes.
NFITSHAPE = 7             No. of PSF parameters to get shape and mags.
NFITBOXFIRST_X = 31       Size of fit box in x for first pass.
NFITBOXFIRST_Y = 31       Size of fit box in y for first pass.
CHI2MINBIG = 16           Critical CHI-squared for a large object.
XTRA = 25                 We need more S/N if some pixels are missing.
SIGMA1 = 0.10             Max. frac. scatter in sigma_x for stars.
SIGMA2 = 0.10             Max. scatter in xy cross term for stars.
SIGMA3 = 0.10             Max. frac. scatter in sigma_y for stars.
ENUFF4 = 0.50             Fraction of pixels needed for 4-param fit.
ENUFF7 = 0.65             Fraction of pixels needed for 7-param fit.
COSOBLSIZE = 0.9          Size of obliteration box for a cosmic ray.
APMAG_MAXERR = 0.1        Max anticipated error for aperture phot report.
PIXTHRESH = 1.0           Trigger on pixels higher than noise*PIXTHRESH.
BETA4 = 1.0               R**4 coefficient modifier.
BETA6 = 1.0               R**6 coefficient modifier.
SCALEFITBOX = 3.0         Size of fit box in units of FWHM.
FITBOXMIN = 5.0           Smallest allowed fit box size.
SCALEAPBOX = 6.0          Size of aperture phot box in units of FWHM.
APBOXMIN = 7.0            Smallest allowed aperture phot box size.
SCALEMASKBOX = 1.5        Size of mask box in units of FWHM.
AMASKBOXMIN = 5.0         Smallest allowed mask box size.
SIGMAIBOTTOM = 10.0       Level of IBOTTOM below sky in units of noise.
```

```
SIGMATHRESHMIN = 2.0    Level of THRESHMIN above sky in units of noise.
RELACC1 = 0.01          Convergence criterion for sky.
RELACC2 = -0.03         Convergence criterion for x-position.
RELACC3 = -0.03         Convergence criterion for y-position.
RELACC4 = 0.01          Convergence criterion for for central intensity.
RELACC5 = 0.03          Convergence criterion for sigma-x.
RELACC6 = 0.1           Convergence criterion for sigma-xy.
RELACC7 = 0.03          Convergence criterion for sigma-y.
ABSLIM1 = -1.0e8        Allowed range for sky value.
ABSLIM2 = -1.0e3        Allowed range for x-position.
ABSLIM3 = -1.0e3        Allowed range for y-position.
ABSLIM4 = -1.0e8        Allowed range for central intensity.
ABSLIM5 = -1.0e3        Allowed range for sigma-x.
ABSLIM6 = -1.0e3        Allowed range for sigma-xy.
ABSLIM7 = -1.0e3        Allowed range for sigma-y.
END
```

B.2 The Midas Reduction Scripts

This section contains the Midas scripts that were used to reduce the data obtained from Canopus Observatory. The reduction process entailed five basic steps as described in Section 3.4.1. Similar scripts were used for the CTIO data.

hobart1.prg

```
write/out "============================================================"
write/out "This script prepares the Hobart fits frames."
write/out "1. First it converts it to .bdf format."
write/out "2. The pixel range is scaled to be between 0 and 32767."
write/out "3. The new electrons per data number (EPERDN) is calculated"
write/out "   and written to an image descriptor."
write/out "4. The Julian Date (JD) is calculated and written to an image"
write/out "   descriptor."
write/out "5. Lastly the pixels are converted to 16bit integers."
write/out "============================================================"

define/par P1 ? C "Name of frame(s) to prepare?"
define/par P2 ? C "RA (hour,min,sec)?"
define/par P3 ? C "DEC (degree,min,sec)?"
define/par P4 ? C "Year of observations (eg, 1997)?"

define/local file/c/1/30 ?
define/local ifctrl/i/1/2 0.0
define/local n/i/1/1 0
define/local i/i/1/1 0
define/local uthour/i/1/1 0
define/local month/c/1/2
```

```
define/local EPERDN/r/1/1 0.0
define/local JD/d/1/1 0.0
define/local etc/r/1/1 0.0

set/format I4 F18.8,F18.8

compute/key n = M$INDEX(P1,".mt")
if n .eq. 0 then
   $ls {P1}.mt > printtemp.cat
else
   $ls {P1} > printtemp.cat
endif

open/file printtemp.cat READ ifctrl
write/out

process_file:
   write/key file " "
   read/file {ifctrl(1)} file 30
   if ifctrl(2) .lt. 0 goto finish
   write/out "==> Starting on image" {file}

! Convert the frame to .bdf format
   indisk/fits {file} xx

! Dophot will only accept images with a pixel range of 0 to +32767.
! The image will now be scaled to lie between these two values.
   stat xx
   if {outputr(2)} .gt. 32767 then
      comp yy = (xx / {outputr(2)}) * 32767
   else
      comp yy = xx
   endif

! Compute the electrons per data number (EPERDN) and write it in
! the header of the image.
   if {outputr(2)} .gt. 32767 then
      EPERDN = (6.7 / 32767) * {outputr(2)}
   else
      EPERDN = 6.7
   endif
   write/desc yy EPERDN/r/1/1 {EPERDN}
   write/out "The electrons per data number for this image is" {EPERDN}

! Calculate the JD and save it in a descriptor.
! First, the correct UT hour is calculated.
   uthour = {yy,time(1:2)} - 10
   if uthour .lt. 0 then
      uthour = {yy,time(1:2)} + 14
   endif
```

```
! The month of October is recorded in the rawfile descriptor as "a".
! This will convert it to the number 10.
   compute/key month = "{yy,rawfile(7:7)}"
   if month .eq. "a" then
      month = "10"
   endif

! Then the geocentric JD is calculated.
   compute/st {P4},{month},{yy,rawfile(5:6)} {uthour},{yy,time(4:5)},
{yy,time(7:8)} -212,10,1.2
   JD = {outputd(1)}

! To this is added the heliocentric correction.
   compute/barycorr {P4},{month},{yy,rawfile(5:6)} {uthour},{yy,time(4:5)},
{yy,time(7:8)} {P2} {P3} -212,10,1.2 -42,51,0
   JD = JD + outputd(2)
   write/out "The heliocentric correction is:   " {outputd(2)}

! Finally, half the exposure time is added.
   etc = {yy,exposure}
   etc = etc / 17280000
   JD = JD + etc
   write/out "The exposure time correction is:  " {etc}

   write/desc yy JD/d/1/1 {JD}
   write/out "The Heliocentric Julian Date for this image is" {JD}

! Convert pixels to 16bit integers
   compute/key i = M$INDEX(file,".mt")
   i = i - 1
   copy/ii yy {file(1:{i})} I2

! Display the subframe
   write/out "Displaying the final extracted frame ..."
   load {file(1:{i})} cuts=f,1sigma scale=1

   write/out
   write/out "============================================================"
   write/out

   goto process_file

finish:
   write/out "####################################"
   write/out "#     All frames completed!!       #"
   write/out "# Now proceed directly to hobart2 #"
   write/out "####################################"
   close/file {ifctrl}
   $rm xx.bdf
   $rm yy.bdf
   $rm printtemp.cat
```

hobart2.prg

```
write/out "============================================================="
write/out "This procedure will get a fwhm and sky estimate for each"
write/out "of the specified frames. The output is written to fwhm.dat"
write/out "in the form xfwhm, yfwhm, sky, file name"
write/out "============================================================="

define/par P1 ? C "Name of frame(s) to be processed?"

define/local file/c/1/40 ?
define/local ifctrl/i/1/2 0,0
define/local ofctrl/i/1/2 0,0
define/local n/i/1/1 0
define/local outrec/c/1/100 ?
define/local dmag/r/1/1 0.0
define/local tilt/r/1/1 0.0

set/format F11.2,F11.2

compute/key n = M$INDEX(P1,".bdf")
if n .eq. 0 then
   $ls {P1}.bdf > printtemp.cat
else
   $ls {P1} > printtemp.cat
endif

open/file printtemp.cat READ ifctrl
open/file fwhm.dat WRITE ofctrl

process_file:
   write/key file " "
   read/file {ifctrl(1)} file 30
   if ifctrl(2) .lt. 0 goto finish
   write/out "==> Starting on image" {file}
   extract/ima subimage = {file}[@1,@1:@375,@241]

   load subimage cuts=f,1sigma scale=1
   cent/iqe

   set/format I3 f5.2,f5.2
   outrec(1:6) = "{outputr(12)}"
   outrec(7:12) = "{outputr(13)}"
   tilt = {outputr(15)}
   tilt = tilt - 180.0
   if tilt .gt. 360.0 tilt = tilt - 360.00
   if tilt .lt. -360.0 tilt = tilt + 360.0
   set/format I3 f5.1,f5.1
```

```
   outrec(13:19) = "{tilt} "
   stat/ima {file} ? ? ? FN
   set/format i3 f7.1,f7.1
   outrec(20:27) = "{{file},statistic(12)} "
   n = ifctrl(2) + 28
   outrec(28:{n}) = "{file(1:{ifctrl(2)})}"
   write/file {ofctrl(1)},key outrec(1:{n})
   clear/channel over

   write/out
   write/out "============================================================="
   write/out

   goto process_file

finish:
   write/out "#####################################################################"
   write/out "#                          Finished!!                               #"
   write/out "#  Now you need to look at fwhm.dat and decide which image  #"
   write/out "#    to use as a template before you proceed to hobart3     #"
   write/out "#####################################################################"
   close/file {ifctrl}
   close/file {ofctrl}
   $rm subimage.bdf
   $rm printtemp.cat
```

hobart3.prg

```
def/par P1 ? C "Name of frame to be used as the template?"

write/out "============================================================="

define/local n/i/1/1 0
define/local ntest/i/1/1 0

set/format I5 F6.2

compute/key n = M$INDEX(P1,".bdf")
if n .eq. 0 then
   $cp {P1}.bdf template.bdf
else
   $cp {P1} template.bdf
endif

ntest = M$existD("template","HISTORY")
if ntest .eq. 1 delete/desc template HISTORY
ntest = M$existD("template","DISPLAY_DATA")
if ntest .eq. 1 delete/desc template DISPLAY_DATA
ntest = M$existD("template","HIST_BINS")
```

```
if ntest .eq. 1 delete/desc template HIST_BINS
ntest = M$existD("template","HISTOGRAM")
if ntest .eq. 1 delete/desc template HISTOGRAM
ntest = M$existD("template","STATISTIC")
if ntest .eq. 1 delete/desc template STATISTIC

outdisk/fits template template.mt

write/out "#########################################################"
write/out "#      Your template fits file is now ready       #"
write/out "#    You now need to run dophot on template.mt    #"
write/out "#      using param_template as the mod file       #"
write/out "#   Make changes to FWHM, AXIS_RATIO, TILT, SKY   #"
write/out "#                    and EPERDN                   #"
write/out "#########################################################"
write/out

write/out "Here is the EPERDN from the descriptor of" {P1}
read/desc {P1} EPERDN
$rm template.bdf
```

hobart4.prg

```
write/out "============================================================="
write/out "This procedure will extract all stars of types 1 (a perfect"
write/out "star), 3 (one component of two very close stars), and 7 (faint"
write/out "object - photometry is okay provided the object is a star)."
write/out "These objects are written out to a new dophot output file."
write/out "============================================================="

define/par P1 template_raw.dop C "Name of input file?"
define/par P2 template.dop C "Name of output file?"
define/par P3 1,3,7 C "ID's of stars to keep?"

define/local file/c/1/140 ?
define/local fname/c/1/30 ?
define/local ifctrl/i/1/2 0,0
define/local ofctrl/i/1/2 0,0
define/local i/i/1/1 0
define/local k/i/1/1 0
define/local outrec/c/1/400 ?
define/local dmag/r/1/1 0.0
define/local x/r/1/22 0.0 all
define/local y/r/1/22 0.0 all
define/local n/i/1/22 0 all
define/local recno/i/1/1 0
define/local refnum/i/1/1 0
define/local id/i/1/1 0
define/local type/i/1/1 0
```

```
set/format I5 F6.2

compute/key n = M$exist(P1)
if n .eq. 0 then
   write/out "ERROR ==> {P1} does not exist."
   return
endif

compute/key n = M$exist(P2)
if n .ne. 0 then
   write/out "ERROR ==> {P2} already exists."
   return
endif

open/file {P1} READ ifctrl
open/file {P2} WRITE ofctrl

refnum = 0
k = m$parse("{P3}","type")
set/format I2 f4.1,f4.1

read_pos:
   read/file {ifctrl(1)} file 139
   if ifctrl(2) .lt. 0 goto finish_pos
   id = {file(7:8)}
   do i = 1 k
      if id .eq. {type{i}} then
         write/file {ofctrl(1)},key file(1:{ifctrl(2)})
         refnum = refnum + 1
         goto read_pos
      endif
   enddo
   goto read_pos

finish_pos:
   write/out "Finished cleaning template_raw.dop"
   write/out "{refnum} stars selected"
   write/out "Cleaned Dophot output file is called template.dop"
   write/out "################################################"
   write/out "# Now you need to create a file containing  #"
   write/out "#  the x-position (XXX), y-position (YYY),  #"
   write/out "# and box size (ZZZ) for the target and the #"
   write/out "#     10 reference stars in the form:       #"
   write/out "#                XXXYYYZZZ                  #"
   write/out "#   Name the file ref.dat then proceed to   #"
   write/out "#                 hobart5                   #"
   write/out "################################################"
   close/file {ifctrl}
   close/file {ofctrl}
```

hobart5.prg

```
write/out "============================================================="
write/out "This procedure will run dophot on each of the input fits images"
write/out "and then transform the coordinates in the dophot output file to"
write/out "the coordinate system of the template file. It will then use the"
write/out "positions in the reference star file to extract the photometry"
write/out "for the specified objects. It reads the time of the observation"
write/out "from the header in the fits input image and writes it all to a"
write/out "single line in the ascii output file."
write/out "============================================================="

define/par P1 fwhm.dat C "Name of fwhm file?"
define/par P2 ref.dat C "Name of Ref. star posn. file?"
define/par P3 template.dop C "Name of template file?"
define/par P4 ? C "Name of output file?"
define/par P5 ? C "Name of the output directory?"

define/local file/c/1/50 ?
define/local fname/c/1/30 ?
define/local xfwhm/r/1/1 0.0
define/local yfwhm/r/1/1 0.0
define/local fwhm/r/1/1 0.0
define/local ratio/r/1/1 0.0
define/local tilt/r/1/1 0.0
define/local sky/r/1/1 0.0
define/local ifctrl/i/1/2 0,0
define/local ofctrl/i/1/2 0,0
define/local i/i/1/1 0
define/local k/i/1/1 0
define/local outrec/c/1/400 ?
define/local x/r/1/22 0.0 all
define/local y/r/1/22 0.0 all
define/local n/i/1/22 0 all
define/local refnum/i/1/1 0
define/local imlen/i/1/1 0
define/local catrec/c/1/100
define/local scale/r/1/1 1.0
define/local FITBOX/i/1/1 0
define/local sFITBOX/i/1/1 0
define/local APBOX/i/1/1 0
define/local MASKBOX/i/1/1 0
define/local EPERDN/r/1/1 0.0
define/local ntest/i/1/1 0
define/local PD/r/1/1 0.0

set/format I5 F6.2

! Check to make sure that the three input files exist.
compute/key ntest = M$exist(P1)
if ntest .eq. 0 then
```

```
   write/out "ERROR ==> {P1} does not exist."
   return
endif
compute/key ntest = M$exist(P2)
if ntest .eq. 0 then
   write/out "ERROR ==> {P2} does not exist."
   return
endif
compute/key ntest = M$exist(P3)
if ntest .eq. 0 then
   write/out "ERROR ==> {P3} does not exist."
   return
endif

! If the last parameter exists then interpret it as a directory
! where we will store the residual images, dophot output files,
! and dophot parameter files. If the catalogue file doesn't exist
! then create a new one, otherwise append to the existing one.
if "{P5(1:1)}" .ne. "?" then
   compute/key ntest = M$exist(P5)
   if ntest .eq. 0 then
      $mkdir {P5}
      $touch {P5}/cat.dat
   else
      ntest = M$exist("{P5}/cat.dat")
      if ntest .eq. 0 $touch {P5}/cat.dat
   endif
endif

! Open the star position file and read the positions into the x,y,n
! arrays. x,y is the position and n is the box size in pixels that
! will be searched. The maximum number of objects is 22.
open/file {P2} READ ifctrl
refnum = 0
set/format I3 f4.1,f4.1

read_pos:
   read/file {ifctrl(1)} file 30
   if ifctrl(2) .lt. 0 goto finish_pos
   refnum = refnum + 1
   x({refnum}) = {file(1:3)}
   y({refnum}) = {file(4:6)}
   n({refnum}) = {file(7:9)}
   write/out {refnum} "-> " {x({refnum})} {y({refnum})} {n({refnum})}
   if refnum .lt. 22 goto read_pos
      write/out "Too many reference stars (maximum = 22)"
      return

finish_pos:

close/file {ifctrl}
```

```
! Open the FWHM input file (generated using hobart2).
open/file {P1} READ ifctrl

! Open the output ascii file
open/file {P4} WRITE ofctrl

! Process the data files
set/format f11.2,f11.2

process_file:
   ! Get the x & y fwhm, sky and file name from the input file
   write/key file " "
   read/file {ifctrl(1)} file 50
   if ifctrl(2) .lt. 0 goto finish
   xfwhm = {file(1:6)}  !major axis
   yfwhm = {file(7:12)} !minor axis
   fwhm = (xfwhm + yfwhm) / 2
   ratio = yfwhm / xfwhm
   tilt = {file(13:19)}
   sky =   {file(20:27)}
   fname = "{file(28:{ifctrl(2)})}"

   ! If the descriptor EPERDN exists in the image header, then the
   ! corresponding value is used for the electrons per data number.
   ! Otherwise, 6.7 is used. Similarly for the image scale and the
   ! size of the fitbox.
   ntest = M$existD("{fname}","EPERDN")
   if ntest .eq. 1 then
      EPERDN = {{fname},EPERDN}
   else
      EPERDN = 6.7
   endif

   ntest = M$existD("{fname}","scale")
   if ntest .eq. 1 then
      SCALE = {{fname},scale}
   else
      SCALE = 1.0
   endif

   ntest = M$existD("{fname}","fitbox")
   if ntest .eq. 1 then
      FITBOX = {{fname},fitbox}
   else
      FITBOX = 3.8 * xfwhm
      if {FITBOX} .gt. 31 FITBOX = 31
      if {FITBOX} .lt. 9 FITBOX = 9
   endif

   sFITBOX = 2.8 * xfwhm
```

```
   if {sFITBOX} .gt. 31 sFITBOX = 31
   if {sFITBOX} .lt. 9 sFITBOX = 9

   ntest = M$existD("{fname}","MASKBOX")
   if ntest .eq. 1 then
      MASKBOX = {{fname},maskbox}
   else
      MASKBOX = 1.8 * xfwhm
      if {MASKBOX} .lt. 6  MASKBOX = 6
      if {MASKBOX} .gt. 13 MASKBOX = 13
   endif

   APBOX = 5.0 * xfwhm

   write/out "************************************************************"
   write/out {fname} {sky} {xfwhm} {yfwhm} {tilt}

! Copy the file to x.bdf. Then convert x.bdf to the fits file x.mt.
! We need to delete some of the descriptors as they cause buffer
! overflow in dophot.
   $cp {fname} x.bdf
   ntest = M$existD("x","HISTORY")
   if ntest .eq. 1 delete/desc x HISTORY
   ntest = M$existD("x","DISPLAY_DATA")
   if ntest .eq. 1 delete/desc x DISPLAY_DATA
   ntest = M$existD("x","HIST_BINS")
   if ntest .eq. 1 delete/desc x HIST_BINS
   ntest = M$existD("x","HISTOGRAM")
   if ntest .eq. 1 delete/desc x HISTOGRAM
   ntest = M$existD("x","STATISTIC")
   if ntest .eq. 1 delete/desc x STATISTIC
   outdisk/fits x x.mt

   ! Now make 2 dophot paramater files using param_mod as the template.
   ! The first file will have a high THRESHMIN (200) and a high
   ! THRESHMAX (22000). The second will have a low THRESHMAX (100) and
   ! a lower THRESHMIN (25). The two files will be called param_mod_x
   ! and param_mod_xt
   $rm -f param_mod_x
   $echo "FWHM = {fwhm}" >>param_mod_x
   $echo "AXIS_RATIO = {ratio}" >>param_mod_x
   $echo "TILT = {tilt}" >>param_mod_x
   $echo "SKY = {sky}" >>param_mod_x
   $echo "MASKBOX_X = {MASKBOX}" >>param_mod_x
   $echo "MASKBOX_Y = {MASKBOX}" >>param_mod_x
   $echo "APBOX_X = {APBOX}" >>param_mod_x
   $echo "APBOX_Y = {APBOX}" >>param_mod_x
   $echo "EPERDN = {EPERDN}" >>param_mod_x

   ! Common parameters to this point
   $cp param_mod_x param_mod_xt
```

```
$echo "NFITBOX_X = {sFITBOX}" >>param_mod_x
$echo "NFITBOX_Y = {sFITBOX}" >>param_mod_x
$echo "THRESHMAX = 22000" >>param_mod_x
$echo "THRESHMIN = 200" >>param_mod_x

! Note $$ stops midas interpreting the '
$$echo "OBJECTS_OUT = 'obj_out_x.dop"' >>param_mod_x
$cat param_mod >>param_mod_x
$echo "NFITBOX_X = {FITBOX}" >>param_mod_xt
$echo "NFITBOX_Y = {FITBOX}" >>param_mod_xt
$echo "THRESHMAX = 100" >>param_mod_xt
$echo "THRESHMIN = 25" >>param_mod_xt
$$echo "FIXPOS = 'YES"' >>param_mod_xt
$$echo "OBJECTS_OUT = 'obj_out_x.dop"' >>param_mod_xt
$$echo "OBJECTS_IN = 'obj_temp_x.dop"' >>param_mod_xt
$cat param_mod >>param_mod_xt

! Now run dophot using the param_mod_x file.  Need enough stars to be
! able to get the coordinate transformation for the template frame.
$rm -f doin
$echo param_mod_x > doin
$dophot <doin

! Now remove any records that have *'s in them as it'll cause offset
! to crash.
$cat obj_out_x.dop | sed /*/d > new_x.dop
$mv new_x.dop obj_out_x.dop

! Now get the coordinate transformation from the template to the data
! frame and apply it to the template objects in template.dop.
set/format f6.3,f6.3

$rm -f offset.in
$rm -f obj_temp_x.dop
$echo 2 > offset.in
$echo obj_out_x.dop >> offset.in
$echo {P3} >> offset.in
$echo {scale} 0.01 >> offset.in
$echo y >> offset.in
$echo obj_temp_x.dop >> offset.in
$echo N >> offset.in
$offsetkh < offset.in

! Now run dophot with fixed position stars from the template.
$rm -f doin
$echo param_mod_xt > doin
$dophot <doin

! Again remove any records that have *'s in them as it'll cause
! offset to crash.
$cat obj_out_x.dop | sed /*/d > new_x.dop
```

```
   $mv new_x.dop obj_out_x.dop

   ! Now calculate the coordinate transformation to the template frame
   ! and use it to transform the coordinates in the dophot output file
   ! to the same system as in the template frame. Use offsetkh to do
   ! this job.
   ntest = m$exist("trans.dat")
   if ntest .eq. 0 then
      $echo {fname} >> errors
      goto process_file
   else
      $echo obj_out_x.dop > applyit.in
      $echo obj_out_x_trans.dop >> applyit.in
      $applyit < applyit.in
   endif

   ! Displaying the subtracted image and calculating the PLANET date (PD).
   load/ima image_out_x.mt scale=1 cuts=f,2sigma
   set/format I3 f12.7,f12.7
   outrec = " "
   PD = {{fname},JD} - 2450000
   outrec(1:13) = "{PD}"//" "
   k = 14
   set/format I3 f6.1,f6.1

   ! The data for the event and reference stars is extracted using getstar.
   ! getstar is a unix shell script that returns a (17 char) string of the
   ! fixed format: " 7  -8.983  0.135"  i.e. I2,x,f7.3,x,f6.3
   ! It searches the dophot file for the object closest to the specified
   ! box centre.
   do i = 1 refnum
      $getstar obj_out_x_trans.dop {x({i})} {y({i})} {n({i})} | write/keyw
outrec/c/{k}/17
      k = k +17
   end do

   ! Add the fwhm to the output file
   set/format I3 f5.3,f5.3
   write/keyword outrec/c/{k}/5 {fwhm}
   k =  k + 4
   write/file {ofctrl(1)},key outrec(1:{k})

   ! Finally copy the results to the save directory if it exists
   if "{P5}" .ne. "?" then
      imlen = m$index(fname,".")
      imlen = imlen - 1
      if imlen .le. 0 imlen = m$len(fname)
      $mv obj_out_x_trans.dop {P5}/{fname(1:{imlen})}.dop
      $mv image_out_x.mt  {P5}/image_out_{fname(1:{imlen})}.mt
      $mv param_mod_xt {P5}/param_mod{fname(1:{imlen})}.par
      $mv trans.dat {P5}/trans_{fname(1:{imlen})}
```

```
      $dd if=x.mt bs=2880 count=2 of={P5}/{fname(1:{imlen})}.fits
      set/format I4 f12.5,f12.5
      catrec(1:12) = "{{fname(1:{imlen})},o_time(1)}"
      catrec(13:16) = "{x(1)}"
      catrec(16:20) = " {y(1)}"
      set/format I4 f5.2,f5.2
      catrec(20:25) = " {scale}"
      set/format I7
      $echo "{catrec(1:25)}" >> {P5}/cat.dat
   endif

   goto process_file

finish:
   write/out finished
   close/file {ifctrl}
   close/file {ofctrl}
   $rm doin FITZ* x.bdf x.mt
   $rm stars offset.in applyit.in fort.11 param_out_x
   $rm Mid*Pipe midlis*.prg obj_out_x.dop obj_temp_x.dop param_mod_x
```

B.3 The Pipeline Directory Structure

This section contains a brief outline of the directory structure that is used in the process of using the pipeline and archiving the data. This will mostly concentrate on items that would normally need to be modified in a routine reduction with a minor emphasis on recompiling the source code.

Directory: ARCHIVE

This is where the archive files will be stored, as specified in *csh_set* by:
`setenv OUT_FILE_QUY $PLHOME/ARCHIVE/`
`setenv OUT_FILE $PLHOME/ARCHIVE/`

Directory: EXE

The directory contains all the executable files used by the pipeline and archive. Whenever any of the programs are recompiled, the executable should be copied to this directory.

Directory: csh

This directory is where all the C shell scripts are kept and is the most important directory to become familiar with.

csh_archive

This script is used to create the archive for a specified event. Before use, the original script should first be copied to another name, for example:

```
> cp $SCRIPT_CODE/csh_archive $SCRIPT_CODE/csh_archiveUOB98018
```

Then the following lines should be modified:

```
set pixscale = "0.491"
set telescope = "Canopus 1m, ST6 Camera"
set coord = "??:??:??  -??:??:??"
set NameFieldLong = "MACHO Bulge 1998 event 006"
set RefV = 1
set RefI = 1
```

The archive can then be created by executing the archive script in the form:

```
> $SCRIPT_CODE/csh_archive event archive colour min max flag
```

For example, the archive for the I band of UOB98018 may be created as follows:

```
> $SCRIPT_CODE/csh_archiveUOB98018 UOB98018 UOB98018 I 001 024 X
```

This will create the archive UOB98018I (the flag X denotes that the archive is to be created) and will include images 001 to 024.

Adding images to the archive is a simply a matter of repeating the above steps except the flag used should be any letter *other than X*. For example, if it was required to add images 025 to 029 to the UOB98018I archive:

```
> $SCRIPT_CODE/csh_archiveUOB98018 UOB98018 UOB98018 I 025 029 U
```

When the script is run then all the fixed position DoPHOT output files are copied from the *$OUT_DOP* directory to the *$OUT_DOPCLEAN* directory where they are 'cleaned'. This essentially means that '*****' and 'NaN' messages are removed from the DoPHOT output files.

The archive's header will list the *cat{template}.dop* as the reference frame even though *m{template}.dop* was used as the template. In principle, the reference frame's 'cat' file should be the same as the 'm' file but there can be some small insignificant differences when the reference frame is re-processed using the 'm' file as a template.

csh_kron

The *csh_kron* script is designed to work in conjunction with *kron* to search the *$IN_IMAGE* directory for new images to process and then create a lock file while the image is being processed. The script is executed by a continually running cron job which does so every minute.

csh_off

This script is used to perform a fixed position Dophot run on an image. It is executed as follows:

```
> $SCRIPT_CODE/csh_off template image FWHM SKY THRESMIN THRESMAX
```

For example:
```
> $SCRIPT_CODE/csh_off UOB98018I019 UOB98018I001 7.68 8000 50 300
30000
```

The script firstly performs a non-deep DoPHOT run on the image and produces *o{image}.dop*. This file contains a list of the brightest stars in the image and is used to calculate the geometrical transformation.

The script secondly performs photometry on those stars contained in the template file and produces *cat{image}.dop*. This is the result of the fixed position DoPHOT run.

csh_off_fs

This operates the same as *csh_off* except that it uses the values of FWHM, SKY, THRESHMIN, and THRESHMAX that are contained in the header of the image. It's usage is simply:
```
> $SCRIPT_CODE/csh_off_fs template image
```
For example:
```
> $SCRIPT_CODE/csh_off_fs UOB98018I019 UOB98018I001
```

csh_set

This script is the *very first step* in the pipeline/archiving process. It sets the C shell environment variables so that the pipeline and archive programs know where to find images, where to place DoPHOT output files, etc. Each of the variables should be checked carefully but typically the only variables that need to be changed between microlensed sources are:
```
setenv IN_DOPHOT $PLHOME/dophotparam/ST6/
setenv IN_IMAGE /data/data/pipeline/ST6/
```
depending on whether ST6 or SITE camera images are being reduced.

After all the environment variables are set correctly, type:
```
> source csh_set
```
Thereafter, the environment variables set in *csh_set* can be used to change directories, the most commonly used ones being *$IN_IMAGE*, *$SCRIPT_CODE*, and *$PL_WORK*.

csh_template

This script processes a template image which will be used for the fixed position DoPHOT run. It is executed as follows:
```
> $SCRIPT_CODE/csh_template template FWHM SKY THRESMIN THRESMAX
```
For example:
```
> $SCRIPT_CODE/csh_template UOB98018I019 3.67 1000 50 2000
```

The script firstly performs a non-deep DoPHOT run on the image and produces *o{template}.dop*. This file contains a list of the brightest stars in the image and is used to calculate the geometrical transformation.

The script secondly performs a deep DoPHOT run on the image and produces *m{template}.dop*. This file is the template file and is used to do the photometry. Only stars listed in this file will be processed.

csh_template_fs

This operates the same as *csh_template* except that it uses the values of FWHM, SKY, THRESHMIN, and THRESHMAX that are contained in the header of the image. It's usage is simply:

```
> $SCRIPT_CODE/csh_template_fs template
```

For example:

```
> $SCRIPT_CODE/csh_template_fs UOB98018I019
```

template98.list

This file tells *csh_kron* which images to process and which of the images to use as the template. The format of the file is to simply list the names of the events followed by the template image for each filter. Typically the same template image is used for both filters.

template98.list.ST6

This is the template list file for the ST6 camera, whose images are generally denoted by a prefix "T". Whenever the file is updated it should be copied to *template98.list* as follows:

```
> cp $SCRIPT_CODE/template98.list.ST6 $SCRIPT_CODE/template98.list
```

template98.list.SITE

This is the template list file for the SITE camera, whose images are generally denoted by a prefix "U". Whenever the file is updated it should be copied to *template98.list* as follows:

```
> cp $SCRIPT_CODE/template98.list.SITE $SCRIPT_CODE/template98.list
```

Directory: dophotcode

This directory contains the code for recompiling DoPHOT, a task which will become necessary after one of the files has been edited. This can be done by typing the following:

```
> $DOPHOT_CODE/rm *.o
```

```
> $DOPHOT_CODE/make
> cp $DOPHOT_CODE/dophot $EXE_DOPHOT/
```

Directory: dophotparam

This directory contains all the DoPHOT parameter files that are used by the pipeline. These files are copied to the *$PL_WORK* directory by *csh_set.*

In this directory, there are two directories named *SITE* and *ST6* which contain the appropriate DoPHOT parameter files for the SITE camera and ST6 camera respectively. This needs to be specified in the *csh_set* script in the following line: `setenv IN_DOPHOT $PLHOME/dophotparam/ST6/`

Directory: offset

This directory contains the code for compiling the OFFSET program. To recompile OFFSET, type the following:

```
> $OFFSET_CODE/rm *.o
> $OFFSET_CODE/make
> cp $OFFSET_CODE/offset $EXEARCH/
```

Appendix C

Relative Flux Calculation

This appendix describes how the fluxes and errors are calculated in the SuperMongo script `plot.sm`. Let st_n and $sterr_n$ be the DoPHOT fit magnitude and DoPHOT fit magnitude error respectively for each of the 10 reference stars (n is valued from 1 to 10). Then the flux of reference star n is given by

$$F_n = 10^{-st_n/2.5}$$

and the upper and lower errors are given by

$$E1_n = 10^{(-st_n+sterr_n)/2.5} - F_n \text{ and } E2_n = F_n - 10^{(-st_n-sterr_n)/2.5}$$

The average flux of the 10 reference stars is then

$$averageflux = \frac{\sum_{n=1}^{10} F_n}{10}$$

where the associated errors are given by

$$averagerr1 = \sqrt{\frac{\sum_{n=1}^{10} E1_n}{10}} \text{ and } averagerr2 = \sqrt{\frac{\sum_{n=1}^{10} E2_n}{10}}$$

Let the DoPHOT fit magnitude and DoPHOT fit magnitude error be represented by the variables *sourcemag* and *sourcemagerr* respectively for the microlensed source. The flux of the microlensed source may then be expressed as

$$sourceflux = 10^{sourcemag/2.5}$$

and the upper and lower errors are given by

$$sourcerr1 = 10^{(-sourcemag+sourcemagerr)/2.5} - sourceflux$$

and

$$sourcerr2 = sourceflux - 10^{(-sourcemag-sourcemagerr)/2.5}$$

The relative intensity can then be calculated

$$amp = \frac{sourceflux}{averageflux}$$

where the associated errors are given by

$$amperr1 = amp\sqrt{\left(\frac{sourcerr1}{sourceflux}\right)^2 + \left(\frac{averagerr1}{averageflux}\right)^2}$$

and

$$amperr2 = amp\sqrt{\left(\frac{sourcerr2}{sourceflux}\right)^2 + \left(\frac{averagerr2}{averageflux}\right)^2}$$

The script `plot.sm` is given below.

```
#
#  @@@@   @       @@@   @@@@@      @@@   @     @
#  @   @  @      @   @    @       @   @  @@   @@
#  @   @  @      @   @    @       @      @ @ @ @
#  @@@@   @      @   @    @        @@@   @  @  @
#  @      @      @   @    @           @  @     @
#  @      @      @   @    @       @   @  @     @
#  @      @@@@@   @@@     @    @   @@@   @     @
#
# Type "plot" to begin
#

plot    define file ? <Name of data file?>
        define event ? <Name of event?>
        define site ? <Hobart 96 (1), Hobart 97 (2), CTIO (3)>
        define plotstars ? <Plot reference stars? (Yes 1 No 0)>
        define format ? <Create postscript file? (Yes 1 No 0)>
        data $file
        define Ftot 0
        define nos 10
        define i 0
        do r=1,10 {define foutstar$r 0}
        loop

        # User decides which reference stars are to be excluded
        # from calculations

loop    define i ($i+1)
        define foutstar$i ? <Reference star to ignore $i>
        if ($foutstar$i==0) {process}
        if ($foutstar$i>0) {loop}

process if ($format==1) {device postencap $file.ps}
```

```
if ($format==0) {device x11}
erase
set sumerr1=0
set sumerr2=0
set Ftot=0
define r 0
read {date 1 sourcemag 3 sourcemagerr 4 seeing 35}

# The arcsec/pixel of the CCD is determined by the site

if ($site==1) {set seeing = seeing * 0.8804}
if ($site==2) {set seeing = seeing * 0.4545}
if ($site==3) {set seeing = seeing * 0.396}

# Calculate fluxes and errors of reference stars

do r=3,30,3 {
  define stcol ($r+3)
  define sterrcol ($r+4)
  define n ($r/3)
  read st$n $stcol
  read sterr$n $sterrcol
  set F$n = (10**(-st$n/2.5))
  set E1$n = (10**((-st$n+sterr$n)/2.5))-F$n
  set E2$n = F$n-(10**((-st$n-sterr$n)/2.5))
  set Ffout$n = 0
  set E1fout$n = 0
  set E2fout$n = 0

  # This loop decides if reference star n is to be included

  do t=1,10 {
    if ($foutstar$t == $n){
      set Ffout$n = (F$n)
      set E1fout$n = (E1$n)
      set E2fout$n = (E2$n)
      define nos ($nos-1)}
  }
  set Ftot = (Ftot + F$n - Ffout$n)
  set sumerr1 = (sumerr1 + (E1$n - E1fout$n)**2)
  set sumerr2 = (sumerr2 + (E2$n - E2fout$n)**2)
}
set averageflux = (Ftot/$nos)
set averagerr1 = (sqrt(sumerr1/$nos))
set averagerr2 = (sqrt(sumerr2/$nos))

# Calculate fluxes and errors of the source star

set sourceflux=(10**(-sourcemag/2.5))
set sourcerr1=10**((-sourcemag+sourcemagerr)/2.5)-sourceflux
set sourcerr2=sourceflux-10**((-sourcemag-sourcemagerr)/2.5)
```

```
        # Calculate the amplitude of the source

        set amp = (sourceflux/averageflux)
        set amperr1 = amp*sqrt((sourcerr1/sourceflux)**2+
(averagerr1/averageflux)**2)
        set amperr2 = amp*sqrt((sourcerr2/sourceflux)**2+
(averagerr2/averageflux)**2)
        limits date amp
        ctype black
        if ($plotstars == 1) {expand 0.8 window -2 -6 1 6 box 0 2 1 3}
        if ($plotstars == 0) {expand 1.1 window 1 1 1 1 box}
        expand 0.8
        ptype 20 3
        ctype red
        points date amp
        errorbar date amp amperr1 2
        errorbar date amp amperr2 4
        ctype black
        define sigmatot 0

        # Reference stars ARE plotted

        if ($plotstars == 1){
          do k=1,10 {
            set amp$k=(F$k/averageflux)
            set erramp1$k=amp$k*sqrt((E1$k/F$k)**2+
(averagerr1/averageflux)**2)
            set erramp2$k=amp$k*sqrt((E2$k/F$k)**2+
(averagerr2/averageflux)**2)
            stats amp$k mean$k sigma$k kur$k
            define min$k ($mean$k-$sigma$k)
            define max$k ($mean$k+$sigma$k)
            define uplim$k ($mean$k+5*$sigma$k)
            define lowlim$k ($mean$k-5*$sigma$k)
            define realsigma$k ($sigma$k/$mean$k)
            echo "sigma star"$k " = " $realsigma$k
            define sigmatot ($sigmatot+$realsigma$k)
            do t=1,10 {
              if ($foutstar$t == $k) {
                define sigmatot ($sigmatot-$realsigma$k)
              }
            }

            define m (6-$k)
            expand 0.8
            if ( $k < 6 ) {
              window -2 -6 1 $m
              limits date $lowlim$k $uplim$k
              if ($k == 1) {box 0 2 0 3}
              if ($k == 2) {box 0 2 0 3}
```

```
    if ($k == 3) {box 0 2 0 3}
    if ($k == 4) {box 0 2 0 3}
    if ($k == 5) {box 1 2 0 3}
    ptype 20 3
    expand 0.5
    points date amp$k
    line $mean$k $min$k $max$k
    rlabel
  }

  define m (11-$k)
  expand 0.8
  if ($k > 5) {
    window -2 -6 2 $m
    limits date $lowlim$k $uplim$k
    if ($k == 6)  {box 0 3 3 2}
    if ($k == 7)  {box 0 3 0 2}
    if ($k == 8)  {box 0 3 0 2}
    if ($k == 9)  {box 0 3 0 2}
    if ($k == 10) {box 1 3 0 2}
    ptype 20 3
    expand 0.5
    points date amp$k
    line $mean$k $min$k $max$k
    rlabel
  }
}
expand 0.9
window -2 -6 1 6
limits 0 100 0 100
relocate 75 80
# It may be more suitable to label the other side
# relocate 5 80
label $event
define avesigma ($sigmatot/$nos)
echo "average sigma  = " $avesigma
expand 0.8
limits date seeing
ticksize 0 0 0.2 1
window -2 -6 2 6
box 0 3 1 2
ptype 20 3
ctype green
points date seeing
ctype black
window 1 1 1 1
limits 0 100 0 100
relocate 104 97
angle 270
label seeing (\")
expand 1.3
```

```
          relocate -8 35
          angle 90
          label Relative Intensity
          relocate 36 -6
          angle 0
          label HJD - 2450000
          angle 0
          ticksize 0 0 0 0
        }

        # Reference stars ARE NOT plotted

        if ($plotstars==0){
          expand 1.5
          xlabel HJD - 2450000
          ylabel Relative Intensity
          limits 0 100 0 100
          relocate 79 93
          label $event
          expand 1.1
          ctype black
          relocate 60 90
          limits date amp
        }

        # Label the reference stars

rlabel  expand 0.9
        limits 0 100 0 100
        relocate 90 80
        label \#$k
        do ls=1,10 {
          if ($foutstar$ls==$k) {relocate 5 80 label Ignored}
        }
        expand 0.5
        limits date $lowlim$k $uplim$k

        # Macro to plot the mean and 1 sigma lines

line 3  ltype 0
        relocate 0 $1
        draw 1000 $1
        ltype 3
        relocate 0 $3
        draw 1000 $3
        relocate 0 $2
        draw 1000 $2
        ltype 0
```

Appendix D

χ^2 Minimization Program

The SuperMongo program `model.sm` was used to fit models to the PLANET data sets studied in Chapter 5. This script is shown below.

```
#
# @     @   @@@   @@@@   @@@@@  @          @@@   @     @
# @@   @@  @   @  @   @  @      @         @   @  @@   @@
# @ @ @ @  @   @  @   @  @      @         @      @ @ @ @
# @  @  @  @   @  @   @  @@@@@  @          @@@   @  @  @
# @     @  @   @  @   @  @      @             @  @     @
# @     @  @   @  @   @  @      @         @   @  @     @
# @     @   @@@   @@@@   @@@@@  @@@@@  @   @@@   @     @
#
# Type "model" to begin
#

model   # Script designed to fit a microlensing model to a data
        # set. The input files needed are the output files from
        # the archive program 'plotref'.

        define errx 2.0  # Factor to multiply errors by
        define numb ? <Number of data files to use in modelling?>
        echo Enter file names starting with the baseline file
        do i=1,$numb {
          define file$i ? <Name of file $i?>
          name
          define offsetx ? <Adjust date? (Yes 1 No 0)>
          if ($offsetx==1) {
            define offsetx$i -281.5
          } else {
            define offsetx$i 0
          }
          define offsety$i 0
        }
        device x11
        setlim
```

```
        align
        define dof 0
        do i=1,$numb {
          define dim$i (dimen(date$i))
          define dof ($dof+$dim$i)
        }
        set dimen(sigres)=$dof
        echo
        echo [1] Point Source - Point Lens
        echo [2] Blended Point Source - Point Lens
        echo [3] Binary Source - Point Lens
        define fit ? <Which model would you like to attempt to fit?>
        if ($fit==1) {pspl}
        if ($fit==2) {blend}
        if ($fit==3) {bspl}
        fit
        plot
        finish


name    if ('$file$i'=='baseline') {define fname$i "Baseline"}
        if ('$file$i'=='canopus') {define fname$i "Canopus"}
        if ('$file$i'=='ctio') {define fname$i "CTIO"}
        if ('$file$i'=='saao') {define fname$i "SAAO"}
        if ('$file$i'=='lasilla') {define fname$i "La Silla"}


setlim  do i=1,$numb {
          data $file$i
          read {date 4 mag 2 err 3}
          set date$i = date + $offsetx$i
          set mag$i = mag + $offsety$i
          set err$i = err
          limits date$i mag$i
          if ($i==1) {
            define xmin $fx1
            define xmax $fx2
            define ymin $fy1
            define ymax $fy2
          } else {
            if ($fx1<$xmin) {define xmin $fx1}
            if ($fx2>$xmax) {define xmax $fx2}
            if ($fy1<$ymin) {define ymin $fy1}
            if ($fy2>$ymax) {define ymax $fy2}
          }
        }


align   erase
        limits $xmin $xmax $ymax $ymin
        expand 1.1
```

```
        ctype black
        location 3500 31000 3500 31000
        box
        expand 1.3
        xlabel Date HJD - 2450000
        ylabel Magnitude
        expand 1.0
        ptype 20 3
        do i=1,$numb {
          data $file$i
          read {date 4 mag 2}
          set date$i = date + $offsetx$i
          set mag$i = mag + $offsety$i
          define colour ($i+2)
          ctype $colour
          points date$i mag$i
        }
        limits 0 100 0 100
        do i=1,$numb {
          define colour ($i+2)
          ctype $colour
          define j (100-$i*5)
          relocate 85 $j
          putlabel 5 $file$i
        }
        define adjust ? <Adjust offsets? (Yes 1 No 0)>
        if ($adjust==1) {
          do i=1,$numb {
            define offsety$i ? <Value for offset$i?>
          }
          setlim
          align
        }


pspl    define np 3
        define pc1 "t_0"
        define pi1 0.01
        define pe1 1
        define pc2 "u_{min}"
        define pi2 0.001
        define pe2 0
        define pc3 "t_E"
        define pi3 0.01
        define pe3 0


blend   define np 4
        define pc1 "t_0"
        define pi1 0.01
        define pe1 1
```

```
        define pc2 "u_{min}"
        define pi2 0.001
        define pe2 0
        define pc3 "t_E"
        define pi3 0.01
        define pe3 0
        define pc4 "f"
        define pi4 0.01
        define pe4 0


bspl    define np 6
        define pc1 "t_{0,1}"
        define pi1 0.01
        define pe1 1
        define pc2 "t_{0,2}"
        define pi2 0.01
        define pe2 1
        define pc3 "u_{min,1}"
        define pi3 0.001
        define pe3 0
        define pc4 "u_{min,2}"
        define pi4 0.001
        define pe4 0
        define pc5 "t_E"
        define pi5 0.01
        define pe5 0
        define pc6 "\omega"
        define pi6 0.01
        define pe6 0


fit     # Baseline magnitudes are converted to amplification
        # and the average is calculated.
        set amp1 = 10**(-mag1/2.5)
        define bl 0
        do i=0,$dim1-1 {
          define bl ($bl+amp1[$i])
        }
        define bl ($bl/$dim1)
        # This is used to normalize the amplifications of the
        # data sets.
        do i=1,$numb {
          set amp$i = (10**(-mag$i/2.5))/$bl
          set error$i = ((10**((-mag$i+err$i*$errx)/2.5))/$bl)-amp$i
        }
        # First guesses of parameters are required.
        define dof ($dof-$numb-$np+2)
        guess
        # Iterations adjusting the parameters are performed until
        # chi^2 has converged.
```

```
        define rchi2 0
        define ni 0
        set diff = 1
        repeat iter while diff > 0.001
        do i=1,$np {
          echo "Estimate for" $pc$i "is" $p$i
        }
        echo "The final fit for" $dof "degrees of freedom"
        echo "produced a reduced chi^2 of" $rchi2
        echo "after" $ni "iterations."


iter    define redchi2 ($rchi2)
        do i=1,$np {
          define tchi2 (10**20)
          define parity 1
          set finish = 0
          # Subroutine min is used to minimize the chi^2.
          repeat min while finish < 3
          define rchi2 ($fchi2/$dof)
        }
        set diff = abs($redchi2-$rchi2)
        define ni ($ni+1)


guess   echo Enter first guesses for parameters
        do i=1,$np {
          define p$i ? <Guess for $pc$i?>
        }
        define gchi2 0
        do i=1,$numb {
          set dimen(A) = $dim$i
          set dimen(chi) = $dim$i
          if ($fit<3) {
            set dimen(u) = $dim$i
            do j=0,$dim$i-1 {
              set u[$j] = sqrt($p2**2+((date$i[$j]-$p1)/$p3)**2)
              set A[$j] = (u[$j]**2+2)/(u[$j]*sqrt(u[$j]**2+4))
              if ($fit==2) {set A[$j] = $p4*A[$j]+1-$p4}
              set chi[$j] = ((A[$j]-amp$i[$j])**2)/(error$i[$j]**2)
              define gchi2 ($gchi2+chi[$j])
            }
          }
          if ($fit==3) {
            set dimen(u1) = $dim$i
            set dimen(u2) = $dim$i
            set dimen(A1) = $dim$i
            set dimen(A2) = $dim$i
            do j=0,$dim$i-1 {
              set u1[$j] = sqrt($p3**2+((date$i[$j]-$p1)/$p5)**2)
              set u2[$j] = sqrt($p4**2+((date$i[$j]-$p2)/$p5)**2)
```

```
            set A1[$j] = (u1[$j]**2+2)/(u1[$j]*sqrt(u1[$j]**2+4))
            set A2[$j] = (u2[$j]**2+2)/(u2[$j]*sqrt(u2[$j]**2+4))
            set A[$j] = (1-$p6)*A1[$j]+$p6*A2[$j]
            set chi[$j] = ((A[$j]-amp$i[$j])**2)/(error$i[$j]**2)
            define gchi2 ($gchi2+chi[$j])
          }
        }
      }
      define rchi2 ($gchi2/$dof)
      echo "Reduced chi^2 is" $rchi2
      plot
      define adjust ? <Adjust parameters? (Yes 1 No 0)>
      if ($adjust==1) {
        guess
      }


min   define chi2 0
      do j=1,$numb {
        set dimen(A) = $dim$j
        set dimen(chi) = $dim$j
        if ($fit<3) {
          set dimen(u) = $dim$j
          do k=0,$dim$j-1 {
            set u[$k] = sqrt($p2**2+((date$j[$k]-$p1)/$p3)**2)
            set A[$k] = (u[$k]**2+2)/(u[$k]*sqrt(u[$k]**2+4))
            if ($fit==2) {set A[$k] = $p4*A[$k]+1-$p4}
            set chi[$k] = ((A[$k]-amp$j[$k])**2)/(error$j[$k]**2)
            define chi2 ($chi2+chi[$k])
          }
        }
        if ($fit==3) {
          set dimen(u1) = $dim$j
          set dimen(u2) = $dim$j
          set dimen(A1) = $dim$j
          set dimen(A2) = $dim$j
          do k=0,$dim$j-1 {
            set u1[$k] = sqrt($p3**2+((date$j[$k]-$p1)/$p5)**2)
            set u2[$k] = sqrt($p4**2+((date$j[$k]-$p2)/$p5)**2)
            set A1[$k] = (u1[$k]**2+2)/(u1[$k]*sqrt(u1[$k]**2+4))
            set A2[$k] = (u2[$k]**2+2)/(u2[$k]*sqrt(u2[$k]**2+4))
            set A[$k] = (1-$p6)*A1[$k]+$p6*A2[$k]
            set chi[$k] = ((A[$k]-amp$j[$k])**2)/(error$j[$k]**2)
            define chi2 ($chi2+chi[$k])
          }
        }
      }
      define rchi2 ($chi2/$dof)
      echo "Adjusting" $pc$i "| Current reduced chi^2:" $rchi2
      if ($chi2<=$tchi2) {
        define fchi2 $chi2
```

```
        } else {
          define parity ($parity*(-1))
          set finish = finish + 1
        }
        define tchi2 $chi2
        define p$i ($p$i+$parity*$pi$i)


plot    # Calculate the residuals
        define k 0
        do i=1,$numb {
          set dimen(A) = $dim$i
          set dimen(res$i) = $dim$i
          if ($fit<3) {
            set dimen(u) = $dim$i
            do j=0,$dim$i-1 {
              set u[$j] = sqrt($p2**2+((date$i[$j]-$p1)/$p3)**2)
              set A[$j] = (u[$j]**2+2)/(u[$j]*sqrt(u[$j]**2+4))
              if ($fit==2) {set A[$j] = $p4*A[$j]+1-$p4}
              set res$i[$j] = A[$j] - amp$i[$j]
              set sigres[$k] = res$i[$j] / A[$j]
              define k ($k+1)
            }
          }
          if ($fit==3) {
            set dimen(u1) = $dim$i
            set dimen(u2) = $dim$i
            set dimen(A1) = $dim$i
            set dimen(A2) = $dim$i
            do j=0,$dim$i-1 {
              set u1[$j] = sqrt($p3**2+((date$i[$j]-$p1)/$p5)**2)
              set u2[$j] = sqrt($p4**2+((date$i[$j]-$p2)/$p5)**2)
              set A1[$j] = (u1[$j]**2+2)/(u1[$j]*sqrt(u1[$j]**2+4))
              set A2[$j] = (u2[$j]**2+2)/(u2[$j]*sqrt(u2[$j]**2+4))
              set A[$j] = (1-$p6)*A1[$j]+$p6*A2[$j]
              set res$i[$j] = A[$j] - amp$i[$j]
              set sigres[$k] = res$i[$j] / A[$j]
              define k ($k+1)
            }
          }
          limits date$i res$i
          if ($i==1) {
            define ymin $fy1
            define ymax $fy2
          } else {
            if ($fy1<$ymin) {define ymin $fy1}
            if ($fy2>$ymax) {define ymax $fy2}
          }
        }
        stats sigres mean sigma kur
        do i=1,$numb {
```

```
          limits date$i amp$i
          if ($i==1) {
            define ymin1 $fy1
            define ymax1 $fy2
          } else {
            if ($fy1<$ymin1) {define ymin1 $fy1}
            if ($fy2>$ymax1) {define ymax1 $fy2}
          }
        }
        define xmin1 ($xmin*0.98)
        define xmax1 ($xmax*1.02)
        define ymin1 ($ymin1*0.90)
        define ymax1 ($ymax1*1.05)
        erase
        # Plot the residuals
        limits $xmin1 $xmax1 $ymin $ymax
        expand 1.1
        ctype black
        location 3500 31000 3500 10000
        box 1 2
        expand 1.3
        xlabel Date HJD - 2450000
        ylabel Residuals
        expand 1.0
        ltype 1
        relocate $xmin1 0
        draw $xmax1 0
        ltype 0
        ptype 20 3
        do i=1,$numb {
          define colour ($i+2)
          ctype $colour
          points date$i res$i
          errorbar date$i res$i error$i 2
          errorbar date$i res$i error$i 4
        }
        limits 0 100 0 100
        expand 1.1
        ctype black
        relocate 65 80
        define sigma (sprintf('%4.3f',$sigma))
        putlabel 6 \sigma = $sigma
# Plot the light curve data
        limits $xmin1 $xmax1 $ymin1 $ymax1
        expand 1.1
        ctype black
        location 3500 31000 10000 31000
        box 0 2
        expand 1.3
        ylabel Amplification
        expand 1.0
```

```
ptype 20 3
do i=1,$numb {
  define colour ($i+2)
  ctype $colour
  points date$i amp$i
  errorbar date$i amp$i error$i 2
  errorbar date$i amp$i error$i 4
}
# Plot the model with current fit parameters
ctype black
set t=$xmin1,$xmax1,0.01
if ($fit<3) {
  set u = sqrt($p2**2+((t-$p1)/$p3)**2)
  set A = (u**2+2)/(u*sqrt(u**2+4))
  if ($fit==2) {set A = $p4*A+1-$p4}
}
if ($fit==3) {
  set u1 = sqrt($p3**2+((t-$p1)/$p5)**2)
  set u2 = sqrt($p4**2+((t-$p2)/$p5)**2)
  set A1 = (u1**2+2)/(u1*sqrt(u1**2+4))
  set A2 = (u2**2+2)/(u2*sqrt(u2**2+4))
  set A = (1-$p6)*A1+$p6*A2
}
connect t A
# Label the different data sets
limits 0 100 0 100
expand 1.1
do i=1,$numb {
  define colour ($i+2)
  ctype $colour
  define j (100-$i*5)
  relocate 65 $j
  putlabel 6 $fname$i
}
ctype black
define j (100-$numb*5-5)
relocate 65 $j
define rchi2 (sprintf('%4.3f',$rchi2))
putlabel 6 \chi^2 = $rchi2
define j ($j-5)
relocate 65 $j
putlabel 6 d.o.f. = $dof
do i=1,$np {
  define j ($j-5)
  relocate 65 $j
  define hi$i (sprintf('%4.3f',$pi$i))
  if ($pe$i==1) {
    define he$i ($sigma*2)
  } else {
    define he$i ($sigma*$p$i)
  }
```

```
      define k (int(abs(lg($hi$i))))
      if ($k==1) {
        define h$i (sprintf('%4.1f',$p$i))
        define he$i (sprintf('%4.1f',$he$i))
      }
      if ($k==2) {
        define h$i (sprintf('%4.2f',$p$i))
        define he$i (sprintf('%4.2f',$he$i))
      }
      if ($k==3) {
        define h$i (sprintf('%4.3f',$p$i))
        define he$i (sprintf('%4.3f',$he$i))
      }
      putlabel 6 $pc$i "=" $h$i"\pm" $he$i
    }


finish  define format ? <Make postscript file? (Yes 1 No 0)>
    if ($format==1) {
      device postencap model.ps
      plot
    }
```

Appendix E

Galactic Bulge Model Calculations

E.1 Optical Depth for Constant Density

This section details the evaluation of the integral in Equation 6.11. The integral

$$I = \int_0^d x^{-D_s/d} D_s^2 \, dD_s$$

may be solved using repeated integration by parts

$$\int f^{(n)} g \, dx = f^{(n-1)} g - f^{(n-2)} g' + f^{(n-3)} g'' - \cdots (-1)^n \int f g^{(n)} \, dx$$

in the following manner

$$\begin{aligned} I &= \left(D_s^2 \left[(x^{-D_s/d}) \left(-\frac{d}{\ln x} \right) \right] 2z \left[(x^{-D_s/d}) \left(-\frac{d}{\ln x} \right)^2 \right] \right. \\ &\quad \left. + 2 \left[(x^{-D_s/d}) \left(-\frac{d}{\ln x} \right)^3 \right] \right) \Bigg|_{D_s=0}^{D_s=d} \\ &= -x^{-D_s/d} \left[\frac{dD_s^2}{\ln x} + \frac{2d^2 D_s}{(\ln x)^2} + \frac{2d^3}{(\ln x)^3} \right] \Bigg|_{D_s=0}^{D_s=d} \\ &= -x^{-1} \left[\frac{d^3}{\ln x} + \frac{2d^3}{(\ln x)^2} + \frac{2d^3}{(\ln x)^3} \right] + \left[\frac{2d^3}{(\ln x)^3} \right] \\ &= \frac{d^3}{\ln x} \left(\frac{2}{(\ln x)^2} - \frac{1}{x} - \frac{2}{x \ln x} - \frac{2}{x(\ln x)^2} \right) \end{aligned} \tag{E.1}$$

which is the required result.

E.2 Fractional Area for Exponential Density

This section details the evaluation of the integral in Equation 6.22. Let the integral be defined as

$$I = \int_0^{D_s} \exp\left[-\frac{|R_0 - D_d|}{i_0}\right] \frac{D_d(D_s - D_d)}{D_s}\, dD_d \tag{E.2}$$

Due to the absolute value of $R_0 - D_d$, this integral is a boundary value problem around the Galactocentric distance R_0. Hence, the integral needs to be separated into two integrals defined on either of the boundary R_0, as follows

$$I_1 = \int_0^{D_s} \exp\left[-\frac{(R_0 - D_d)}{i_0}\right] \frac{D_d(D_s - D_d)}{D_s}\, dD_d$$

for $D_s < R_0$, and

$$\begin{aligned} I_2 &= \int_0^{R_0} \exp\left[-\frac{(R_0 - D_d)}{i_0}\right] \frac{D_d(D_s - D_d)}{D_s}\, dD_d \\ &\quad + \int_{R_0}^{D_s} \exp\left[-\frac{(D_d - R_0)}{i_0}\right] \frac{D_d(D_s - D_d)}{D_s}\, dD_d \end{aligned}$$

for $D_s > R_0$. These two integrals will now be considered separately.

Source Distance Less Than R_0

The integral I_1 may be expanded into two parts

$$I_1 = \int_0^{D_s} D_d \exp\left[-\frac{(R_0 - D_d)}{i_0}\right] dD_d - \int_0^{D_s} \frac{D_d^2}{D_s} \exp\left[-\frac{(R_0 - D_d)}{i_0}\right] dD_d \tag{E.3}$$

Both of these integrals may be evaluated using integration by parts:

$$\int u\frac{dv}{dx}\, dx = uv - \int v\frac{du}{dx}\, dx$$

In the case of the first integral, it is most convenient to define

$$u = D_d \text{ and } \frac{dv}{dD_d} = \exp\left[-\frac{(R_0 - D_d)}{i_0}\right]$$

Then it follows that

$$\frac{du}{D_d} = 1 \text{ and } v = \int \exp\left[-\frac{(R_0 - D_d)}{i_0}\right] D_d$$

By substituting $\gamma = (R_0 - D_d)/i_0$, v becomes

$$\begin{aligned} v &= -i_0 \int e^{-\gamma}\, d\gamma \\ &= i_0 e^{-\gamma} \\ &= i_0 \exp\left[-\frac{(R_0 - D_d)}{i_0}\right] \end{aligned}$$

Then using integration by parts

$$\begin{aligned} \int u \frac{dv}{dD_d}\, dD_d &= D_d i_0 \exp\left[-\frac{(R_0 - D_d)}{i_0}\right] - i_0 \int \exp\left[-\frac{(R_0 - D_d)}{i_0}\right] dD_d \\ &= i_0 D_d \exp\left[-\frac{(R_0 - D_d)}{i_0}\right] - i_0^2 \exp\left[-\frac{(R_0 - D_d)}{i_0}\right] \\ &= i_0 \exp\left[-\frac{(R_0 - D_d)}{i_0}\right](D_d - i_0) \end{aligned} \tag{E.4}$$

In the case of the second integral, it is convenient to define

$$u = \frac{D_d^2}{D_s} \text{ and } \frac{dv}{dD_d} = \exp\left[-\frac{(R_0 - D_d)}{i_0}\right]$$

Then it follows that

$$\frac{du}{D_d} = \frac{2D_d}{D_s} \text{ and } v = i_0 \exp\left[-\frac{(R_0 - D_d)}{i_0}\right]$$

Then using integration by parts

$$\begin{aligned} \int u \frac{dv}{dD_d}\, dD_d &= \frac{D_d^2}{D_s} i_0 \exp\left[-\frac{(R_0 - D_d)}{i_0}\right] - \frac{2i_0}{D_s} \int D_d \exp\left[-\frac{(R_0 - D_d)}{i_0}\right] dD_d \\ &= i_0 \frac{D_d^2}{D_s} \exp\left[-\frac{(R_0 - D_d)}{i_0}\right] - \frac{2i_0^2}{D_s} \exp\left[-\frac{(R_0 - D_d)}{i_0}\right](D_d - i_0) \\ &= \frac{i_0}{D_s} \exp\left[-\frac{(R_0 - D_d)}{i_0}\right](D_d^2 - 2i_0 D_d + 2i_0^2) \end{aligned} \tag{E.5}$$

Combining Equation E.4 and Equation E.5 yields

$$I_1 = i_0 \exp\left[-\frac{(R_0 - D_d)}{i_0}\right]\left(D_d - i_0 - \frac{D_d^2}{D_s} + \frac{2i_0 D_d}{D_s} - \frac{2i_0^2}{D_s}\right)\Bigg|_{D_d=0}^{D_d=D_s} \tag{E.6}$$

$$\begin{aligned} &= i_0^2 \exp\left[-\frac{(R_0 - D_s)}{i_0}\right]\left(1 - \frac{2i_0}{D_s}\right) + i_0^2 \exp\left[-\frac{R_0}{i_0}\right]\left(1 + \frac{2i_0}{D_s}\right) \\ &= \frac{i_0^2 e^{-R_0/i_0}(D_s(1 + e^{D_s/i_0}) + 2i_0(1 - e^{D_s/i_0}))}{D_s} \end{aligned} \tag{E.7}$$

Source Distance Greater Than R_0

Since the first component of integral I_2 is identical to integral I_1 except for the limits, this component may be solved by simply substituting the limits $0 \rightarrow R_0$ into Equation E.6.

$$\begin{aligned} I_{2.1} &= i_0 \exp\left[-\frac{(R_0 - D_d)}{i_0}\right]\left(D_d - i_0 - \frac{D_d^2}{D_s} + \frac{2i_0 D_d}{D_s} - \frac{2i_0^2}{D_s}\right)\Bigg|_{D_d=0}^{D_d=R_0} \\ &= i_0\left(R_0 - i_0 - \frac{R_0^2}{D_s} + \frac{2i_0 R_0}{D_s} - \frac{2i_0^2}{D_s}\right) - i_0 \exp\left[-\frac{R_0}{i_0}\right]\left(-i_0 - \frac{2i_0^2}{D_s}\right) \\ &= \frac{i_0(R_0 D_s + 2i_0 R_0 + i_0 e^{-R_0/i_0}(D_s + 2i_0) - i_0 D_s - 2i_0^2 - R_0^2)}{D_s} \end{aligned} \tag{E.8}$$

As was the case for integral I_1, the second component of integral I_2 may be solved by expanding the integral into two parts

$$I_{2.2} = \int_{R_0}^{D_s} D_d \exp\left[-\frac{(D_d - R_0)}{i_0}\right] dD_d - \int_{R_0}^{D_s} \frac{D_d^2}{D_s} \exp\left[-\frac{(D_d - R_0)}{i_0}\right] dD_d$$

Using integration by parts, the first integral becomes

$$I_{2.2.1} = -i_0 \exp\left[-\frac{(D_d - R_0)}{i_0}\right](D_d + i_0) \tag{E.9}$$

and the second integral becomes

$$I_{2.2.2} = -\frac{i_0}{D_s} \exp\left[-\frac{(D_d - R_0)}{i_0}\right](D_d^2 + 2i_0 D_d + 2i_0^2) \tag{E.10}$$

so that combining Equation E.9 and Equation E.10 yields

$$\begin{aligned} I_{2.2} &= i_0 \exp\left[-\frac{(D_d - R_0)}{i_0}\right]\left(-D_d - i_0 + \frac{D_d^2}{D_s} + \frac{2i_0 D_d}{D_s} + \frac{2i_0^2}{D_s}\right)\Bigg|_{D_d=R_0}^{D_d=D_s} \\ &= i_0 \exp\left[-\frac{(D_s - R_0)}{i_0}\right]\left(i_0 + \frac{2i_0^2}{D_s}\right) - i_0\left(-R_0 - i_0 + \frac{R_0^2}{D_s} + \frac{2i_0 R_0}{D_s} + \frac{2i_0^2}{D_s}\right) \\ &= \frac{i_0(i_0 D_s - 2i_0^2 + i_0 e^{-(D_s - R_0)/i_0}(D_s + 2i_0) + R_0 D_s - 2i_0 R_0 - R_0^2)}{D_s} \end{aligned} \tag{E.11}$$

Combining Equation E.8 and Equation E.11 leads to the expression for integral I_2

$$I_2 = \frac{i_0\left(2i_0^2\left(e^{-\frac{D_s - R_0}{i_0}} + e^{-\frac{R_0}{i_0}} - 2\right) - 2R_0^2 + D_s\left(i_0 e^{-\frac{D_s - R_0}{i_0}} + i_0 e^{-\frac{R_0}{i_0}} + 2R_0\right)\right)}{D_s} \tag{E.12}$$

Appendix F

The Spectral Typing Routine

The MIDAS script `specfit.prg` was used to estimate the spectral type of the spectra described in Chapter 8 and was also used to estimate the interstellar extinction in the spectra. This script is shown below.

```
! The purpose of this script is to determine the interstellar
! extinction in a measured spectrum and estimate the spectral
! type by fitting a Kurucz model spectrum.
!
! Using this script requires that the directory "models" be
! copied to the location where the spectra to be processed
! reside. Input in the form of a file require the file to
! contain a number which defines the number of spectra to be
! combined followed by the appropriate files names of the
! spectra. For example:
! 2
! spec_b150.bdf
! spec_o150.bdf
! Spectra which are processed directly rather than from a file
! need not include the .bdf extension.

input:
   define/par P1 ? C "Read spectra from file? (Y/N)"
   if P1 .ne. "Y" .and. P1 .ne. "N" then
      write/out "Choose Yes (Y) or No (N)!"
      goto input
   endif
   if P1 .eq. "Y" then
      define/par P2 ? C "Name of file?"
      $cp {P2} printtemp.cat
      define/local infile/i/1/1 1
   else
      define/par P2 ? C "Name of spectrum?"
      define/local infile/i/1/1 0
   endif
```

```
help:
   define/par P3 ? C "Spectral type to fit (? for help)?"
   if P3 .eq. "?" then
      write/out "Available spectral types are:"
      write/out " O3I    O4I    O5I    O7I    O8I    O9I"
      write/out " O3III  O4III  O5III  O6III  O7III  O8III  O9III"
      write/out " O3V    O4V    O5V    O6V    O7V    O8V    O9V"
      write/out " BOI    B1I    B2I    B3I    B5I    B6I    B7I    B8I
B9I"
      write/out " BOIII  B1III  B2III  B3III  B5III  B6III  B7III  B8III
B9III"
      write/out " BOV    B1V    B2V    B3V    B5V    B6V    B7V    B8V
B9V"
      write/out " AOI    A1I    A2I    A3I    A5I    A7I    A8I"
      write/out " AOIII  A1III  A2III  A3III  A5III  A7III  A8III"
      write/out " AOV    A1V    A2V    A3V    A5V    A7V    A8V"
      write/out " FOI    F2I    F5I    F8I    GOI    G2I    G5I"
      write/out " FOIII  F2III  F5III  F8III  GOIII  G2III  G5III  G8III"
      write/out " FOV    F2V    F5V    F8V    GOV    G5V    G8V"
      write/out " KOI    K1I    K2I    K3I    K5I"
      write/out " KOIII  K2III  K3III  K4III  K5III"
      write/out " KOV    K2V    K3V    K4V    K5V    K7V"
      write/out " MOI    M2I    MOIII  M2III  MOV    M2V    M3V"
      write/out "These spectra are of solar metallicity. Appending the letter"
      write/out "m fits a spectrum of 0.1 solar metallicity."
      write/out "Also, you can select:"
      write/out " ALL - attempts to fit all spectral types."
      write/out " FM - lower mass stars of types F to M."
      write/out " GM - lower mass stars of types G to M."
      write/out " KM - lower mass stars of types K to M."
      write/out " O - all type O models; B - all type B models; etc."
      goto help
   endif

define/local file/c/1/30 ?
define/local file1/c/1/30 ?
define/local file2/c/1/30 ?
define/local file3/c/1/30 ?
define/local name/c/1/30 ?
define/local mspec/c/1/10 ?
define/local ifctrl/i/1/2 0,0
define/local fctrl/i/1/2 0,0
define/local ofctrl/i/1/2 0,0
define/local outrec/c/1/100 ?
define/local one/i/1/1 0
define/local grism/i/1/1 0
define/local year/i/1/1 0
define/local m/i/1/1 0
define/local n/i/1/1 0
define/local min/i/1/1 0
define/local max/i/1/1 0
```

```
define/local ebv/r/1/1 0.0
define/local x/r/1/1 0.0
define/local y/r/1/1 0.0
define/local slope/r/1/1 0.0
define/local chi2/r/1/1 0.0
define/local prechi2/r/1/1 1.0E+10

set/format I4 F18.18,F18.18

! Test to see if a graphics window already exists. If not
! then create one.
n = DAZDEVR(11)
if n .eq. -1 then
   create/graphics
endif
set/graphics pmode=0 frame=square font=1

if P3 .eq. "ALL" then
   $cp models/ALL ./
endif
if P3 .eq. "FM" then
   $cp models/FM ./ALL
   define/local P3/c/1/5 "ALL"
endif
if P3 .eq. "GM" then
   $cp models/GM ./ALL
   define/local P3/c/1/5 "ALL"
endif
if P3 .eq. "KM" then
   $cp models/KM ./ALL
   define/local P3/c/1/5 "ALL"
endif
if P3 .eq. "O" then
   $cp models/O ./ALL
   define/local P3/c/1/5 "ALL"
endif
if P3 .eq. "B" then
   $cp models/B ./ALL
   define/local P3/c/1/5 "ALL"
endif
if P3 .eq. "A" then
   $cp models/A ./ALL
   define/local P3/c/1/5 "ALL"
endif
if P3 .eq. "F" then
   $cp models/F ./ALL
   define/local P3/c/1/5 "ALL"
endif
if P3 .eq. "G" then
   $cp models/G ./ALL
   define/local P3/c/1/5 "ALL"
```

```
endif
if P3 .eq. "K" then
   $cp models/K ./ALL
   define/local P3/c/1/5 "ALL"
endif
if P3 .eq. "M" then
   $cp models/M ./ALL
   define/local P3/c/1/5 "ALL"
endif

if {infile} .eq. 0 then
   compute/key n = M$INDEX(P2,".bdf")
   if n .eq. 0 then
      $ls {P2}.bdf > printtemp.cat
   else
      $ls {P2} > printtemp.cat
   endif
endif

open/file printtemp.cat READ ifctrl
log/off

loop:
   ! Beginning of loop for each spectrum that is to
   ! be analysed.
   write/key file " "
   read/file {ifctrl(1)} file 30
   if ifctrl(2) .lt. 0 goto finish
   if P3 .eq. "ALL" .and. {infile} .eq. 0 then
      open/file ALL READ fctrl
      open/file {file}.fit WRITE ofctrl
   endif
   one = 0
   if {infile} .eq. 1 then
      if P3 .eq. "ALL" then
         open/file ALL READ fctrl
      endif
      if {file} .eq. 1 then
         write/key file " "
         read/file {ifctrl(1)} file 30
         one = 1
         if P3 .eq. "ALL" then
            open/file {file}.fit WRITE ofctrl
         endif
         goto choose_grism
      endif
      if {file} .eq. 2 then
         write/key file1 " "
         read/file {ifctrl(1)} file1 30
         write/key file2 " "
         read/file {ifctrl(1)} file2 30
```

```
         min = 3790
         max = 6970
         write/out "Combining spectra" {file1} "and" {file2}
         if P3 .eq. "ALL" then
            open/file {file2}.fit WRITE ofctrl
         endif
         goto setup
      endif
      if {file} .eq. 3 then
         write/key file1 " "
         read/file {ifctrl(1)} file1 30
         write/key file2 " "
         read/file {ifctrl(1)} file2 30
         write/key file3 " "
         read/file {ifctrl(1)} file3 30
         min = 3790
         max = 9200
         write/out "Combining spectra" {file1} "," {file2} "and" {file3}
         if P3 .eq. "ALL" then
            open/file {file2}.fit WRITE ofctrl
         endif
         goto setup
      endif
   endif

choose_grism:
   ! Set wavelength boundaries for each grism. The grism
   ! used is determined from the image header.
   write/out "Starting spectrum" {file}
   grism = {{file},GRISMNR}
   year = {{file},O_TIME(1)}
   year = year(1:4)
   ! Grism B150
   if {grism} .eq. 10 then
      min = 3790
      max = 5500
   endif
   if {grism} .eq. 4 .and. year .eq. 1996 then
      min = 3790
      max = 5500
   endif
   ! Grism B300
   if {grism} .eq. 2 then
      min = 3750
      max = 6950
   endif
   ! Grism O150
   if {grism} .eq. 4 .and. year .eq. 1995 then
      min = 5230
      max = 6970
   endif
```

```
   ! Grism R300. The maximum value was changed from 9920
   ! to 9200 due to limitations in the Kurucz model spectra.
   if {grism} .eq. 3 then
      min = 6000
      max = 9200
   endif

setup:
   ! The spectrum and the model are prepared so that they
   ! have the same minimum and maximum values and have a
   ! step size equal to 1.
   if P3 .eq. "ALL" then
      write/key mspec " "
      read/file {fctrl(1)} mspec 10
      if fctrl(2) .lt. 0 then
         close/file {fctrl}
         close/file {ofctrl}
         prechi2 = 1.0E+10
         goto loop
      endif
      $cp models/{mspec} ./
      create/table model 2 10001 {mspec}
   else
      $cp models/{P3} ./
      create/table model 2 10001 {P3}
   endif
   create/image model 1,12000 1000,1
   convert/table model = model #1 #2 model SPLINE
   convert/table exti = exti #1 #2 model SPLINE
   extract/image model = model [{min}:{max}]
   extract/image exti = exti [{min}:{max}]
   comp model = model*1.0E+16
   if {infile} .eq. 0 then
      rebin/linear {file} spec ? ? {min}
      extract/image spec = spec [{min}:{max}]
      $cp spec.bdf {file}.spec
   else
      if {one} .eq. 1 then
         rebin/linear {file} spec ? ? {min}
         extract/image spec = spec [{min}:{max}]
         $cp spec.bdf {file}.spec
      else
         rebin/linear {file1} spec1 ? ? 3790
         rebin/linear {file2} spec2 ? ? 5230
         if {file} .eq. 3 then
            rebin/linear {file3} spec3 ? ? 6000
         endif
         $cp model.bdf spec.bdf
         comp spec = 0
         extract/image sub1 = spec1 [3790:5500]
         extract/image sub2 = spec2 [5501:6970]
```

```
         if {file} .eq. 3 then
            extract/image sub3 = spec3 [6971:9200]
            stat sub2 [6960:6970] ? ? RN
            x = outputr(3)
            stat sub3 [6971:6981] ? ? RN
            y = outputr(3)
            comp sub2 = sub2 * ({y}/{x})
         endif
         stat sub1 [5490:5500] ? ? RN
         x = outputr(3)
         stat sub2 [5501:5511] ? ? RN
         y = outputr(3)
         comp sub1 = sub1 * ({y}/{x})
         insert/image sub1 spec
         insert/image sub2 spec
         $rm sub1.bdf sub2.bdf spec1.bdf spec2.bdf
         if {file} .eq. 3 then
            insert/image sub3 spec
            $rm sub3.bdf spec3.bdf
         endif
         $cp spec.bdf {file2}.spec
      endif
   endif

fitting:
   ! Extinction is increasingly applied to the model spectrum
   ! until the slope of the real spectrum divided by the model
   ! spectrum (calculated by linear regression) is
   ! approximately equal to zero.
   comp corr = model/(10**({ebv}*exti/2.5))
   comp fit = spec / corr
   statistics fit ? ? ? RN
   comp fit = fit / {outputr(3)}
   copy/it fit fit wavelength
   regression/linear fit #2 #1 ? >Null
   slope = outputd(2)*1000
   if P3 .ne. "ALL" then
      plot fit
      set/format I4 F18.4,F18.4
      write/out "Current slope is" {slope}
      set/format I4 F18.18,F18.18
   endif
   if {slope} .le. 0 goto complete
   ebv = ebv + 0.01
   goto fitting

complete:
   ! Finished estimating the extinction and now preparations
   ! are made to estimate the spectral type of the star.
   if P3 .ne. "ALL" then
      write/out "Fitting routine complete!"
```

```
      set/format I4 F18.4,F18.4
      write/out "Interstellar extinction is E(B-V) =" {ebv}
      set/format I4 F18.18,F18.18
      write/out "Starting spectral typing routine ..."
   endif
   n = max - 30
   statistics spec [{n}:{max}] ? ? RN
   x = outputr(3)
   statistics corr [{n}:{max}] ? ? RN
   y = outputr(3)
   x = x / y
   comp corr = corr * {x}
   m = min

type_spectrum:
   ! Provide a fit parameter which can be used to determine
   ! the spectral type of the star.
   n = m + 10
   if {n} .gt. {max} goto results
   statistics spec [{m}:{n}] ? ? RN
   x = outputr(3)/10
   statistics corr [{m}:{n}] ? ? RN
   y = outputr(3)/10
   chi2 = chi2 + (x - y)**2
   m = m + 10
   goto type_spectrum

results:
   ! Results are outputed and, if more than one model is
   ! being fitted to the spectrum, are outputed to a file.
   plot spec
   over corr
   if {chi2} .lt. {prechi2} then
      prechi2 = chi2
      if {infile} .eq. 1 .and. {one} .eq. 0 then
         $mv corr.bdf {file2}.model
      else
         $mv corr.bdf {file}.model
      endif
   else
      $rm corr.bdf
   endif
   set/format I4 F18.6,F18.6
   if P3 .eq. "ALL" then
      write/out "Model:" {mspec} ", Fit =" {chi2} ", E(B-V) =" {ebv}
      outrec(1:10) = "{mspec}"
      outrec(11:30) = "{chi2}"
      outrec(31:40) = "{ebv}"
      write/file {ofctrl(1)},key outrec(1:35)
      set/format I4 F18.18,F18.18
      ebv = 0.0
```

```
      chi2 = 0.0
      $rm {mspec}
      goto setup
   else
      write/out "Final fit for model" {P3} "is" {chi2}
      set/format I4 F18.18,F18.18
      $rm {P3}
      ebv = 0.0
      chi2 = 0.0
      prechi2 = 1.0E+10
      goto loop
   endif

finish:
   close/file {ifctrl}
   log/on
   $rm model.bdf model.tbl fit.bdf fit.tbl
   $rm spec.bdf exti.bdf printtemp.cat
   if P3 .eq. "ALL" then
      $rm ALL
   endif
```

Bibliography

[1] Abt, H.A., 1983, ARA&A, **21**, 343

[2] Alard, C., Mao, S., Guibert, J., 1995, A&A, **300**, L17

[3] Alard, C., Lupton, R.H., 1998, ApJ, **503**, 325

[4] Albrow, M., *et al.*, 1996, in Proc. IAU Symp. 173, "Astrophysical Applications of Gravitational Lensing", ed. C. Kochanek & J. Hewitt, p.227

[5] Albrow, M., *et al.*, 1997, ASP Conf. Series, Vol. 119, "Planets Beyond the Solar System and the Next Generation of Space Missions", ed. D. Soderblom, p.91

[6] Albrow, M., *et al.*, 1997, Proc. 12th IAP Colloq., "Variables Stars and the Astrophysical Returns of the Microlensing Surveys", ed. R. Ferlet, J.-P. Maillard, B. Raban, p.135

[7] Albrow, M., *et al.*, 1998, ApJ, **509**, 687

[8] Albrow, M., *et al.*, 1999, ApJ, **522**, 1011

[9] Albrow, M., *et al.*, 1999, in press (astro-ph/9909325)

[10] Albrow, M., *et al.*, 1999, in press (astro-ph/9910307)

[11] Alcock, C., *et al,*. 1993, ASP Conf. Series, Vol. 43, "Sky Surveys: Protostars to Protogalaxies", ed. B.T. Soifer

[12] Alcock, C., *et al.*, 1993, Nature, **365**, 621

[13] Alcock, C., *et al.*, 1995, ApJ, **454**, L125

[14] Alcock, C., *et al.*, 1997, ApJ, **479**, 119

[15] Alcock, C., *et al.*, 1997, ApJ, **486**, 697

[16] Alcock, C., *et al.*, 1998, ApJ, **491**, 436

[17] Alcock, C., *et al.*, 2000, in press (astro-ph/0008282)

[18] Allen, C.W., 1973, "Astrophysical Quantities, 3rd Ed.", (The Athlone Press/University of London)

[19] Aubourg, C., *et al.*, 1993, Nature, **365**, 623

[20] Bennett, D.P., *et al.*, 1994, Proceedings of the 5th Annual October Astrophysics Conference in Maryland, in press (astro-ph/9411114)

[21] Bennett, D.P., Rhie, S.H., 1996, ApJ, **472**, 660

[22] Bertelli, G., *et al.*, 1994, A&AS, **106**, 275

[23] Bolatto, A.D., Falco, E.E., 1994, ApJ, **436**, 112

[24] Buchalter, A., Kamionkowski, M., 1997, ApJ, **482**, 782

[25] Buil, C., 1991, "CCD Astronomy: Construction and Use of an Astronomical CCD Camera", (Willmann-Bell, Inc.)

[26] Cardone, V.F, de Ritis, R., Marino, A.A., 1998, in press (astro-ph/9812037)

[27] Danks, A.C, Dennefeld, M., 1994, PASP, **106**, 382

[28] Di Stefano, R., Esin, A.A., 1995, ApJ, **448**, L1

[29] Dominik, M., 1996, PhD Thesis, Universität Dortmund

[30] Dominik, M., 1998, A&A, **329**, 361

[31] Dominik, M., 1998, A&A, **333**, 893

[32] Dominik, M., 1998, A&A, **333**, L79

[33] Dominik, M., Sahu, K.C., 2000, ApJ, **534**, 213

[34] Dravins, D., 1999, in Proc. IAU Symp. 170, "Precise Stellar Radial Velocities", ed. J.B. Hearnshaw & C.D. Scarfe, p.268

[35] Dwek, E., *et al.*, 1995, ApJ, **472**, 660

[36] Einstein, A., 1936, Science, **84**, 506

[37] Gaudi, B.S., Naber, R.M., Sackett, P.D., 1998, ApJ, **502**, L33

[38] Gaudi, B.S., Gould, A., 1999, ApJ, **513**, 619

[39] Gaudi, B.S., Sackett, P.D., 2000, ApJ, **528**, 56

[40] Gondolo, P., 1999, ApJ, **510**, L29

[41] Gould, A., 1992, ApJ, **392**, 442

[42] Gould, A., Loeb, A., 1992, ApJ, **396**, 104

[43] Gould, A., 1997, ApJ, **483**, 98

[44] Gould, A., 1999, ApJ, **517**, 719

[45] Griest, K., *et al.*, 1991, ApJ, **372**, L79

[46] Griest, K., Hu, W., 1992, ApJ, **397**, 362

[47] Grison, P., *et al*, 1995, A&AS, **109**, 447

[48] Han, C., Gould, A., 1995, ApJ, **449**, 521

[49] Han. C., Gould, A., 1997, ApJ, **480**, 196

[50] Han, C., Jeong, Y., 1998, MNRAS, **301**, 231

[51] Jacoby, G.H., Hunter, D.A., Christian, C.A., 1984, ApJS, **56**, 257

[52] Jeong, Y., Han, C., Park, S.-H., 1999, ApJ, **511**, 569

[53] Kane, S., Sahu, K.C., 2000, in preparation

[54] Kiraga, M., Paczyński, B., 1994, ApJ, **430**, L101

[55] Kroupa, P., Tout, C.A., Gilmore, G., 1993, MNRAS, **262**, 545

[56] Kurucz, R., 1970, "Atlas: A computer program for calculating model stellar atmospheres", SAO Special Report, Cambridge: Smithsonian Astrophysical Observatory

[57] Kurucz, R., 1993, ATLAS9 Stellar Atmosphere Programs and 2 km/s grid. Kurucz CD-ROM No. 13. Cambridge, MA: Smithsonian Astrophysical Observatory

[58] Lennon, D.J., *et al.*, 1996, ApJ, **471**, L23

[59] Manduca, A., Bell, R.A., Gustafsson, B., 1977, A&A, **61**, 809

[60] Mao, S., Paczyński, B., 1991, ApJ, **374**, L37

[61] Mao, S., Di Stefano, R., 1995, ApJ, **440**, 22

[62] Mao, S., Paczyński, B., 1996, ApJ, **473**, 57

[63] Mao, S., Reetz, J., Lennon, D.J., 1998, A&A, **338**, 56

[64] Mao, S., Witt, H.J., 1998, MNRAS, **300**, 1041

[65] Mao, S., 1999, A&A, **350**, L19

[66] Maoz, D., Gould, A., 1994, ApJ, **425**, L67

[67] Meeus, J., 1991, "Astronomical Algorithms", (Willmann-Bell)

[68] Méra, D., Chabrier, G., Schaeffer, R., 1998, A&A, **330**, 937

[69] Mollerach, S., Roulet, E., 1996, ApJ, **458**, L9

[70] Morgan, W.W., Keenan, P.C., Kellman, E., 1943, "An Atlas of Stellar Spectra with an Outline of Spectral Classification" (University of Chicago Press)

[71] Morse, J.A., Mathieu, R.D., Levine, S.E., 1991, AJ, **101**, 1495

[72] Nair, V., Miralda-Escudé, J., 1999, ApJ, **515**, 206

[73] Nelder, J.A., Mead, R., 1965, Computer Journal, **7**, 308

[74] Paczyński, B., 1986, ApJ, **304**, 1

[75] Paczyński, B., 1991, ApJ, **371**, L63

[76] Paczyński, B., *et al.*, 1994, AJ, **107**, 2060

[77] Paczyński, B., *et al.*, 1994, ApJ, **435**, L113

[78] Paczyński, B., 1996, Ann. Rev. Astron. Astrophys., **34**, 419

[79] Paczyński, B., 1997, in press (astro-ph/9711007)

[80] Paczyński, B., Stanek, K.Z., 1998, ApJ, **494**, L219

[81] Peale, S.J., 1997, Icarus, **127**, 269

[82] Press, W.H, Teukolsky, S.A., Vetterling, W.T., Flannery, B.P., 1994, "Numerical Recipes in FORTRAN, 2nd Ed.", (Cambridge University Press)

[83] Rhie, S.H., *et al.*, 1999, in press (astro-ph/9905151)

[84] Sahu, K.C., 1994, PASP, **106**, 942

[85] Sahu, K.C., 1994, Nature, **370**, 275

[86] Sahu, K.C., Sahu, M.S., 1998, ApJ, **508**, L147

[87] Sackett, P.D., 1998, NATO-ASI Series, "Planets outside the Solar System: Theory and Observations", ed. J.-M. Mariotti &D. Alloin, in press (astro-ph/9811269)

[88] Savaglio, S., Benetti, S., Pasquini, L., 1997, "EFOSC1 Operating Manual", downloadable from `www.eso.org`

[89] Schechter, P.L., Mateo, M., Saha, A., 1993, PASP, **105**, 1342

[90] Schmidt-Kaler, T., 1982, BICDS, **23**, 2

[91] Schneider, P., Weiss, A., 1986, A&A, **164**, 237

[92] Schneider, P., Ehlers, J., Falco, E.E., 1992, "Gravitational Lensing", (Springer-Verlag)

[93] Seaton, M.J., 1979, MNRAS, **187**, 73p

[94] Stanek, K.Z., *et al.*, 1994, ApJ, **429**, L73

[95] Stanek, K.Z., 1995, ApJ, **441**, L29

[96] Stanek, K.Z., 1996, ApJ, **460**, L37

[97] Sutherland, W., 1998, Rev. Mod. Phys. 'Colloquium' article, in press (astro-ph/9811185)

[98] Szymański, M., Udalski, A., 1993, Acta Astron., **43**, 91

[99] Terndrup, D.M., 1988, AJ, **96**, 884

[100] Tonry, J., Davis, M., 1979, AJ, **84**, 1511

[101] Torres-Dodgen, A.V., Weaver, W.B., 1993, PASP, **105**, 693

[102] Tytler, D., 1996, Jet Propulsion Laboratory Publication 92-22, Pasadena, CA

[103] Udalski, A., *et al.*, 1993, Acta Astron., **43**, 69

[104] Udalski, A., *et al.*, 1993, Acta Astron., **43**, 289

[105] Udalski, A., *et al.*, 1994, Acta Astron., **44**, 165

[106] Udalski, A., *et al.*, 1994, Acta Astron., **44**, 227

[107] Udalski, A., *et al.*, 1994, ApJ, **436**, L103

[108] Udalski, A., Kubiak, M., Szymański, M., 1997, Acta Astron., **47**, 319

[109] Udry, S., *et al.*, 1999, in Proc. IAU Symp. 170, "Precise Stellar Radial Velocities", ed. J.B. Hearnshaw & C.D. Scarfe, p.383

[110] Vietri, M., Ostriker, J.P., 1983, ApJ, **267**, 488

[111] Walker, M.A., 1997, MNRAS, **287**, 629

[112] Waterworth, M.D., 1980, Proc. ASA, **4**, (1), p.14

[113] Weilen, R., Jahreiss, H., Krüger, R., 1983, in IAU Colloq. 76, "The Nearby Stars and the Stellar Luminosity Function", ed. A.G. Davis Philip & A.R. Upgren (Schenectady: Davis), p.163

[114] Witt, H.J., 1990 A&A, **236**, 311

[115] Witt, H.J., Mao, S., 1994, ApJ, **430**, 505

[116] Witt, H.J., Mao, S., 1995, ApJ, **447**, L105

[117] Woźniak, P., Paczyński, B., 1997, ApJ, **487**, 55

[118] Woźniak, P., Szymański, M., 1998, Acta Astron., **48**, 269

[119] Zhao, H., Spergel, D.N., Rich, R.M., 1995, ApJ, **440**, L13

[120] Zhao, H., Mao, S., 1996, MNRAS, **283**, 1197